A STUDY OF RESPIRATOR CARBONS

by

Jock W.H. Smith

Submitted in partial fulfillment of the requirements
for the degree of Doctor of Philosophy

at

Dalhousie University
Halifax, Nova Scotia
August 2012

DALHOUSIE UNIVERSITY

DEPARTMENT OF PHYSICS AND ATMOSPHERIC SCIENCE

The undersigned hereby certify that they have read and recommend to the Faculty of Graduate Studies for acceptance a thesis entitled "A STUDY OF RESPIRATOR CARBONS" by Jock W.H. Smith in partial fulfillment of the requirements for the degree of Doctor of Philosophy.

Dated: August 27, 2012

External Examiner: ____________________

Research Supervisor: ____________________

Examining Committee: ____________________

____

Departmental Representative: ____________________

DALHOUSIE UNIVERSITY

DATE: August 27, 2012

AUTHOR: Jock W.H. Smith

TITLE: A STUDY OF RESPIRATOR CARBONS

DEPARTMENT OR SCHOOL: Department of Physics and Atmospheric Science

DEGREE: Ph.D. CONVOCATION: May YEAR: 2013

Signature of Author

I would like to dedicate this thesis to my mother, Bonnie Darlene Smith

Table of Contents

List of Tables

List of Figures

Abstract

Porous, high surface area activated carbon (AC) can be used to remove certain irritating and toxic gases from contaminated air streams. Impregnating AC with carefully selected chemicals can improve ACs adsorption capacity for certain gases and provide adsorption capacity for gases that un-impregnated AC cannot filter. Impregnated activated carbons (IACs) and ACs can be used as the active component in respirators.

Comparative studies of different commercially available AC samples and of IAC samples, prepared from a wide variety of different chemicals, were performed. The gas adsorption capacity of the samples was tested using sulfur dioxide (SO_2), ammonia (NH_3), hydrogen cyanide (HCN) and cyclohexane (C_6H_{12}) challenge gases and compared to results obtained from a commercially available broad spectrum respirator carbon. The samples were characterized using wide angle x-ray diffraction (XRD), small angle x-ray scattering (SAXS), nitrogen adsorption isotherms, thermal gravimetric analysis (TGA) and scanning electron microscopy (SEM).

Highlights of this work include the discovery of a IAC sample prepared from zinc nitrate ($Zn(NO_3)_2$) and nitric acid (HNO_3) that, after heating at 180°C under argon, had overall dry gas adsorption capacity that was greater than the commercially available sample. The importance of pore size on the C_6H_{12} adsorption capacity of AC was demonstrated using SAXS and nitrogen adsorption data. A relationship between decreased humid C_6H_{12} capacity and pre-adsorbed water was shown using SAXS, TGA and gravimetric studies.

List of Abbreviations and Symbols Used

α	Scale parameter in Weibull distribution
β	Measured full width at half maximum intensity of diffraction peak
γ	Surface tension
$\gamma(\mathbf{r})$	Autocorrelation function
θ	Scattering angle
Θ	Contact angle
λ	Wavelength
μ	Mean value
μ/ρ	Mass absorption coefficient
ρ	Density
$\rho\ _e$	Electron density
$\Delta\rho\ _e$	Difference in electron density
σ	Standard deviation
χ^2	Goodness of fit parameter
ω	Cross sectional area of probe molecule used in gas adsorption porisometry
a	Autocorrelation length
A	Constant proportional to macropore surface area in the Kalliat equation
A($\mathbf{q}$)	Scattered amplitude
$\mathrm{att}_{calc.}$	Calculated attenuation factor
$\mathrm{att}_{exp.}$	Experimentally determined attenuation factor
B	Constant proportional to micropore surface area in the Kalliat equation
c	Speed of light
C	Constant used in the Brunauer-Emmett-Teller equation

$\bar{d}_{SAXS}$	Average pore diameter determined from small angle x-ray scattering data
DFT	Density Functional Theory
DSC	Differential Scanning Calorimetry
EDX	Energy Dispersive X-Ray Analyzer
$f(x_i)$	Fit to the data at the i^{th} data point
G(a)	Gaussian distribution function
ΔH_A	Enthalpy of adsorption
ΔH_L	Enthalpy of liquification
I_o	Intensity of the incoming x-ray beam
$I(\mathbf{q})$	Intensity as a function of scattering vector
I_x	Intensity of the scattered x-ray beam
IR	Infrared detector
k	Shape parameter in Weibull distribution
$\mathbf{k}$	Incoming wave vector
$\mathbf{k'}$	Scattered wave vector
K	Fitting factor used in Scherrer equation
l	Sample thickness
L_{hkl}	Mean crystallite dimension estimated from Scherrer equation
M_V	Volume occupied by one mole of ideal gas at STP
N_A	Avogadro's constant
ppm	Parts per million
P	Pressure
P_o	Saturated vapour pressure
$\mathbf{q}$	Scattering vector
R	Universal gas constant
R_g	Radius of gyration
sccm	Standard cubic centimeter per minute
SAXS	Small Angle X-Ray Scattering
S_{BET}	Brunauer-Emmett-Teller surface area

SEM	Scanning Electron Microscopy
STP	Standard Temperature and Pressure
T	Temperature
T_f	Maximum final heating temperature
TGA	Thermogravimetric Analysis
ΔTGA	Derivative Thermogravimetric Analysis data
UHP	Ultra High Purity
V	Volume
V_m	Monolayer adsorption capacity
$\bar{w}_{Area}$	Area weighted average pore width
w_f	Final mass
w_i	Initial mass
w_n	Mass fraction
$\bar{w}_{Vol}$	Volume weighted average pore width
W(a)	Weibull distribution function
XRD	Wide angle x-ray diffraction
y_i	The i^{th} data point

Acknowledgements

I would like to thank the Natural Sciences and Engineering Research Council of Canada, and 3M Canada Company for their generous financial support of this research.

I would like to thank my supervisor, Dr. Jeff Dahn, for his generous financial support, encouragement and guidance. I have had many useful discussions and arguments with Dr. Dahn over the last several years that have been very helpful to my development as a researcher. Working in Dr. Dahn's lab has allowed me to access state of the art research equipment and have contact to world class researchers in industrial and academic fields.

I would like to thank Dr. Ian Hill and Dr. Harm Rotermund for their useful suggestions and comments while serving on my thesis supervisory committee. I wish to thank former Dahn lab members Dr. Hubert Fortier and Dr. Philippe Westreich for their valuable contributions to the respirator carbon project. In particular I would like to acknowledge Dr. Fortier's design of the dynamic flow testing apparatus and the software he wrote to allow for computerized data acquisition. I would like to thank Dr. Jennifer Romero for her contributions to the respirator carbon project. I would like to extend my thanks to all the people who have worked on the respirator carbon project, past and present. Matt Mcdonald, Landan MacDonald, Braden Sullivan, Tara Dahn, Matthew Mallay and Kevin Dunphy have all made direct contributions to the work presented in this thesis. I would like to thank Dr. David Stevens and Dr. Robbie Sanderson for always making time to assist me, no matter how busy their schedules were. I would like to extend my sincere thanks for all present and former members of the Dahn lab for their assistance and support during my time as a graduate student.

I would like to thank the present and former staff in the Department of Physics and Atmospheric Science for their assistance during my time, it was greatly appreciated. Thank you to Anne Murphy, Barbara Gauvin, Anne-Marie Jeffery, Krista Cullymore, Tanya Timmins, Jennifer Currie and Heather Anne Jennex in the physics office. I would also like to thank Andy George, Kevin Borgel and Simon Trussler for their help and advice. I would like to extend my thanks to Patricia Scallion for her assistance using the SEM. I have received a great deal of help and support during my years at Dalhousie and am sure I have missed some people in my acknowledgments, to those people I say thank you and apologize for my forgetfulness.

During this research project I have had the privilege of collaborating with workers at 3M Canada Company and 3M. I would like to thanks Dr. Lisa Croll and Dr. Simon Smith at 3M Canada for their tremendous contributions to this project over the years. Special thanks to Carrie Andress and Monika Simon for their gas testing expertise. Carrie has been very helpful in co-ordinating sample shipments to and from the Brockville facility as well. I would like to thank all of the scientists, engineers, managers and other staff at 3M who allowed us to participate in the annual sorbent summit. In particular Dr. Tom Wood, Dr. Allen Siedle, Dr. Larry Brey and Dr. Kevin Frankel have offered suggestions, advice and materials that have had a direct impact on this project.

I would like to thank my family and friends for all of their support and assistance during my graduate studies. Thanks go out my brother Matthew, his wife Amber and their boys Archer, Lexx, and Nolan for being there for me whenever it was needed. I look forward to the frequent phone calls and visits at the beach immensely. A very special thank you to Carol and Jav Stevenson for providing support (and shelter) whenever it was required.

Finally I would like to thank my wife, Catherine and son, Oren for everything.

Halifax, August 2012

Jock W. H. Smith

Chapter 1

Introduction

1.1 Background

Activated carbon (AC) has numerous applications in modern society. Examples are their use in energy storage devices such as super-capacitors [1–3], water filtration [4] and adsorption of irritating or toxic gases from contaminated airstreams [5] to name a few. It is beyond the scope of this document to review all of these applications. A brief review of AC materials for gas mask applications, focusing mainly on multi-gas adsorption, will be presented here.

The use of AC to remove toxins from the air has been reported as early as 1793 when it was employed to reduce odours caused by gangrene [4]. One of the earliest reported gas masks to use carbonaceous materials was invented by John Stenhouse in 1854 [6]. This early mask was capable of removing hydrogen sulphide (H_2S), ammonia (NH_3) and chlorine (Cl_2) gases from the air. The AC substrate can also be impregnated with chemicals. These types of materials are known as impregnated activated carbons (IACs). It is generally accepted that the greatest amount of research involving AC or IAC began after the advent of modern chemical warfare during World War I [4]. Early work in preparing IACs with metal and metal oxide impregnants was largely focused on the removal of chemical warfare agents such as arsine (AsH_3), phosgene (CCl_2O) and hydrogen cyanide (HCN). One of the earliest reports of this work was captured in the patent by Wilson and Whetzel [7] where they reported impregnating AC with oxides of copper, zinc or metallic silver. Materials prepared using methods similar to Wilson and Whetzel are still known as Whetlerites. Some shortcomings of the early Whetlerites were their inability to capture NH_3 and the generation of the toxic by-product, cyanogen (NCCN), when challenged with HCN gas. In the presence of Cu^{2+} impregnant (e.g. copper oxide (CuO) or copper carbonate) HCN gas is oxidized via the net reaction [4, 8]:

$$\mathrm{CuO(s) + 2HCN(g) \rightarrow CuCN(s) + \tfrac{1}{2}NCCN(g) + H_2O(l)} \qquad (1.1)$$

To control the generation of NCCN gas, hexavalent chromium (Cr^{6+}) or molybdenum (Mo^{6+}) compounds can be co-impregnated with the Cu^{2+} species. The most common procedure to prepare IACs of this type was to use ammonium salts and/or ammonium hydroxide to dissolve and distribute the metallic salts. One of the largest collections of work detailing the physical, chemical and adsorptive properties of IACs prepared in this manner was reported in 1946 by the U.S. National Defence Research Committee [9]. Detailed reports of IACs impregnated with Cu^{2+}/Cr^{6+} for the removal of HCN from airstreams have been presented in the literature [4, 8, 10]. Hexavalent chromium is environmentally damaging and a human carcinogen [11,12] so it is desirable to avoid using it in respiratory devices. Work detailed in the patent by Doughty et al [13] outlines an improved method of preparing IACs capable of HCN/NCCN adsorption by replacing toxic Cr^{6+} compound(s) with Mo^{6+} in the impregnating solution.

The IACs described in Ref. [13] are also impregnated with a sulphate (${SO_4}^{2-}$)-containing compound to chemisorb NH_3 gas. This was a major advancement over earlier Whetlerite formulations. The work described in Ref. [13] has been assigned to Calgon Carbon Corporation (Pittsburgh, Pa). Commercially produced multi-gas IACs prepared using this method are known as Universal Respirator Carbons (URC). These IACs are widely used in both industrial and military applications. The gas adsorption capacity of IAC samples prepared in this project were directly compared to URC.

An improvement to the URC process was reported in the patent by Brey et al [14]. In this work the authors showed that a hexavalent tungsten (W^{6+})-containing compound can be substituted for the Mo^{6+} compound without losing HCN/NCCN adsorption capability.

A major disadvantage of the traditional Whetlerite process is its reliance on ammonium salts and/or ammonia-based solutions to dissolve and distribute the metallic impregnants. Impregnating samples with ammonium salts or ammonia-based impregnating solution produces large amounts of gaseous and liquid waste which are expensive to manage from both an economic and environmental standpoint. In addition, ammonia is considered a toxic substance in some jurisdictions [15] so zoning for industrial processing of IACs prepared from NH_3-based solutions may also be an issue. There have also been some reported cases of NH_3 desorption from Whetlerite IACs [16]. Desorption of NH_3 can cause discomfort and respiratory tract irritation to the user of the gas mask.

Much of the IAC research reported in the literature focuses only on materials characterisation or gas testing results of only one or two challenge gases [10, 17–20]. More information on multi-gas IACs has been presented in the form of books, reports and patents [4, 9, 13, 14, 21], but these documents are sometimes difficult to access or lacking in scientific detail. Previous studies of IACs performed in the Dahn group have reported gas test results for many challenge gases [22–25] and this tradition is continued in the work of this thesis. In a serious study of IACs capable of multi-gas adsorption, it is important to include gas testing results for multiple challenge gases in the study.

1.2 Motivation

High levels of industrialization in the developed world and rapid increases in the level of industrialization in developing nations such as China and India require a large workforce. Keeping industrial workers safe and healthy makes sense from both humanitarian and financial perspectives. Injured workers can create strains on the health care system and cause decreased productivity for their employer. Research and development of respiratory protection devices, such as gas masks, plays an important role in protecting the health of industrial workers and making sure they are adequately protected as technology evolves. In North America, agencies such as the National Institute for Occupational Safety and Health (NIOSH) set respirator standards [26]. The safety standards in emerging nations such as China are far less stringent, but improvements in respirator standards have been recently reported [27]. As respirator standards are improved in emerging economies there will be great financial opportunities for companies that provide respiratory protection devices.

Industrial accidents and political instability are two other reasons why it is important to continue research and development of gas masks and other protective devices. The disaster at Japan's Fukushima Daiichi nuclear reactor [28] should serve as a reminder of the importance of being able to respond quickly to industrial accidents. Political instability in countries with chemical weapon stockpiles, such as Libya [29], can pose a serious threat to populations throughout the world. First responders, military personnel, or workers responding to an industrial accident may not immediately know the type of airborne contaminant they are being exposed to. In this type of situation, providing a gas mask capable of multi-gas adsorption offers better respiratory protection to the responder and allows shorter response times. The goal of this research project is to discover, characterize and optimize IACs capable of multi-gas adsorption for respirator carbon applications.

1.3 Some Properties of Activated Carbon

Activated carbon (AC) can be prepared from cheap, readily available materials such as coal, wood, sugar, fruit pits and shells to name a few. The selection criteria for precursor materials is discussed in more detail in the literature [4]. The precursor is heated at high temperature in an oxygen deprived environment to char it [30]. The carbonaceous material is then activated by either physical or chemical means [30, 31]. Typically either oxygen (O_2), carbon dioxide (CO_2) or steam (H_2O) is used in the physical activation process. Common chemicals used in chemical activation are phosphoric acid (H_3PO_4), zinc chloride ($ZnCl_2$) or potassium hydroxide (KOH) [4]. Activation is performed at elevated temperatures, typically in the range of 400°C - 1100°C [30]. The carbon content of the AC depends on the precursor used and is usually high, on the order of 95% atomic carbon for materials produced from coconut shells, for example. Typical impurities found in AC are potassium, sodium, aluminium, silicon and/or iron oxides [30]. The amount of impurity in an activated carbon can be determined gravimetrically from its ash content (remaining mass after burning the carbon).

Controlling parameters such as heating temperature, activation type and amount of carbon burn off allows control of the surface area and distribution of pore sizes of

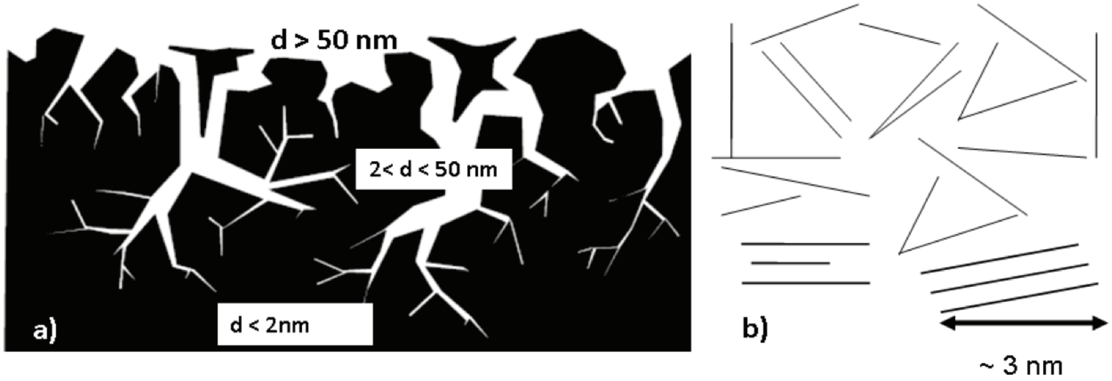

Figure 1.1: Panel (a) shows a representation of the pore size distribution for a typical AC absorbent. Panel (b) shows a schematic diagram of activated carbon based on the "House of Cards" model. The solid lines in panel (b) represent single graphene sheets. Panels (a) and (b) are based on diagrams in Ref. [4] and Ref. [2] respectively.

the AC [2,4,31]. Pore size distributions have been classified in the following manner: (1) Micropores which have widths less than 2 nm, (2) Mesopores with widths ranging from 2 nm to 50 nm, and (3) Macropores with widths larger than 50 nm [32,33]. The system of pores in AC determines its ability to transport and physically adsorb gases. Figure 1.1(a) shows a representative diagram of the pore distribution in an AC. The specific surface area (m^2/g) of AC is most commonly reported using the models of Langmuir [34] or Brunauer, Emmett and Teller (BET) [35]. Typical reported surface areas for AC are on the order of 1000 m^2/g [30,31], however BET surface areas as high as 2000 - 3000 m^2/g have been reported [4,36,37]. For reference, the calculated surface area of a single graphene sheet is approximately 2630 m^2/g. Reported surface areas higher than theoretical values are due to shortcomings of the models used to calculate them [4].

Another important parameter of the final AC product is its surface chemistry. Surface chemistry of the AC substrate can be influenced either during activation, or by post treatments after activation. The surface chemistry of AC can have great influence over its adsorptive properties. A useful discussion of the importance of surface chemistry is provided by Bandosz and Ania [4].

The allotropic form of carbon that AC is most similar to is hexagonal graphite [4], however it does not exhibit the long range periodic order or well ordered stacking that are present in graphite. The “House of Cards” model presented by Dahn et al [2] provides a useful conceptual description of the physical structure of AC. Figure 1.1(b) shows a schematic diagram of AC based on the “House of Cards” model. The solid lines represent single graphene sheets. Parallel lines represent regions in the AC that exhibit higher order.

The high surface area, wide distribution of pore sizes, and low cost make AC well-suited for gas adsorption applications. Un-impregnated AC is capable of physically adsorbing certain gases, mainly organic vapours [5, 38]. Strategically selected chemicals can be impregnated to enhance ACs adsorption capacity for certain gases and allow IAC samples to adsorb toxins that un-impregnated AC cannot.

1.4 Structure of this Thesis

The work presented in this thesis was performed to discover, optimize, and better understand multi-gas IACs. Chapter 2 describes the experimental methods and theoretical considerations that were used in this study.

Chapter 3 describes the materials used in this work. A comparative study of commercially available ACs is presented. An experimental study was performed on the commercially available URC sample to better understand the product that was used as a comparative standard for our IAC samples.

Chapter 4 describes a comparative study of IAC samples prepared from different metallic nitrate precursors. The importance of sample heating temperature is discussed. Wide angle x-ray diffraction experiments were performed on the IAC samples to identify the dominant impregnant species after heating. Dynamic flow tests were performed to allow the overall gas adsorption capacity of the IAC samples to be ranked.

Chapter 5 describes a comparative study of IACs prepared from aqueous copper nitrate ($Cu(NO_3)_2$) and zinc nitrate ($Zn(NO_3)_2$) solutions. The concentration of the $Cu(NO_3)_2$ (or $Zn(NO_3)_2$) solutions was 2.4 M. The effects of co-impregnating the samples with HNO_3 and heating the samples at different temperatures were studied. XRD data was collected to identify the dominant impregnant phase after heating and to study the dispersion of the impregnant on the AC substrate. IACs were flow tested under dry and humid conditions. The most effective multi-gas IACs were found to be samples prepared from 2.4 M $Cu(NO_3)_2$ and 4 M HNO_3 or 2.4 M $Zn(NO_3)_2$ and 4 M HNO_3 solutions that were heated at 180°C under argon.

Chapter 6 describes a comparative study of IACs prepared from $Cu(NO_3)_2$ or $Zn(NO_3)_2$ solutions. The effect of impregnant loading, co-impregnation with different concentrations of HNO_3 and effect of different heating temperatures were studied for samples prepared from aqueous $Cu(NO_3)_2$ solutions. The effect of heating the IACs at different temperatures was studied for IACs prepared from 2.4 M $Zn(NO_3)_2$/4 M HNO_3 solutions. SAXS, XRD, contact angle measurements and nitrogen adsorption isotherms were used to charecterize the IACs in this study. Dynamic flow testing was performed to determine the multi-gas adsorption capacity of the Cu-based samples. Good agreement was observed in results obtained from XRD and SAXS measurements and between SAXS and nitrogen adsorption isotherm measurements. Good impregnant dispersion was found to result in improved SO_2, NH_3 and HCN adsorption capacity for the Cu-based IACs.

Chapter 7 presents work that demonstrated the effect of co-impregnation with mixed metal nitrate precursors and phosphomolybdic acid on broad spectrum respirator carbons. In the first section of this chapter a comparative study of IACs prepared from $Cu(NO_3)_3$ co-impregnated with different metal nitrate precursors and phosphomolybdic acid ($H_3PO_4{\bullet}12MoO_3$) is described. The goal of this work was to observe the effect that co-impregnation with $H_3PO_4{\bullet}12MoO_3$ had on overall gas adsorption capacity and to identify materials that were active when co-impregnated with the Cu^{2+} species.

In the second section of chapter 7, a comparative study of IACs prepared from $Cu(NO_3)_2$ and $Mn(NO_3)_2$ or $Zn(NO_3)_2$ and $Mn(NO_3)_2$ is described. These materials were studied to determine if the different impregnant species interacted during thermal treatments and what, if any, effect this had on multi-gas adsorption capacity.

In the final section of chapter 7, a comparative study of IACs prepared from $Cu(NO_3)_2$, $Zn(NO_3)_2$, HNO_3 and $H_3PO_4{\bullet}12MoO_3$ is described. The IACs are studied as a function of impregnant loading to determine the optimal mixture of the $Cu(NO_3)_2$, $Zn(NO_3)_2$ and $H_3PO_4{\bullet}12MoO_3$ precursors for preparing multi-gas IACs.

Chapter 8 describes a comparative study of IACs co-impregnated with $Zn(NO_3)_2$ and different acids. The IACs were heated at temperatures sufficient to promote thermal decomposition of the $Zn(NO_3)_2$ to ZnO. Gravimetric and XRD analysis were used to identify the dominant impregnant phase present on the IAC after heating. XRD analysis was used to study impregnant distribution. The dry gas adsorption of the samples was tested using SO_2, NH_3 and HCN challenge gases. Humid flow tests were performed using C_6H_{12} challenge gas. The interactions between the co-impregnated acid and $Zn(NO_3)_2$ precursor during heating are discussed. The relationship between impregnant species, impregnant dispersion and gas adsorption capacity are discussed.

Chapter 9 describes a comparative study of IACs prepared from $Zn(NO_3)_2$ or $Cu(NO_3)_2$ and different types of co-impregnated sugars. The motivation for this study was to prepare IACs with improved humid C_6H_{12} adsorption without losing adsorption capacity for SO_2, NH_3 and HCN gases. Promising results were obtained from IACs prepared from $Zn(NO_3)_2$ / copper D-gluconate ($C_{12}H_{22}CuO_{14}$) solutions and $Cu(NO_3)_2$ / gluconic acid ($C_6H_{12}O_7$) - or $Zn(NO_3)_2$ / $C_6H_{12}O_7$-containing solutions (after appropriate thermal treatments were applied). Certain samples had improved humid C_6H_{12} adsorption capacity, but did not exhibit improved overall multi-gas performance compared to URC or HNO_3 co-impregnated IACs. XRD and SAXS data were used to demonstrate some of the advantages and difficulties encountered when preparing IACs with co-impregnated sugars.

Chapter 10 describes a comparative study of IACs prepared using impregnants chosen to improve humid C_6H_{12} adsorption. Certain IACs prepared from single component imbibing solutions (with appropriate thermal treatments) had better humid C_6H_{12} adsorption than un-impregnated GC. When the C_6H_{12}-targeting impregnants were combined with other multi-gas impregnants, the improved humid C_6H_{12} adsorption capacity was not retained.

Chapter 2

Experimental and Theoretical Considerations

Section 2.7 has been included in a manuscript submitted for publication in the journal Carbon. The manuscript title is “Small and wide angle X-ray studies of impregnated activated carbons”. The authors are Jock Smith, Matt Mcdonald, Landan MacDonald, Jennifer Romero and Jeff Dahn. The contribution of Jock Smith consists of the organization of all experiments, preparation and X-ray analysis of all IAC samples, all of the data analysis and preparation of the figures and manuscript. The figures and tables have been reproduced by permission of the journal in accordance with the terms of the publishing company (Elsevier) copyright release (see Appendix A). Some of the text, figure numbers and references have been modified for inclusion in this thesis.

2.1 Sample Preparation

Commercially available ACs were used exclusively in this work. The most commonly used AC was Kuraray GC (available from Kuraray Chemical Co., Osaka, Japan). In this dissertation Kuraray GC will be referred to as ’GC’. Details of this AC are provided in Section 3.1. The incipient wetness (imbibing method) was used to prepare all of the IAC samples reported in this work. Prior to impregnation the AC was dried at 120°C in air to remove excess moisture. A known mass of AC (typically 10-15 g) was placed in a Mason jar and a pipette was used to dispense a known volume of impregnating solution on the AC. The jar was then sealed and shaken for 30-60 s. After shaking, the contents of the jar were visually inspected. If the carbon appeared dry, more impregnating solution was added and the above process was repeated. Once the impregnated AC became wet and barely stuck to the sides of the jar, but no excess solution was visible, the sample was deemed to have reached its imbibing limit. Detailed descriptions of the imbibing method have been reported previously [39–41].

After impregnation the IACs were heated either in air or under flowing argon depending on the sensitivity of the impregnated sample to air exposure during heating. Typically a 10-15 g sample would be held at the maximum final heating temperature (T_f) for 2-3 hrs. The IACs were then allowed to return to room temperature prior to further handling. Heating temperatures used in this work ranged from $120^\circ \leq T_f \leq 500^\circ$ and are clearly indicated where appropriate.

The impregnant loading after heating was determined either gravimetrically (% loading (wt.)) or predicted from the volume and concentration of impregnating solution added (predicted % loading (wt.) or mmol impregnant/g AC). The % loading is calculated using:

$$\% \text{ loading (wt.)} = [(\text{mass}_{final} - \text{mass}_{initial})/\text{mass}_{initial}]\cdot 100\% \tag{2.1}$$

where mass_{final} is the mass of the IAC after heating (g) and $\text{mass}_{initial}$ is the mass of the AC prior to the heating step (g). The uncertainty associated with the % loading (wt.) is 2 - 3 % primarily due to the inability to avoid some exposure to moist air while weighing and storing the samples. The uncertainty on the predicted % impregnant loading is ± 2%. The relative uncertainty on the predicted amount of impregnant is ± 0.1 mmol impregnant/g AC.

2.2 Dynamic Flow Testing

Dynamic flow testing was performed using sulphur dioxide (SO_2), NH_3, cyclohexane (C_6H_{12}) and HCN challenge gases. Flow test results denoted as “dry” had challenge gas streams with a relative humidity (RH) $\leq$ 15%. In-line humidity measurments performed using a handheld humidity detector (HMI41 indicator, Vaisala) showed the tank air had $\leq$ 5% RH. Measurments on the SO_2 or NH_3 gases were not performed to avoid damaging the detector. The actual RH of the dry challenge gas stream is likely $\approx$ 5% RH. Flow test results denoted as “wet” or “humid” had challenge gas streams with RH = (80 ± 5)% . The SO_2 and NH_3 tests were performed at Dalhousie University.

The flow test system used in this work was designed by Dr. Hubert Fortier during his PhD work in the Dahn lab and has been described in the literature [22,39,40]. The

SO_2 and NH_3 gases were supplied by Praxair (Dartmouth, Nova Scotia, Canada) and were of certified standard grade. The gas streams used for flow testing were prepared by diluting 5000 ppm SO_2 or NH_3 with air to obtain a (1000 ± 50) ppm challenge gas stream flowing at (200 ± 5) sccm. The flow of gases was monitored using rotameters obtained from Cole-Parmer. The IAC sample was exposed to the challenge gas and the effluent gas stream was bubbled into a scrubbing solution containing approximately 0.5 g of either sodium chloride (NaCl) or potassium chloride (KCl) dissolved in 100 mL of deionized water. The pH of the scrubbing solution was monitored using a single junction silver/silver chloride (Ag/AgCl) pH electrode. The uncertainty on the pH measurement is ± 0.03 pH units at 25°C. A computerized data collection system collects data points every (4 ± 1) s. Full details of the data acquisition system are provided in Ref. [40]. The breakthrough time, or time that the challenge gas had penetrated the carbon bed, was chosen as the time when 36 ppm SO_2 (or 3.6 ppm NH_3) was detected in the scrubbing solution. The breakthrough times reported for IACs tested versus SO_2 and NH_3 are an average of 2-4 measurements for each sample. Representative pH versus time curves for the challenge gas being bubbled directly into scrubbing solution or passing through AC and IAC samples have been reported in the literature [22, 39, 40, 42].

Figure 2.1 shows dry SO_2 and NH_3 flow test results obtained from flow testing GC activated carbon. GC was the base carbon most often used for preparation of IAC samples and was also used as a calibration standard for gas testing. Each data point represents the monthly average breakthrough time for the respective gas. The error bars represent the standard deviation from that value. The results shown span the time range from December 2010 to February 2012. The data presented in Figure 2.1 is based on over 250 individual SO_2 and NH_3 gas tests.

Figure 2.1 shows small month to month deviations in the gas test results. The stability of the flow test system gives confidence when comparing flow test results from recent samples to those prepared much earlier in the project. A GC baseline test is run on each flow test station prior to gas testing. Similar calibration tests are run under wet conditions. Comparative standards will be discussed in more detail in Chapter 3.

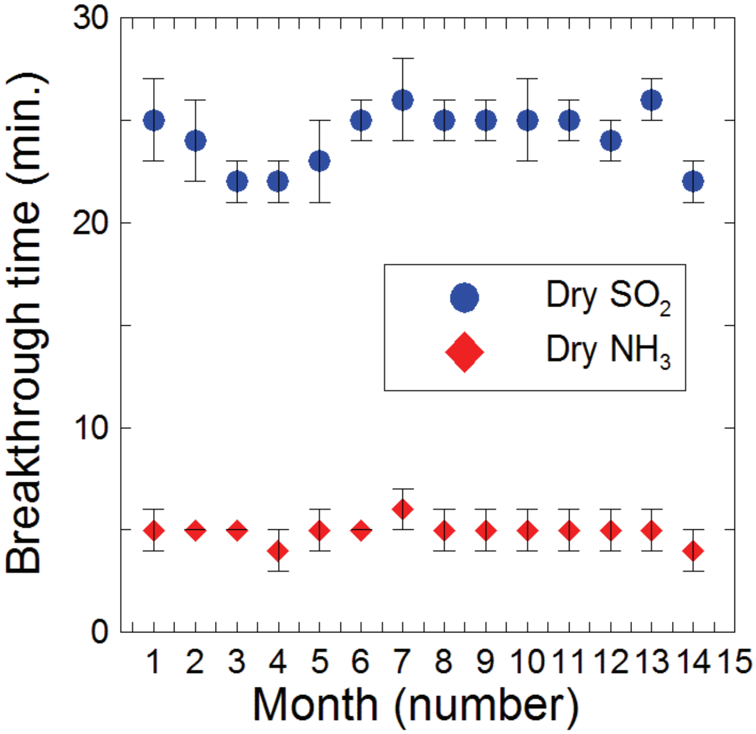

Figure 2.1: Dry SO_2 and NH_3 flow test results obtained from flow testing GC. Monthly results are shown for time span from December 2010 to February 2012.

Samples were tested for C_6H_{12} and HCN adsorption capacity at 3M Canada (Brockville Ontario) by senior lab technicians Judy Reynolds and Monika Simon (HCN testing) and Carrie Andress (C_6H_{12} testing). The HCN concentration was (2000± 100) ppm at a flow rate of (260 ± 30) sccm. The breakthrough time for HCN was chosen at the time when 5 ppm HCN was detected in the effluent gas stream. Due to the evolution of NCCN as described in Eq. (1.1), the effluent gas stream from the HCN tested samples was also monitored for NCCN. The breakthrough concentration for NCCN was also 5 ppm. A gas chromatograph with a flame ionization detector (FID) was used for both HCN and NCCN detection. In most cases only a single test for each sample was performed.

The C_6H_{12} challenge gas concentration was (2000 ± 100) ppm at a flow rate of (200 ± 3) sccm. The breakthrough time for C_6H_{12} was chosen as the time 5 ppm was detected in the effluent gas stream. An infrared spectrometer (Miran 205B SapphIRe-Portable Air Analyzer) was used for C_6H_{12} detection. The wavelength used to detect the presence of C_6H_{12} gas was 3.333 μm. The accuracy of the IR detector was checked using a closed calibration loop generated by 0.1 μL injections. The absorbency is checked at five different levels. In most cases only a single test for each sample was performed.

Theoretical descriptions of the kinetics of gas adsorption by AC or IAC are complicated [43] and require experimentally determined constants. The reaction steps of gas adsorption by AC or IAC have been described by Jonas [44] and are reviewed in this author's Masters dissertation [39] or in the work by Fortier [40]. Arguably the most commonly used equation for predicting challenge gas breakthrough times is the Wheeler-Jonas equation [45, 46]. This equation has been most successfully applied to the adsorption of organic vapours [47], but has been extended to describe the adsorption of inorganic vapours on AC or IAC [48–50]. There are no theoretical predictions made in this dissertation. The performance of AC or IAC samples will be ranked comparatively. The effectiveness of impregnants will be discussed in terms of breakthrough times or the stoichiometric ratio of reaction (SRR), which is the number of moles of toxin adsorbed per mole of impregnant.

2.3 Humidity Chambers

Equilibrium water adsorption experiments and sample conditioning for humid flow tests were performed in a closed humidity chamber which contained a saturated potassium bromide (KBr) solution. A Tenney Versa Tenn III environmental chamber (model THJR) was also used. The RH in either chamber was (80 ± 5)% and the interior temperature of the chamber was maintained at (25 ± 3)°C as monitored by a thermometer/hygrometer (Sper Scientific model number 800039). Samples were stored in the humidified environment until their mass no longer increased; typically 48 hours were sufficient for 0.75 - 1.00 g samples. The mass gain due to humidification was measured gravimetrically using a Sartorius balance with an accuracy of ±1 mg. The results obtained from the humidity chamber were in good agreement with those obtained using the environmental chamber so no distinction will be made between measurements made by these devices.

2.4 Gas Adsorption Porosimetry

Selected AC and IAC samples were characterised using gas adsorption porosimetry. Measurements were performed using a Micromeritics ASAP 2010 gas adsorption porosimeter. In this work, nitrogen gas (N_2) was used as the adsorbate and measurements were taken with the sample tube immersed in a liquid nitrogen bath (boiling point 77 K). At each point on the adsorption isotherm, the initial and equilibrium pressures were measured and the volume of N_2 gas adsorbed was calculated at each equilibriated partial pressure. The data is corrected for the free-space in the sample tube and for any deviations from the ideal gas law. The amount of N_2 adsorbed per gram of adsorbent is reported at standard temperature and pressure (STP), 273.15 K and 1 atm respectively.

A typical experimental procedure was started by mounting a clean sample tube on the ASAP 2010 gas port. The tube was evacuated, then back-filled with helium (He, UHP grade obtained from Praxair, Dartmouth, N.S.) until a pressure of approximately 760 mmHg was achieved. The tube filled with He gas was then weighed on a Sartorius balance and its mass was recorded for reference. Approximately 0.5 g of AC or IAC sample (pre-dried at 120°C) was added to the sample tube. The tube containing the sample was mounted to the degassing station of the ASAP 2010 and evacuated at an elevated temperature until any adsorbed species, such as water, were removed. When dealing with IAC samples the temperature applied during degassing was always less than the maximum final heating temperature the IAC was exposed to during sample preparation. Degassing continued until out-gassing from the sample was negligible, at least 24 - 36 hours for the samples examined in this work. After degassing, the tube containing the sample was back-filled with He to a pressure of 760 mmHg and the tube containing the sample and He gas was re-weighed. The sample mass was obtained by subtracting the mass of the back-filled empty tube from the mass of the back-filled tube that contained the sample. After recording the sample mass, the sample tube was mounted on the analysis port of the ASAP 2010 and evacuated until the system pressure was stable. After degassing was complete the sample tube was immersed in liquid nitrogen and allowed to equilibriate under vacuum. Once the sample was stable, measurements were performed by dosing the manifold and sample tube, at user defined partial pressures, up to a relative pressure (P/P_o) of 0.9. Desorption measurements were also performed by applying a vacuum to the system's manifold until a lower partial pressure was achieved and then allowing the system to reach equilibrium with the valve to the sample tube open.

There are a large number of theoretical models available to analyze adsorption isotherms. Some of the most common are Langmuir's model for monolayer adsorption [34], the extension of the Langmuir model which allowed for multi-layer adsorption derived by Brunauer, Emmet and Teller (BET) [35], and models based on adsorption potential distribution by Dubinin and co-workers (reviewed in [4]). Excellent reviews of the models, their merits and shortcomings are detailed in the literature [4,31,51]. The N_2 adsorption isotherms collected in this work were analyzed using the BET equation [35] to determine their specific surface area (m^2/g). The BET equation is commonly expressed as:

$$\frac{P/P_o}{V(1-P/P_o)} = \frac{1}{V_m C} + \frac{C-1}{V_m C}\frac{P}{P_o}, \tag{2.2}$$

where V is the amount of N_2 adsorbed per gram of carbon (cm^3/g), V_m is the monolayer capacity, $\frac{P}{P_o}$ is the equilibrium pressure of the gas (P) relative to its saturated vapour pressure (P_o). The constant C is given by:

$$\mathrm{C} = exp[\frac{\Delta H_A - \Delta H_L}{RT}], \tag{2.3}$$

where ΔH_A and ΔH_L are the enthalpy of adsorption of the first adsorbed layer (J/mol) and enthalpy of liquefaction of the subsequent layers (J/mol), respectively. The symbol R is the universal gas constant ($JK^{-1}mol^{-1}$) and T is the temperature (K). Detailed explanations of the BET model have been given in the literature, for example the section by Jaroniec and Choma in [4] or by Sing in [31]. Derivations of the BET equation have been included in earlier dissertations by Dahn lab members [40,52].

Plotting $\frac{P/P_o}{V(1-P/P_o)}$, as a function of P/P_o should produce a linear graph from which the values for V_m and C can be extracted using the slope and intercept. Once V_m is known the BET surface area (S_{BET}) can be calculated:

$$\mathrm{S}_{BET} = \frac{V_m \omega N_A}{M_V}, \tag{2.4}$$

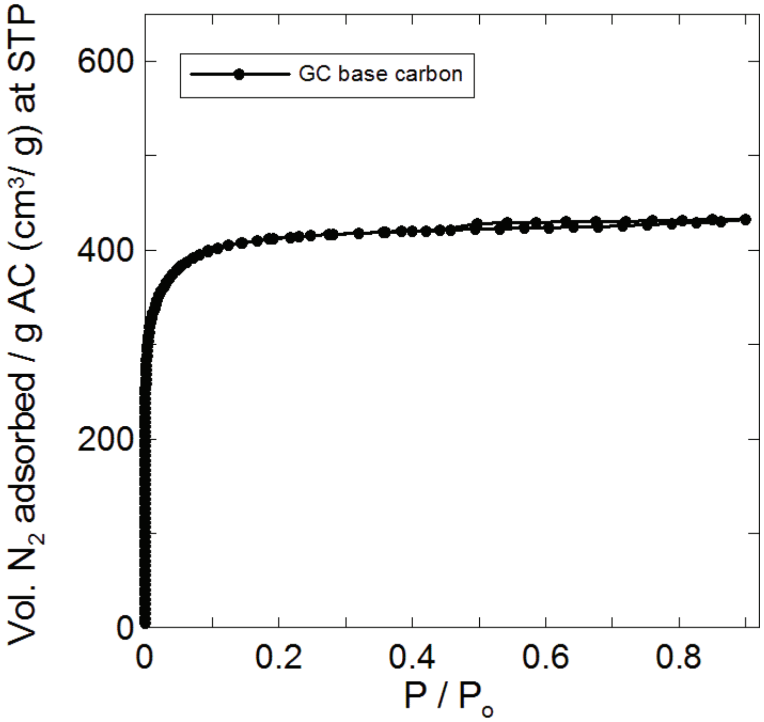

Figure 2.2: N_2 adsorption isotherm data collected from a GC sample.

where ω is the cross-sectional area of the probe molecule, $\omega = 0.162$ nm^2 for N_2 [4,31], N_A is Avogadro's constant (mol^{-1}) and M_V is the volume occupied by one mole of ideal gas at STP.

Figure 2.2 shows a N_2 adsorption isotherm collected from GC base carbon. The steep adsorption at low partial pressure followed by a plateau at $P/P_o \geq 0.2$ is characteristic of a mainly micropourous carbon. The data in Figure 2.2 is classified as a Type I isotherm [4,31]. The small hysteresis is indicative of the presence of mesopores [4].

Figure 2.3 shows the data from Figure 2.2 plotted according to Eq.(2.2). The data in panel (a) shows large deviations from the linear BET relation at higher partial pressures. Deviations from linearity in BET plots can be explained by different adsorption mechanisms. At low partial pressures ($P/P_o \leq 0.2$) it is believed that strong adsorbate-adsorbent interactions can occur and the dominant adsorption mechanism is due to micropore filling [31]. At higher relative pressures adsorption is due to capillary condensation. Panel (b) shows that in a restricted partial pressure range, the BET model can be successfully applied. Due to the restricted range over which the

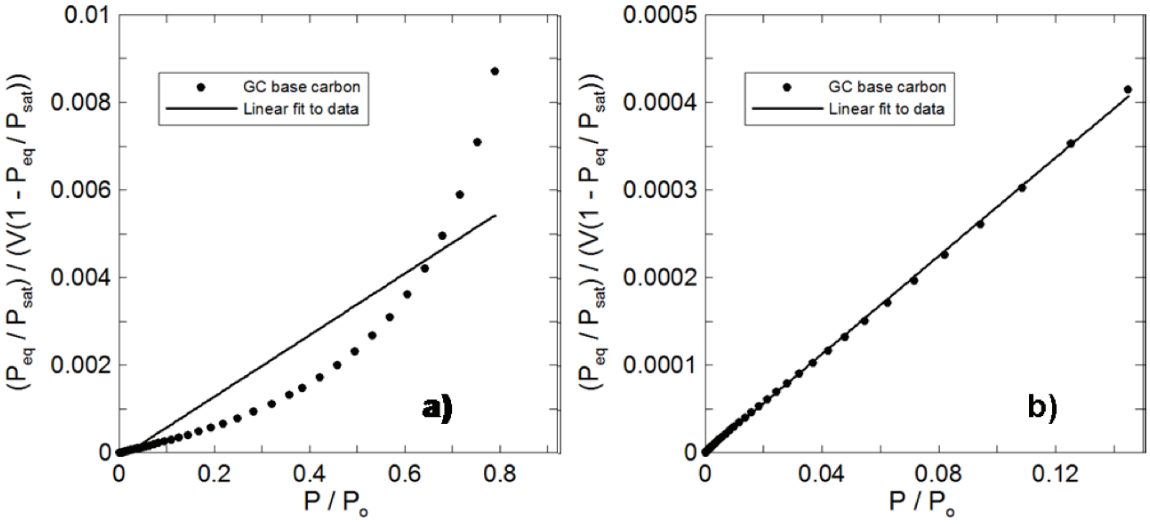

Figure 2.3: Data from Figure 2.2 plotted according to the BET equation. Panel a shows the full range of partial pressures scanned during the experiment. Panel B shows the partial pressure range over which the BET equation is valid

BET equation is valid, the specific surface areas reported using this model will be designated BET surface area or S_{BET}. Despite its shortcomings, the BET model is widely used in the field of AC research [4]

Several methods for determining the distribution of pore sizes in AC are presented in the literature [31, 51]. In this work pore size distributions were calculated using software provided with the ASAP 2010 porisometer. The software performs calculations based on density functional theory (DFT) and uses a slit shaped model of the pores. Details of calculations based on DFT are reviewed by Choma and Jaroniec in Ref. [4]. For a more detailed description, the paper by Olivier is recommended [53].

2.5 Wide Angle X-ray Diffraction

In this project the AC and IAC samples were examined using powder x-ray diffraction techniques. Prior to the start of an experiment the samples were ground to a fine powder using a mortar and pestle.

Several different x-ray diffractometers were used to make wide angle x-ray diffraction (XRD) measurements during this project. The machine most often used employs a Phillips PW 1720 x-ray generator with a copper (Cu) x-ray tube and an incident beam monochrometer which selects Cu K_α radiation of wavelength, $\lambda = 1.5418$ Å. The system is coupled to an Inel CPS 120 curved position sensitive detector. Typical conditions used were: dwell time of approximately 1200 s/sample with the generator set at 40 kV and 30 mA. The Inel machine has a programmable, movable stage to facilitate XRD experiments on several samples at a time. Typically a 3 x 3 array of powder samples was loaded. Approximately 3 hours were required to run this type of experiment.

A Rigaku mini-flex x-ray diffractometer was also used. Typical operating conditions were a scan rate of 0.05°/step and a dwell time of 30 s/step. The generator settings were 30 kV and 15 mA. This diffractometer uses variable slits to keep the size of the x-ray beam on the sample constant as the scattering angle is varied. A Siemens D5000 x-ray diffractometer was also used to conduct some XRD measurements. Typical scan conditions used for this machine were 0.05°/step with a dwell time of 6 s/step. The D5000 is equipped with a Cu target x-ray tube and is operated at 40 kV and 30 mA. This machine uses fixed slits to define the size of the incident beam impinging on the sample. Fixed slits are also used to condition the diffracted beam. A graphite monachromater is used on the diffracted beam to remove radiation caused by fluorescence prior to the x-ray beam reaching the detector.

The full theory of x-ray diffraction is beyond the scope of this thesis. In depth discussion of the theoretical considerations required for analysis of XRD patterns can be found in the text by Klug and Alexander [54] or Cullity and Hall [55]. The data from XRD experiments performed on IACs allowed the determination of the impregnant species present after heating and gave information about how the impregnant was dispersed on the AC substrate. Figure 2.4 shows XRD data obtained from GC base carbon and a series of 3 IACs prepared from aqueous 2.4 M $Zn(NO_3)_2$ solution and dried in a flowing argon environment. The only difference in the samples was their heating temperature, which is indicated in Figure 2.4. For reference, the main zinc oxide (ZnO) Bragg peak positions have been indicated ([00-089-1397] in [56]).

Figure 2.4 shows that all the samples exhibit broad peaks at scattering angles of approximately 22° and 44°. These peaks are characteristic of disordered carbon structures [2]. The dominant impregnant species present in all the IAC samples after

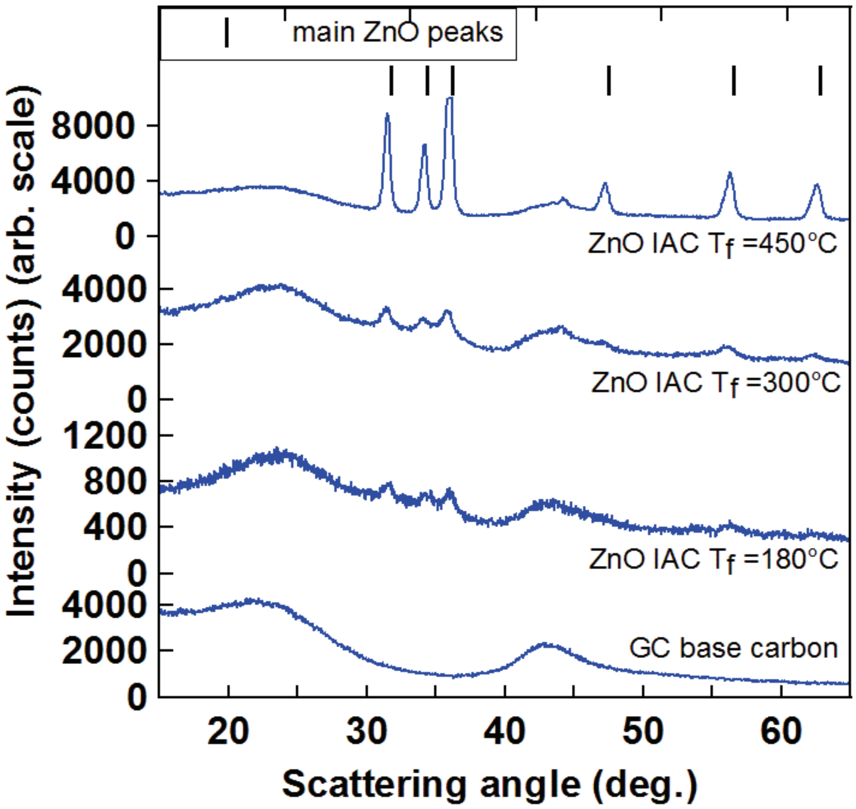

Figure 2.4: XRD data obtained from GC base carbon and a series of Zn-based IACs. The IAC samples were prepared using aqueous 2.4 M $Zn(NO_3)_2$ and heated under flowing argon. The maximum final heating temperature (T_f) for each of the IAC samples is indicated in the figure

heating was ZnO as indicated by the presence of the narrower, more intense Bragg peaks, especially in the 30° to 40° range. The IAC data shows that as the heating temperature is increased the intensity and sharpness of the ZnO diffraction peaks increased. This is indicative of increasing ZnO grain size as can be inferred from the Scherrer equation [54]:

$$\mathrm{L}_{hkl} = \frac{K\lambda}{\beta cos\theta}, \tag{2.5}$$

where L_{hkl} is the mean crystallite dimension (units of distance), K = 0.9 is a fitting factor and β is the measured full width at half maximum intensity of the diffraction peak (in radians) and θ is $\frac{1}{2}$ the scattering angle of the diffraction peak.

Another useful measure to determine the relative amount of impregnant present on the AC substrate was to integrate the area under the diffraction peaks of the intensity versus scattering angle plots. The integrations were performed using Fityk software [57].

2.6 Small Angle X-ray Scattering

Small angle x-ray scattering (SAXS) experiments were performed using a Bruker Nanostar system. The system is equipped with a Cu target x-ray tube that is operated at 40 kV and 650 μA. The relatively low power consumption of this tube means that water cooling is not required. This system uses cross-coupled Göbel mirrors to select Cu Kα radiation [58]. The x-ray beam is conditioned further using a series of pinhole collimators. The collimators help to remove unwanted radiation and define the size and shape of the x-ray beam. Figure 2.5 shows a schematic diagram of the system used to condition the x-ray beam in the Bruker Nanostar system. The collimator labelled P1 in Figure 2.5 is used to reduce the primary beam size and define its shape. P2 is the beam defining pinhole, the diameter of the beam impinging on the sample is 400 μm in this system. The final pinhole, labelled P3 acts as a 'mask' for

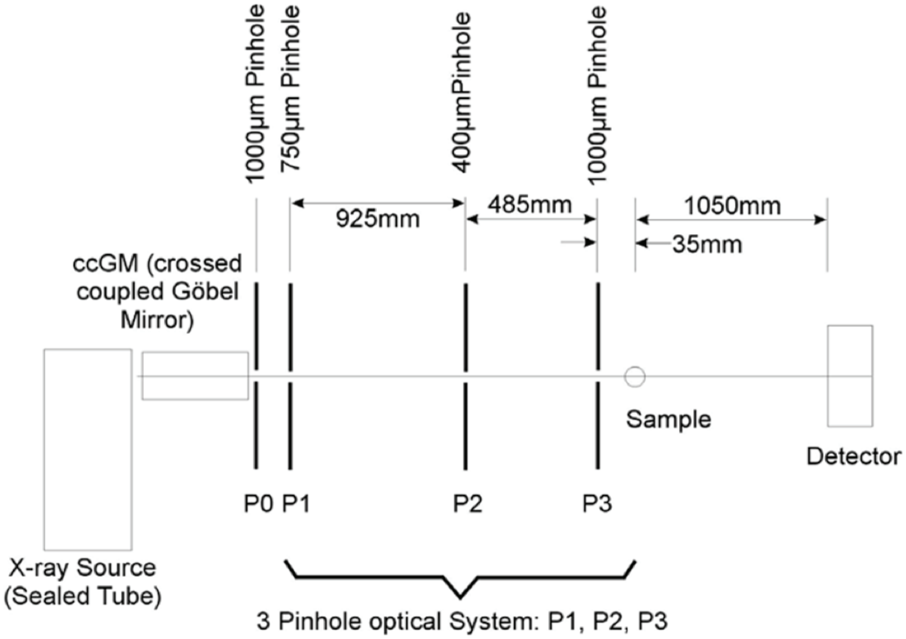

Figure 2.5: Schematic diagram of x-ray beam conditioning performed in the Bruker Nanostar system. Image obtained from Ref. [59]

the primary beam and is used to remove parasitic scattering from the edges of P2.

This system is equipped with a Bruker Vantec 2000 area detector. A typical experiment has a scattering angle range from 0.22° to 5.0° and a counting time of 1000 s/sample. Samples for SAXS analysis were finely ground with a mortar and pestle and packed in a sample well in a stainless steel plate. Scotch tape (3M Co.) was used on both sides of the hole to hold the sample in place. The Bruker Nanostar has a translation stage that can accept a variety of different sample holders. In this work a sample holder with 9 wells was most often used. This holder had a thickness of 1.62 ± 0.02 mm and the volume of each well was approximately 0.03 cm^3. Sample mass varied with impregnant loading for IAC samples, ranging between approximately 10 - 15 mg. Un-impregnated GC activated carbons had a mass of 12 ± 1 mg. SAXS measurements were performed under vacuum in the pressure range of approximately 60 - 100 mTorr.

To account for absorption of x-rays by the samples, the intensity of the collected SAXS data was scaled by an attenuation factor. Determination of the attenuation factor was accomplished either by experimental measurements or by calculation. To determine the attenuation factor experimentally, the beam intensity (I_o) was measured by placing a glassy carbon disc in front of the incoming x-ray beam. The total number of counts over a 100 s interval was recorded. Next, the sample was placed in front of the glassy carbon and the measurement was performed again. The total number of counts recorded (in 100 s) was denoted as the sample intensity, I_x. The attenuation factor is the ratio of I_o and I_x:

$$\mathrm{att}_{exp.} = \frac{I_o}{I_x}, \tag{2.6}$$

To calculate the attenuation factor the density of the sample (ρ), sample thickness (l) and mass absorption coefficient (μ/ρ) must be known:

$$\mathrm{att}_{calc.} = \frac{I_o}{I_x} = e^{(\frac{\mu}{\rho})\rho l} \tag{2.7}$$

The sample density and thickness are known from the mass of the sample and dimensions of the sample holder. The mass absorption coefficient was obtained from tabulated values in Ref. [55]. For IAC samples with one or more impregnants present the sample mass absorption coefficient was calculated from the weighted average of

Table 2.1: Measured and calculated attenuation factors for various AC and IAC samples.

Sample components	% impregnant loading	att$_{exp.}$	att$_{calc.}$
GC	0	1.33	1.31
$ZnCl_2$, GC	5	1.57	1.54
$ZnCl_2$, GC	89	114.27	126.86
K_2CO_3, GC	5	1.53	1.47
K_2CO_3, GC	20	2.76	3.30
CuO, GC	16	1.93	2.05

the constituent materials [55]:

$$\frac{\mu}{\rho} = w_1(\frac{\mu}{\rho})_1 + w_2(\frac{\mu}{\rho})_2 + ..., \tag{2.8}$$

where w$_n$ is the mass fraction of each element. Table 2.1 shows measured and calculated attenuation factors for select AC and IAC samples with different impregnants and impregnant loading. Table 2.1 shows good agreement between measured and calculated attenuation factors. Larger discrepancies occur as the impregnant loading on the IAC samples is increased. Calculations similar to those displayed in Table 2.1 have yielded an average agreement within ± 7% for att$_{exp.}$ and att$_{calc}$ for samples studied in this work.

Figure 2.6 shows a screen shot of data collected using the Bruker Nanostar system. The data was collected from GC activated carbon. The symmetric pattern shows that this sample has no preferred orientation. An angular integral was performed to convert the 2 dimensional data to an Intensity versus scattering vector (or scattering angle) plot.

The treatment of the SAXS data presented in this thesis follows the model proposed by Debye, Anderson and Brumberger (DAB) [60]. The theory stated here is ample to motivate our interpretation of the SAXS data but is not meant to be a full review of the theory behind small-angle scattering. In depth discussions of the theory behind SAXS are presented in the texts by Guinier [61] or Glatter [62]. Excellent discussions (including derivations) of SAXS applied to the study of carbons can be found in the dissertations by Buiel [63] or Stevens [52].

Figure 2.7 shows a schematic diagram of elastic scattering in a SAXS experiment. The incoming x-ray beam, represented by the wave vector **k**, impinges on the sample.

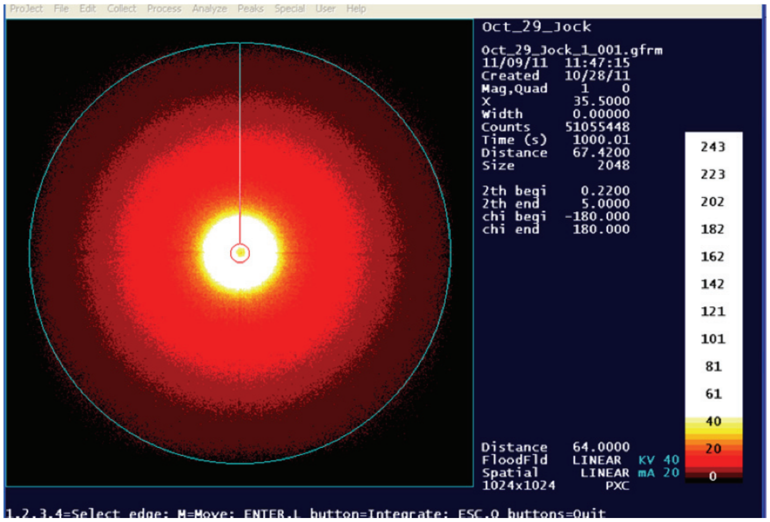

```
Oct_29_Jock

Oct_29_Jock_1_001.gfrm
11/09/11   11:47:15
Created    10/28/11
Mag,Quad      1    0
X           35.5000
Width       0.00000
Counts     51055448
Time (s)    1000.01
Distance    67.4200
Size           2048

2th begi     0.2200
2th end      5.0000
chi begi   -180.000
chi end     180.000

Distance    64.0000
FloodFld    LINEAR   KV 40
Spatial      LINEAR  mA 20
1024x1024       PXC
```

```
1,2,3,4=Select edge; M=Move; ENTER,L button=Integrate; ESC,Q buttons=Quit
```

Figure 2.6: Screen shot of data collected from a GC activated carbon using the Bruker Nanostar SAXS system

In a SAXS experiment most of the incoming x-ray beam would go straight through the sample and be absorbed by the beam stop. The x-ray radiation that is scattered by the sample is represented by the wave vector **k'**. It is the scattered x-ray radiation that is measured by the detector. The scattering vector is calculated from the difference in the wave vectors, $\mathbf{q} = \mathbf{k'} - \mathbf{k}$ and has a magnitude equal to $(4\ \pi\ \sin\theta)/\ \lambda$.

The amplitude of the scattered wave from an object (typically a sphere) with radius, r and constant electron density, ρ_e can be found by performing the volume integral:

$$\mathrm{A}(\mathbf{q}) = \rho_e \int_0^r e^{i\mathbf{q}\cdot\mathbf{r}}\, \mathrm{d}V \tag{2.9}$$

The intensity, $\mathrm{I}(\mathbf{q})$, is given by the amplitude squared. For randomly distributed two phase systems Debye, Anderson and Brumberger introduced the auto correlation function [60]:

$$\gamma(\mathbf{r}) = \mathrm{e}^{-\frac{\mathbf{r}}{\mathrm{a}}}, \tag{2.10}$$

where a is the distance between interfaces in the two phase system (correlation length). The intensity of scattering from the two phase system using this model is given by:

$$\mathrm{I}(\mathbf{q}) = 4\pi\rho_{\mathrm{e}}^2\mathrm{V}\int_0^\infty \mathrm{r}^2\gamma(\mathbf{r})\frac{\sin(\mathrm{qr})}{\mathrm{qr}}\,\mathrm{dr}, \tag{2.11}$$

where V is the volume of sample illuminated by the x-ray beam. The solution to Eq.

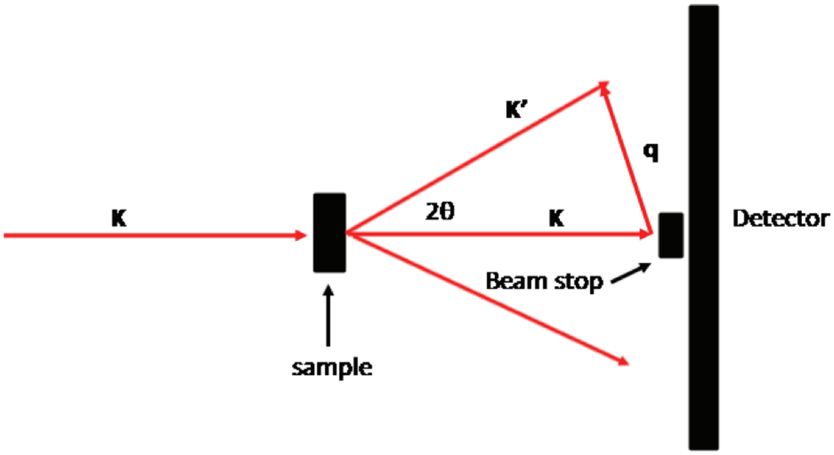

Figure 2.7: Schematic diagram of scattering in a SAXS experiment.

2.11 is given as:

$$\mathrm{I(q)} = \frac{2\pi\rho_e^2 \mathrm{S}}{(\frac{1}{a^2} + q^2)^2}, \tag{2.12}$$

where S is a term related to the surface area per unit mass of the scatterer. The intensity is shown to be proportional to the square of the electron density contrast in the two phase system. The correlation length, a, gives insight into the size of the scatterer. For scattering from large objects, qa >> 1 and the intensity of the scattering can be approximated by the relation:

$$\mathrm{I(q)} \approx \frac{\mathrm{A}}{q^4} \tag{2.13}$$

Equation 2.13 is also known as Porods law [62]. For scattering from small objects qa < 1 and the intensity of the scattering can be described using Eq. 2.12.

Kalliat and co-workers successfully modified the DAB model to describe small angle scattering from different ranks of coals [64]. Variations on this model have been used to describe small angle scattering data obtained from coals, pyrolyzed sugars and activated carbons [65–69]. The form of the Kalliat model used to analyze the data from un-impregnated AC is given by:

$$\mathrm{I(q)} = \frac{\mathrm{A}}{q^n} + \frac{\mathrm{B}a^4}{(1 + a^2q^2)^2}, \tag{2.14}$$

where A is a constant that is proportional to the surface area of macropores (and larger mesopores) and B is a constant that is proportional to the surface area of

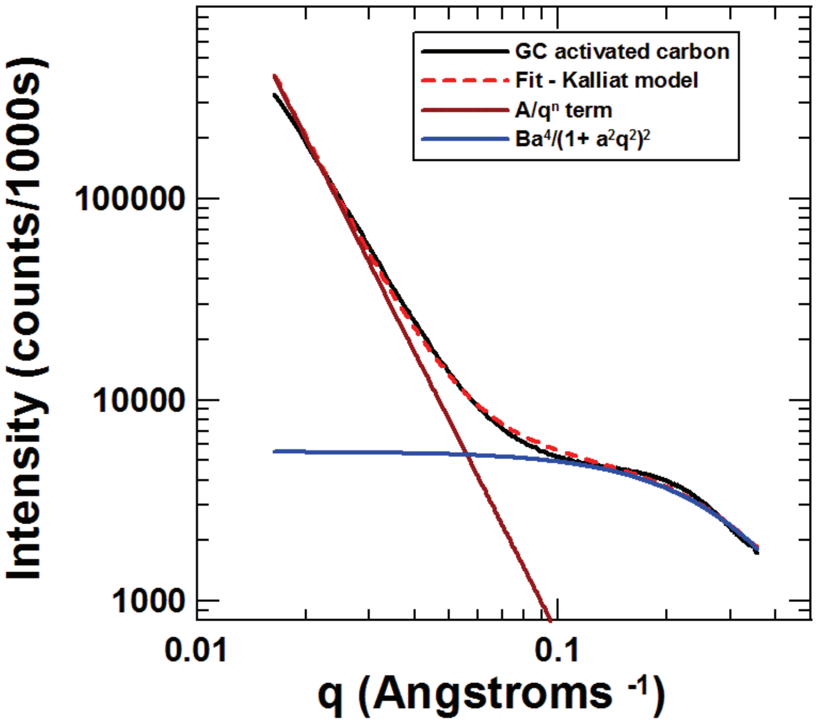

Figure 2.8: SAXS data collected from a GC sample and a fit to the data using the Kalliat model. The components of the fit have been included.

micropores (and smaller mesopores). Comparison of Eq. 2.12 and Eq. 2.14 shows that other constants are also absorbed into the A and B terms. In Eq. 2.14 n is a constant. The value of n has been reported as a measure of the smoothness of the scattering surface [70]. Values of n = 4 correspond to scattering from a smooth surface and values of n $<$ 4 are indicative of scattering from rough surfaces. The Debye correlation length is represented by a. The radius of gyration, R_g, is another useful measure of micropore size. R_g can be described as the average distance of the scatterers from their center of mass [61]. The Debye correlation length and R_g have been shown to be related for spheres by $R_g = \sqrt{6}$ a using second order Taylor expansion [64].

Figure 2.8 shows SAXS data obtained from a GC sample. The data is plotted as intensity versus scattering vector on a logarithmic scale. A fit to the data using the Kalliat model and the components of the fit are included.

Figure 2.8 shows that reasonable fits to GC can be achieved using Eq. 2.14. Modifications to the Kalliat model were made to perform fits to the IAC samples and will be discussed further where appropriate. Considerations made when implementing the Kalliat model are discussed below.

2.7 Discussion of the Kalliat Model

Due to the large number of samples prepared and charecterized in this work a robust, easy-to-implement model was required for data fitting. The Kalliat model met these criteria. In this section some of the considerations used in implementing the Kalliat model are discussed.

Fitting the data shown in Figure 2.8 with Eq. 2.14 gives a value of n $\approx$ 3.5 for the exponent in the Porod term and not the expected value of n = 4. To investigate this discrepancy, calculations were performed using the second term (pore term) in Equation 2.14. Figure 2.9 shows a SAXS curve calculated using the pore term from the Kalliat model. The values used in the calculation were: correlation length, a = 90 Å (R_g = 220 Å) and B = 1. For reference the lower and upper limits used in experimental measurements have been indicated.

Figure 2.9 shows that for $q \geq 0.03$ Å^{-1} the slope of the calculated SAXS pattern is linear on the log-log scale and has a slope of n = 3.9. For $q < 0.03$ Å^{-1} there is an increasing amount of curvature in the SAXS pattern with decreasing q values. Figure 2.9 shows that the influence of mesopore scattering could be experimentally measured using the Bruker Nanostar system. Figure 2.8 shows a small amount of curvature in the SAXS signal obtained from GC activated carbon in the $q < 0.02$ Å^{-1} range. It is possible that this curvature is due to mesopore scattering.

Fitting experimental data using Eq. 2.14 allows for only an average pore dimension to be determined. Activated carbons have a distribution of pore sizes. Calculations were performed to determine the difference between SAXS curves constructed using an average pore dimension compared to those calculated using a distribution of pore sizes. The Kalliat pore term (second term in Eq. 2.14) was used in the calculations. Gaussian and Weibull probability distribution functions were used to generate the range of pore sizes. These distributions have been used to help describe the physical adsorption of gases or vapours on microporous adsorbents. For example the Weibull distribution [71] has been used in the Dubinin-Radushkevich and Dubinin-Astakhov

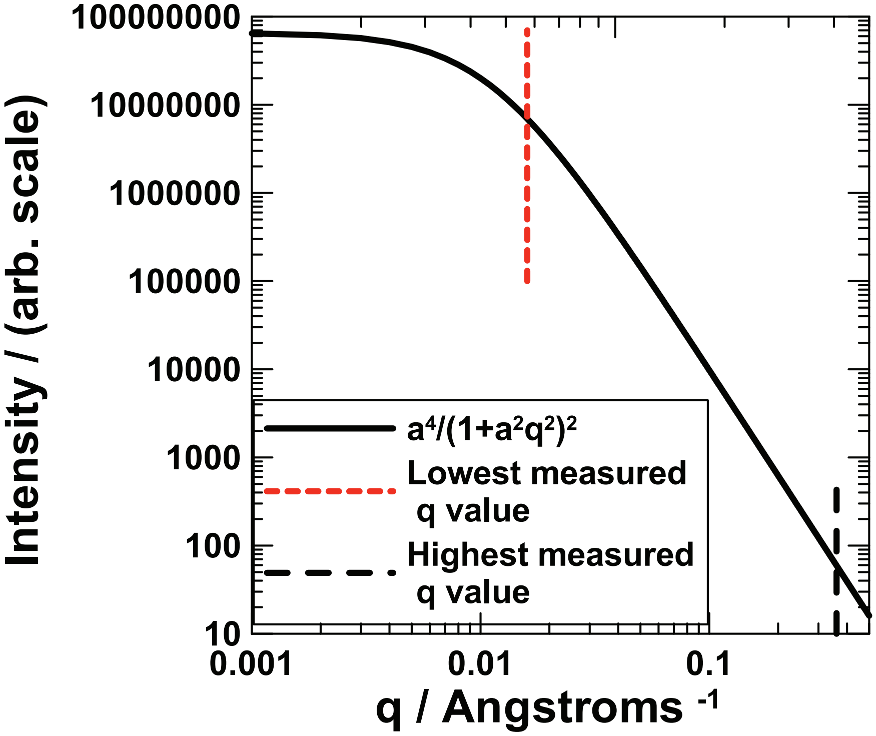

Figure 2.9: SAXS curve calculated using second term in Eq. 2.14. For reference the limits of experimental measurements have been indicated.

equations [72–74]. Using these distributions to generate a distribution of pore sizes for the SAXS calculations seemed to be a reasonable choice. The equation used to perform the Gaussian-weighted calculations is given by:

$$\mathrm{I_G(q)} = \frac{1}{\sigma\sqrt{2\pi}}\int_0^{30} \frac{\mathrm{a}^4}{(1+\mathrm{a}^2\mathrm{q}^2)^2}\,\mathrm{e}^{\frac{-1}{2}(\frac{\mathrm{a}-\mu}{\sigma})^2}\mathrm{da}, \tag{2.15}$$

where σ is the standard deviation and μ is the mean (or expected) value. The equation used to perform the Weibull-weighted calculations is given by:

$$\mathrm{I_W(q)} = \int_0^{30} \frac{\mathrm{a}^4}{(1+\mathrm{a}^2\mathrm{q}^2)^2}\,\frac{\mathrm{k}}{\alpha}\,(\frac{\mathrm{a}}{\alpha})^{\mathrm{k}-1}\,\mathrm{e}^{-(\frac{\mathrm{a}}{\alpha})^{\mathrm{k}}}\mathrm{da}, \tag{2.16}$$

where k is the shape parameter and α is the scale parameter. Equations 2.15 and 2.16 were evaluated numerically using computer software.

Figure 2.10 shows Gaussian (G(a)) and Weibull (W(a)) distributions plotted versus correlation length, a, in panels (a) and (b) respectively. The parameters used in the Gaussian distribution calculations were $\sigma = 3$ and $\mu = 10$ Å, the parameters used

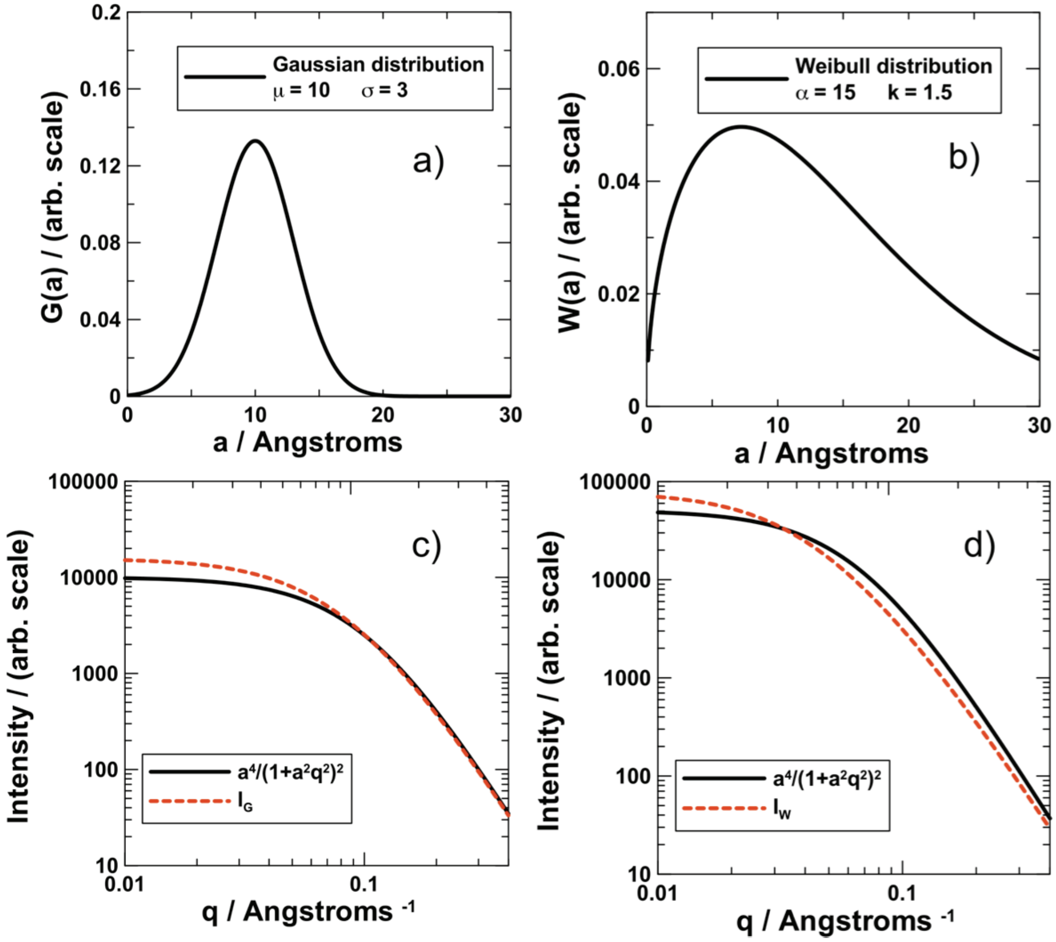

Figure 2.10: Gaussian (G(a)) and Weibull (W(a)) distributions are displayed in panels (a) and (b) respectively. The parameters used in the calculations are indicated in their respective legend. I_G and the Kalliat pore term (a = 10 Å) are displayed in panel (c). Panel (d) shows I_W and the Kalliat pore term (a = 15 Å).

in the Weibull distribution were k = 1.5 and α = 15 Å. Figure 2.10(c) shows I_G and the Kalliat pore term (with a = 10 Å) plotted versus q. Panel (d) shows I_W and the Kalliat pore term (with a = 15 Å) plotted versus q. Panels (c) and (d) are plotted on a log-log scale.

Figure 2.10(c) shows that the calculated curves from I_G and the Kalliat pore term (with a = 10 Å) are in reasonably good agreement. Panel (d) shows that there is reasonable agreement between I_W and the Kalliat pore term (with a = 15 Å) as well. Figure 2.10 shows that scattering from a reasonably close distribution of pore sizes can be adequately described using the Kalliat model with an average pore dimension.

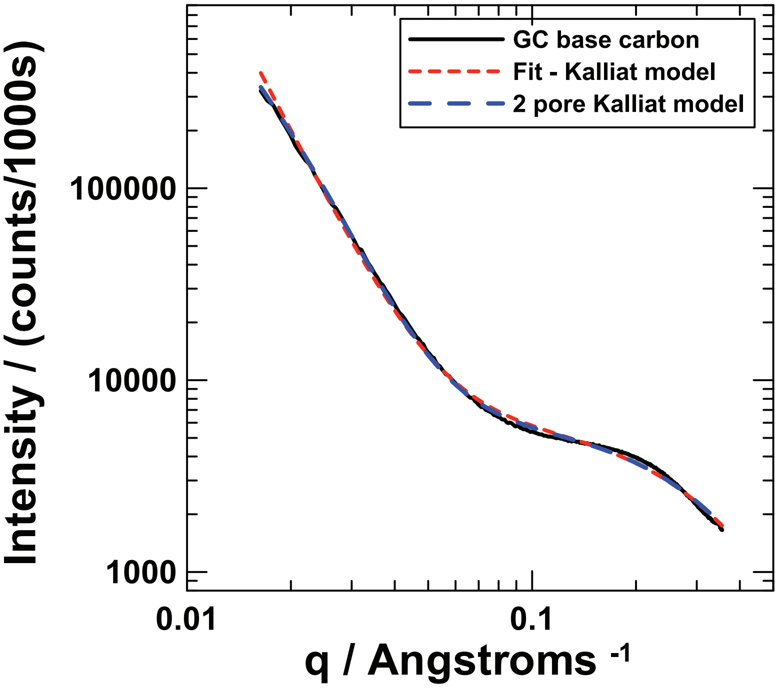

Figure 2.11: SAXS data obtained from a GC sample and fits to the data using Eq. 2.14 (Kalliat model, red dashed line) and Eq. 2.17 (2 pore Kalliat model, blue dashed line).

Using the Kallait model with an average pore dimension as opposed to a distribution of pore sizes allows for more rapid data fitting.

A modification to Eq. 2.14 was performed to replace the Porod term with a second Kalliat pore term. The modified kalliat equation is given by:

$$\mathrm{I_K(q)} = \frac{\mathrm{B_1 a_1^4}}{(1+\mathrm{a_1^2 q^2})^2} + \frac{\mathrm{B_2 a_2^4}}{(1+\mathrm{a_2^2 q^2})^2}, \tag{2.17}$$

where $\mathrm{a_1}$ and $\mathrm{a_2}$ represent the correlation lengths for two different average pore sizes and $\mathrm{B_1}$ and $\mathrm{B_2}$ are constants proportional to the surface area of those pores.

Figure 2.11 shows SAXS data obtained from GC activated carbon and fits to the data using Eq. 2.14 and Eq. 2.17 as described in the figure caption. Parameters extracted from fits to the data are listed in Table 2.2.

Figure 2.11 shows that at lower values of q ($q \leq 0.02$ Å^{-1}) Eq. 2.17 fits the data better than Eq. 2.14. In the range from q ≈ 0.06 - 0.2 Å^{-1} both equations provide reasonable, equivalent fits to the data. Table 2.2 shows that the terms related to

Table 2.2: Parameters extracted from fits to the SAXS data obtained from GC using equations 2.14 (one pore Kalliat model) and 2.17 (2 pore Kalliat model).

Single pore	A	B	n	R_g (Å)	χ^2
	0.18	136	3.49	6.2	1.3
Two pore	B_1	R_{g1} (Å)	B_2	R_{g2} (Å)	χ^2
	131	6.4	0.06	201	0.9

micropore surface area (B and B_1) and average micropore dimenssion (R_g and R_{g1}) are similar for fits to the data using equations 2.14 and 2.17 respectively. For the work presented in this thesis Eq. 2.14 was chosen to fit the un-impregnated AC data. Figure 2.11 shows that Eq. 2.17 could be used just as effectively to fit the SAXS data.

2.8 Thermal Analysis

Thermogravimetric analysis (TGA) experiments were performed using an SDT Q600 simultaneous TGA/DSC (Differential Scanning Calorimetry) from TA Instruments. Approximately 10 - 20 mg of AC or IAC sample was used for each experiment. Typical scan conditions were a 5°C/minute ramp rate under 50 mL/min purge gas flow (either argon or air). For experiments performed under air, the samples were usually heated from room temperature to 600°C; samples heated under argon were heated to temperatures as high as 1000°C.

Thermal analysis has been used in the respirator carbon project to determine parameters such as the thermal decomposition temperature of impregnants on the AC substrate [23, 25], and how certain impregnants affect the combustion temperature of the sample [24, 75–77]. Thermal analysis techniques have been used to study the desorption of surface oxygen groups as a function of heating temperature on IAC samples [78]. Thermal analysis has also been employed to determine physical properties of chemicals prior to impregnation, for example to determine the number of moles of water (x) in phosphomolybdic acid hydrate ($H_3PO_4 \bullet 12MoO_3 \bullet xH_2O$).

2.9 Scanning Electron Microscopy

Scanning electron microscopy (SEM) experiments were performed using a Hitachi S-4700 field emission SEM that is fitted with an Oxford Instruments energy dispersive x-ray analyzer (EDX). Typical operating conditions employed were 10-20 kV accelerating voltage with 15 μA extraction current and approximately 12 mm working distance. The AC or IAC granules were mounted in a conducting carbon paste to facilitate imaging. Prior to mounting, the granules were sometimes cut with a scalpel to allow imaging of the internal pores.

SEM has been used in the Dahn-lab respirator carbon project to study impregnant distribution on the AC substrate [22–25, 42]. EDX studies have allowed a qualitative examination of how different impregnant species interact on the AC surface. A specific example of this useful technique is the intimate contact between Cu and Mo species present on an IAC prepared from an ammonia-based solution as is shown in Figure 1 of Ref. [23].

2.10 Titrations

Titrations and pH measurements were performed using a Mettler DL21 titrator. This device performs automated titrations and is coupled to a data logging computer. A typical titration would have 0.2 mL increments in the volume dispensed and 1 s stir time between measurements. This device performs potentiometric measurements. Boehm titrations were performed on certain AC and IAC samples to determine the number of acidic surface functional groups present [79]. A typical experiment involved soaking approximately 0.5 g of AC or IAC sample in 50 mL of 0.050 M KOH solution. The mixture was stirred for approximately 24 hours. After stirring, the basic solution was separated from the carbon by pouring through filter paper. The KOH solution was titrated with 0.05 M HNO_3. Results from the Boehm titrations will be discussed further where appropriate.

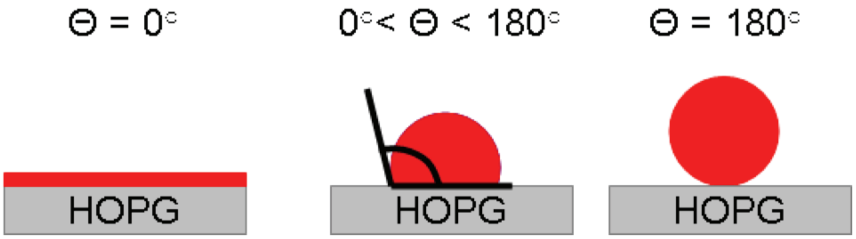

Figure 2.12: Schematic illustrations of contact angle at a solid-liquid interface. The images from left to right depict a solution that fully wets a solid, partially wets the solid and does not wet the solid. Image reproduced from Ref. [40]

2.11 Contact Angle Measurements

Contact angle measurements were performed using a First Ten Angstroms (FTA) 135 drop shape analyzer. A drop of solution was deposited onto a highly oriented pyrolytic graphite (HOPG) substrate by slowly lowering the syringe until the drop contacted the substrate. Then the syringe was lifted up. The base of the deposited drop was approximately 3 mm in diameter. A snapshot of the drop was then taken and the data was imported into a computer where the drop shape was analyzed using software supplied by the manufacturer. The HOPG substrates were obtained from SPI supplies. Grades of SPI-1 and SPI-3 were used and there were no discernible differences in the results obtained from the two different grades. The HOPG was cleaved after each measurement using adhesive tape. The reported contact angle measurements are an average of 6-12 measurements per solution.

The contact angle (Θ) of a drop of liquid on a solid can be described using Young's equation [80]:

$$\gamma_{LV}\cos\Theta = \gamma_{SV} - \gamma_{SL}, \tag{2.18}$$

where γ_{LV}, γ_{SV} and γ_{SL} are the surface tensions of the liquid-vapour, solid-vapour and solid-liquid interfaces respectively. The surface tension is a measure of the energy required to change the area of an interface. Figure 2.12 shows a schematic illustration of contact angles at a solid-liquid interface for three different situations. The image on the left shows the situation where the liquid fully wets the solid, the central image shows partial wetting and the image on the right shows no wetting. Contact angle measurements will be used to discuss impregnant distribution on the AC substrate.

Earlier work in the respirator carbon project showed that contact angle measurements performed on a HOPG substrate were a reasonable model for solid-liquid interactions in AC [41].

Chapter 3

Materials Used

3.1 Study of Commercially Available Activated Carbons

A comparative study was performed on commercially available activated carbons prepared from different precursors. Table 3.1 lists the types of AC studied, the manufacturer of each AC and some typical specifications. The products GC and GG are both produced by Kuraray Chemical Company. GC is acid-washed GG.

The mesh size denotes the number of wires per inch in each direction for the screen used to size the AC particles. For example, a mesh size of 12 x 35 means that the largest particles that can pass through the screen are 1.70 mm and the smallest particles that can be retained by the screen are 0.50 mm. The tap density was determined by adding a known mass of AC to a graduated glass (or plastic) cylinder. The diameter of the cylinder used was 6.8 ± 0.1 mm. The base of the cylinder was tapped on a hard surface until the AC particles had settled. The height of the carbon bed was recorded and the tap density calculated from the mass of AC and the volume it occupied in the cylinder.

The ash content is a measure of the amount of impurity in the AC. The values reported in Table 3.1 were obtained by two methods. The first method was to heat the samples in a TGA, under air flowing at 50 mL/min, from room temperature to 800°C. The second method involved heating approximately 1 g of AC at 650°C in air for approximately 6 hours. The ash content was determined from the ratio of the mass of sample after heating (w_f) and the mass prior to heating (w_i). There was good agreement in the results obtained from the two methods.

Boehm titrations [79] were performed on certain samples to estimate the number of acidic surface groups present on the AC. The results in Table 3.1 show that relatively few acidic surface groups are present on the AC samples that were examined. Similar results were reported for these types of AC in the dissertation by Fortier [40].

Table 3.1: Some properties of the commercially available activated carbons studied in this work.

Carbon	GC	GG	CDND	NORIT	NUCHAR
Manufacturer	Kuraray	Kuraray	Calgon	Norit	MeadWestvaco
Precursor	coconut shell	coconut shell	coal	coal	wood
Mesh size	12 x 35	12 x 20	12 x 30	12 x 30	10 x 25
Particle size (mm)	1.70 x 0.50	1.70 x 0.84	1.70 x 0.60	1.70 x 0.60	2.00 x 0.71
Tap density ($\pm$ 0.01 g/cm^3)	0.43	0.44	0.45	0.44	0.27
Ash content ($\frac{w_f}{w_i}$x100%)	0.7 $\pm$ 0.1	2.9 $\pm$ 0.8	7 $\pm$ 1	7 $\pm$ 1	8 $\pm$ 1
Acidic sites: KOH (mmol/g)	0.18 $\pm$ 0.01	n/a	0.20 $\pm$ 0.05	n/a	n/a
S_{BET} ($\pm$ 50 m^2/g)	1570	1500	1250	1170	1540

Figure 3.1 shows nitrogen adsorption isotherms collected from the different AC samples described in the caption. The isotherms collected from the coconut based ACs (GC and GG) were similar to one another. These samples showed higher adsorption than the coal derived samples (CDND and NORIT). The isotherms collected from GC, GG, CDND and NORIT ACs show sharp adsorption at low partial pressures followed by a plateau (GC and GG) or slowly increasing adsorption (CDND and NORIT) for partial pressures above 0.2. These isotherms also displayed small amounts of hysteresis in the partial pressure range between 0.9 and 0.5. The data collected from coconut and coal derived ACs is indicative of materials with micropores and mesopores present. The isotherm collected from the wood derived sample (NUCHAR) had a much different shape relative to the other ACs studied. This sample displayed increasing adsorption with increasing partial pressure and a much more pronounced hysteresis, which is indicative of a more mesoporous AC [4]. The BET surface areas (S_{BET}) were calculated using partial pressure data up to approximately 0.1 and are presented in Table 3.1.

Figure 3.2 shows pore size distributions for pore width up to 3 nm for the AC samples studied in this section. The calculations were performed using software provided with the Micromeritics ASAP 2010 porosimeter as discussed in section 2.4. The calculations are based on a slit shaped pore model [53, 81, 82].

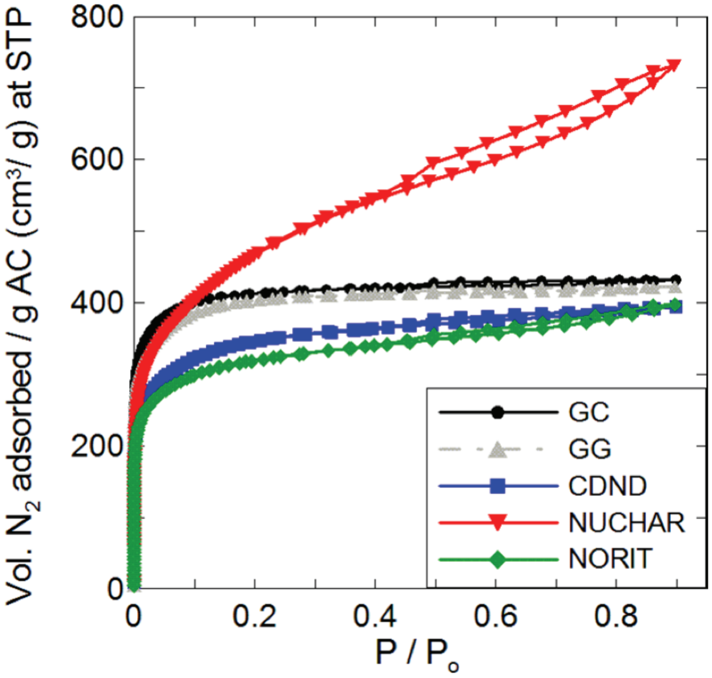

Figure 3.1: Nitrogen adsorption isotherms collected from different AC samples.

Figure 3.2 shows that GC, GG, CDND and NORIT are mainly microporous carbons and NUCHAR is more mesopourous. The average pore width of each AC was calculated by performing a weighted average of the differential pore volume with respect to pore volume:

$$\bar{w}_{Vol} = \frac{\sum_{i=0\,\mathrm{nm}}^{16\,\mathrm{nm}} w_i V_i}{\sum_{i=0\,\mathrm{nm}}^{16\,\mathrm{nm}} V_i}, \tag{3.1}$$

where w is the width of the pore (Å) and V is the differential pore volume (cm^3/g). Similarly the average pore width can also be calculated by performing a weighted average of the differential surface area:

$$\bar{w}_{Area} = \frac{\sum_{i=0\,\mathrm{nm}}^{16\,\mathrm{nm}} w_i A_i}{\sum_{i=0\,\mathrm{nm}}^{16\,\mathrm{nm}} A_i}, \tag{3.2}$$

where A is the differential pore surface area (m^2/g). Results from average pore widths calculated from N_2 adsorption data will be compared with results from small angle x-ray scattering experiments below.

Figure 3.3 shows SAXS data obtained from the different AC samples investigated in this study as denoted in the legend. Fits to the data were calculated using Eq.

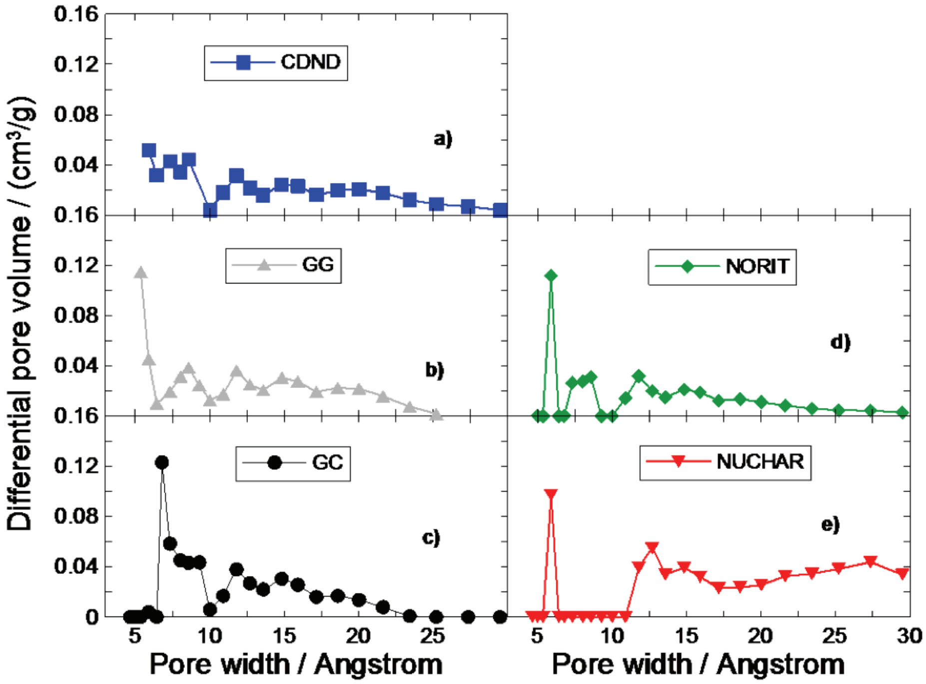

Figure 3.2: Pore size distributions for the different AC samples studied in this section.

2.14 using a minimized least squares fitting routine (reduced χ^2). In this work the reduced χ^2 is defined as:

$$\chi^2 = \sum_{i=1}^{N} [ln(y_i) - ln(f(x_i))]^2, \tag{3.3}$$

where N is the number of data points, $f(x_i)$ is the fit to the data at the ith data point and y_i is the ith data point. The data is represented by the solid lines, the fits are represented by dashed lines. For improved visualization the dashed lines are a different colour than the solid lines.

Figure 3.3 shows that reasonable fits to the data can be achieved using Eq. 2.14. Table 3.2 lists the extracted values from the fits to the data shown in Figure 3.3. The values reported for GC are averaged from 17 separate SAXS experiments. The GC samples are used as a consistency check for the SAXS system and are examined during each run. Results with an uncertainty in Table 3.2 are average values. The stated uncertainty represents the deviation from the average value. Analysis of the SAXS data shows that the average R$_g$ values rank as GC $<$ GG $<$ NORIT $<$ CDND $<$ NUCHAR. The SAXS data shows that CDND, NUCHAR and NORIT have more

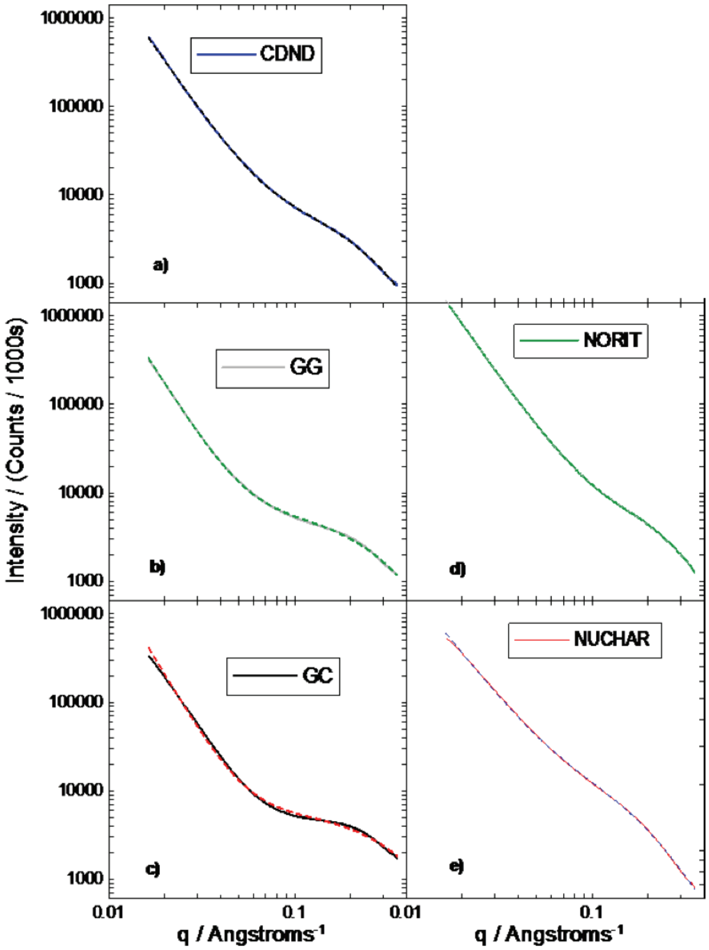

Figure 3.3: SAXS data obtained from different AC samples investigated in this work. The solid lines represent the data, the dashed lines represent fits to the data. For improved visualization the dashed lines are a different colour than the solid lines.

macropore and larger mesopore surface area (higher A value) relative to GC and GG. Samples GC, GG and NORIT have higher micropore and small mesopore surface area (B value) compared to CDND and NUCHAR. These results are in reasonable agreement with the trends observed in the N_2 adsorption data.

Table 3.3 shows the average pore dimension obtained from analysis of the N_2 adsorption and SAXS data. The pore diameter calculated from the SAXS data ($\bar{d}_{SAXS}$) is 2 times the R_g value. No pore shape was assumed when modelling the SAXS data. The values in Table 3.3 show that calculated values of $\bar{w}_{Area}$ are smaller than those reported for $\bar{w}_{Vol}$. The values of $\bar{w}_{Vol}$ and $\bar{d}_{SAXS}$ are in reasonable agreement for the GC and GG samples, but differ for the other ACs in this study. All the pore size

Table 3.2: Parameters extracted from fits to the SAXS data using the Kalliat model for the ACs studied in this section. The values for A and B have units of counts/Å^n and counts/Å^4 respectively.

Carbon	A	B	n	R$_g$ (Å)	χ^2
GC	0.18 ± 0.04	130 ± 21	3.54 ± 0.03	6.2 ± 0.2	1.9 ± 0.4
GG	0.33 ± 0.04	64 ± 2	3.36 ± 0.03	7 ± 1	0.5 ± 0.2
CDND	2.2 ± 0.1	36 ± 1	3.06 ± 0.03	9 ± 1	0.18 ± 0.01
NORIT	8.4	73	3.02	8.6	0.1
NUCHAR	13.1	15	2.6	12.8	0.3

Table 3.3: Average pore dimensions calculated from N_2 adsorption data and SAXS data.

Carbon	$\bar{w}_{Vol}$ (Å)	$\bar{w}_{Area}$ (Å)	$\bar{d}_{SAXS}$ (Å)
GC	12 ± 1	9.4 ± 0.1	12.4 ± 0.4
GG	12 ± 1	8.8 ± 0.1	14 ± 2
CDND	13 ± 1	10.2 ± 0.1	18 ± 2
NORIT	12 ± 1	9.3 ± 0.1	17.2
NUCHAR	37 ± 1	18.6 ± 0.1	25.6

calculations showed that NUCHAR had the largest average pore size as was expected due to the greater degree of mesoporosity observed in this sample. The average pore size values will be discussed further when flow test results are presented.

Figure 3.4 shows average breakthrough times obtained from challenging certain AC samples in this study with SO_2, NH_3 and HCN challenge gases under dry and humid conditions. Samples tested under dry conditions had $< 5\%$ adsorbed moisture and $\leq 15\%$ RH challenge gas stream. Samples tested under wet conditions were fully humidified and had $\geq 80\%$ RH challenge gas stream. Figure 3.4 shows that the samples tested all had breakthrough times under 20 minutes for dry NH_3 and HCN flow tests. Longer breakthrough times were observed in results obtained from the SO_2 flow tests. The GG sample had the longest SO_2 breakthrough time under dry conditions. Only the GC and CDND samples were flow tested under humid conditions using these challenge gases. Panel (b) shows that the GC and CDND samples had reasonably short breakthrough times when challenged with humid NH_3 and HCN. Both samples had significantly longer humid SO_2 breakthrough times. The presence of water has been reported to enhance the adsorption of SO_2 on AC [83, 84]. The

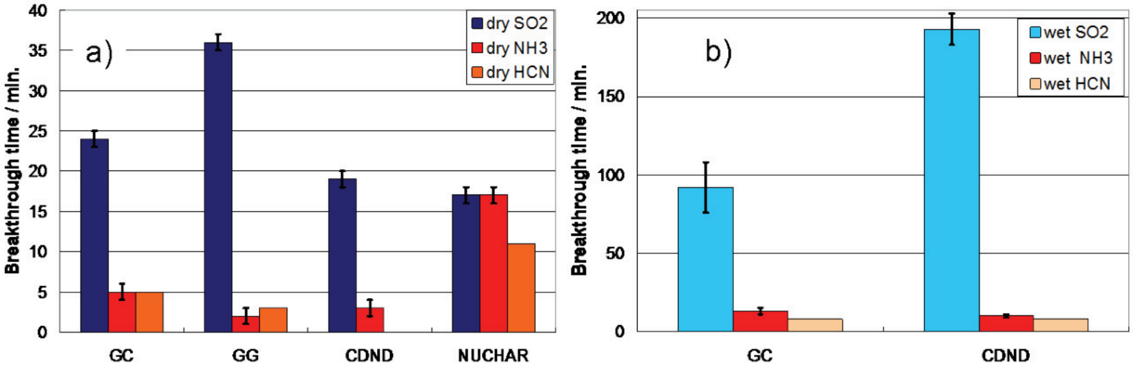

Figure 3.4: Average breakthrough times obtained from challenging the AC samples in this study with SO_2, NH_3 and HCN challenge gases. Results obtained under dry and humid conditions are shown in panels (a) and (b) respectively. Note the change in scale on the y-axis between panels (a) and (b)

CDND sample has approximately twice the humid SO_2 capacity of the GC sample. Data presented in Table 3.1 shows that CDND has a higher ash content than GC. It has been reported [85] that certain impurities increase the SO_2 adsorption on AC, especially in the presence of water.

Figure 3.5 shows breakthrough times obtained by challenging the ACs used in this study with C_6H_{12} under dry and humid conditions. Figure 3.5 shows that dry C_6H_{12} capacity ranks as GC > GG > CDND > NORIT > NUCHAR. Results from the wet flow tests show that there is a drastic reduction in C_6H_{12} adsorption relative to dry conditions. The wet C_6H_{12} capacity ranks as NORIT > CDND > GC > GG > NUCHAR. Under dry conditions the coconut shell derived carbons had the longest breakthrough times but under humid conditions the coal derived ACs performed best. Possible explanations for this behaviour are discussed below. Under both test conditions NUCHAR has the lowest C_6H_{12} capacity. Table 3.1 shows that NUCHAR had much lower tap density than the other samples which may help explain its relatively poor performance.

Figure 3.6 shows dry C_6H_{12} flow test results plotted against the average pore widths dimensions calculated from the N_2 adsorption data and SAXS data. The data shows dry C_6H_{12} breakthrough times decrease with increasing average pore dimension. The dry C_6H_{12} versus $\bar{d}_{SAXS}$ data shows a reasonably linear decrease in gas

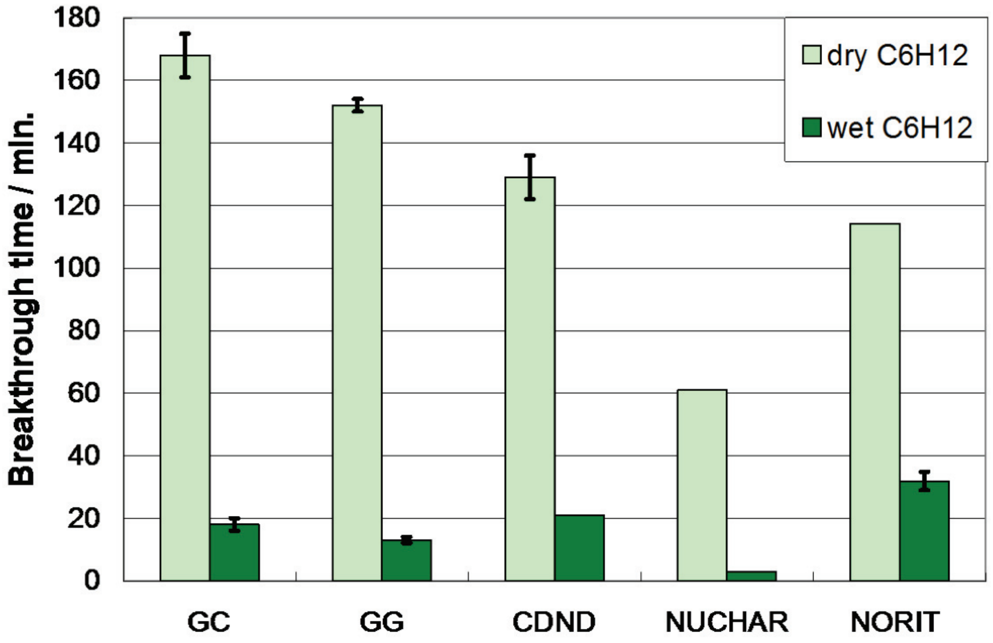

Figure 3.5: Breakthrough times obtained from challenging the AC samples in this study with C_6H_{12} under dry and humid conditions.

adsorption with increasing pore width. To physically adsorb gases it is important to have pore diameters slightly larger than the diameter of the gas and have larger mesopores available to transport the gas [4]. It has been reported that for non-polar interactions having a pore width less than 2 times the molecular diameter leads to enhanced adsorbate-adsorbent interactions [31]. The molecular dimension of C_6H_{12} has been reported as 5.8 Å [86] so it is not surprising that GC ($\bar{d}_{SAXS} = 12.4$ Å) has relatively high adsorption under dry conditions. The importance of matching pore size to molecular diameter has been reported for other types of adsorbents [87] and for energy storage devices [88].

Figure 3.7 shows wet C_6H_{12} breakthrough times plotted against the percent mass gain on humidification for the ACs tested in this work. Figure 3.7 shows that wet C_6H_{12} capacity decreases as the amount of pre-adsorbed water increases. The % mass gain on humidification for the ACs in this study ranked as: NORIT $<$ CDND $<$ GG $\approx$ GC $<$ NUCHAR. The coal based carbons exhibit the lowest water uptake and highest wet C_6H_{12} capacity of the ACs examined in this study. Water adsorption

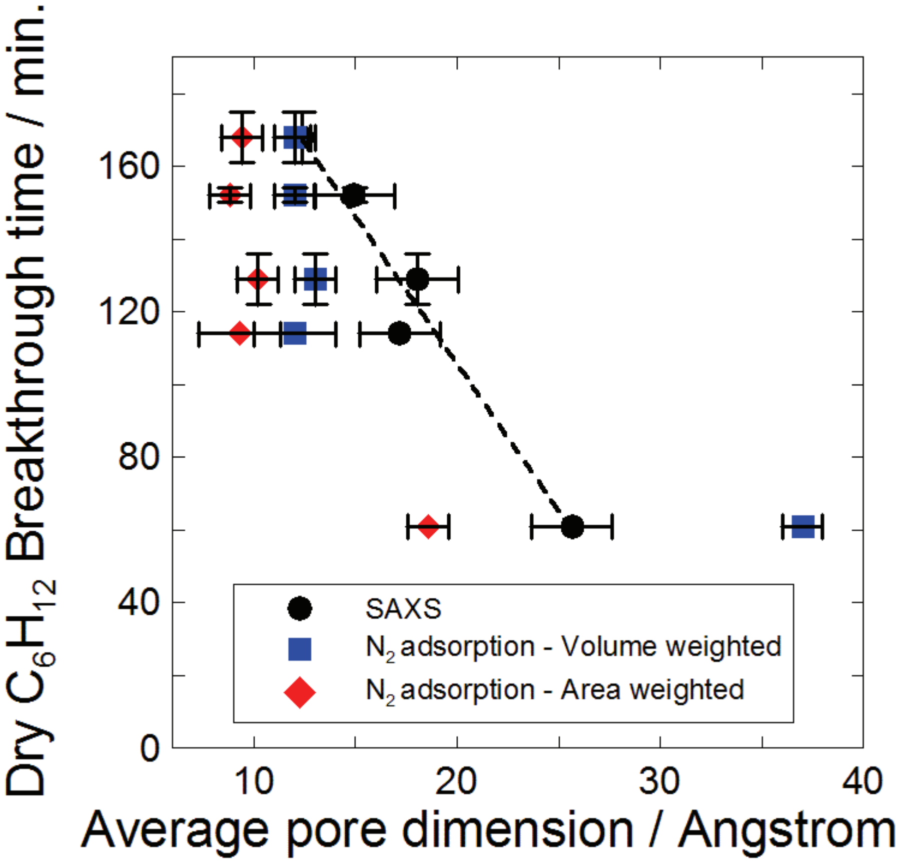

Figure 3.6: Dry C_6H_{12} breakthrough times plotted against average pore dimension for the AC samples studied in this work. The dashed line was inserted as a guide to the eye.

and competition between water and organic vapours have been reported to cause significant reductions in ACs ability to adsorb insoluble organic vapours under humid conditions [22, 89].

To further examine how pre-adsorbed water and C_6H_{12} may be competing for adsorption sites, a GC sample was examined using SAXS. Figure 3.8 shows SAXS data obtained from GC, GC exposed to dry 2000 ppm C_6H_{12} for 4 hours and a GC sample that was fully humidified in a 80 % RH humidity chamber. The mass gain due to exposure was approximately 35 % and 48 % for the dry C_6H_{12} and water vapour exposed samples respectively. Prior to performing the SAXS experiments, the GC samples were ground to a fine powder using a motar and pestle. The powdered samples were packed into 2.0 mm capillary tubes (supplied by the Charles Supper

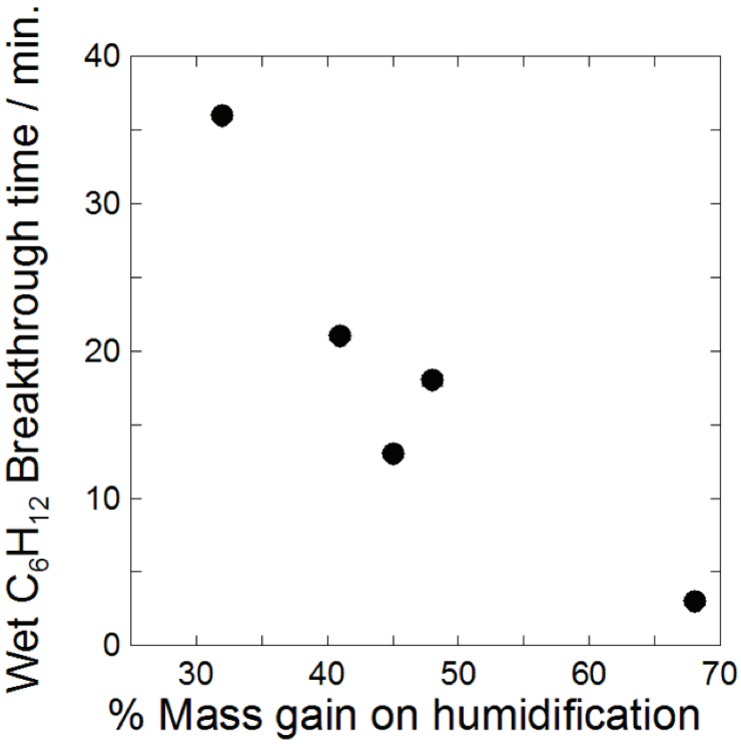

Figure 3.7: Wet C_6H_{12} breakthrough times plotted against % mass gain on humidification for the AC samples studied in this work.

company) and sealed using Torr seal epoxy. The epoxy was allowed to cure at room temperature for 24 hours prior to measurement.

Figure 3.8 shows the data obtained from the humidified GC sample has lower intensity than the unexposed GC sample at $q \geq 0.1$ Å^{-1}. This decrease in intensity is caused by the loss of electron density contrast due to micropores filling with water, as can be inferred from Eq. 2.12. Data obtained from the C_6H_{12} exposed sample has lower intensity than the unexposed GC sample at q ≥ approximately 0.2 Å^{-1} (which is again due to the loss of electron density contrast as C_6H_{12} fills the micropores). The data shows that the signal from the humidified GC sample decreases faster than the C_6H_{12} sample, possibly due to the higher mass of adsorbed species. The data in Figure 3.8 shows that water and C_6H_{12} populate the micropores and small mesopores of their respective samples. Since C_6H_{12} is not soluble in water the pre-adsorbed water must desorb to allow C_6H_{12} adsorption in humidified AC samples.

Both the exposed samples have higher intensity than GC for lower values of q,

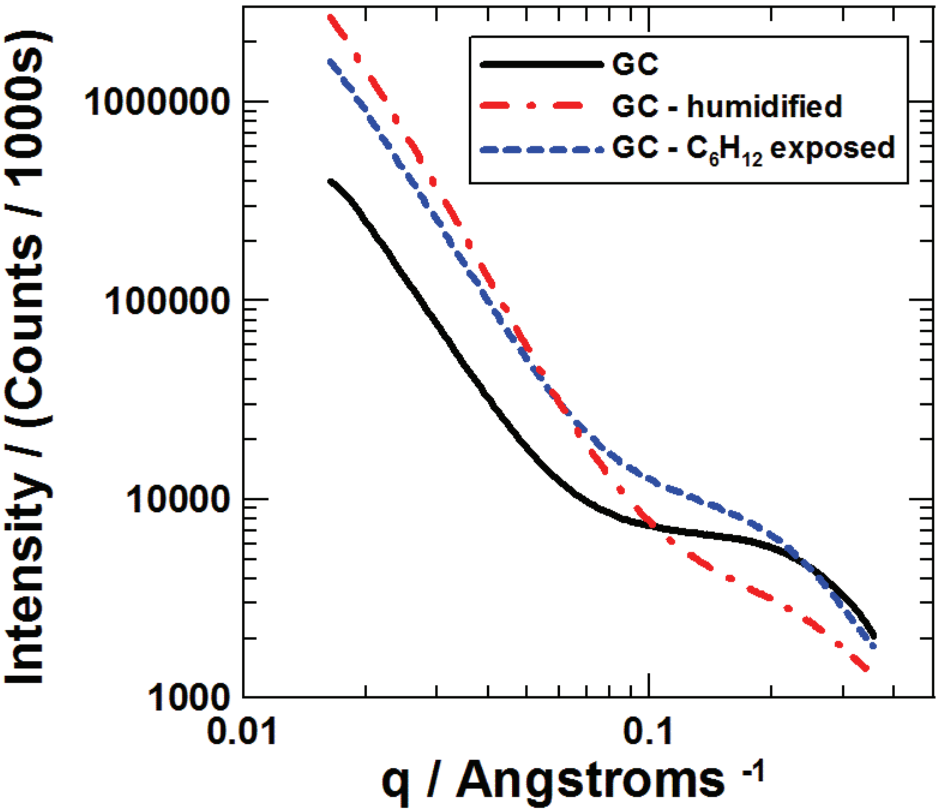

Figure 3.8: SAXS data collected from GC, GC sample exposed to C_6H_{12} and GC sample humidified in presence of water vapor.

specifically for q < 0.1 $Å^{-1}$ in the case of the humidified GC sample and q < 0.2 $Å^{-1}$ in the case of the C_6H_{12} exposed sample. The reason for the increased intensity is not immediately apparent. For scattering from larger pores (i.e. lower values of q), the contrast in electron density between carbon and pores is increased due to the presence of water (C_6H_{12}). It has been reported in the literature [90] that micropores filled with water effectively increase the density of carbon causing a higher electron density contrast at lower values of q. It is also possible that a monolayer of water forms on the carbon in the larger pores which would also effectively increase the electron density contrast between carbon and air.

3.2 Effects of HNO_3 Treatment

GC samples were treated with HNO_3 using 2 different methods. The first method involved boiling GC in 5 M HNO_3 for 5 hours, this sample is denoted A-GC. The

Table 3.4: Results of Boehm titrations performed on GC, GC-4M A-140 and A-GC samples.

Carbon	GC	GC-4M A-140	A-GC
Acidic sites: KOH (mmol/g)	0.18 ± 0.01	1.09 ± 0.01	3.1 ± 0.2

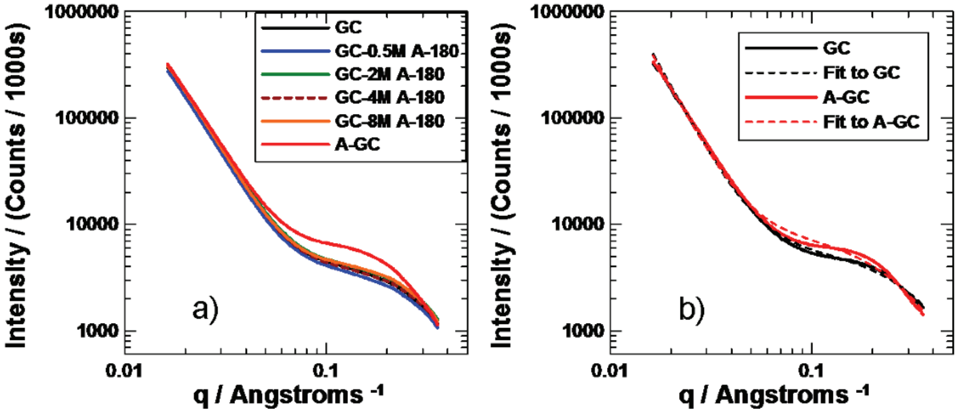

Figure 3.9: Panel (a) shows SAXS data collected from a GC sample and HNO_3 treated GC samples. The concentration of imbibed HNO_3 used was 0.5 M, 2 M, 4 M and 8 M as indicated in the legend. The A-GC sample was boiled in 5 M HNO_3. Panel (b) shows SAXS data (solid lines) and fits to the data (dashed lines) obtained from GC and A-GC samples as indicated in the legend.

second method was to imbibe GC with 4 M HNO_3. This sample was heated under argon at 140°C after impregnation and is denoted GC-4M A-140. To assess changes in the surface chemistry caused by the acid treatment, Boehm titrations were performed using the methods outlined in section 2.9. The samples were rinsed with deionized water until the rinse water had a pH $>$ 5 before the Boehm titrations were performed. Table 3.4 lists the results obtained from Boehm titrations using KOH base as the soaking solution.

Table 3.4 shows the A-GC sample has the highest number of acidic surface groups of the 3 samples. Oxidation of AC using HNO_3 has been reported to enhance the adsorption of metal ions from aqueous solutions [91] and improve the adsorption of toxins from the air [92]. The effect of HNO_3 treatments on IACs prepared from aqueous solutions containing metal ions will be discussed in more detail in chapter 4. The effect of the HNO_3 treatment on gas adsorption will be discussed below.

Samples were prepared for a SAXS study to determine how impregnation with HNO_3 affects the GC substrate. SAXS measurments were performed on GC and A-GC samples. Additional GC samples were imbibed with 0.5 M, 2 M, 4 M and 8 M HNO_3. These IACs were heated at 180°C prior to the SAXS experiments. The HNO_3 imbibed samples will be denoted as GC-0.5M A-180, GC-2M A-180, GC-4M A-180 and GC-8M A-180 to differentiate the concentration of HNO_3 used in the impregnating solution. The elevated heating temperature was chosen because it is a typical heating temperature used for multi-gas IACs as will be discussed later.

Figure 3.9(a) shows SAXS data collected from GC samples and GC samples with different HNO_3 treatments as detailed in the figure caption. Figure 3.9(b) shows SAXS data collected from GC (black line) and A-GC (red line) samples. The dashed lines represent the fits to the data using Eq. 2.14.

Figure 3.9(a) shows that the SAXS curves obtained from GC samples imbibed with $\leq$ 8 M HNO_3 are almost identical to the SAXS curve obtained from the GC sample. This indicates that imbibing the GC substrate with $\leq$ 8 M HNO_3, followed by heating at 180°C, does not significantly modify the carbon surface. The intensity of the data collected from the A-GC sample in the intermediate q range (q = 0.06 - 0.2 Å^{-1}) increased and shifted to lower values of q. This indicates that some of the micropores are becoming larger due to the agressive HNO_3 treatments.

Figure 3.9 shows the signals obtained from the GC and A-GC samples at $q < 0.07$ Å^{-1} are almost identical. In the $0.07 < q < 0.2$ Å^{-1} range the A-GC sample has higher intensity than the GC sample. Analysis of the 2 samples in panel (b) showed an increase in the R_g value of the A-GC sample (R_g = 7.4 Å) relative to the GC sample (R_g = 6.3 Å), however the error associated with the fit to the A-GC sample ($\chi^2 = 3.3$) was much higher than the GC sample ($\chi^2 = 1.3$). The observed differences between data and fit was highest in the $0.07 < q < 0.2$ Å^{-1} range. The data in Figures 3.9(a) and 3.9(b) shows that imbibing GC with $\leq$ 8 M HNO_3 does not significantly affect the carbon surface. Boiling GC in 5 M HNO_3 for 5 hours was observed to cause the greatest change to the carbon surface. The SAXS data collected from the A-GC sample indicates that some micropores are increasing in dimension due to the aggressive HNO_3 treatment. The effects of co-impregnating IACs with

HNO_3 and metal ion containing solutions will be studied in more detail in chapter 4.

Figure 3.10 shows flow test results obtained from challenging the samples in this study with SO_2, NH_3 and HCN gases. The samples in panel (a) and (b) were tested under dry and wet conditions respectively. Only the GC and A-GC samples were tested under wet conditions.

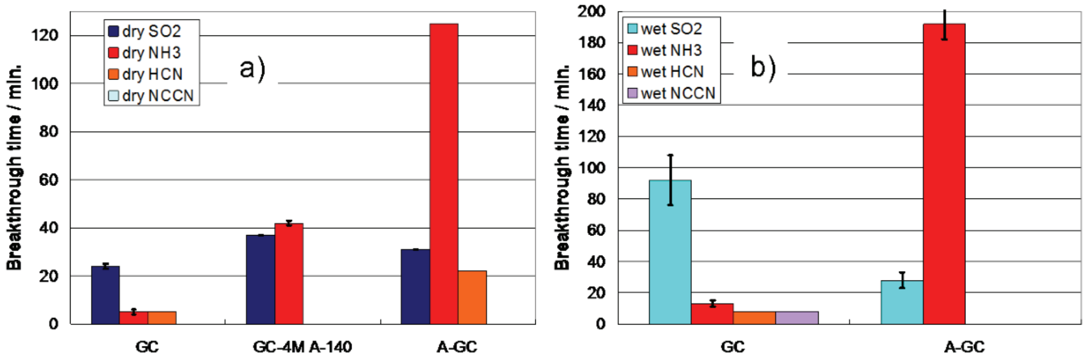

Figure 3.10: Flow test results obtained from challenging the samples in this study with SO_2, NH_3 and HCN gases. Results obtained from dry and wet tests are shown in panels (a) and (b), respectively.

Figure 3.10 shows that the HNO_3 treated GC samples have slightly longer dry SO_2 breakthrough times than the GC sample, possibly due to the SO_2 gas interacting with oxygen rich surface groups [83] via the reaction:

$$SO_2 + \frac{1}{2}\,O_2 \rightarrow SO_3 \tag{3.4}$$

The SO_3 molecule reacts with water to form sulfuric acid (H_2SO_4). The data in panel (a) shows that the A-GC sample has a longer HCN breakthrough time than the GC sample. The increase in breakthrough time could possibly be due to the presence of oxygen containing surface groups [18]. The dry SO_2 and HCN capacities of these samples are low relative to impregnated AC samples used for multi-gas applications. Figure 3.10 (a) shows that dry NH_3 capacity ranks as A-GC > GC-4M A-140 > GC. Table 3.4 shows the number of acidic surface functional groups ranks as A-GC > GC-4M A-140 > GC. This data shows that as the number of oxygen rich surface groups (introduced by the HNO_3 treatment) increases the dry NH_3 capacity increases.

Figure 3.10 (b) shows that under humid conditions GC has a much longer SO_2

breakthrough time compared to A-GC. The formation of surface acid upon humidification on the A-GC sample is likely the cause of the lower wet SO_2 capacity. Under humid conditions the GC sample has poor HCN capacity and the A-GC was not tested for wet HCN capacity. The wet NH_3 capacity of the A-GC sample is much greater than the GC sample as was explained earlier. The wet NH_3 capacity of the A-GC sample is higher than the dry capacity. The formation of surface acid upon humidification in the A-GC sample may help explain the additional capacity when challenged with a basic gas.

Figure 3.11 shows the C_6H_{12} breakthrough times obtained from the samples in this study under dry and wet conditions.The A-GC sample was not tested for dry C_6H_{12} capacity. The data shows that the GC and GC-4M A-140 samples have approximately the same dry C_6H_{12} breakthrough times. This supports the earlier observation that $\leq$ 4 M HNO_3 treatment does not significantly alter the pore size of the treated samples. Figure 3.11 shows that the wet C_6H_{12} capacity of the samples in this study ranks as GC $>$ GC-4M A-140 $>$ A-GC. The percent weight gain upon humidification for these samples was GC = 48 ± 1 %, GC-4M A-140 = 31 % and A-GC = 50 ± 1 %. Comparing the wet C_6H_{12} breakthrough times to the equillibrium mass gain on

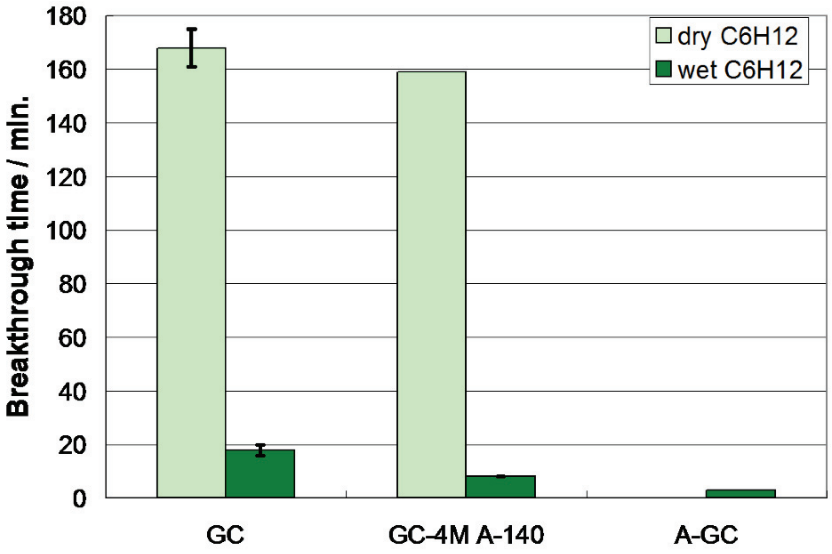

Figure 3.11: C_6H_{12} breakthrough times obtained from the samples in this study under dry and wet conditions.

humidification for the GC and HNO_3 treated samples shows that it is not the amount of pre-adsorbed water that is the cause of the decreased wet C_6H_{12} capacity. The oxidation of the AC causes the HNO_3 samples to have stronger retention of the pre-adsorbed water compared to the un-treated GC. The strength of these interactions and the effect of heating temperature on HNO_3 treatments will be discussed in more detail in chapter 4.

3.3 Universal Respirator Carbon (URC)

The performance of the IAC samples prepared in this work were compared to results obtained from URC as described earlier. Some of the important features of the URC samples are reported here. Figure 3.12 shows TGA and derivative TGA data obtained from URC samples as received and after heating at 120 °C in air.

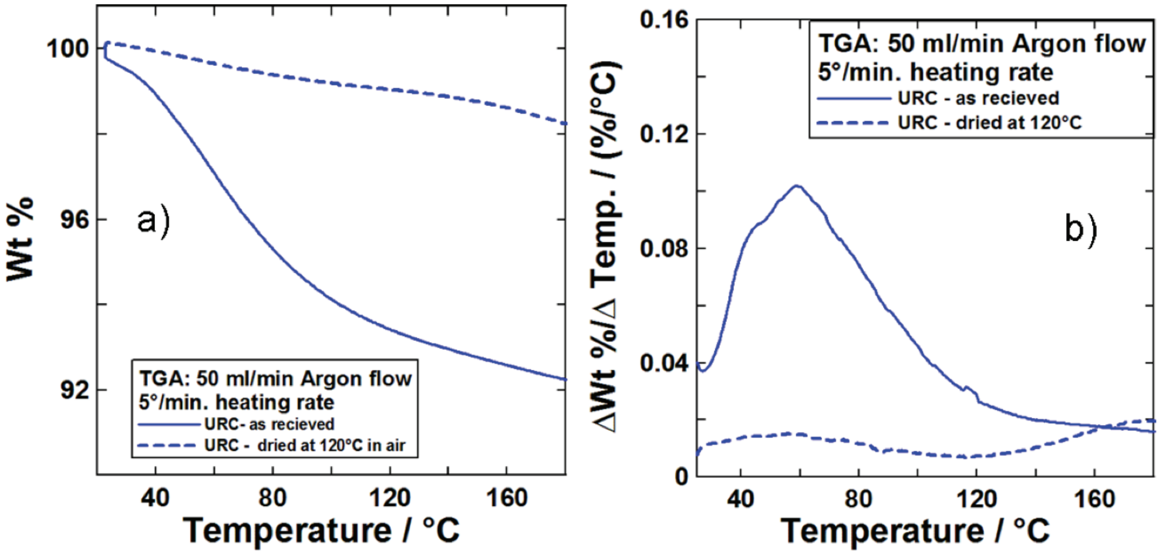

Figure 3.12: TGA and derivative TGA data obtained from URC samples are shown in panels (a) and (b) respectively. Experiments were performed on as-received URC and URC that had been heated at 120°C in air.

Figure 3.12 (a) shows that the weight of the as-recieved URC sample decreases by approximately 8% over the temperature range shown in the graph. The URC sample that was pre-dried at 120°C prior to testing has only 2 wt.% decrease over the same range. Panel (b) shows a broad peak, centered at approximately 70°C, in the derivative TGA data obtained from the as-recieved URC sample. The derivative TGA data obtained from the pre-dried URC sample remains relatively constant over the entire heating temperature range shown in panel (b). The higher mass loss exhibited by the as-received sample compared to the pre-dried sample is likely due to desorption of water. Patent information describing the URC process describes using water as an impregnant [13]. The effect impregnated water has on gas adsorption capacity will be discussed below.

Figure 3.13 shows wide angle x-ray diffraction data obtained from a URC sample and an unimpregnated CDND sample. For reference, the Bragg peak positions for ammonium copper molybdate ($(NH_4)_2Cu(MoO_4)_2$) are indicated [56]. Figure 3.13 shows weak diffraction peaks likely associated with the $(NH_4)_2Cu(MoO_4)_2$ impregnant phase for the URC sample. In earlier work that studied the URC process it was reported that the Cu and Mo species are in intimate contact on the AC substrate and that the presence of the Mo-containing compound affected the crystallization of the Cu species [23]. The absence of sharp diffraction peaks in the XRD pattern obtained from the URC sample is indicative of small grain size impregnant that is well dispersed on the AC substrate as can be inferred from Eq. 2.5.

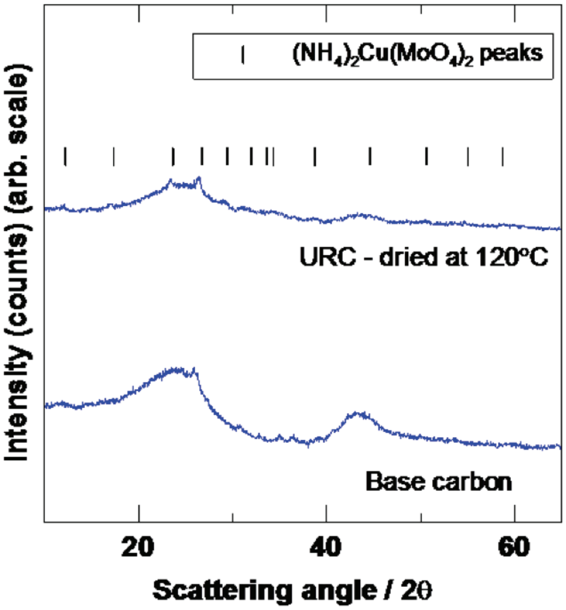

Figure 3.13: Wide angle x-ray diffraction data (XRD) obtained from pre-dried URC sample and an unimpregnated CDND sample. For reference, the Bragg peak positions for ammonium copper molybdate are indicated.

Figure 3.14 shows flow test results obtained from the pre-dried and as-received URC samples denoted URC-dry and URC-AR respectively. The challenge gases used were SO_2, NH_3, HCN and C_6H_{12}. Breakthrough times obtained from dry and wet flow tests are reported in panels (a) and (b) respectively. Under wet conditions both URC samples are fully humidified so no distinction between the wet flow test results is made.

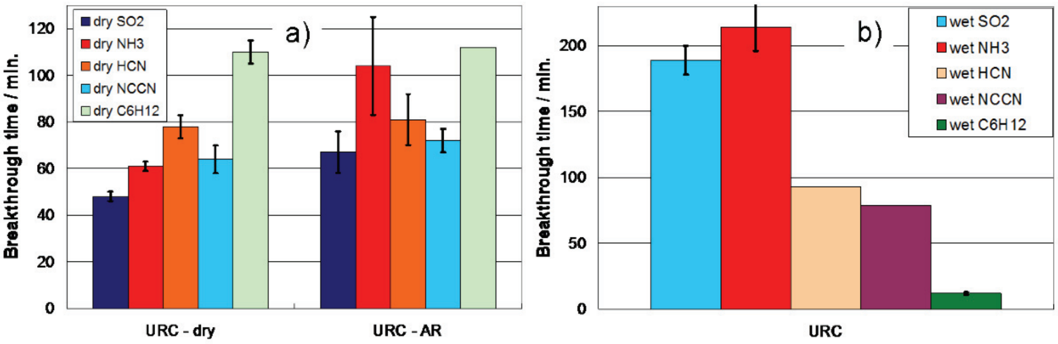

Figure 3.14: Flow test results obtained from the pre-dried and as-received URC samples , denoted URC-dry and URC-AR respectively. The challenge gases used were SO_2, NH_3, HCN and C_6H_{12}. Breakthrough times obtained from dry and wet flow tests are reported in panels (a) and (b) respectively.

Figure 3.14 shows that the as-received URC sample has longer dry SO_2 and NH_3 breakthrough times than the pre-dried sample that are caused by the presence of water as an impregnant in the as-received URC sample. Increased SO_2 capacity in humidified samples was explained in section 3.1. NH_3 is soluble in water [93] so the increased capacity for the sample with impregnated water is expected. The dry HCN and C_6H_{12} breakthrough times are the same for the 2 URC samples. A decrease in dry C_6H_{12} capacity for the as-received URC sample may have been expected due to the presence of water but it was not observed.

Figure 3.14 (b) shows the flow test results obtained under humid conditions. The wet SO_2, NH_3 and HCN flow breakthrough times are longer than those obtained under dry conditions. The presence of water may increase the contact time between the Cu^{2+} impregnant and HCN, improving the efficiency of the reaction described in Eq. (1.1). Comparison of the wet and dry C_6H_{12} capacity shows a dramatic decrease in adsorption of the organic vapour under humid conditions due to the competition between pre-adsorbed water and the organic vapour for adsorption sites.

Chapter 4

Comparative Study of Metallic Nitrate Precursors for use in Multi-gas Impregnated Activated Carbons

In this chapter a comparative study of IACs prepared from different metal nitrate precursors is described. The precursors studied in this work were copper nitrate ($Cu(NO_3)_2$), zinc nitrate ($Zn(NO_3)_2$), iron (III) nitrate ($Fe(NO_3)_3$), manganese nitrate ($Mn(NO_3)_2$), aluminium nitrate ($Al(NO_3)_3$) and calcium nitrate ($Ca(NO_3)_2$). The precursors chosen for this study are known impregnants from whetlerite studies [9].

4.1 Experimental Details

4.1.1 Chemicals Used

The chemicals used to prepare the impregnating solutions were copper nitrate hemipentahydrate ($Cu(NO_3)_2\bullet 2.5H_2O$ Alfa Aesar, reagent grade), zinc nitrate hexahydrate ($Zn(NO_3)_2\bullet 6H_2O$), manganese nitrate hydrate ($Mn(NO_3)_2\bullet xH_2O$), aluminium nitrate nonahydrate ($Al(NO_3)_3\bullet 9H_2O$), calcium nitrate tetrahydrate ($Ca(NO_3)_2\bullet 4H_2O$) (all 4 were obtained from Sigma Aldrich, reagent grade), iron (III) nitrate nonahydrate ($Fe(NO_3)_3\bullet 9H_2O$, Anachemia, A.C.S. grade) and 70% concentrated nitric acid (HNO_3). The solutions were prepared by dissolving the selected compound in deionized water. Solutions prepared with $Mn(NO_3)_2\bullet xH_2O$ used deaerated, deionized water. A value of $x = 4$ for $Mn(NO_3)_2\bullet xH_2O$ was determined from a TGA experiment.

4.1.2 Sample Preparation

IAC samples were prepared by impregnating GC activated carbon. GC was previously described in section 3.1. The GC substrate was impregnated using the imbibing method. The samples prepared from $Cu(NO_3)_2$, $Zn(NO_3)_2$ and $Mn(NO_3)_2$ were impregnated with 2.4 M solutions. The sample prepared from $Ca(NO_3)_2$ used a 2.5 M solution. All of the preceding samples were prepared in one imbibing step. The samples prepared from $Al(NO_3)_3$ or $Fe(NO_3)_3$ were impregnated with 1.3 M solutions, these samples required two imbibing steps to achieve the desired impregnant loading.

All of the IACs prepared in this study were heated under argon flowing at approximately 60 mL/min. The furnace was purged for at least $\frac{1}{2}$ hour prior to heating. The samples were heated to maximum final heating temperatures, $T_f = 120$, 140, 160, 180 and 200°C. Typically the IACs were held at T_f for approximately 0.2 hours per gram of sample (e.g. a 15 g sample would be held at T_f for approximately 3 hours). The samples that required 2 imbibing steps also required 2 heating steps. After the first imbibe the samples were heated (under argon) at 115°C for approximately 2 hours, then allowed to cool to room temperature prior to the second imbibe. The second heating cycle was performed at the designated value of T_f.

The overall weight percent impregnant loading was determined by gravametric analysis according to Eq. 2.1. Commercially available URC samples were used for comparative purposes. Flow test results obtained from the URC samples will be denoted 'URC'. Prior to flow testing the GC and URC samples were pre-dried at 120°C in air to lower their moisture content to $< 5\%$ (wt.).

4.2 Results and Discussion

IAC samples studied in this work have approximately the same loading of metallic impregnant (1.8 ± 0.1 mmol/g GC). Samples will be denoted by the abbreviation for their metallic impregnant followed by the heating temperature (where appropriate). For example Fe-120 denotes a sample prepared from $Fe(NO_3)_3$ that was heated at 120°C.

4.2.1 Sample Characterization Results

Figure 4.1 shows the impregnant loading of the IAC samples prepared in this work as detailed in the figure caption. The data is expressed as % loading as a function of heating temperature (T_f). For reference the predicted loadings for GC impregnated with copper oxide (CuO), copper nitrate hydroxide ($Cu_2(OH)_3NO_3$), zinc oxide (ZnO), iron(III)oxide (Fe_2O_3), manganese(II, III)oxide (Mn_3O_4) and aluminum oxide are indicated. The predicted loadings are based on the volume and concentration of the impregnating solution and assume full conversion to the impregnant species indicated in the appropriate panel.

Figure 4.1 shows that the heating temperature required to promote conversion to the metal oxide phase varied between the different samples. Panel (a) shows that at $T_f < 160$°C the Cu-IACs had high impregnant loading which is indicative of incomplete conversion of the impregnant. At $T_f = 160$°C the gravimetric data indicates $Cu_2(OH)_3NO_3$ is the dominant impregnant phase. Heating the Cu-IACs at $160° < T_f \leq 190°$ caused conversion of $Cu(NO_3)_2$ to CuO based on mass. Panels (b), (c), (d) and (e) show that heating the IACs at or above 140°C caused conversion of the metallic impregnants primarily to ZnO, Fe_2O_3, Mn_3O_4 and Al_2O_3 based on mass, respectively.

TGA analysis of $Ca(NO_3)_2$ (not shown) was performed prior to sample preparation. It was observed that a relatively high heating temperature was required to convert $Ca(NO_3)_2$ to CaO. For this reason only one IAC was prepared using $Ca(NO_3)_2$. The sample was heated at $T_f = 200$°C under argon. The observed impregnant loading was 18% (wt.) and the theoretical loading assuming the impregnant had converted to CaO was 10% (wt.).

Powder XRD was performed after heating to help identify the phase of the impregnant on the GC substrate. Figure 4.2 shows XRD results from IAC samples prepared in this study as detailed in the figure caption. Results from the IACs heated at temperatures between $T_f = 120$°C and 200° are shown. The Cu-based IACs heated at $T_f \leq 180$°C, the Zn-based IACs and the Ca-based IAC were analyzed using a Rigaku mini-flex x-ray diffractometer. The Fe- and Mn-based IACs were analyzed using a Siemens D5000 x-ray diffractometer equipped with a graphite monachrometer to remove radiation caused by fluorescence prior to the x-ray beam reaching the detector. Samples Fe-120, Fe-200 and Mn-200 were analyzed. The Cu-190 sample and Al-based IACs were analyzed using an Inel x-ray diffractometer. For reference the strongest Bragg peak positions for CuO, $Cu_2(OH)_3NO_3$, ZnO, Fe_2O_3 and Mn_3O_4

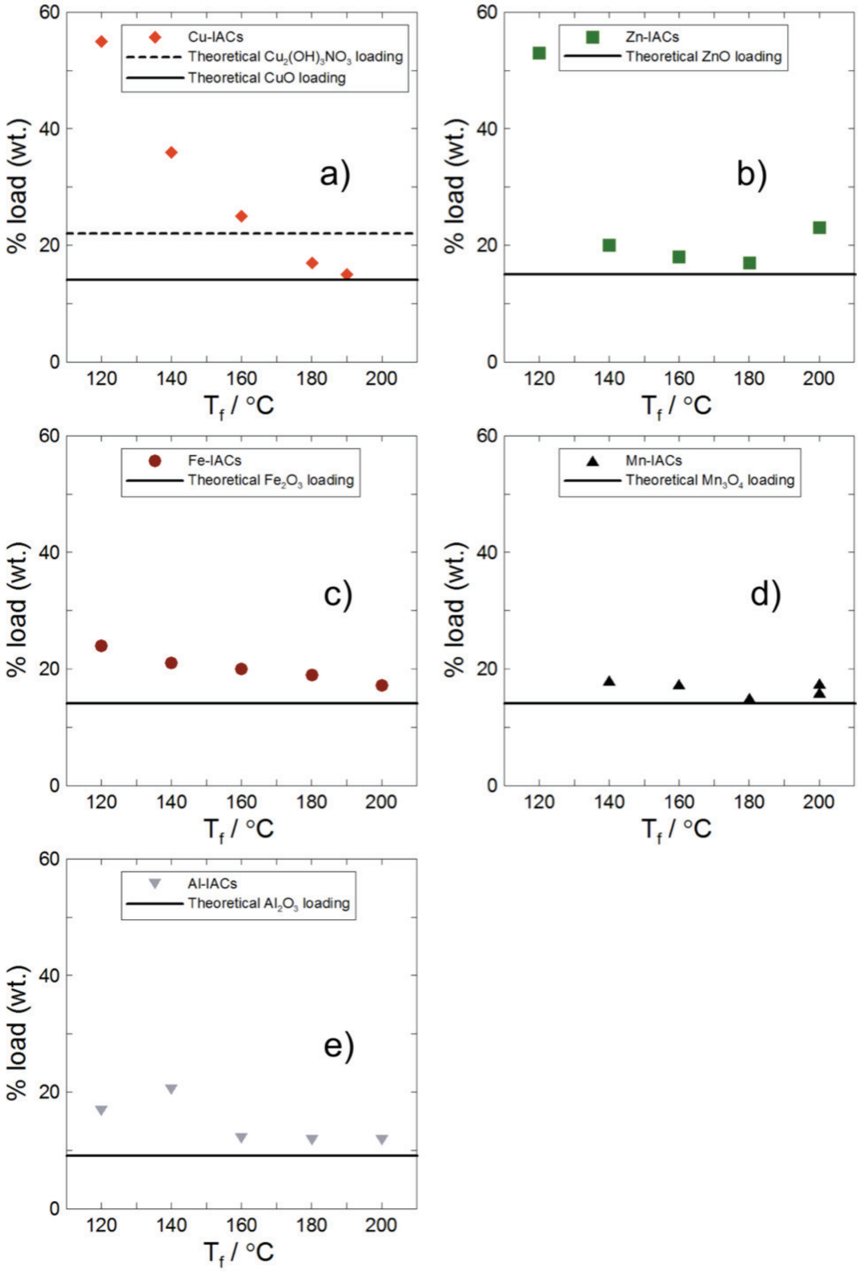

Figure 4.1: Impregnant loading of IAC samples as a function of temperature. Panels (a), (b), (c), (d), and (e) show data obtained from Cu-based, Zn-based, Fe-based, Mn-based and Al-based IACs respectively. The theoretical loadings if the impregnate fully converted to CuO, $Cu_2(OH)_3NO_3$, ZnO, Fe_2O_3, Mn_3O_4 or Al_2O_3 are indicated for reference.

are indicated [56].

Figure 4.2(a) shows that Cu-based IACs heated at $T_f \leq 160$°C tend to convert

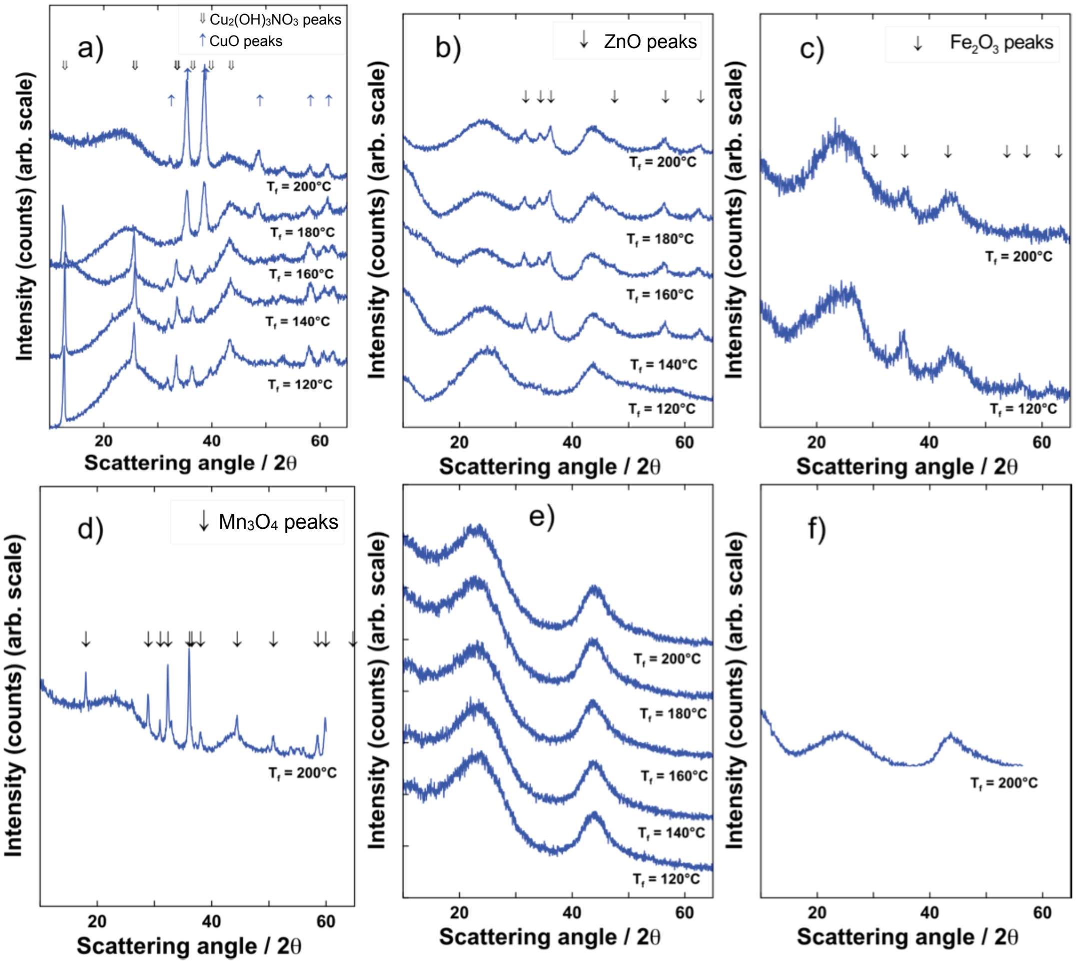

Figure 4.2: XRD data obtained from the IAC samples in this study. Panels (a), (b), (c), (d), (e) and (f) show data obtained from Cu-based, Zn-based, Fe-based, Mn-based, Al-based and Ca-based IACs respectively. The value of T_f is indicated for each sample. For reference the strongest Bragg peak positions for CuO, $Cu_2(OH)_3NO_3$, ZnO, Fe_2O_3 and Mn_3O_4 are indicated [56].

to $Cu_2(OH)_3NO_3$ while samples heated at $T_f \geq 180°$ show CuO is the dominant impregnant phase. Figure 4.2(b) shows that the Zn-based IACs tend to convert to ZnO at 140°C $\leq T_f \leq$ 200°C. Comparison of panels (a) and (b) shows the Zn-based IACs tend to convert to the metal oxide phase at lower heating temperatures than the Cu-based IACs. Figure 4.2(c) shows that the data obtained from the Fe-120 and Fe-200 samples have an impregnant related diffraction peak located at $2\theta \approx 35°$. This peak corresponds to a Bragg peak associated with the Fe_2O_3 phase, but the overall match to this impregnant phase is not convincing. It has been reported in the literature that

$Fe(NO_3)_2$ thermally decomposes to α-Fe_2O_3 at heating temperatures similar to those used in this study [94]. Figure 4.2(d) shows that the dominant impregnant phase for the Mn-200 IAC is Mn_3O_4. The impregnant loading data in Figure 4.1(d) shows all of the Mn-based samples had similar impregnant loading. Based on the data in Figures 4.1 and 4.2 it is reasonable to assume the dominant impregnant phase for the Mn-based samples is Mn_3O_4. Figures 4.2(e) and (f) show there are no impregnant related diffraction peaks present for the Al-based IACs and Ca-based sample respectively. Heating $Al(NO_3)_3$ at temperatures similar to those used in this study has been reported to result in amorphous decomposition products [95]. The XRD data in panel (f) does not provide any information about the impregnant species present on the Ca-200 sample.

The XRD data shown in Figure 4.2 was useful to help identify the dominant impregnant species present after heating in many of the IAC samples studied in this work. Comparison of the different panels in Figure 4.2 shows the intensity and width of the impregnant related diffraction peaks varies widely depending on the species present. This indicates a wide variance in impregnant grain size and impregnant dispersion as can be inferred from Eq. 2.5. The effect of impregnant grain size and impregnant dispersion will be discussed in detail in later chapters.

4.2.2 Gas Adsorption Capacity

Figure 4.3 shows dry SO_2 breakthrough time plotted against T_f for the IAC samples prepared in this study as detailed by the figure caption.Flow test results obtained from testing GC and URC have been included. Figure 4.3 shows all of the IACs prepared in this work have breakthrough times equal to or greater than URC and greater than GC. Samples whose impregnant loading and or XRD data showed the dominant impregnant phase was metal oxide (see Figures 4.1 and 4.2 respectively) typically had constant SO_2 breakthrough times versus T_f. The flow test results obtained from the Cu-based IACs heated at $T_f \leq 160^\circ$ vary widely, likely due to incomplete thermal decomposition of the impregnant to the desired CuO phase. Long breakthrough times have been reported for IACs with $Cu_2(OH)_3NO_3$ as the dominant impregnant phase, but this type of IAC is not a suitable multi-gas IAC due to thermal instability [39].

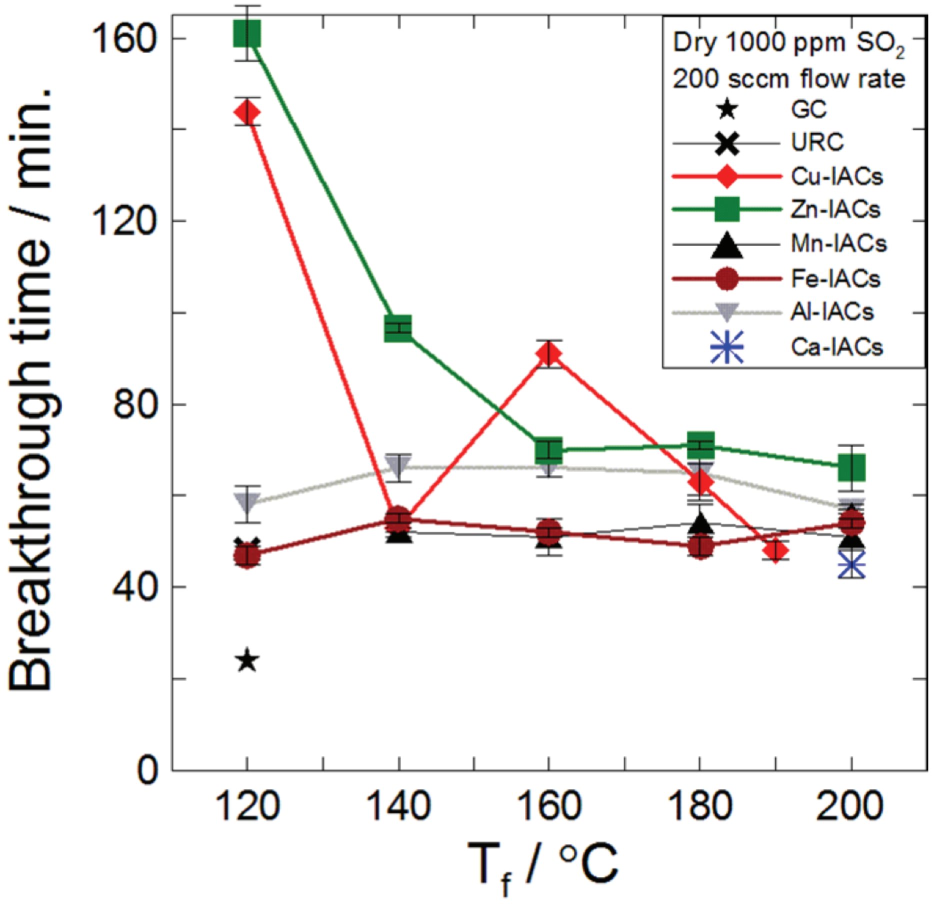

Figure 4.3: Dry SO_2 breakthrough times versus T_f. Data obtained from flow testing the Cu-, Zn-, Fe-, Mn-, Al- and Ca-based IACs is shown for each value of T_f.Results obtained from GC and URC samples are indicated for reference.

The long SO_2 breakthrough times obtained from the Zn-120 and Zn-140 IACs may be attributed to incomplete conversion of the impregnant to ZnO. The overall SO_2 capacity for the IACs heated at $T_f > 160$°C ranks as: Zn-based > Al-based ≈ Cu-based > Fe-based ≈ Mn-based > Ca-based. Based on the data shown in Figures 4.1, 4.2 and 4.3 ZnO is the most effective impregnant for SO_2 adsorption.

Figure 4.4 shows dry NH_3 breakthrough times plotted versus T_f for the IACs prepared in this study as detailed in the figure caption. Results obtained from URC and GC are indicated. Figure 4.4 shows the Cu-160 sample and the Zn-, Fe- and Al-based IACs heated at $T_f \leq 140$°C had dry NH_3 breakthrough times greater than or equal to URC and greater than GC. Samples Cu-120, Cu-140 and Zn-120 (not

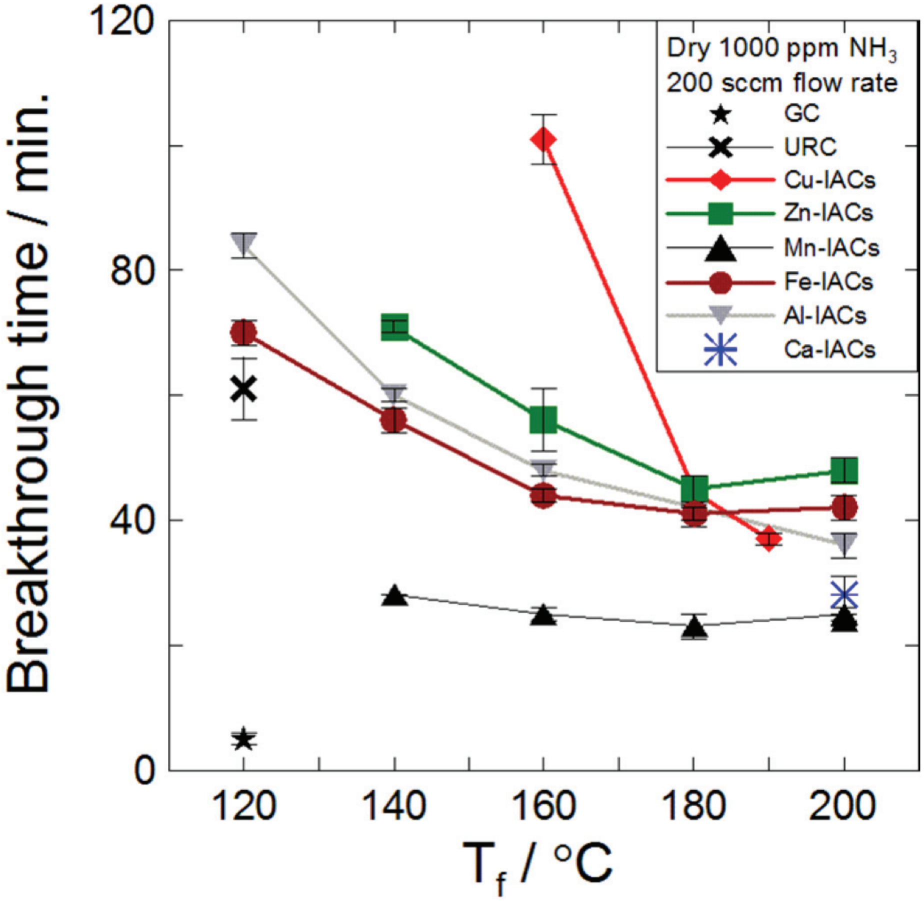

Figure 4.4: Dry NH_3 breakthrough times versus T_f. Data obtained from flow testing the Cu-, Zn-, Fe-, Mn-, Al- and Ca-based IACs is shown for each value of T_f.Results obtained from GC and URC samples are indicated for reference.

shown) had dry NH_3 breakthrough times of (261 ± 8) min., (186 ± 8) min. and 340 min. respectively. Comparing Figures 4.4 and 4.1 shows that samples with higher % impregnant loading typically had longer dry NH_3 breakthrough times. This is likely due to incomplete conversion of the impregnant to the desired metal oxide phase or the pressence of excess moisture. The dry NH_3 capacity for the IACs heated at $T_f > 160°C$ ranks as: Zn-based > Fe-based > Cu-based ≈ Al-based > Ca-based > Mn-based. Based on the data shown in Figures 4.1, 4.2 and 4.4, ZnO is the most effective impregnant for dry NH_3 adsorption.

Figure 4.5(a) shows dry HCN and NCCN breakthrough times plotted versus T_f for the IACs in this study as detailed in the figure caption. The HCN and NCCN

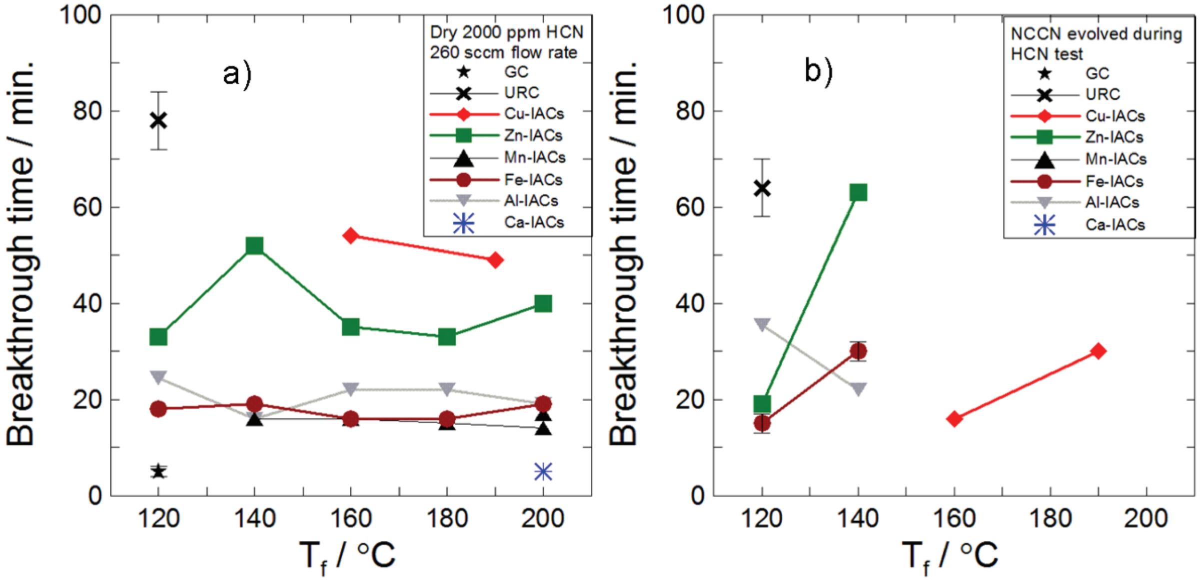

Figure 4.5: Dry HCN and NCCN breakthrough times versus T$_f$ are shown in panels (a) and (b) respectively. Data obtained from flow testing the Cu-, Zn-, Fe-, Mn-, Al- and Ca-based IACs is shown. Results obtained from GC and URC samples are indicated for reference.

breakthrough times are shown in panels (a) and (b) respectively. The only Cu-based IACs tested were samples Cu-180 and Cu-190. In this work the IAC samples were challenged with 2000 ppm HCN gas. The toxic by-product NCCN is generated when HCN gas is oxidized by an impregnant. An example of this is the reaction between CuO impregnant and HCN gas as described in Eq. 1.1.

Figure 4.5 shows all of the IACs tested in this work except for the Ca-200 sample had longer HCN breakthrough times than GC. All of the IACs studied in this work had shorter breakthrough times than the URC sample. Work based on the preferred recipe in Ref. [13] indicated that URC has ≈ 2.3 mmol Cu^{2+}/g AC [23]. The samples in this work have ≈ 1.8 mmol impregnant/g GC. The higher impregnant loading may be one reason the URC sample had a longer HCN breakthrough time compared to the IACs studied in this work. The factors that influence the HCN adsorption capacity of IACs will be discussed in detail in later chapters. The dry HCN capacity of the IAC samples in this study rank as: Cu-based > Zn-based > Al-based > Fe-based ≈ Mn-based > Ca-based. The Al-, Fe-, Mn-, and Ca-Based IACs all had relatively poor HCN capacity compared to the Cu- and Zn-based samples. The results shown in Figures 4.1, 4.2 and 4.5 indicate that CuO is the most effective impregnant for dry HCN adsorption.

Figure 4.5(b) shows that NCCN was evolved during the HCN flow tests for the Cu-180, Cu-190 and the Zn-, Fe- and Al-based IACs heated at $T_f \leq 140°C$. Evolution of NCCN is expected when Cu^{2+} impregnant reacts with HCN gas (see Eq. 1.1). Stable cyanide complexes have been reported for Zn^{2+} impregnant [17] and for Fe^{3+} [96] so the evolution of NCCN for the Zn- and Fe-based samples was unexpected. The evolved NCCN detected during the dry HCN gas test results obtained from the Zn-, Fe- and Al-based IACs heated at $T_f \leq 140°C$ may be due to incomplete conversion of the impregnant to the metal oxide phase. Metal nitrates are strong oxidizing agents so it is reasonable to expect some NCCN generation in samples with incomplete conversion of the impregnant.

4.3 Conclusions

Cu-based IACs required heating temperatures of $T_f \geq 180°C$ to promote full conversion of the impregnant to CuO. The Zn-, Fe-, Mn- and Al-based IACs converted to a metal oxide phase when heated at $T_f \geq 160°C$. For samples heated at $T_f \geq 160°C$, ZnO was the most effective impregnant for dry SO_2 and NH_3 adsorption. The most effective impregnant for dry HCN adsorption was CuO.

Based on the data presented in this section the Zn- and Cu-based samples are the most promising multi-gas IACs. Comparative studies of Zn- and Cu-based samples are reported in chapters 5 and 6. The effects of heating temperature (over an extended range) and co-impregnation with HNO_3 are studied using XRD, TGA, SEM, and flow testing (under dry and humid conditions) in chapter 5. The effects of impregnant loading, heating temperature (over an extended range) and co-impregnation with HNO_3 are studied using XRD, SAXS, gas adsorption porosimetry and flow testing (under dry and humid conditions) in chapter 6.

Chapter 5

The Effect of Heating Temperature and Nitric Acid Treatments on the Performance of Cu- and Zn-based Broad Spectrum Respirator Carbons

The contents of this chapter, including all figures, have been previously published in Ref. [78], The Journal of Colloid and Interface Science, volume 364, issue 1, pages 178-194. The authors are Jock Smith, Jennifer Romero, Tara Dahn, Kevin Dunphy, Braden Sullivan, Matthew Mallay, Lisa Croll, Judy Reynolds, Carrie Andress and Jeff Dahn. The contribution of Jock Smith to this manuscript consists of organization of all experiments, assistance with sample preparation and characterization, all of the data analysis and all of the figure and manuscript preparation. The figures have been reproduced by permission of the Journal of Colloid and Interface Science in accordance with the terms of the publishing company (Elsevier) copyright release (see Appendix A). The text, figure numbers and references have been modified for inclusion in this thesis.

5.1 Experimental Details

5.1.1 Chemicals Used

The chemicals used to prepare the impregnating solutions were copper nitrate hemipentahydrate ($Cu(NO_3)2\bullet2.5H_2O$ Alfa Aesar, reagent grade), zinc nitrate hexahydrate ($Zn(NO_3)2\bullet6H_2O$ Sigma Aldrich reagent grade) and 70% concentrated nitric acid (HNO_3).

5.1.2 Sample Preparation

IAC samples were prepared using GC activated carbon. The properties of GC were presented in section 3.1. IAC samples containing metallic impregnants were prepared by impregnating GC activated carbon with either 2.4 M $Cu(NO_3)_2$ or 2.4 M $Zn(NO_3)_2$ solution. Some of these impregnating solutions also contained either 0.5 M HNO_3 or 4 M HNO_3. The GC substrate was impregnated using the imbibing or incipient wetness method. The impregnating solution was added in a ratio of approximately 0.8 mL of solution per gram GC. This was at or near the imbibing limit.

Some GC substrates were treated with HNO_3 by two methods, the imbibing method or by boiling the GC in 5 M HNO_3 for 5 hours. The imbibed samples were prepared from either 0.5 M HNO_3 or 4 M HNO_3 and will be referred to as GC-0.5M A or GC-4M A respectively. Details of the GC that was boiled in 5 M HNO_3 have been described in section 3.2, and these samples will be referred to as A-GC.

All of the samples prepared in this work were heated under argon in a tube furnace. The tube was purged with argon, (60 mL/min) for approximately $\frac{1}{2}$ hour prior to heating and during heating. The samples were heated to temperatures, T_f, ranging from 120°C to 450°C. Typically, a 15 g sample was held at T_f for 3 hours and cooled under argon.

The overall weight percent impregnant loading was determined by gravimetric analysis according to the Eq. 2.1. Impregnant loading that is expressed in mmol impregnant/g GC was estimated from the volume and concentration of impregnating solution added to the virgin GC. The relative uncertainty is 0.1 mmol impregnant/g GC.

Commercially available URC samples were used for comparative purposes. The flow test results for URC will be referred to as "URC". Prior to dry dynamic flow testing the URC samples and unimpregnated GC samples were heated at 120°C in air to lower the moisture content of the IACs to $< 5\%$ (wt.).

5.2 Results and Discussion

IAC samples studied in this work have approximately the same loading of metallic impregnant (1.8 ± 0.1 mmol/g GC). Samples are denoted by the abbreviation for their metallic impregnant, followed by the concentration of HNO_3 (if any) present in the impregnating solution, followed by the thermal heating temperature. For example, the samples Zn-120, Zn-0.5M A-120 and Zn-4M A-120 correspond to samples prepared from 2.4 M $Zn(NO_3)_2$, $Zn(NO_3)_2$/0.5 M HNO_3 and $Zn(NO_3)_2$/4 M HNO_3 respectively, which were all heated to 120°C. Samples with no metallic impregnant present (i.e. HNO_3 impregnated only) will simply be identified by the concentration of HNO_3 solution they were impregnated with.

5.2.1 Sample Characterization Results

Figure 5.1 shows the impregnant loading of the IAC samples prepared in this study as detailed in the figure caption. The data is expressed in terms of % loading as a function of heating temperature (T_f). For reference, the predicted loadings for GC impregnated with zinc oxide (ZnO), copper oxide (CuO) and copper nitrate hydroxide ($Cu_2(OH)_3NO_3$) are also indicated. The predicted loadings are based on the volume and concentration of the impregnating solution added and do not take into account the introduction of surface sites due to the oxidizing properties of the HNO_3 solution [91, 92] or the loss of carbon from the AC substrate due to the evolution of NO_x and CO_2 [9] which can be described by the equation:

$$4HNO_3 + C \rightarrow 4NO_2 + CO_2 + 2H_2O \tag{5.1}$$

Figure 5.1 shows that IAC samples heated at $T_f \leq 140$°C had a wide variance in impregnant loadings. The Zn-based samples heated to 160°C had better reproducibility than the Cu-based IACs. Heating in the range between 180°C and 300°C caused conversion of the metallic impregnants primarily to ZnO or CuO, based on mass, but heating to 450°C gave lower than expected masses. Sample GC-0.5M A showed little to no residual impregnant after heating. The loading of Sample GC-4M A was approximately 30% loading (wt.) at 120 °C, about 5% at 160°C and about 3% at 300°C. The high impregnant loading for GC-4M A-120 may be due to the presence of a water/HNO_3 azeotrope which has a boiling point of 120.5°C [93].

Powder XRD was performed after heating to identify the phase of the impregnant and the impact of HNO_3 treatments. Figure 5.2 shows XRD results from the Zn- and Cu-based IACs prepared in this study as detailed in the figure caption. Results from samples heated at temperatures between $T_f = 120$°C and 450°C are shown. For reference, the strongest Bragg peak positions for ZnO, $Cu_2(OH)_3NO_3$, CuO, Cu_2O and Cu are indicated [56].

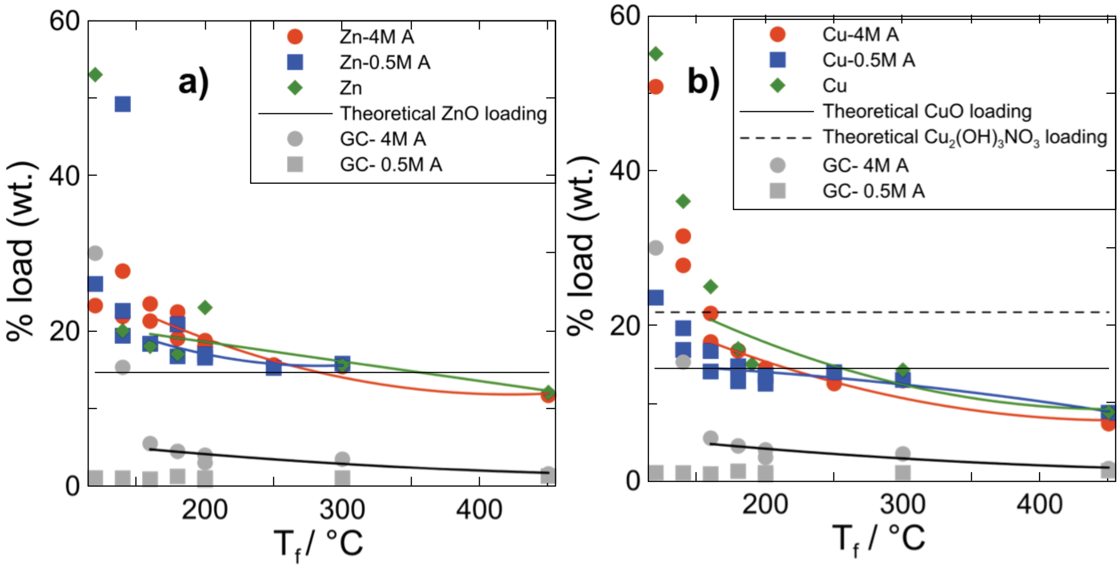

Figure 5.1: Impregnant loading of IAC samples as a function of temperature. Panels (a) and (b) show data obtained from Zn-based and Cu-based IACs with and without HNO_3 present in their impregnating solution, respectively. Data from the GC-4M A and GC-0.5M A samples are shown in both panels for comparative purposes. The theoretical loadings if the impregnant fully converted to ZnO, CuO or $Cu_2(OH)_3NO_3$ are indicated for reference.

Comparison of panels (a) and (d) in Fig. 5.2 shows that the Zn-based IACs tend to convert to ZnO at temperatures as low as 140°C while CuO was not observed until the Cu-based sample was heated to 180°C. When Cu-based samples were heated below 180°C, $Cu_2(OH)_3NO_3$ was the predominant phase observed. $Cu_2(OH)_3NO_3$ is not a desirable impregnant due to thermal stability issues [39].

The results in Fig. 5.2 show that increasing HNO_3 concentration reduces the size of the impregnant grains in samples heated below 200°C. Figures 5.2(a), 5.2(b) and 5.2(c) show that Zn-based samples prepared with more HNO_3 have the weakest and broadest diffraction peaks leading to the smallest impregnant grains as can be inferred from the Scherrer equation (Eq. 2.5). Figures 5.2(d), 5.2(e) and 5.2f show a similar trend for the Cu-based samples. Small impregnant grain size and good impregnant distribution leads to optimal gas adsorption [24, 25, 42] as will be discussed further for the samples included in this study.

The XRD data in Fig. 5.2 shows how the maximum final heating temperature (T_f)

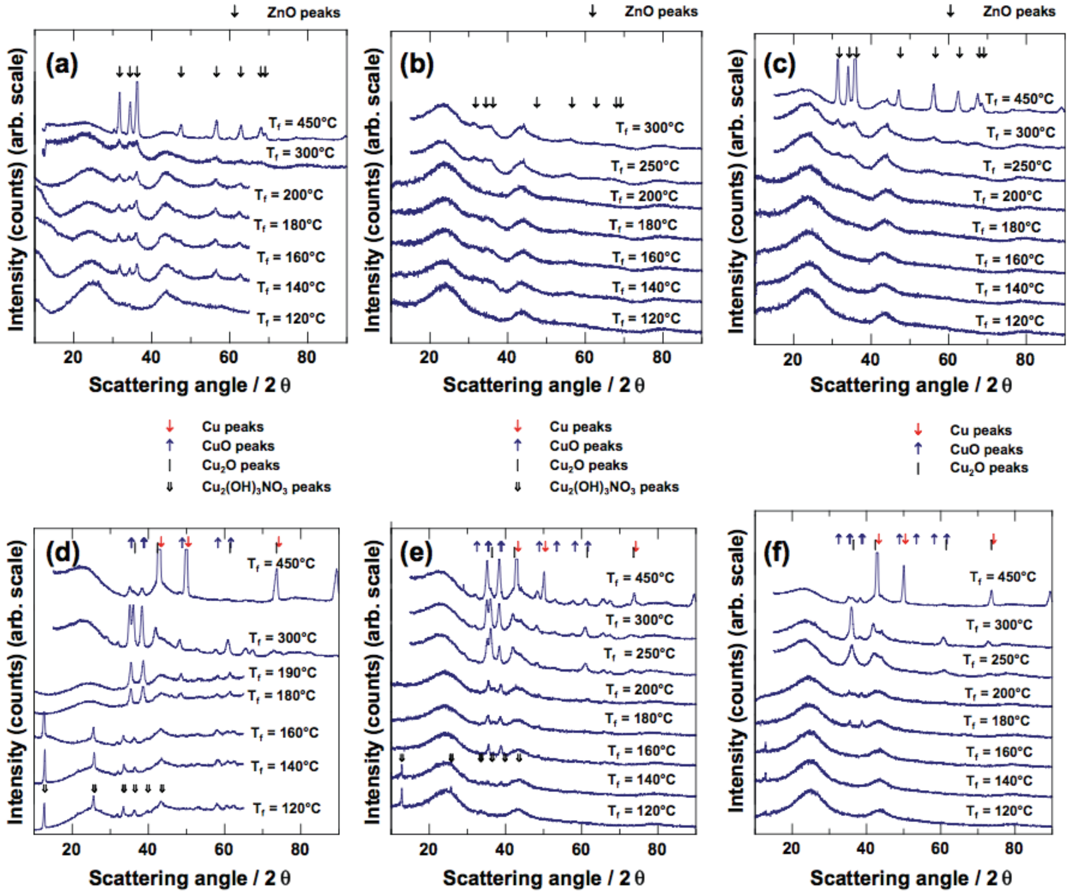

Figure 5.2: Results obtained from experiments performed on the Zn- and Cu-based IACs. Panels (a)-(c) show diffraction patterns obtained from samples Zn, Zn-0.5M A and Zn-4M A respectively. Panels (d)-(f) show XRD data obtained from samples Cu, Cu-0.5M A and Cu-4M A respectively. Results from samples heated at $T_f = 120$, 140, 160, 180, 200, 250, 300 and 450°C are shown.

affects impregnant phase and grain size. The data from the Zn-based IACs displayed in panels (a)-(c) shows that IACs heated at $T_f > 200$°C have sharper, more defined ZnO peaks relative to the samples heated at $T_f \leq 200$°C. Analysis of the ZnO peaks located between 2θ values of 30° and 40° in the diffraction patterns of Zn-based IACs heated at $T_f = 300$°C and 450°C resulted in an average ZnO impregnant grain size of (6 ± 3) nm and (16 ± 1) nm, respectively as calculated using Eq. 2.5.

The XRD data obtained from the Cu-based IAC samples displayed in Fig. 5.2 panels (d)-(f) show a similar trend and also show that the dominant impregnant phase changes as a function of T_f. The dominant impregnant phase observed in the data from Cu, Cu-0.5M A and Cu-4M A samples heated (in argon) to $T_f \leq 160$°C was $Cu_2(OH)_3NO_3$; for IACs prepared at $T_f = 180$°C - 200°C it was CuO; heating to $T_f \geq 200$°C results in Cu_2O and samples prepared at $T_f = 450$°C showed Cu. The formation of CuO can be observed in the diffraction pattern of the Cu-0.5M A-160 sample as is shown in panel (e). For $T_f > 200$°C, the benefits of the HNO_3 treatment are lost as the intensity and sharpness of the diffraction patterns increases. The impact of heating temperatures on the gas adsorption capacity of these IACs will be discussed below.

SEM and EDS experiments were performed on certain samples to further study impregnant distribution on the AC substrate. Figure 5.3 shows SEM images from samples Zn-4M A-180, Zn-4M A-450, Cu-4M A-180 and Cu-4M A-450 respectively as detailed in the figure caption.

Figures 5.3(b) and 5.3(d) show that sample Zn-4M A-450 has relatively large agglomerations on the AC substrate compared to sample Zn-4M A-180 (panels (a) and (c)). A similar observation can be made for samples Cu-4M A-450 and Cu-4M A-180 in panels (f) and (e). The relatively large agglomerations in panel (g) are shown to be rich in metal by the EDS scan in Figure 5.3(h). Figures 5.2 and 5.3 demonstrate that Zn- or Cu-based samples heated to $T_f = 450$°C have agglomerations of impregnant and poor impregnant distribution compared to the samples prepared at $T_f = 180$°C. Thermal gravimetric analysis (TGA) was performed under flowing argon on selected IAC samples that had already been heated to their maximum final drying temperature. Figure 5.4 shows derivative TGA data acquired from the samples prepared in this study as detailed in the figure caption.

Figure 5.4 shows that all samples display a peak located at temperatures below 100°C, which correspond to the desorption of H_2O. The intensity of the water desorption peak decreased with increasing values of T_f. The water still present on the samples is due to small amounts of moisture adsorbed from the air during handling and storage.

Figures 5.4(a)-(c) show that the Zn-based IACs with $T_f = 180$°C display a feature at temperatures above 200°C which diminishes as T_f increases. Figures 5.2(a)-(c) showed that Zn-based IACs heated at $T_f > 200$°C had XRD patterns with ZnO

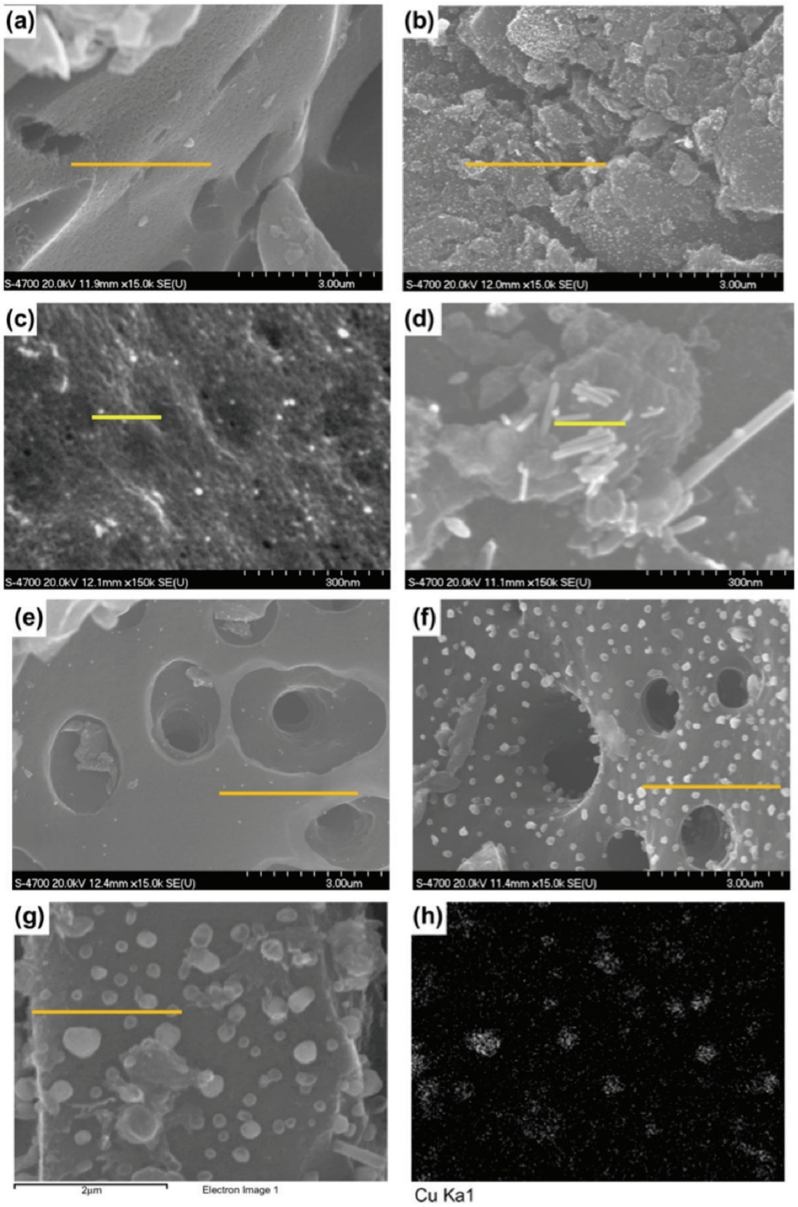

Figure 5.3: SEM and EDS data from IAC samples. Data obtained from sample Zn-4M A-180 is shown in panels (a) and (c), sample Zn-4M A-450 is shown in panels (b) and (d). Data from sample Cu-4M A-180 is shown in panel (e), sample Cu-4M A-450 is shown in panel (f) and (g). An EDS pixel map of the Cu $K_{\alpha 1}$ distribution of the area shown in panel (g) is displayed in panel (h). The scale bars shown in panels (a), (b), (e) and (f) represent 3μm, the scale bar in panels (c) and (d) represents 150 nm and the scale bar in (g) represents 2 μm. The white pixels in panel (h) denote the presence of Cu.

diffraction peaks that increased in intensity and sharpened as T_f increased. Oxidizing an activated carbon substrate with HNO_3 improves its ability to adsorb metallic ions from solution [91]. Both Figures 5.2 and 5.3 demonstrated that as the concentration of HNO_3 in the impregnating solution was increased the impregnant grain size of the heated IAC sample decreased, indicative of improved impregnant distribution. Considering earlier results and the thermal data, it is believed that the feature observed in the derivative TGA data for Zn-180, Zn-0.5M A-180 and Zn-4M A-180 samples above 200°C is likely due to the thermal desorption or reaction (with carbon) of surface oxygen-containing functional groups. As T_f increases, the amount of oxygen on the surface of the IAC decreases. This and the increased mobility of the impregnant contribute to the increase in ZnO grain size with T_f. The peak in Figure 5.4(a)-(c) observed between 800° and 900°C is likely due to the vapourization of the zinc metal and is in reasonable agreement with values found in the literature [93].

Figures 5.4(d)-(f) show that the Cu-based samples prepared at T_f = 180°C have relatively sharp peaks at approximately 250°C and 400°C and a relatively broad hump centered at approximately 700°C. Comparison of these results to the data for the GC-4M A -180 (panel (h)) and the A-GC-120 samples shows that the three features are also present in samples treated only with HNO_3 of concentration$\geq$ 4 M. The desorption peaks observed at approximately 250°C, 400°C and 700°C in the profiles of GC-4M A-180 and A-GC-120 samples (panels (h) and (i) respectively) correspond to the removal of surface oxygen groups and are in reasonable agreement with the literature [97, 98]. Data from the GC-4M A-300, GC-4M A-450, A-GC-300 and A-GC-450 samples show that the peaks at 250°C and 450°C have been reduced or eliminated by heating at T_f = 300°C or above. The Cu-based IACs prepared at T_f = 180°C had more intense derivative TGA peaks at 250°C and 400°C relative to the samples with no metallic impregnant, likely due to additional loss of oxygen occurring when the CuO impregnant is reduced to Cu_2O or Cu. Cu-based IACs prepared at T_f = 300°C display less intense derivative TGA peaks, especially for the peak located at approximately 250°C. Figures 5.2(d)-(f) showed that the Cu-based IACs prepared at T_f = 250°C and 300°C had XRD patterns with more intense impregnant-related diffraction peaks and a large amount of the CuO impregnant was reduced to Cu_2O. Figures 5.4(d)-(f) show that IACs prepared at $T_f = 450°C$ displayed a further reduction/removal of the incremental Wt% loss peaks consistent with the continual conversion of CuO to Cu as shown in Figures 5.2(d)-(f). The relationship between increased heating temperature, increasing impregnant grain size, impregnant phase change and decreasing surface oxygen content will be discussed later in terms of the overall gas adsorption capacity of the IACs.

Figure 5.4(g) shows that the derivative TGA results for the untreated GC and GC-0.5M A samples are similar indicating that the 0.5 M HNO_3 treatment did not significantly affect the AC substrate.

To further study how acid and heating affected the surface of the GC substrate, selected HNO_3-treated IAC samples, with or without metallic impregnants present, were sent for HCNO analysis as a function of T_f. For comparison, unimpregnated GC samples heated at different values of T_f were also analyzed. The work was performed by Canadian Micro Analytic Services Ltd (CMAS), located in Delta, British Columbia, Canada. The data is presented as the weight percent of the oxygen or nitrogen contained in the sample (% gas). Samples that contained metallic impregnants were not evaluated for oxygen content. The error in the measurements is $\pm$ 0.3%.

Figures 5.5(a)-(c) shows nitrogen content versus T_f of the selected IAC samples and the HNO_3-imbibed IAC samples as detailed in the figure caption. Figure 5.5(d) shows the oxygen content of the selected samples versus T_f as detailed in the figure caption (note the change of the y-axis scale in panel (d)).

Figures 5.5(a) and 5.5(b) show that the Zn-based IACs tend to have lower nitrogen content relative to the Cu-based IACs prepared at $T_f < 180°C$. Figure 5.2 showed that ZnO XRD peaks were observed at lower values of T_f relative to the Cu-based samples. The main impregnant phase observed for the Cu-based IACs heated to $T_f < 180°C$ was $Cu_2(OH)_3NO_3$, causing the increased nitrogen content compared to Zn-based IACs in this temperature regime. Figures 5.5(a) and 5.5(b) show that as T_f increased the nitrogen content of the IACs decreased. This trend is especially pronounced for the Cu-4M A samples. Samples prepared at $T_f \geq 180$ °C had relatively low nitrogen content. Figure 5.5(c) shows that the relatively low nitrogen content increases in IAC

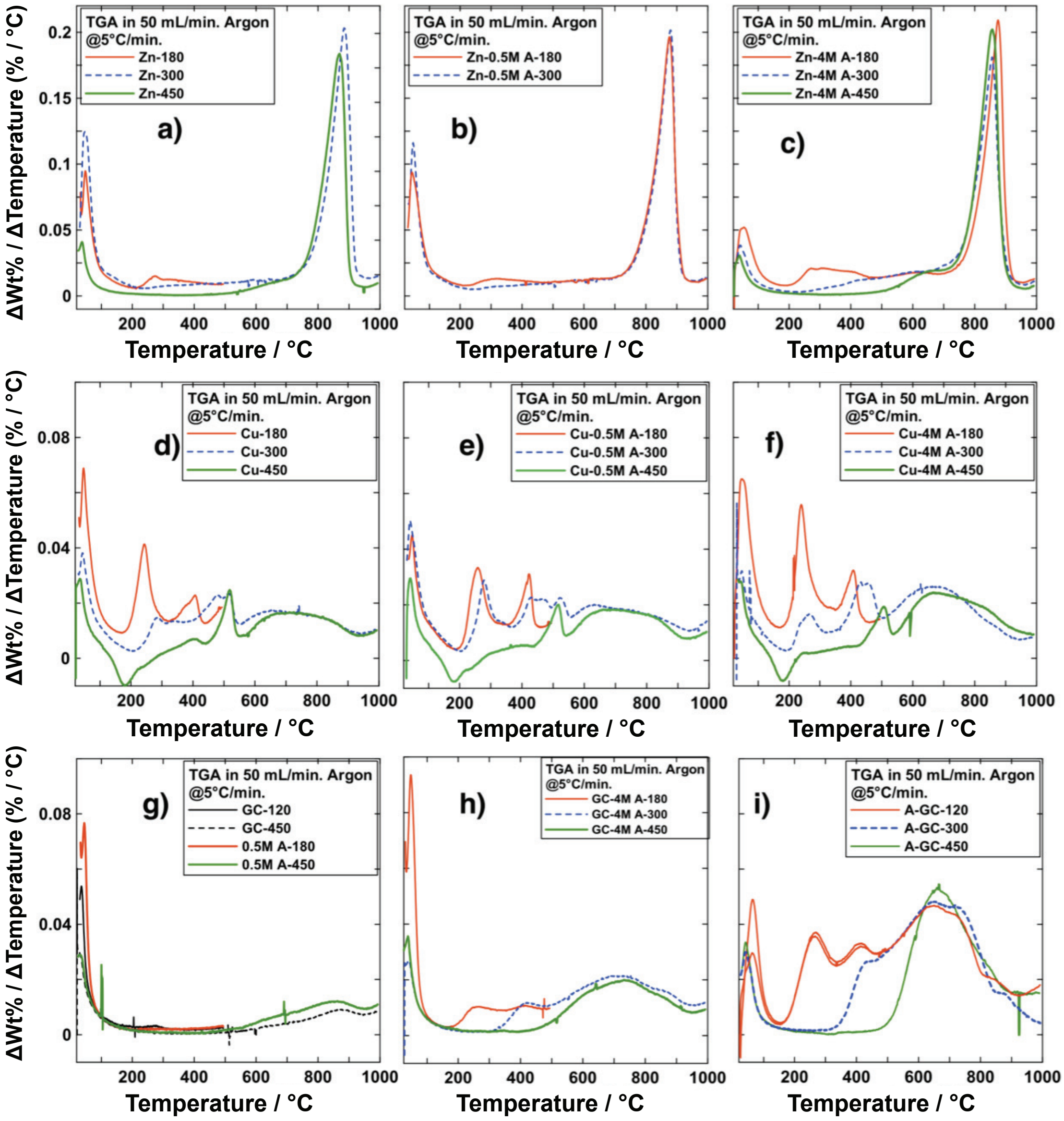

Figure 5.4: Thermal analysis data obtained from Zn-and Cu-based IACs as well as HNO_3 treated and virgin GC samples. Panels (a)-(c) show data obtained from samples Zn, Zn-0.5M A and Zn-4M A respectively. Panels (d)-(f) show data obtained from samples Cu, Cu-0.5M A and Cu-4M A respectively. Panels (g)-(i) show data obtained from GC and GC-0.5M, GC-4M A and A-GC respectively. IACs heated to T_f = 180, 300 and 450°C are shown in panels (a)-(f) and (h). Samples heated to T_f = 120, 180, and 450°C are shown in panel (g). Samples heated to 120, 300 and 450C are shown in panel (i).

samples treated with more concentrated HNO_3.

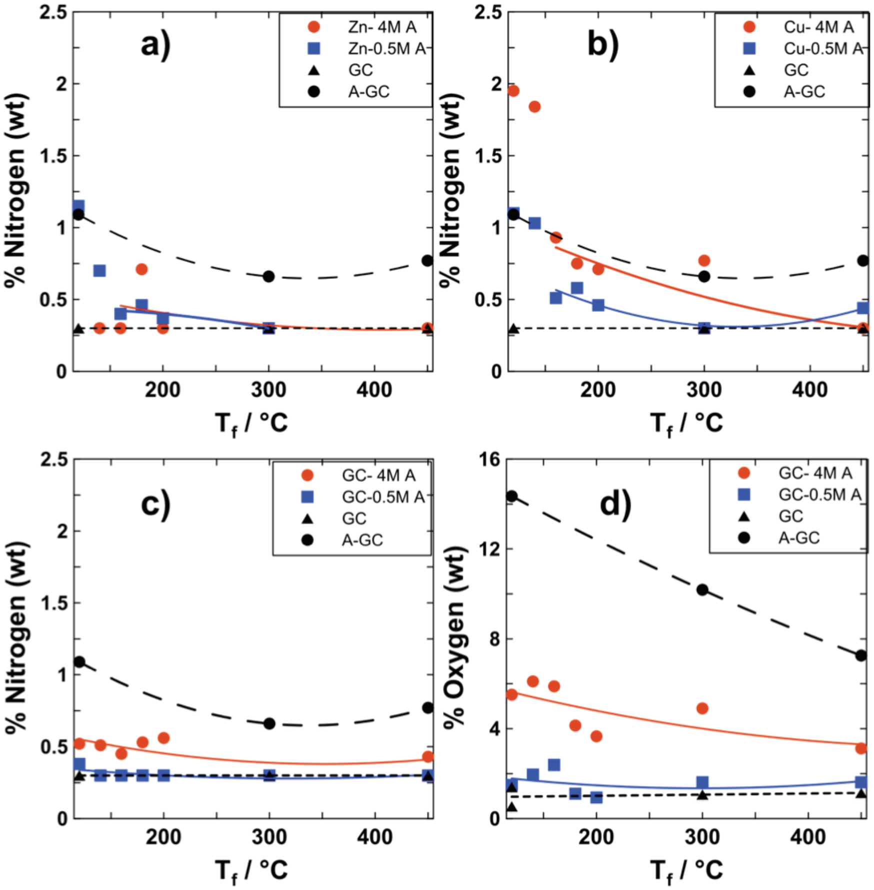

Figure 5.5: The nitrogen content data for the Zn-based IAC samples, Cu-based IAC samples and HNO_3 imbibed IAC samples are shown in panels (a), (b) and (c) respectively. The data from the unimpregnated GC and A-GC samples is displayed in all 3 panels. The oxygen content data for the GC-0.5M A, GC-4M A, A-GC and unimpregnated GC samples is shown in panel (d) (note the change in the y-axis scale bar in panel d). Data was obtained from samples that had been heated to T_f ranging from 120°C to 450°C. **The lines are added as guides for the eye.**

Figure 5.5(d) shows that the oxygen content in the samples increased as the concentration of HNO_3 in the impregnating solution increased and decreased as T_f increased. This trend was most pronounced in the A-GC sample series. Figure 5.4(i) showed that the A-GC sample prepared at T_f =120°C had differential TGA peaks at approximately 250°C and 400°C and that the A-GC samples heated to T_f = 300°C and 450°C displayed a dramatic reduction or elimination of these features. The reduction in the oxygen content of the A-GC sample with T_f is consistent with the features in Figure 5.4(i) being attributed to the removal of surface functional groups containing oxygen. Similar features in the Cu- and Zn-based IAC data shown in Figures 5.4(a)-(f) implies that surface oxygen is also being desorbed from these samples as T_f increases. The removal of the surface oxygen appears to result in larger impregnant grain size and reduced impregnant distribution as can be inferred from the X-ray data in Figures 5.2(a)-(f). Figure 5.5(d) shows that the oxygen content of the GC and 0.5M-A GC samples versus T_f is almost the same implying that the 0.5 M HNO_3 impregnating solution does not significantly oxidize the surface of the activated carbon sample.

Equilibrium water vapour adsorption experiments were performed to further characterize the IAC samples. Figure 5.6 shows the percentage mass gain due to humidification as a function of T_f for the samples prepared in this study as detailed in the figure caption.

Figure 5.6 shows that the increase in mass due to humidification for the IAC samples is lower than the value for GC and decreases with impregnant loading. This shows that the impregnant reduces water adsorption sites and may block pores. Figure 5.2 showed that the Zn- and Cu-based IACs had ZnO and $Cu_2(OH)_3NO_3$, CuO, Cu_2O or Cu as their dominant impregnant phases. These compounds have low solubility in water [93], so one expects a reduction in water adsorption due to the presence of the impregnant. The adsorption of water normally reduces organic vapour adsorption [22, 89], as will be discussed when gas adsorption results are presented below. Figure 5.6(c) shows that the GC, A-GC, GC-0.5M A and GC-4M A samples prepared at $T_f > 140°C$ had similar equilibrium mass gain on humidification (all $> 40\%$).

Figure 5.7 shows water desorption experiments on selected HNO_3 and metal impregant/HNO_3 AC samples as detailed in the figure caption. The experiments were performed using TGA under a 50 mL/min argon flow at 1°C/min (panel (a)) and 0.25 °C/min (panel (b)).

Figure 5.7(a) shows that the Cu-based IACs and the A-GC sample retained water

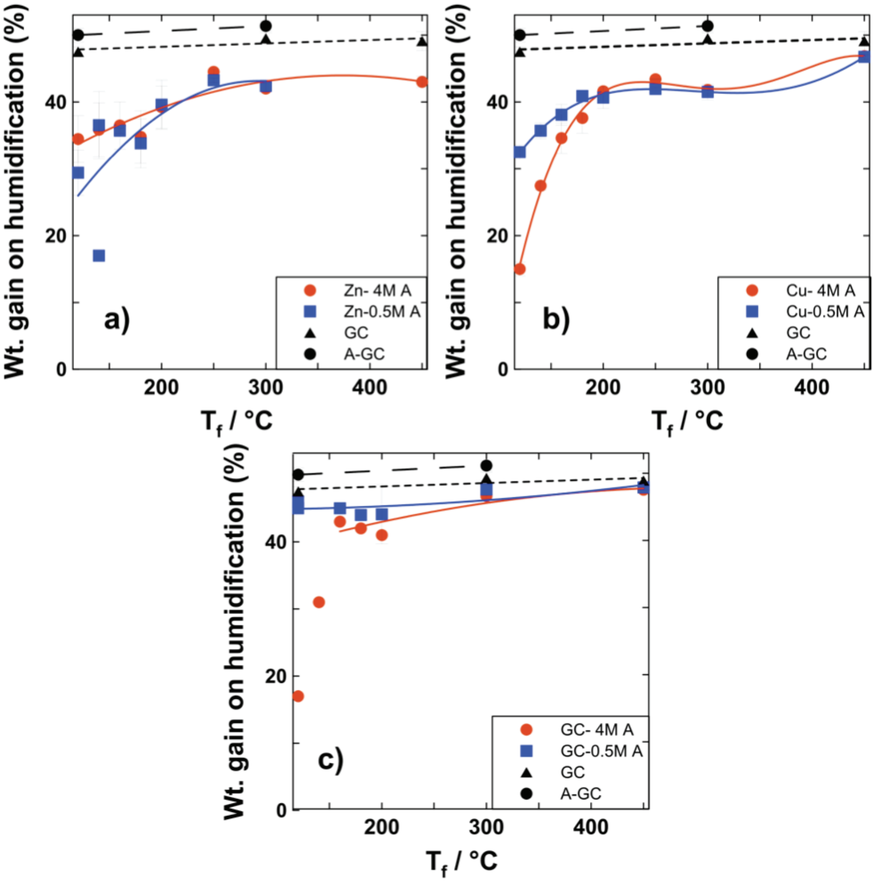

Figure 5.6: Data obtained from equilibrium water vapour adsorption studies. Data obtained from Zn-based, Cu-based and HNO_3 imbibed IACs is shown in panels (a), (b) and (c) respectively. The data obtained from unimpregnated GC and A-GC samples is shown in all 3 panels. **The lines are guides for the eye.**

to higher temperatures than the GC sample. Figure 5.7(b) shows that samples prepared from more concentrated HNO_3 tended to retain the adsorbed water to higher heating temperatures. Figures 5.4(h), 5.4(i) and 5.5(d) showed that the samples treated with more concentrated HNO_3 had a higher concentration of surface oxygen, therefore it is reasonable to conclude that the presence of the surface oxygen groups results in stronger retention of the adsorbed water by the oxidized AC substrate.

5.2.2 Gas Adsorption Capacity

The Zn- and Cu-based IACs prepared in this work all had metallic impregnant loadings of approximately 1.8 mmol/g GC as is listed in Table 1 in the supplementary

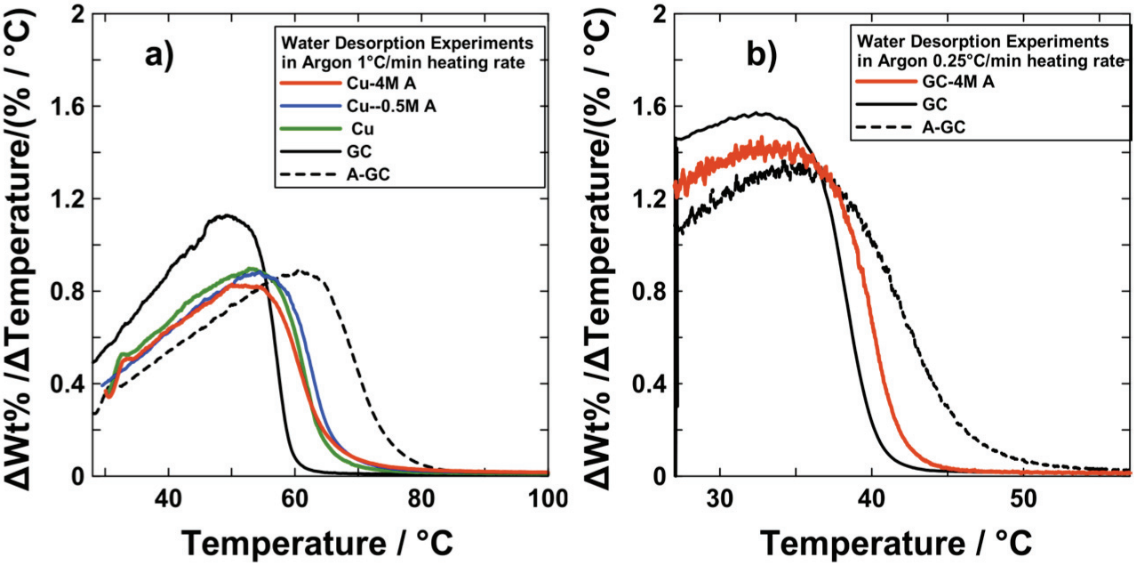

Figure 5.7: Data obtained from water desorption experiments. Panel (a) shows data obtained from GC and A-GC samples prepared at T_f = 120°C, and Cu, Cu-0.5M A and Cu-4M A samples prepared at T_f =180°C. Panel (b) shows data obtained from GC, GC-4M A and A-GC samples all prepared at T_f =120°C. The scan rate was 1°C/min and 0.25°C/min for the data shown in panels (a) and (b), respectively. The argon flow rate was 50 mL/min.

material in Ref. [78]. Gas adsorption capacity is reported as the breakthrough time of the challenge gas [44, 99] as opposed to the relative stoichiometric ratio of reaction (SRR) of the IAC samples at the breakthrough time. The SRR at the breakthrough time can be determined using the ideal gas law and the impregnant loading of the sample. SRRs calculated from the SO_2 and HCN flow test results are listed in Table 1 of the supplementary material in Ref. [78]. Since the metallic impregnant loading of the Zn- and Cu-based IACs is approximately equal, the breakthrough times reported here are proportional to the SRR.

5.2.3 Dry Flow Test Results

Figure 5.8 shows dry SO_2 breakthrough times versus T_f for the samples prepared in this study as detailed by the figure caption. Some of the dry SO_2 flow test results obtained from the IAC samples prepared at $T_f \leq 140$°C had breakthrough times in excess of 110 minutes, (see supplementary material in Ref. [78]) but these display a relatively large amount of scatter and low degree of reproducibility. The long SO_2 breakthrough times for some of the IACs prepared at $T_f \leq 140°C$ can be attributed to incomplete thermal decomposition to the desired oxide phase (Fig. 5.1) or higher than expected moisture content. Long SO_2 breakthrough times have been observed for IACs with $Cu_2(OH)_3NO_3$ as the dominant impregnant phase [39] but this type of IAC is not suitable for a broad spectrum respirator carbon [39].

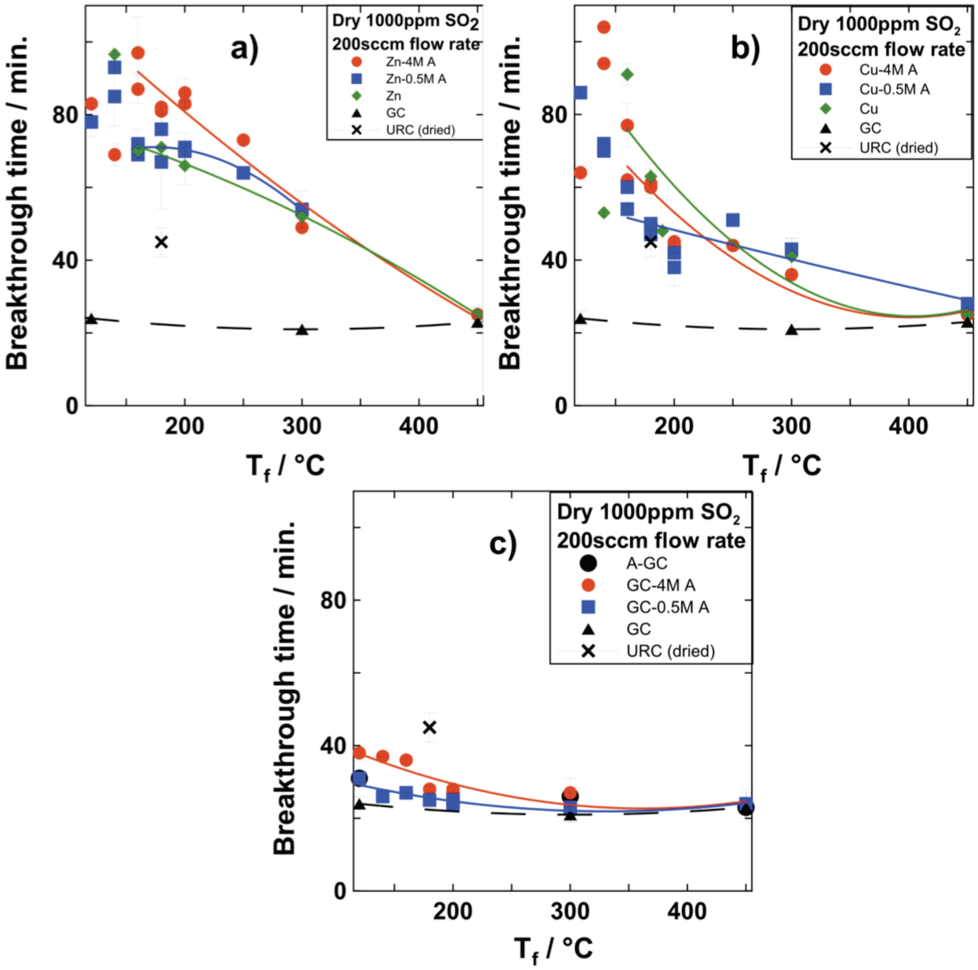

Figure 5.8: Breakthrough time versus T_f for dry SO_2 flow tests. Panel (a) shows results obtained from Zn, Zn-0.5M A and Zn-4M A IAC samples. Panel (b) shows results obtained from Cu, Cu-0.5M A and Cu-4M A IAC samples. Panel (c) shows results obtained from A-GC, GC-4M A and GC-0.5M A samples. Flow test results obtained from GC and the commercially available URC sample (pre-dried at 120°C) are shown for reference. **The lines have been inserted by the author as guides for the eye.**

The adsorption of SO_2 by the Zn- and Cu-based IACs that were prepared between T_f = 160°C - 450°C (for the Zn-based samples) and T_f = 180°C to approximately 300°C (for the Cu-based samples) are proposed to occur via the following net reactions:

$$\mathrm{CuO} + \mathrm{SO_2} + \tfrac{1}{2}\mathrm{O_2} \rightarrow \mathrm{CuSO_4}, \tag{5.2}$$

$$\mathrm{ZnO} + \mathrm{SO_2} + \tfrac{1}{2}\mathrm{O_2} \rightarrow \mathrm{ZnSO_4}. \tag{5.3}$$

We have provided evidence for the validity of equation 5.2 in earlier work [24]. This reaction has been proposed in the literature [100,101]. Figures 5.8(a) and 5.8(b) show that in the temperature range between T_f = 180°C - 250°C Zn-based IACs have a higher SO_2 capacity relative to the Cu-based IACs and the URC sample. Figure 5.2 showed that the Zn-based IACs had less intense, broader impregnant-related X-ray diffraction peaks suggesting that the Zn-based IACs had smaller impregnant grain size [54] and better impregnant distribution relative to the Cu-based IACs, and this resulted in better SO_2 adsorption. Figure 5.8 also shows that the Zn-based IAC samples prepared from impregnating solutions containing more concentrated HNO_3 on average had longer SO_2 breakthrough times (up to $T_f \leq 250$°C). Figures 5.2 and 5.3 showed that increasing the HNO_3 concentration in the impregnating solution of these samples resulted in IACs with smaller, better distributed ZnO impregnant. The HNO_3 treatments also improved impregnant distribution for the Cu-based IACs, however the change in the dominant impregnant phase as a function of T_f that was shown in Fig. 5.2 ($Cu_2(OH)_3NO_3$, CuO, Cu_2O, Cu for T_f = 160°C, 180°C, 250-300°C and 450°C respectively) also reduces the SO_2 breakthrough time of Cu-based samples.

Figure 5.8 shows that all the IAC samples have decreasing SO_2 breakthrough as T_f increases. IACs prepared at T_f = 450°C have approximately the same breakthrough times as GC suggesting that the impregnant is no longer reacting with the SO_2 challenge gas. Comparing the results in Figs. 5.2, 5.4 and 5.8, increased T_f results in lower amounts of surface oxygen, larger grain size impregnant and lower SO_2 filtration capacity.

Figure 5.9 shows the dry NH_3 breakthrough time plotted versus T_f for the samples prepared in this study as detailed in the figure caption. Some of the IAC samples prepared at $T_f \leq 140$°C had dry NH_3 breakthrough times in excess of 130 minutes

(Table 1 in supplementary material in Ref. [78]) with a large amount of scatter in their breakthrough times. The reason for this was discussed earlier.

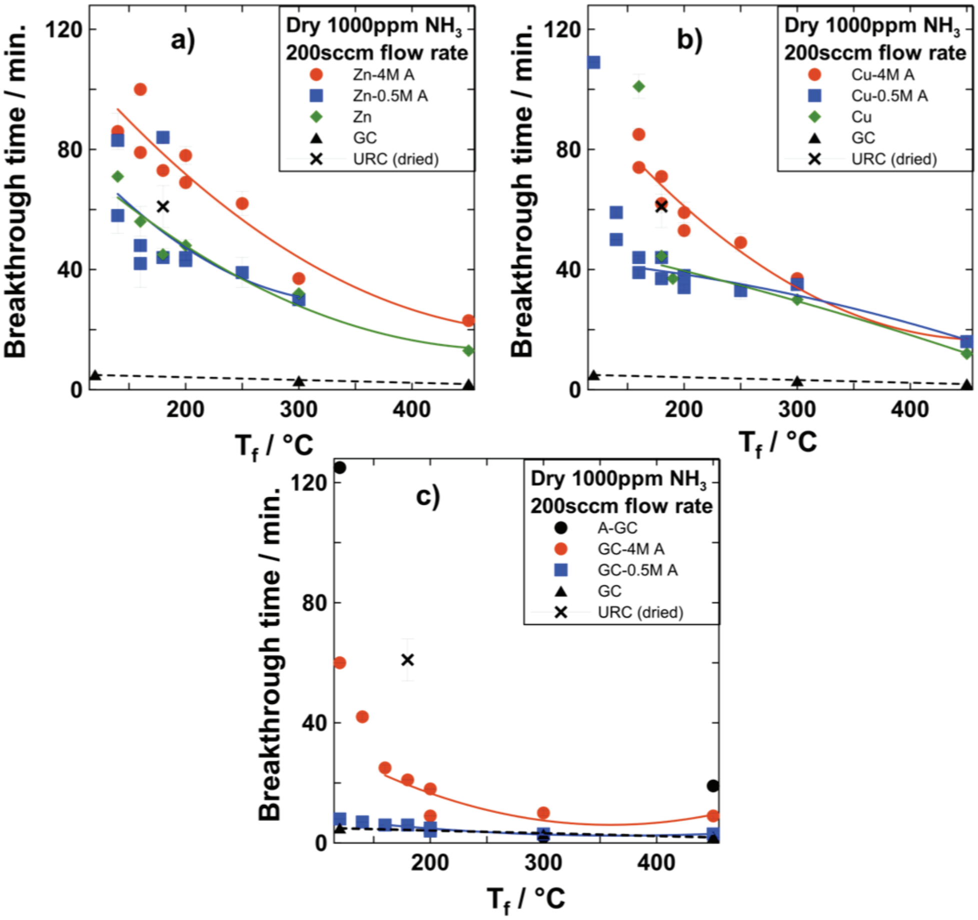

Figure 5.9: Breakthrough time versus T_f for dry NH_3 flow tests. Panel (a) shows results from Zn, Zn-0.5M A and Zn-4M A IAC samples. Panel (b) shows results from Cu, Cu-0.5M A and Cu-4M A IAC samples. Panel (c) shows results from A-GC, GC-4M A and GC-0.5M A samples. Flow test results obtained from GC and the commercially available URC sample (pre-dried at 120°C) are shown for reference. **The lines are inserted as guides for the eye.**

Figures 5.9(a) and 5.9(b) show that, for a given value of T_f, the NH_3 breakthrough times increase as the amount of HNO_3 in the preparation increased. More concentrated HNO_3 treatments introduce more surface oxygen groups and improve impregnant distribution which improves gas adsorption capacity. Figures 5.9(a) and 5.9(b) show that the Zn-4M A (prepared at T_f = 180°C-250°C) and the Cu-4M A samples (prepared at T_f = 180°C-200°C) had NH_3 breakthrough times as good as or better than the URC sample. The dry NH_3 adsorption of URC is largely due to the presence of the sulphate species as discussed in the literature [13]. The Zn-4M A samples had the longest average NH_3 breakthrough times. Figures 5.9(a) and 5.9(b) show that more concentrated HNO_3 treatments did not improve NH_3 capacity for Zn- and Cu-based samples prepared at T_f =300°C. The samples prepared at T_f = 450°C had similar NH_3 capacity to the GC samples. The results in Figures 5.2 and 5.4 showed that Zn- and Cu-based IACs heated to $T_f \geq 300$°C had larger impregnant grains and less surface oxygen relative to IACs prepared at lower heating temperatures so the lower NH_3 capacity is to be expected.

Figure 5.9(c) shows that NH_3 capacity increases with amount of HNO_3 applied to ACs especially for the IACs prepared at T_f = 120°C. The NH_3 capacity is ranked as A-GC > GC-4M A > GC-0.5M A $\approx$ GC. More concentrated HNO_3 treatments introduce more acidic surface oxygen groups and improve NH_3 adsorption [92]. Figure 5.9(c) shows that the NH_3 capacity of the GC-4M A samples decrease as T_f increased. Figures 5.4(h) and 5.5(d) showed that the GC-4M A samples prepared at higher temperatures had less surface oxygen, so reduced NH_3 capacity is expected.

Figures 5.9(a), (b) and (c) show Zn- or Cu-based IACs had larger NH_3 capacity than samples treated with HNO_3 alone as illustrated best by the Zn-4M A, Cu-4M A and GC-4M A samples. The Zn-4M A samples have the highest NH_3 capacity for T_f = 180°C-250°C, the Cu-4M A samples have the next highest capacity, both of which are 3 to 4 times longer than the GC-4M A samples. The reaction between the Zn- or Cu-based samples and NH_3 has not yet been determined. It is not clear if the NH_3 reacts with surface oxygen groups or the metallic impregnant, but clearly, added metallic impregnant increases capacity.

When Cu^{2+} containing IACs are challenged with HCN gas they evolve NCCN gas (Eq. 2). Therefore, Cr^{6+}, Mo^{6+} or W^{6+} compounds are added to control NCCN generation [8,9,13,14,17]. The Cu-based samples were not impregnated with a compound to control NCCN generation so as to have a direct comparison with the the Zn-based IACs. Cu-based IACs prepared from a $Cu(NO_3)_2$ precursor and co-impregnated with HNO_3 and a Mo^{6+} compound have good HCN and NCCN adsorption capacity [24].

A reaction mechanism for Zn-based IACs with HCN has been proposed in the literature [17]:

$$ZnO + 2HCN \rightarrow Zn(CN)_2 + H_2O \tag{5.4}$$

Therefore, the presence of NCCN is not expected, but is monitored for during HCN testing of the Zn-based IACs.

Figure 5.10 shows HCN and NCCN breakthrough times plotted versus T_f for the samples of this study as indicated in the caption. Results obtained from GC and the URC sample (pre-dried at 120°C) are shown in all panels for reference.

Figures 5.10(a), (c) and (e) show that the Cu-based IACs have the longest HCN breakthrough times. For the Cu-based IACs, with $180°C \leq T_f \leq 200°C$, where the dominant impregnant phase was CuO, (Figures 5.1 and 5.2) the HCN capacities were close to that of URC. The capacities decreased in the following order: Cu-4M A > Cu-0.5M A > Cu. Figures 5.2(d)-(f) showed that higher HNO_3 concentration in the impregnating solution reduced the impregnant grain size and this apparently improves HCN capacity. Zn-based IACs prepared with $160°C \leq T_f \leq 200°C$ also showed increased HCN capacity with higher initial HNO_3 content. Cu-based impregnants (usually present as CuO) normally have higher HCN capacity than Zn-based impregnants [17]. However, Figures 5.10(a) to 5.10(d) show that the Zn-4M A samples ($160°C \leq T_f \leq 200°C$) have capacity as good as or better than URC and Cu-based samples when HCN and NCCN breakthrough times are considered together (as they must be for broad spectrum respirator carbons). The evolution of NCCN gas during HCN testing of the Zn-based samples was unexpected and the NCCN breakthroughs occurred at low levels (2 ppm to10 ppm). The observation of any NCCN evolved from the Zn-based samples warrants further study and will be performed in future work. The NCCN breakthrough concentrations observed for Cu-based samples were much higher (on the order of hundreds of ppm). Figures 5.10(c), 5.10(d) and Table 1 (see supplementary material in Ref. [78]) show that IACs with $Cu_2(OH)_3NO_3$ ($T_f \leq 160°C$) impregnant had long HCN breakthrough times, but little ability to control NCCN generation. The samples that displayed conversion to Cu_2O or Cu ($T_f \geq 250°C$) had lower HCN breakthrough times, which implies these impregnant phases are less reactive than CuO towards HCN gas. This is consistent with the literature [9].

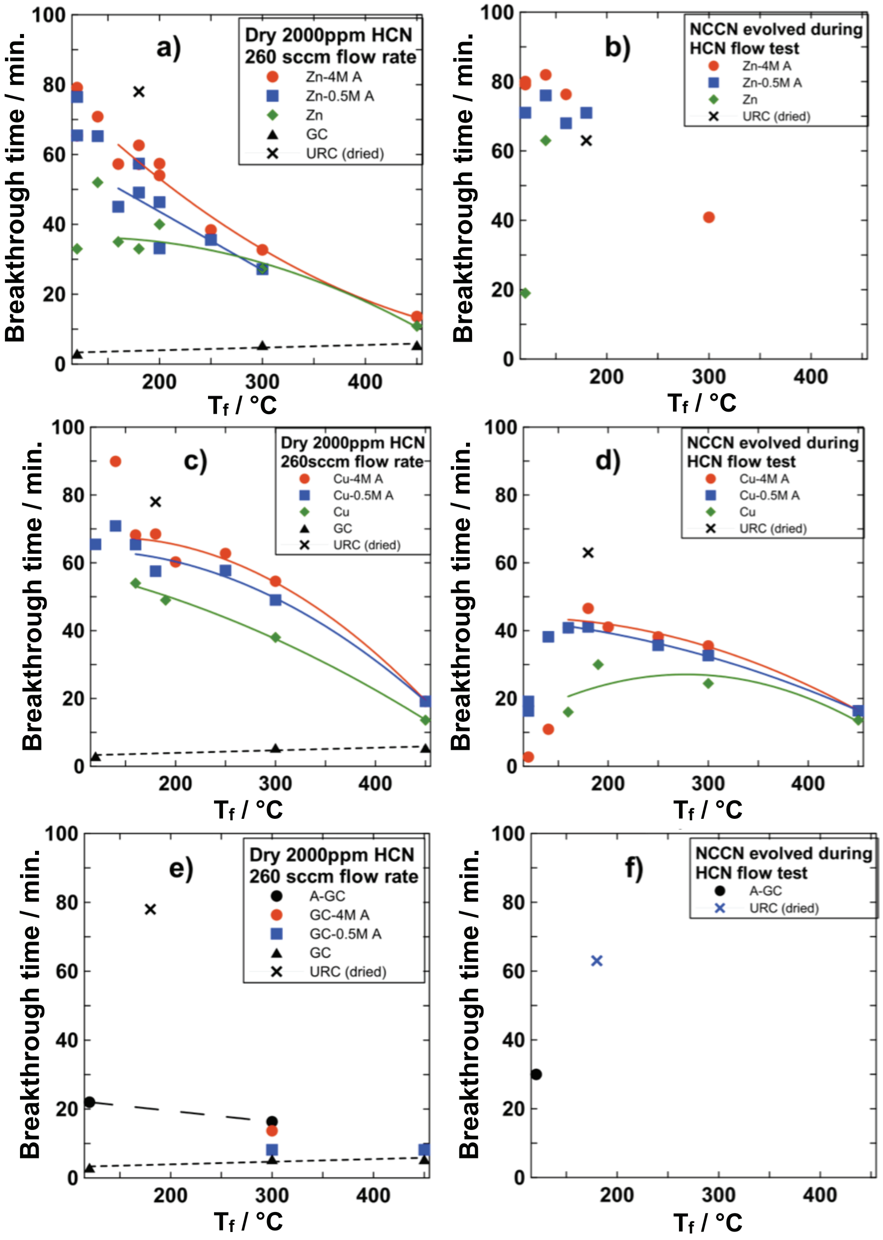

Figure 5.10: Dry HCN breakthrough time plotted versus T_f. Breakthrough times obtained from Zn, Zn-0.5M A and Zn-4M A IAC samples are shown in panels (a) and (b), results obtained from Cu, Cu-0.5M A and Cu-4M A IAC samples are shown in panels (c) and (d) and results from A-GC, GC-4M A and GC-0.5M A samples are shown in panels (e) and (f). Results obtained from GC and the commercially available URC sample (pre-dried at 120°C) are shown in all panels for reference. **The lines are guides for the eye.**

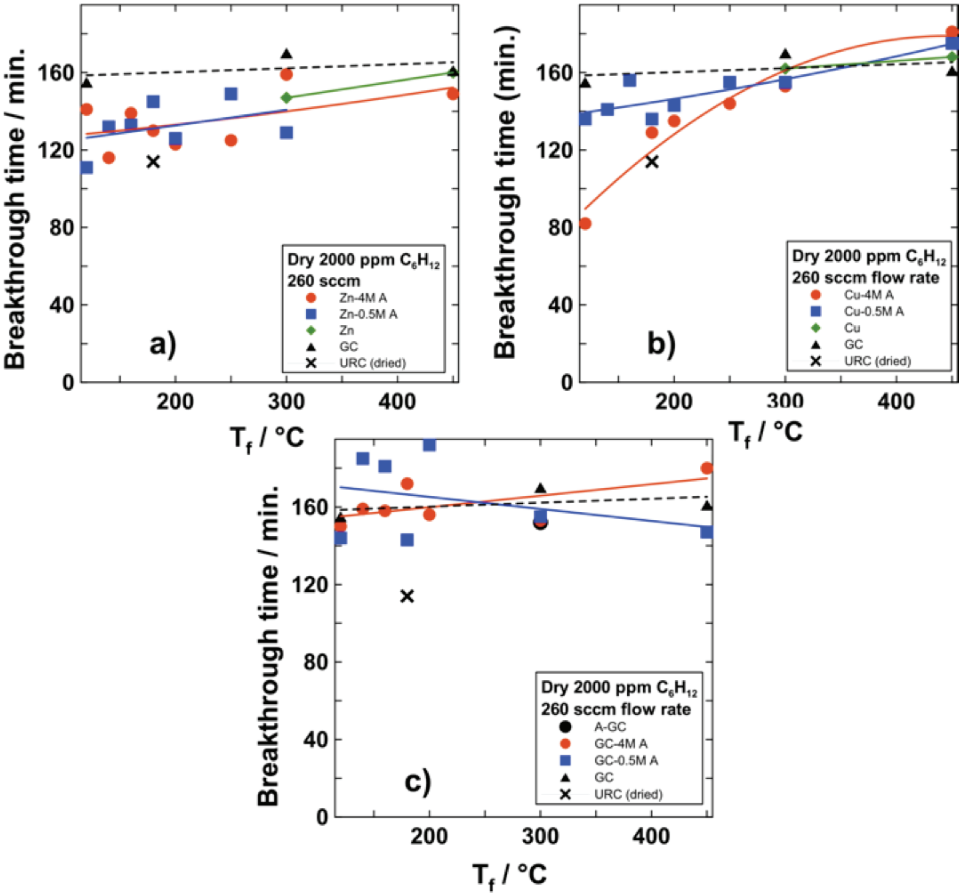

Figure 5.11: Dry C_6H_{12} breakthrough times versus T_f. Results from Zn-4M A, Zn-0.5M A and Zn are shown in panel (a), Cu-4M A, Cu-0.5M A and Cu are in panel (b) and A-GC, GC-4M A and GC-0.5M A are shown in panel (c). Results obtained from URC and GC are included for reference. **The lines are guides for the eye.**

Figures 5.10(e) and 5.10(f) show that samples prepared from more concentrated HNO_3 solutions (GC-4M A and A-GC) have slightly longer HCN breakthrough times than the GC-0.5M A or GC samples, which suggests that the surface oxygen groups can react somewhat with HCN gas, but none of these samples had significant HCN capacity.

Figure 5.11 shows dry C_6H_{12} breakthrough times for the samples of this study as indicated in the caption. Figures 5.11(a) and 5.11(b) show that samples prepared at higher heating temperatures had increased C_6H_{12} capacity. This trend is most noticeable for the Cu-4M A samples. Figures 5.1, 5.6 and 5.10 show that samples with higher impregnant loading had lower mass gain on humidification and lower C_6H_{12} breakthrough times, implying that heavily impregnated samples have a reduced number of surface sites and pores available to the C_6H_{12} gas for physical adsorption of organic vapours [38]. All the samples prepared at $T_f > 140°C$ had longer dry C_6H_{12} breakthrough times than URC.

5.2.4 Wet Flow Test Results

Figure 5.12 shows humid SO_2 breakthrough times plotted versus T_f for the samples of this study as indicated in the figure caption. Figure 5.12 shows that all the Zn- and Cu-based samples tested had wet SO_2 breakthrough times that were longer than those obtained under dry conditions. The presence of water on activated carbon enhances its SO_2 adsorption capacity via a reaction process that results in the formation of sulphuric acid (H_2SO_4) [102, 103] and water has been added as an impregnant to improve SO_2 adsorption [13]. Figure 5.12(c) shows that the HNO_3-treated samples had lower SO_2 capacity relative to the GC or metal impregnated samples and that the SO_2 capacity decreased with HNO_3 concentration. The formation of surface acid upon humidification would result in reduced ability to adsorb acidic gases. The Zn- and Cu-based IACs all have lower SO_2 capacity than URC. URC is prepared from a basic impregnating solution [13, 23] which may help to explain why it has better SO_2 capacity.

Figure 5.13 shows humid NH_3 breakthrough times plotted versus T_f for the samples of this study as indicated in the figure caption. Figure 5.13 shows that humid NH_3 capacity increases with HNO_3 concentration and decreases with increasing T_f. Comparison of panels (a), (b) and (c) shows that, for $160 \leq T_f \leq 200°C$, Zn- or Cu-based samples had larger NH_3 capacity than samples treated with HNO_3 alone. Figures 5.4 and 5.5(d) showed that increasing T_f caused oxygen surface groups to be desorbed, so decreased NH_3 capacity at higher values of T_f should be expected. The Zn- and Cu-based IACs all have lower humid NH_3 capacity than URC. Impregnants used in URC to target NH_3 gas are discussed in the literature [13, 23].

Figure 5.13(c) shows that unimpregnated GC has an average NH_3 breakthrough time of 12-15 minutes. This is higher than the breakthrough time for GC under dry

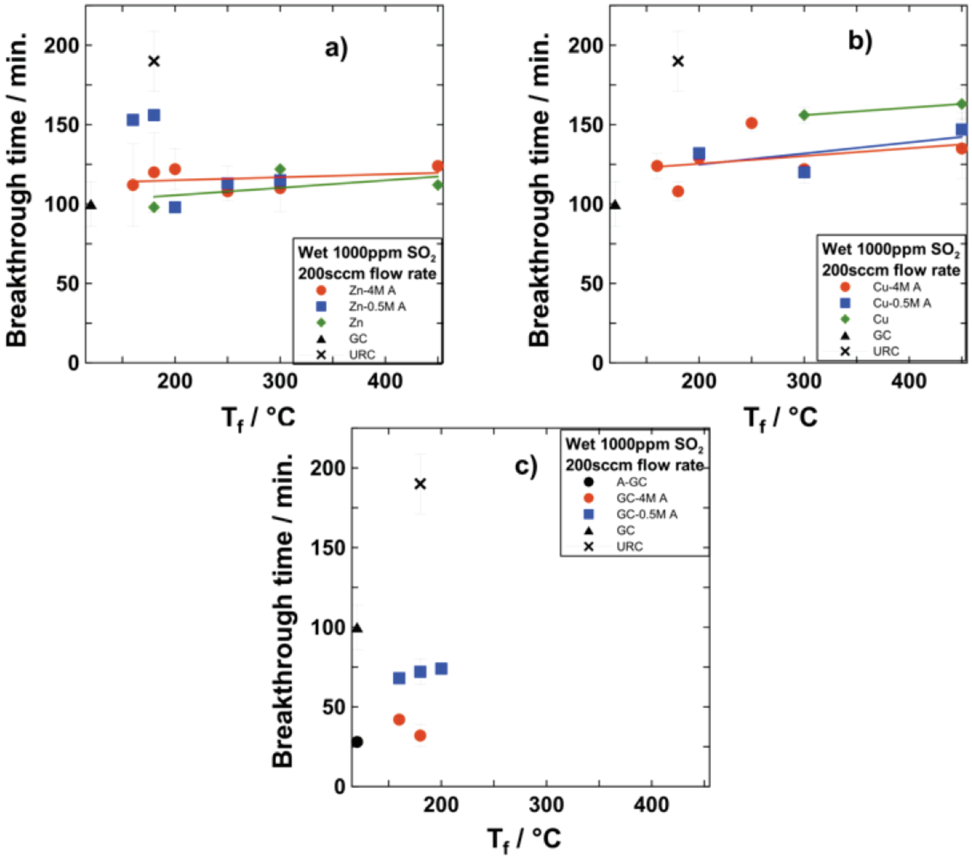

Figure 5.12: Humid SO_2 breakthrough times versus T_f. Panel (a) shows data from Zn-4M A, Zn-0.5M A and Zn samples, panel (b) shows results from Cu-4M A, Cu-0.5M A and Cu samples and panel (c) shows data from A-GC, GC-4M A and GC-0.5M A samples. For reference, results obtained from GC and URC are shown in each panel. **The lines are guides for the eye.**

conditions (approximately 5 minutes, see Figure 5.9(c)). The increased capacity under humid conditions is likely due to the relatively high solubility of NH_3 in water [93].

Figure 5.14 shows breakthrough times for wet HCN and NCCN versus T_f for the samples prepared in this study as detailed in the figure caption. Figures 5.14(a) and 5.14(c) show that there is no correlation between wet HCN capacity and HNO_3 concentration in the impregnating solution or T_f. The humid HCN breakthrough times for the Zn-based samples were shorter than the dry breakthrough times. By contrast, the Cu-based samples had longer wet breakthrough times relative to dry conditions. Both the Zn- and Cu-based samples had shorter wet HCN breakthrough

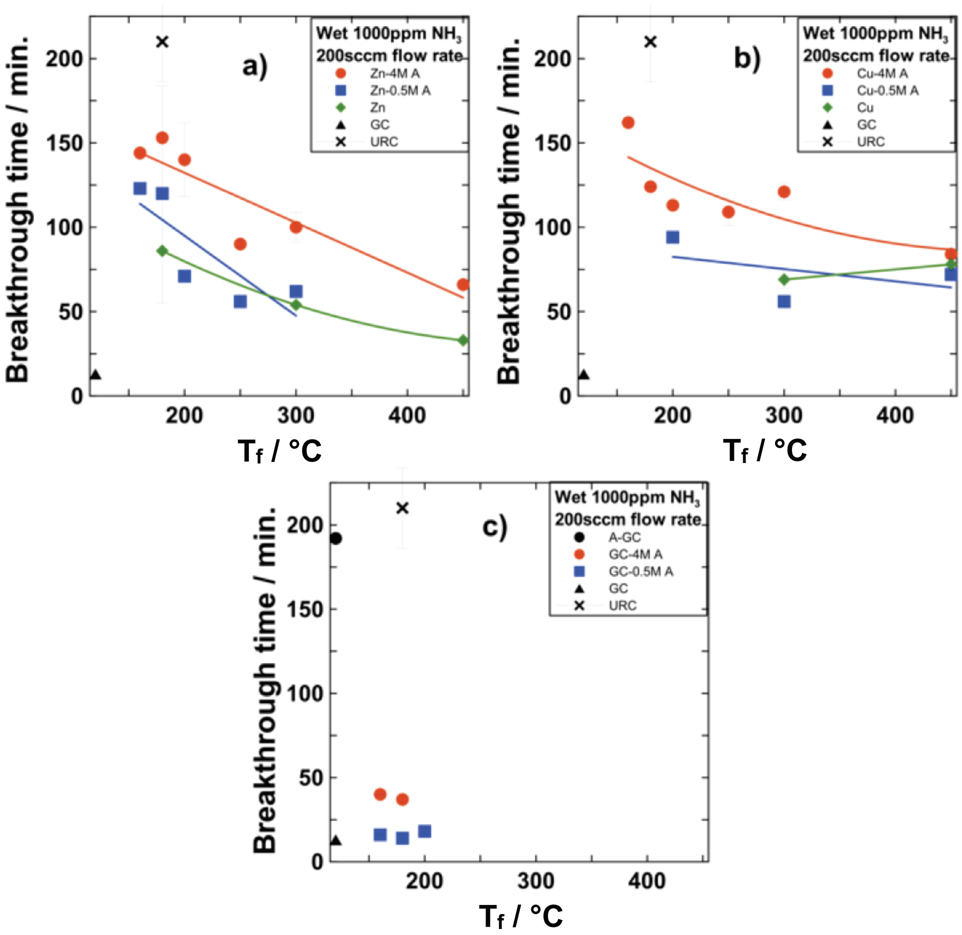

Figure 5.13: Humid NH_3 breakthrough times versus T_f. Panel (a) shows data from Zn-4M A, Zn-0.5M A and Zn samples, panel (b) shows results from Cu-4M A, Cu-0.5M A and Cu samples and panel (c) shows data from A-GC, GC-4M A and GC-0.5M A samples. For reference, results obtained from GC and URC are shown in each panel. **The lines are guides for the eye.**

times than the URC sample. Figures 5.14(e) and 5.14(f) indicate that the GC, A-GC, GC-4M A and GC-0.5M A samples all have short humid HCN breakthrough times and did evolve NCCN under humid conditions.

Figures 5.14(a) and 5.14(b) show that samples with $T_f \geq 160$°C had wet NCCN breakthrough times that were longer than their wet HCN breakthrough times. Figure 5.14(b) shows that as T_f was increased, the NCCN breakthrough times increased. The breakthrough times reported in Figure 5.14(b) were based on relatively low levels (usually 5-10 ppm) of NCCN. Figure 5.4 showed that samples prepared at higher heating temperatures had fewer surface oxygen groups. The production of small amounts of NCCN by the Zn-based samples may be due surface oxygen groups or surface impurities [18, 20] and will be studied further in future work.

Figures 5.14(c) and 5.14(d) show that the increase in wet HCN capacity of the Cu-based samples is offset by extremely low NCCN retention. Water must enhance the efficiency of the reaction described by Eq. 2, possibly by increasing the time the Cu impregnant and HCN toxin are in contact. HCN is highly soluble in water and in conditions of high humidity there may be improved interaction between HCN and the Cu impregnant, which may diminish the importance of small impregnant grain-size. The presence of a Mo^{6+} species gives Cu-based samples, similar to those shown in Figures 5.14(c) and 5.14(d), good HCN and NCCN capacity under humid conditions [21]. Figures 5.14(c) and 5.14(d) show a weak dependence of HCN capacity on T_f.

Figure 5.15 shows humid C_6H_{12} breakthrough times plotted versus T_f for the samples of this study. Figure 5.15 shows that the samples have relatively poor wet C_6H_{12} capacity compared to their dry C_6H_{12} capacity (shown in Figure 5.11). In fact, the breakthrough times have been reduced by about a factor of 8 in the presence of high humidity. Water adsorption and competition between water and the organic vapour can result in a significant reduction in organic vapour adsorption capacity under humid conditions [22, 89].

Figures 5.15(a) and 5.15(b) show that Zn-0.5M A, Zn, Cu-4M A, Cu-0.5M A and Cu samples exhibit small improvements in wet C_6H_{12} capacity as T_f increased. The Zn-4M A sample did not show any improvement. Figure 5.7 showed that samples prepared with metallic impregnants (specifically Cu^{2+} in Figure 5.7(a)) and/or more concentrated HNO_3 treatments retained water more strongly relative to the GC sample. A comparison of Figures 5.15(c) and 5.5(d) suggests that samples with higher oxygen content had lower humid C_6H_{12} adsorption capacity. The presence of these groups results in lower C_6H_{12} capacity. Heating to higher T_f reduces the amount of surface oxygen groups (as was shown in Figure 5.4) and results in modest improvements in humid C_6H_{12} capacity. However none of these samples were able to match the breakthrough times of the GC samples.

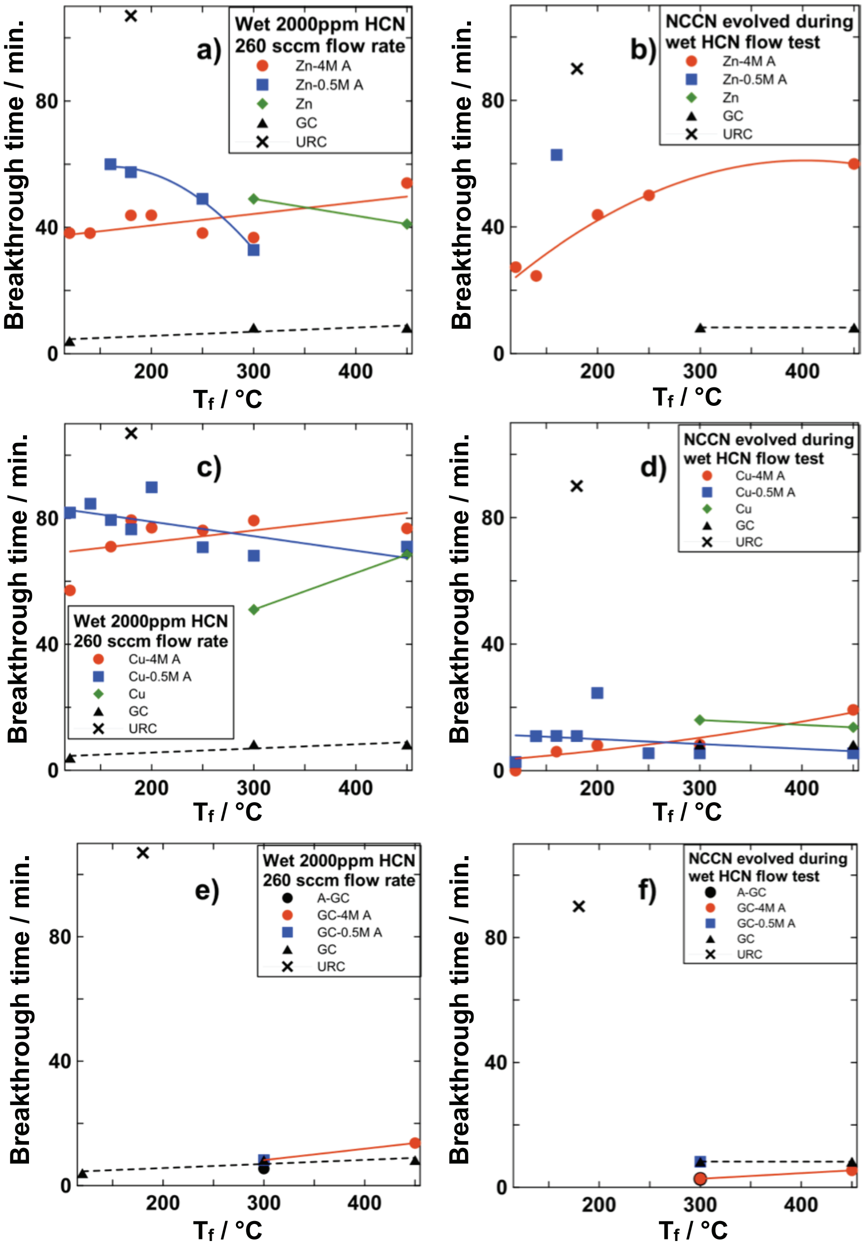

Figure 5.14: Humid HCN and NCCN breakthrough times plotted versus T_f. Results for Zn, Zn-0.5M A and Zn-4M A IAC samples are shown in panels (a) and (b), results from Cu, Cu-0.5M A and Cu-4M A IAC samples are shown in panels (c) and (d) and results from A-GC, GC-4M A and GC-0.5M A samples are shown in panels (e) and (f). Results obtained from GC and URC are shown in all panels for reference.

5.2.5 Summary of the Most Effective Samples

The Zn-4M A samples with 160°C $\leq T_f \leq$ 250°C and the Cu-4M A samples with T_f 180°C $\leq T_f \leq$ 200°C had the best overall performance. These samples had relatively

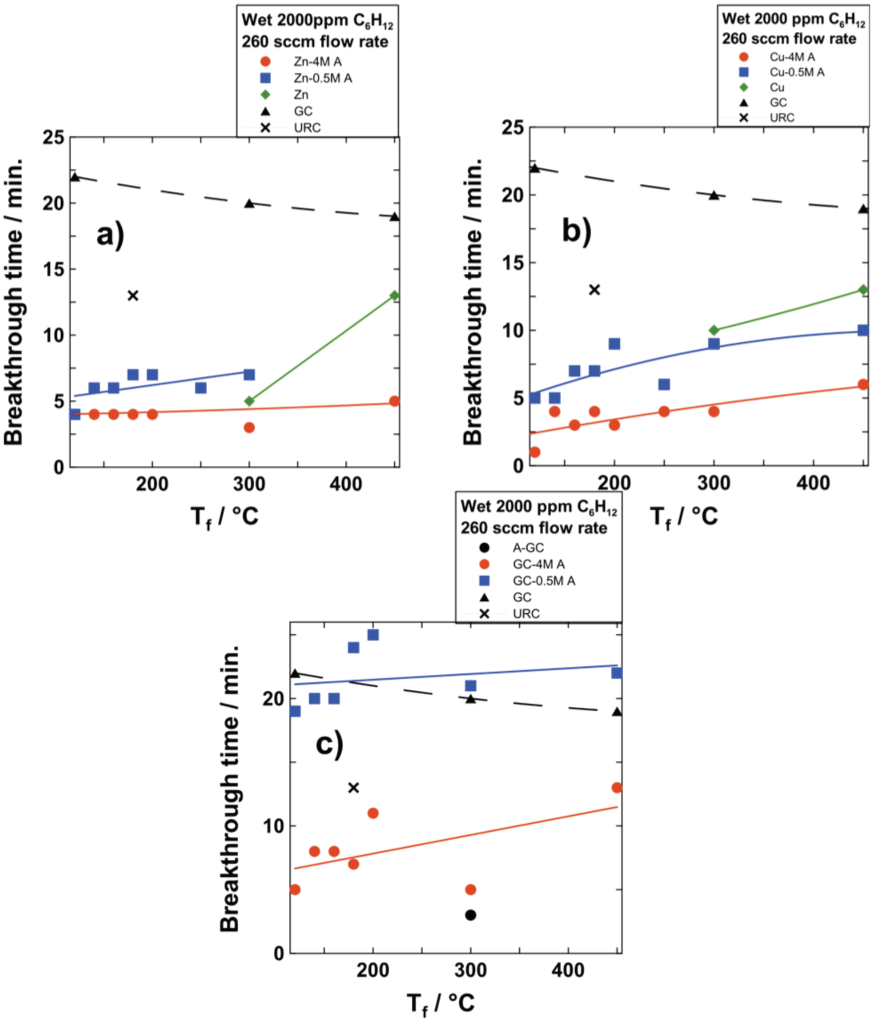

Figure 5.15: Wet C_6H_{12} breakthrough times versus T_f from Zn, Zn-0.5M A and Zn-4M A IAC samples are shown in panel (a), results from Cu, Cu-0.5M A and Cu-4M A IAC samples are shown in panel (b) and results from A-GC, GC-4M A and GC-0.5M A samples are shown in panel (c). Results obtained from GC and URC are shown in all panels for reference. **The lines are guides for the eye.**

small grain-size impregnant that was well distributed on the AC substrate as was shown in Figures 5.2 and 5.3. Co-impregnation with HNO_3 was key in achieving good impregnant distribution. Figure 5.16 shows a summary radar plot of dry and wet breakthrough times from the Zn-4M A-180 and Cu-4M A-180 samples as detailed in the figure caption.

Figure 5.16(a) shows that the Zn-4M A-180 sample had better dry SO_2 and NH_3

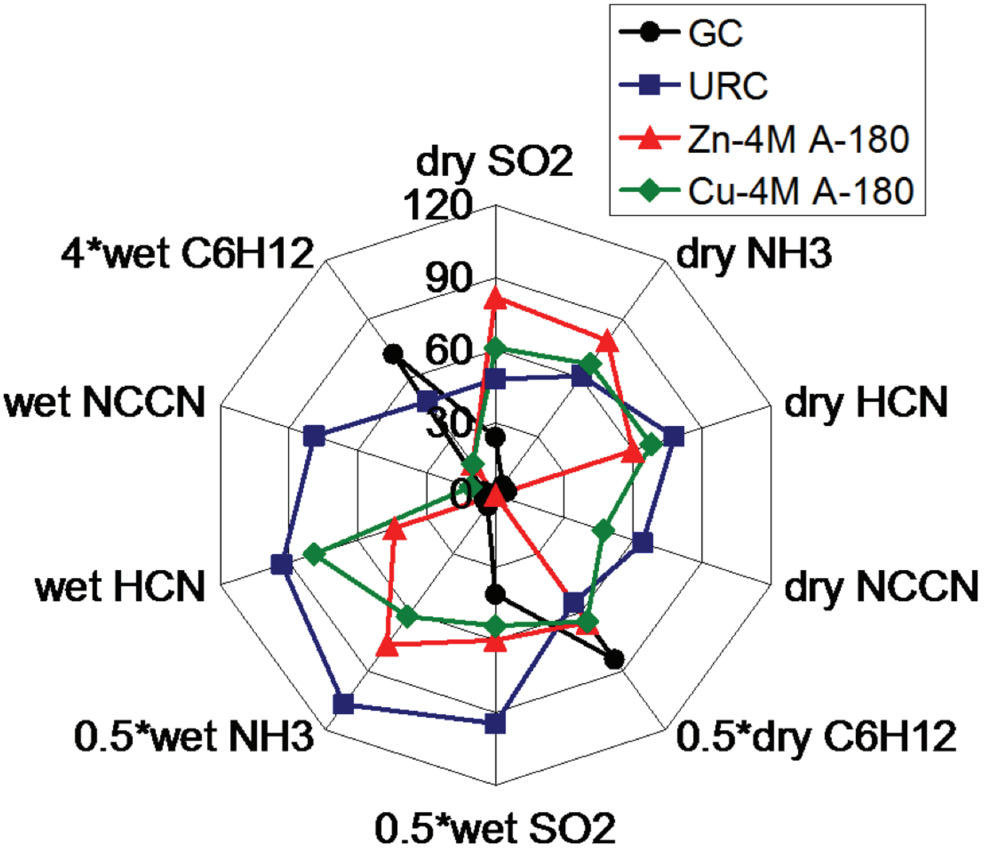

Figure 5.16: Radar plot of flow test results obtained from Zn-4M A-180 and Cu-4M A-180 samples. The breakthrough times are reported in minutes. Gas test results obtained from the different challenge gases are presented on individual axes. Dry C_6H_{12} and humid SO_2, NH_3, and C_6H_{12} breakthrough times have been scaled by the amount indicated on their respective axis, to allow for better presentation of the data. For reference results obtained from the GC and URC samples are included.

capacity; and dry C_6H_{12} and HCN/NCCN breakthrough times as good as or better than the Cu-4M A, URC or GC samples. The relatively low NCCN breakthrough time for the Cu-4M A-180 sample can be attributed to the lack of Mo^{6+} [21,24]. Under humid conditions the Zn-4M A-180 and Cu-4M A-180 samples were outperformed by the URC sample. These samples still had reasonably good wet SO_2, NH_3 and HCN capacities but had poor wet C_6H_{12} breakthrough times. The longer humid SO_2 and C_6H_{12} breakthrough times obtained from the URC sample are partly due to the use of a different base carbon. The URC samples were prepared on coal derrived AC, the Zn-4M A-180 and Cu-4M A-180 samples were prepared on GC (coconut derived AC).

Figures 3.4 and 3.5 show that coal derrived AC had longer humid SO_2 and C_6H_{12} breakthrough times than coconut derived AC. It is probable that the wet HCN results are higher for the URC sample relative to our Cu-based samples because the URC sample has higher Cu^{2+} impregnant loading according to the preferred formulation in the literature [13]. The longer humid NH_3 breakthrough times achieved by the URC samples are likely due to the additional presence of a Mo-containing species. Mo-based impregnants are effective for removing NH_3 and this effect seems to be enhanced under humid conditions [104]. Cu-based IACs prepared in the same manner as Cu-4M A-180, including a Mo species, had enhanced wet NH_3 adsorption [21].

5.3 Conclusions

Studying Zn- and Cu-based IACs as a function of T_f and HNO_3 concentration present in the impregnating solution allowed several important observations to be made. The optimal heating temperature range (in Argon) for the Zn-based samples was $160°C \leq T_f \leq 250°C$ and for the Cu-based samples it was $180°C \leq T_f \leq 200°C$. Heating at lower T_f resulted in poor reproducibility and incomplete decomposition to the desired impregnant phase. Heating to $T_f \geq 250°C$ for the Zn-based samples gave relatively large grain-size impregnant and poor impregnant distribution, resulting in lower dry gas adsorption capacity. Similar observations were made for the Cu-based samples. Heating the Cu-based IACs to $T_f > 200°C$ resulted in the formation of Cu_2O and Cu impregnant phases, which also contributed to shorter breakthrough times.

The addition of HNO_3 to the Zn- and Cu-based samples resulted in higher amounts of surface oxygen on the AC substrate. This caused improved impregnant distribution and smaller grain-size impregnant when the appropriate thermal treatment was used. Samples with good impregnant distribution had relatively good dry gas adsorption capacity.

The Zn- and Cu-based samples discussed here have reasonable performance under humid conditions when challenged with SO_2, NH_3 and HCN challenge gases, but have poor C_6H_{12} capacity. Work on improving humid gas adsorption capacity will be reported in subsequent chapters.

The results from this work indicate that the Zn-4M A IACs prepared in the range of 160°C $\leq$ T$_f$ $\leq$ 250°C may be candidates for use in broad spectrum gas mask filters. The simple chemistry and preparation of these samples coupled with no need for a relatively expensive Mo^{6+} impregnant may make them of commercial interest. A U.S. patent application based on the Zn-based IACs reported in this work has been filed [105].

Chapter 6

Small and Wide Angle X-Ray and Nitrogen Adsorption Porosimetry Studies of Impregnated Activated Carbons

Sections of this chapter, including certain figures, have been submitted for publication in the journal Carbon. The manuscript title is "Small and wide angle X-ray studies of impregnated activated carbons". The authors are Jock Smith, Matt Mcdonald, Landan MacDonald, Jennifer Romero and Jeff Dahn. The contribution of Jock Smith consists of the organization of all experiments, preparation and X-ray analysis of all IAC samples, all of the data analysis and preparation of the figures and manuscript. The figures and tables have been reproduced by permission of the journal in accordance with the terms of the publishing company (Elsevier) copyright release (see Appendix A). Some of the text, figure numbers and references have been modified for inclusion in this thesis.

6.1 Experimental Details

6.1.1 Chemicals Used

The chemicals used to prepare the impregnating solutions were reagent grade copper nitrate hemi-pentahydrate ($Cu(NO_3)_2 \bullet 2.5H_2O$), zinc nitrate hexahydrate ($Zn(NO_3)_2 \bullet 6H_2O$) and 70% concentrated nitric acid (HNO_3) obtained from Sigma-Aldrich.

6.1.2 Sample Preparation

All of the IACs described in this chapter were prepared using GC activated carbon which was previously described in section 3.1. IAC samples that were studied as a function of concentration of the impregnating solution were co-impregnated with $Cu(NO_3)_2$ and HNO_3. The concentrations of $Cu(NO_3)_2$ used were 0.31 M, 0.79 M, 1.60 M, 2.40 M and 3.10 M and the concentrations of HNO_3 used were 0 M, 0.5 M, 2.0 M, 4.0 M and 8.0 M. The imbibing solution with the highest combined concentration of impregnants was 2.0 M $Cu(NO_3)_2$ / 6.6 M HNO_3. The IAC samples prepared for the heating study were impregnated with 2.4 M $Cu(NO_3)_2$ / 4 M HNO_3 or 2.4 M $Zn(NO_3)_2$ / 4 M HNO_3. All of the IACs were impregnated using the imbibing method. Typically 11 - 12 mL of solution was added to approximately 15 g of GC.

The IAC samples were heated under flowing argon in a sealed, cylindrical aluminum container that was located inside an oven. Prior to heating, the container was purged with argon flowing at approximately 200 mL/min. The argon flow rate was approximately 60 mL/min during heating. The IACs that were studied as a function of concentration were heated at T_f = 180°C for approximately 3 hours. The IACs prepared for the heating study were heated to T_f = 120, 140, 160, 180, 200, 250 and 300°C for approximately 3 hours. After heating, all of the IACs were cooled under flowing argon until they reached room temperature. IACs heated at 250°C and 300°C were heated in a tube furnace, but the argon flow rates were the same as for other samples.

The impregnant loading after heating was determined according to Eq. 2.1. The predicted impregnant loading (expressed in mmol impregnant/g GC) was discussed in Chapter 2.

6.2 Results and Discussion

6.2.1 Impregnant Loading

Figure 6.1 shows the impregnant loading, after heating at T_f = 180°C under argon, for IACs prepared from $Cu(NO_3)_2$ and HNO_3 solutions. The data is presented as percent impregnant loading as a function of $Cu(NO_3)_2$ concentration in the impregnating solution. The concentration of HNO_3 used in each sample set is indicated in the legend. The predicted impregnant loading has been indicated for reference. The predicted loading assumes full conversion of the $Cu(NO_3)_2$ precursor to CuO. The predicted impregnant loading does not account for mass gain due to the introduction of surface oxygen groups from the action of the HNO_3 on the AC substrate [91], or for mass loss due to the consumption of carbon from the AC substrate that may be evolved as CO or CO_2 according to Eq. 5.1 or similar reactions in reference [9].

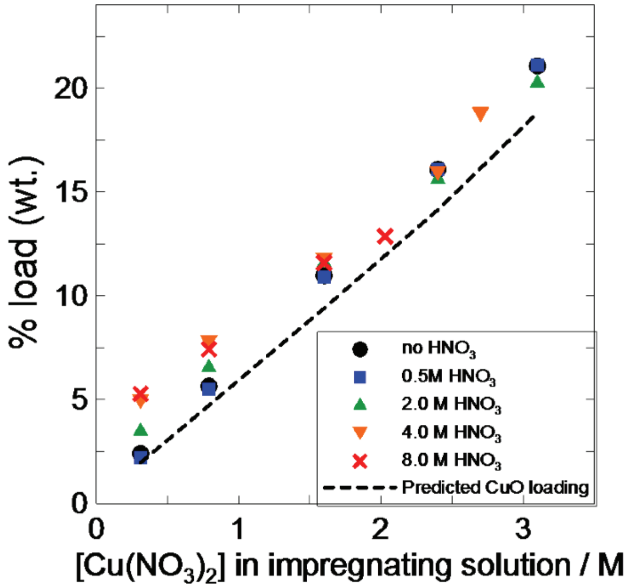

Figure 6.1: Observed impregnant loading (after heating at T_f = 180°C under argon) as a function of $Cu(NO_3)_2$ concentration in the impregnating solution for samples co-impregnated with 0 M, 0.5 M, 2.0 M, 4.0 M and 8.0 M HNO_3. The predicted loading has also been indicated.

Figure 6.1 shows a reasonably linear increase in impregnant loading with increasing $Cu(NO_3)_2$ concentration for all of the IAC samples prepared in this work. The observed loadings are in reasonable agreement with the $Cu(NO_3)_2$ precursor decomposing to CuO during heating. At the two lowest $Cu(NO_3)_2$ concentrations, the loading increases with HNO_3 molarity.

IAC samples were also prepared from 2.4 M $Cu(NO_3)_2$ / 4 M HNO_3 or 2.4 M $Zn(NO_3)_2$ / 4 M HNO_3 solutions for a heating study. Figure 6.2 shows the observed impregnant loading as a function of maximum final heating temperature, T_f. Figure 6.2(a) shows the Cu-based IACs and Figure 6.2(b) shows the Zn-based IACs as described in the Figure caption.

Figure 6.2 shows that samples prepared from the $Cu(NO_3)_2$ precursor have decreasing impregnant loading with increasing heating temperature. For 180°C $\leq T_f \leq$ 250°C, the Cu-based IACs appear to have CuO or Cu_2O impregnant present, based on mass. The IACs prepared from $Zn(NO_3)_2$-containing solutions appear to thermally

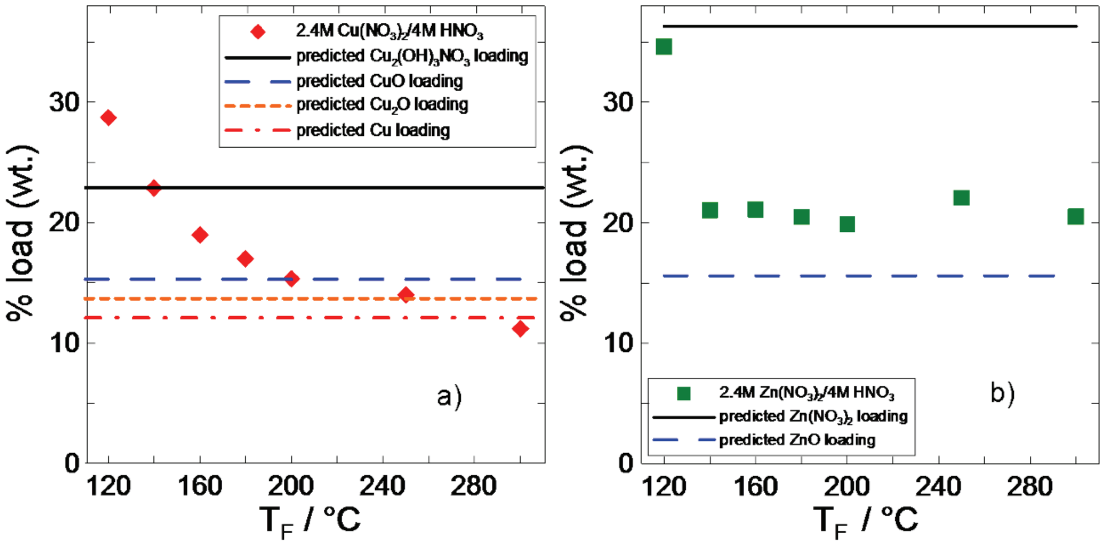

Figure 6.2: Observed impregnant loading for IACs prepared for the heating study. Panels (a) and (b) show the data obtained from 2.4 M $Cu(NO_3)_2$ / 4 M HNO_3 and 2.4 M $Zn(NO_3)_2$ / 4 M HNO_3 precursors respectively. IACs were heated under flowing argon at T_f = 120, 140, 160, 180, 200, 250 and 300°C respectively. The predicted impregnant loadings of $Cu_2(OH)_3NO_3$, CuO, Cu_2O and Cu are shown in panel (a) and $Zn(NO_3)_2$ and ZnO are indicated in panel (b).

decompose to a stable phase at lower heating temperatures than the Cu-based samples. This is in agreement with earlier work presented in chapters 4 and 5. Zn-based IACs heated to $T_f > 140$°C are within approximately 5% (wt.) of the predicted ZnO loading.

6.2.2 X-ray Characterization

Figure 6.3 shows scattered intensity versus the magnitude of the scattering vector, q, collected from the base GC carbon in a number of different SAXS experiments.

Figure 6.3 shows that reproducible SAXS patterns were obtained from the GC base carbon using the sample preparation procedures outlined in section 2.6. The data has been corrected for absorption of x-rays according to Eq. 2.7. The differences in intensity are mainly due to differences in sample mass. The high quality and reproducibility of the data obtained from the GC base carbon gives confidence that changes in the SAXS pattern due to impregnants will be meaningful, even at relatively low loadings.

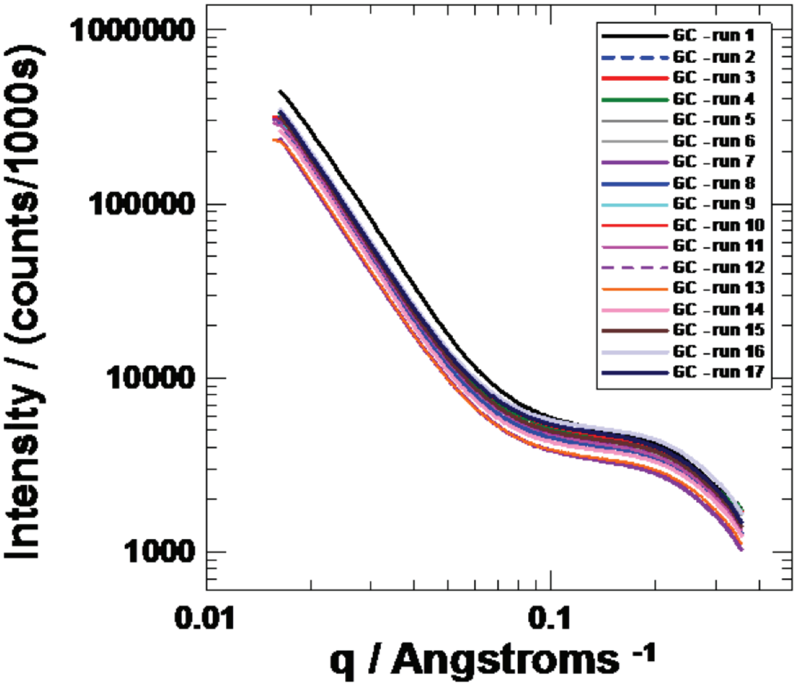

Figure 6.3: SAXS data obtained from GC base carbon for a number of experimental runs. The data is scattered intensity as a function of scattering vector, q, displayed on a log-log plot.

Prior to discussing experimental SAXS results obtained from the IAC samples, it is useful to discuss the treatment of the data. SAXS data obtained from un-impregnated GC samples were fit using the Kalliat model (Eq. 2.14). To model the IACs prepared in this study, Eq. 2.14 was modified using the following assumptions:

1. The micropore size was not significantly changed by the HNO_3 treatment. This assumption is consistent with results shown in Figure 3.9 and with results reported in the literature [70, 90].

2. The value of n can vary, but could not be less than the value recorded for the un-impregnated GC.

3. The Debye autocorrelation length of impregnant in micropores and small mesopores was ≥ 4.7 Å.

4. In a micropore, the contrast in electron density in the 3 phase system can be

described by :

$$\Delta\rho_e = \rho_{e,\text{carbon}} - ((1-x)\rho_{e,\text{void}} + x\,\rho_{e,\text{Cu}}), \tag{6.1}$$

where $\rho_{e,\text{carbon}}$, $\rho_{e,\text{void}}$ and $\rho_{e,\text{Cu}}$ are the electron densities of the carbon, void and CuO impregnant respectively (electrons/cm^3). The value of x can range from 0 to 1. Therefore, as a micropore fills with impregnant (x increases), we expect the scattered intensity to decrease. Care must be exercised when employing Eq. 6.1 to describe impregnants with a high electron density and high impregnant loading. Figure 6.4 shows a plot of calculated ${\Delta\rho_e}^2$ versus x values for impregnants with different electron densities as detailed by the figure legend.

Figure 6.4 shows that for $0 < \text{x} \leq 0.4$ ${\Delta\rho_e}^2$ decreases for all of the impregnants. For $\text{x} > 0.4$ the ${\Delta\rho_e}^2$ values calculated for the CuO and ZnO impregnants increase with increasing values of x. For the IACs studied in this work it is assumed that x is less than 0.4. This assumption will be verified using gas adsorption porosimetry below. The ${\Delta\rho_e}^2$ values calculated for H_2O and C_6H_{12} continually decrease for all values of x.

5. In a macropore or mesopore, it is assumed that the impregnant particle, which is much smaller than these pores, scatters independently from the carbon and is treated as a particle in an air-filled void.

The modified form of the Kalliat model used to fit the IAC data was:

$$\mathrm{I(q)} = \frac{\mathrm{A}}{\mathrm{q^n}} + \frac{\mathrm{Ba^4}}{(1+\mathrm{a^2q^2})^2} + \frac{\mathrm{Cb^4}}{(1+\mathrm{b^2q^2})^2}, \tag{6.2}$$

The constants A, B, n and a were defined in section 2.6. C is a constant proportional to the surface area of small impregnant particles in meso and macropores and b is the Debye autocorrelation length for small impregnant. The Debye length b can be related to the radius of gyration (R_g) by $R_g = \sqrt{6}$ b. Cb^4 (or $C{R_g}^4$) is expected to increase with increasing loading. A is also expected to increase if large (> 10 nm) impregnant particles form in macropores. The R_g values for the micropores and for small particle size impregnant will be denoted R_{g1} and R_{g2} respectively. The constants A, B, C, n, a and b were optimized by performing a least squares fitting routine (minimized χ^2) between the calculated and observed data over the entire experimental range.

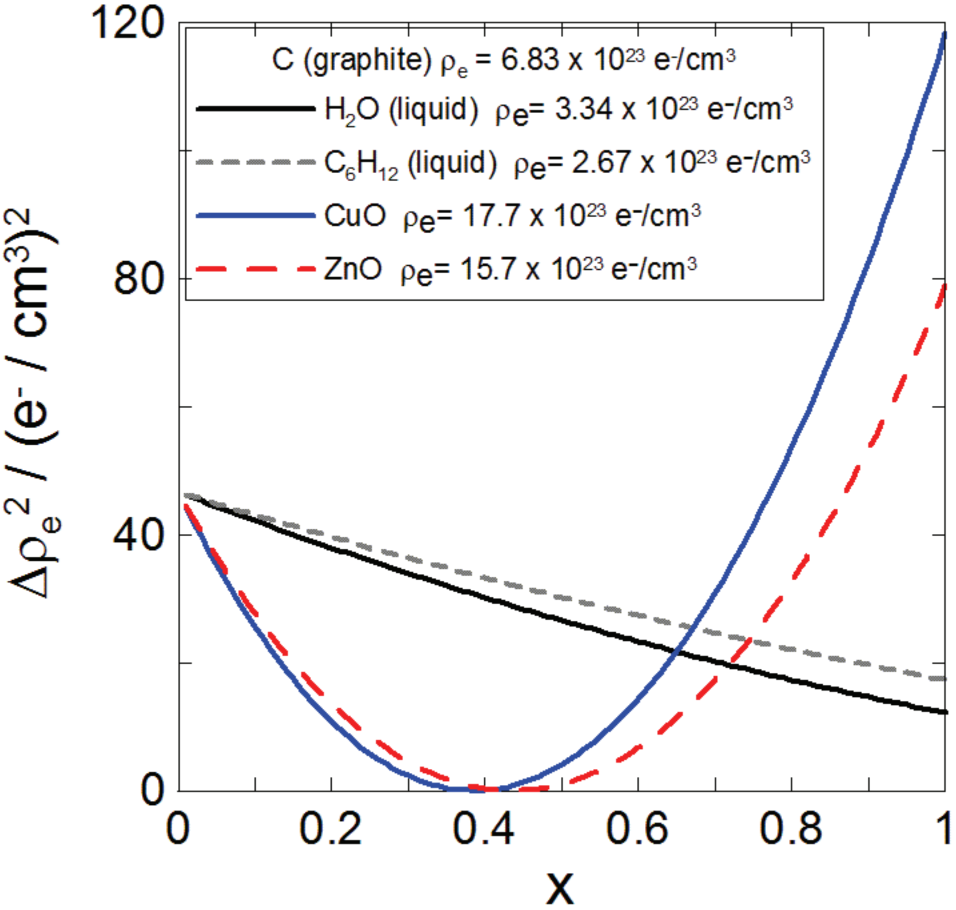

Figure 6.4: Calculated $\Delta\rho_e{}^2$ values versus x for liquid H_2O, liquid C_6H_{12}, CuO and ZnO impregnants. The electron densities for each impregnant and for carbon are indicated in the legend.

Figure 6.5 shows experimental data, fits using Equations 2.14 and 6.2 and the components of the fits for SAXS experiments performed on GC (panel (a)) and an IAC prepared from 2.4 M $Cu(NO_3)_2$/4 M HNO_3. Figure 6.5(a) shows that reasonable fits to the un-impregnated GC can be achieved using Eq. 2.14. Figure 6.5(b) shows that the SAXS pattern obtained from the IAC sample is well-described using Eq. 6.2.

6.2.3 Effect of HNO_3 Concentration on Impregnant Distribution

IACs prepared by co-impregnating GC with aqueous $Cu(NO_3)_2/HNO_3$ solutions were examined using SAXS. Figure 6.6 shows data collected from all of the samples prepared using different concentrations of $Cu(NO_3)_2/HNO_3$. All of the samples shown in

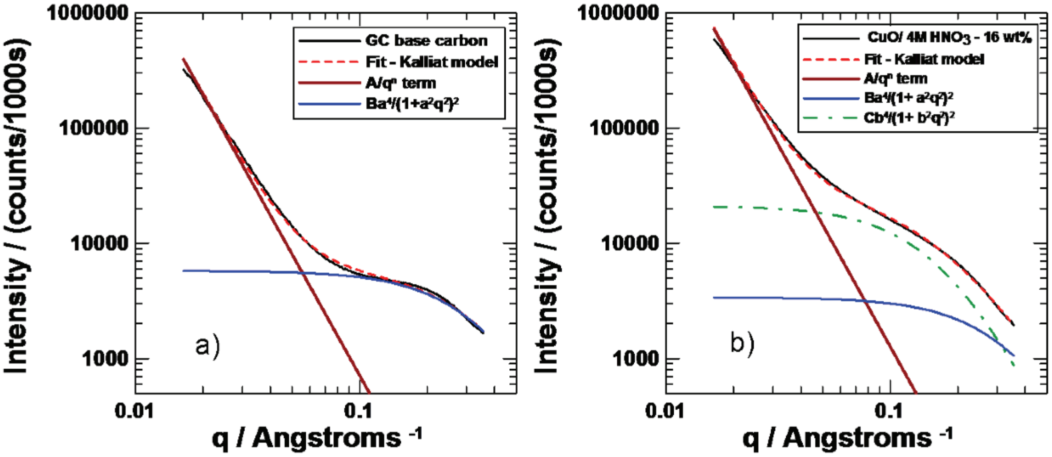

Figure 6.5: Experimental data, fits to the data and the components of each fit are shown for GC (panel (a)) and an IAC prepared from 2.4 M $Cu(NO_3)_2$/4 M HNO_3. The data has been corrected for sample absorption.

Figure 6.6 were heated at T_f = 180°C, under flowing argon, prior to measurements. The impregnant loading and concentration of HNO_3 used are indicated in each panel. The fits to the data are not shown in Figure 6.6. Optimized values from the fits are provided in Table 6.1.

Figure 6.6(a) shows that the intensity at $q \leq 0.06$ Å^{-1} increases with increasing CuO impregnant loading. This occurs because the impregnant is forming large particles in the macropores (and large mesopores). As the HNO_3 concentration was increased (panels (a) → (e)) the sample to sample difference in intensity at $q \leq 0.06$ Å^{-1} with increased loading decreased. Comparing the difference in intensities (at q = 0.02 Å^{-1}) between the base carbon and the samples with the highest CuO loading in Figures 6.6(a), 6.6(d) and 6.6(e), respectively, shows that the differences in intensity decreased by approximately 85 % and 90% for the IACs prepared from 4 M and 6.6 M HNO_3 respectively (compared to the Cu-based IAC with no co-impregnated HNO_3). This implies that the HNO_3 co-impregnation helps to prevent the formation of large impregnant particles.

The data in Figures 6.6(a) - 6.6(e) for $q > 0.2$ Å^{-1} show similarities for all samples. In this region, the intensity of the IACs is close to that of the base carbon. This suggests that little impregnant enters the micropores. The data in the plateau region of Figures 6.6(a) - 6.6(e) (≈ 0.09 Å^{-1} to 0.2 Å^{-1}) shows dramatic differences,

Table 6.1: Parameters from Kalliat models used to fit SAXS data obtained from GC and the IACs in this study. Note the values in columns A, B and C have units of counts/Å^n (A) and counts/Å^4 (B and C). The values stated for GC are average values obtained from analysis of the data shown in Figure 6.3. The uncertainties reported for GC represent the standard deviation.

		A	n	B	R$_{g1}$ (Å)	C	R$_{g2}$ (Å)	χ^2
GC	GC	0.20 ± 0.06	3.5 ± 0.1	134 ± 29	6.1 ± 0.2	0	0	1.6 ± 0.4
% load (wt.)	[HNO$_3$] (M)	A	n	B	R$_{g1}$ (Å)	C	R$_{g2}$ (Å)	χ^2
2	0	0.22	3.6	133	6.1	4	11.5	1.3
6	0	0.25	3.7	90	6.1	14	11.5	0.9
11	0	0.37	3.7	27	6.1	22	11.5	0.3
16	0	0.87	3.7	69	6.1	24	11.5	0.1
21	0	0.51	3.9	92	6.1	16	11.5	0.7
4	0.5	0.22	3.5	114	6.1	3	11.5	0.9
7	0.5	0.28	3.5	105	6.1	4	16.3	0.5
12	0.5	0.40	3.5	99	6.1	6	17.9	0.3
16	0.5	0.99	3.5	88	6.1	12	14.0	0.1
20	0.5	1.54	3.5	77	6.1	16	11.5	0.5
4	2	0.25	3.5	140	6.1	2	11.5	1.4
7	2	0.26	3.5	109	6.1	8	11.5	0.8
12	2	0.33	3.5	114	6.1	9	15.1	0.5
16	2	0.52	3.5	96	6.1	14	14.5	0.3
20	2	1.01	3.5	82	6.1	17	14.1	0.4
5	4	0.22	3.5	130	6.1	1	11.5	1.7
8	4	0.32	3.5	152	6.1	7	11.5	1.2
12	4	0.31	3.5	106	6.1	15	12.6	0.7
16	4	0.40	3.5	86	6.1	22	13.6	0.5
19	4	0.49	3.5	88	6.1	22	14.6	0.4
5	8	0.16	3.5	139	6.1	0	11.5	1.9
7	8	0.23	3.5	151	6.1	3	11.5	2.3
12	8	0.30	3.5	107	6.1	18	11.5	1.0
13	6.6	0.35	3.5	84	6.1	25	11.5	0.7

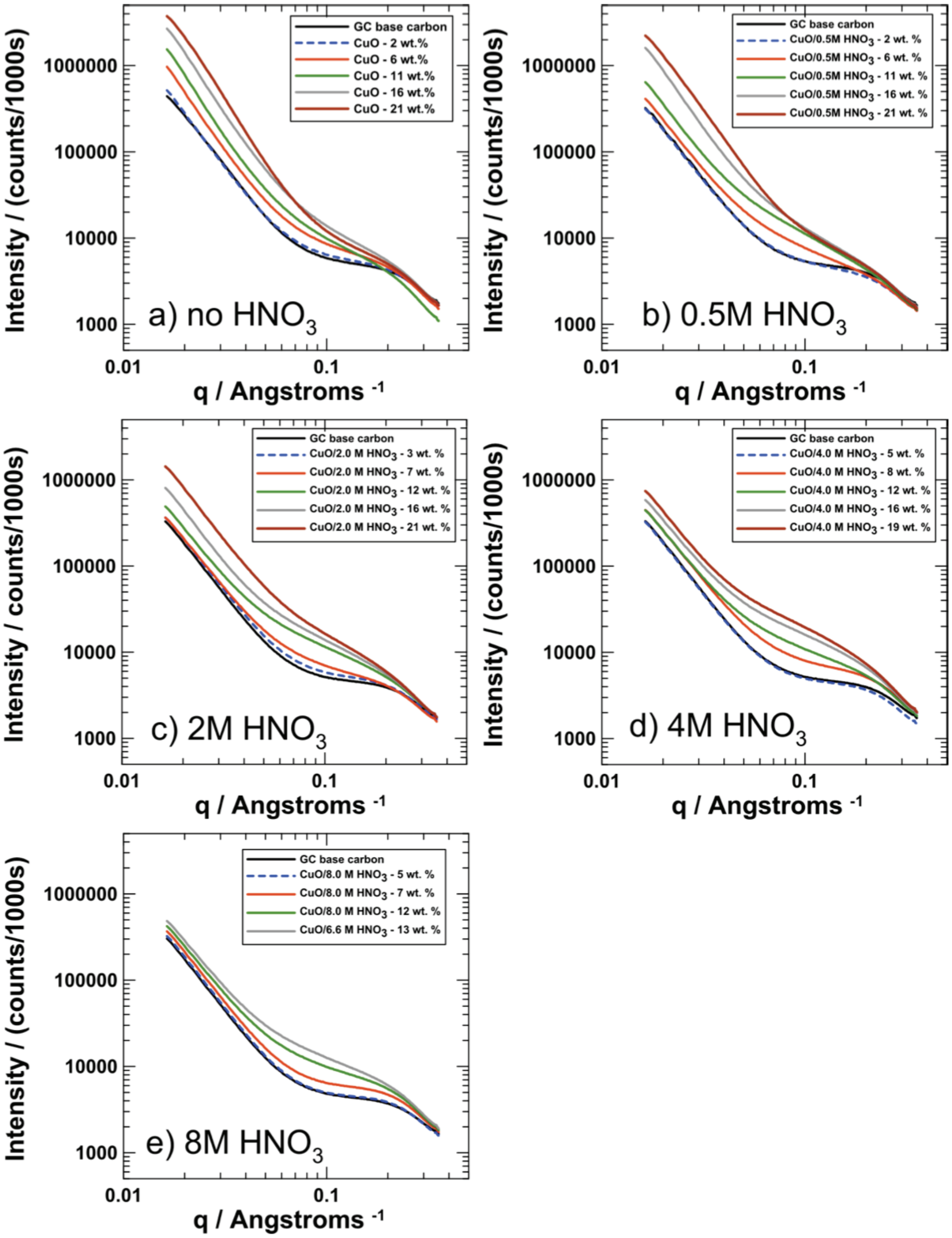

Figure 6.6: SAXS data obtained from IACs co-impregnated with aqueous $Cu(NO_3)_2$ and HNO_3. The impregnant loading after heating is indicated in each legend. Panels (a), (b), (c), (d) and (e) show data from IACs co-impregnated with 0, 0.5, 2, 4 and 8 M HNO_3 respectively. The data has been corrected for sample absorption.

especially between panels (a) and (d). In panel (a) the intensity in this region initially increases slightly with increasing impregnant loading, however at the highest loading, the SAXS curve intersects the curves obtained from samples with lower CuO loading. The decrease in scattering intensity from small impregnant (higher q values) and subsequent increase in scattering from large impregnant particles (lower q values) for the sample with high CuO loading (and no co-impregnated HNO_3) is indicative of impregnant agglomeration on the GC substrate. As the concentration of co-impregnated HNO_3 was increased, the intensity in the plateau region increased with increasing CuO loading. Figure 6.6(d) shows increasing intensity with increasing impregnant loading for $0.09\ \text{Å}^{-1} \leq q \leq 0.2\ \text{Å}^{-1}$. This implies an increase in the number of small ($<$ 3nm) impregnant particles (as detailed in Table 6.1).

Figure 6.7 shows wide angle x-ray diffraction (XRD) data collected from all of the samples described by 6.6. The Bragg peak positions for CuO are indicated in each panel for reference [56]. Figure 6.7(a) shows increasing intensity of the CuO diffraction peaks as the impregnant loading is increased. As the concentration of HNO_3 is increased (panels (a) $\rightarrow$ (e)) the intensity of the CuO peaks decreases, which indicates that co-impregnation with HNO_3 results in smaller, better distributed impregnant. These results are consistent with the SAXS data (Figure 6.6 and with earlier work (Figure 5.2). The samples described by Figures 6.7(d) and 6.7(e) do not have obvious impregnant related diffraction peaks, even at the highest loadings reported here.

Analysis of the data in Figures 6.6 and 6.7 was performed to better compare results obtained from the IAC samples using SAXS and XRD. Figure 6.8(a) shows the observed intensity of the SAXS data at $q = 0.02\ \text{Å}^{-1}$ plotted against the impregnant loading (mmol Cu^{2+} impregnant/g GC) for each series of samples co-impregnated with HNO_3. The HNO_3 concentrations are indicated in the legend. The data point for GC is the average value calculated from the SAXS data obtained from GC (shown in Figure 6.3) and the error bars denote the standard deviation. Figure 6.8(b) shows the average integrated area under the CuO Bragg peaks located at approximately $2\theta = 35.5^\circ$ and 38.8° (Miller indices (11-1) and (111) respectively). The data is plotted against the impregnant loading. The area under the diffraction peaks was integrated

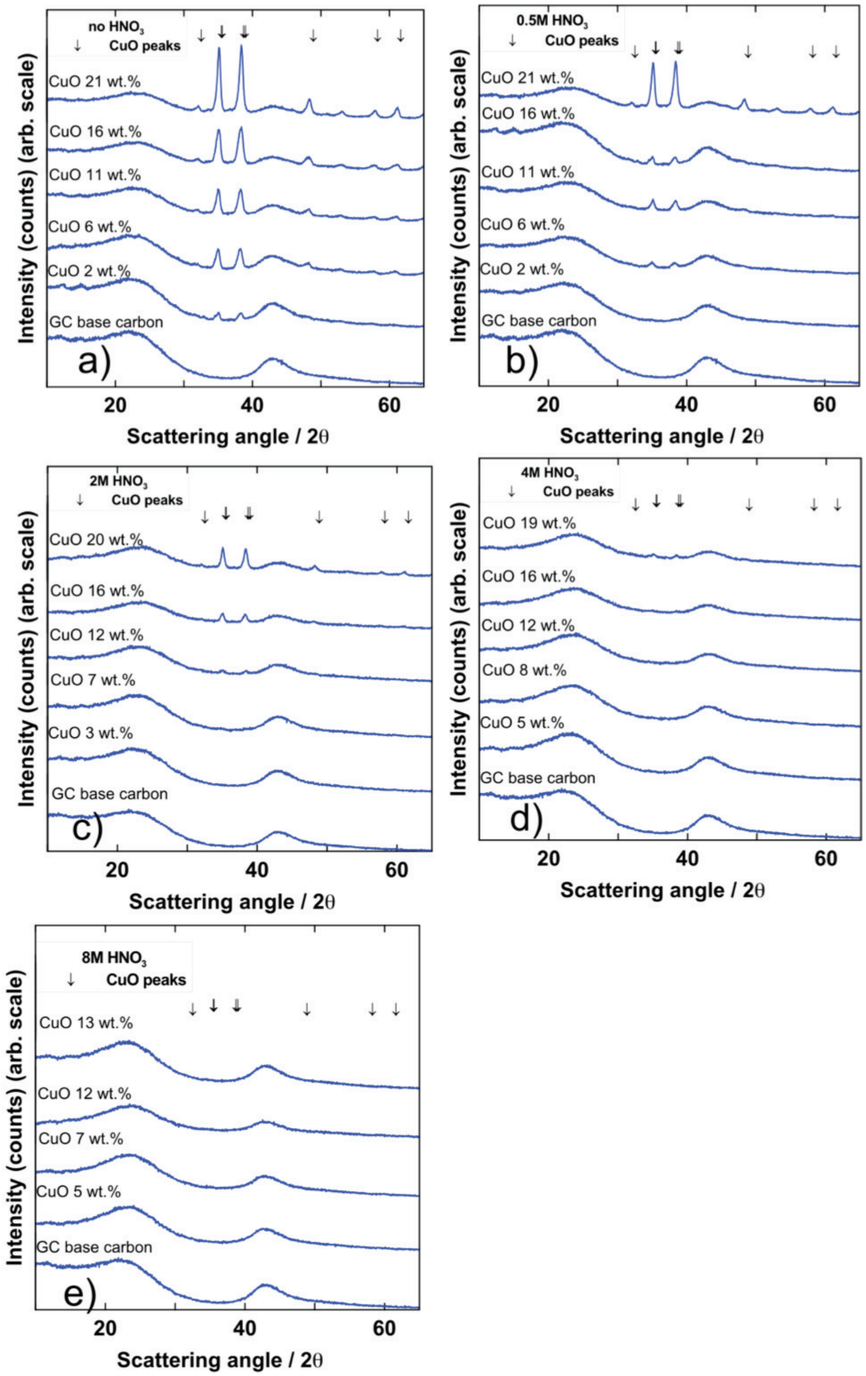

Figure 6.7: XRD data obtained from IACs co-impregnated with aqueous $Cu(NO_3)_2$ and HNO_3. The impregnant loading after heating is indicated in each panel. Panels (a), (b), (c), (d) and (e) show data from IACs co-impregnated with 0, 0.5, 2, 4 and 8 M HNO_3 respectively. The Bragg peak positions for CuO are indicated for reference.

using Fityk software [57].

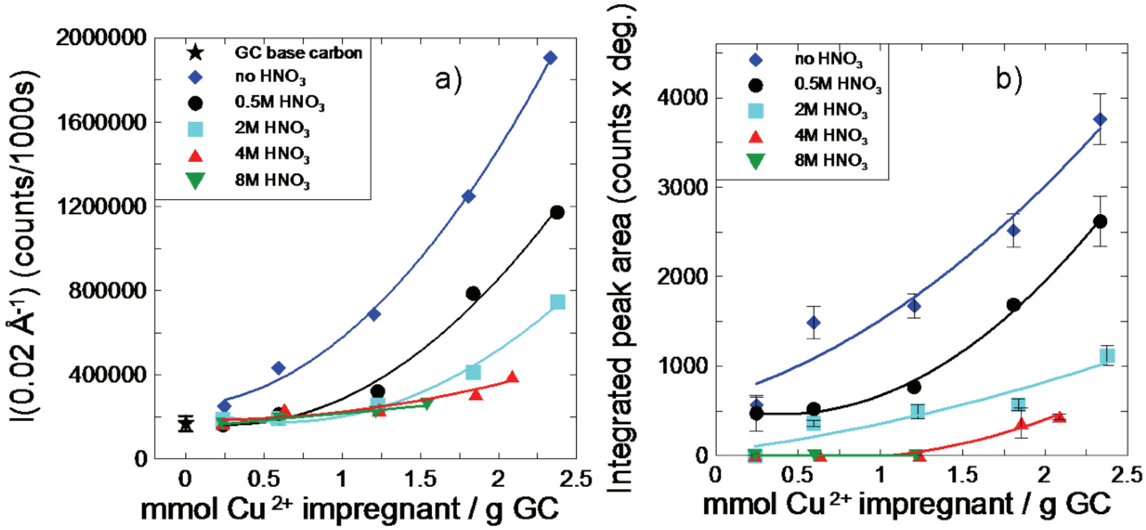

Figure 6.8: Data obtained from IACs prepared with $Cu(NO_3)_2/HNO_3$. Panel (a) shows the observed intensity from the SAXS data at q = 0.02 Å^{-1}. Panel (b) shows the average integrated area under the CuO impregnant peaks located at scattering angles $2\theta = 35.5°$ and $38.8°$. The data is plotted against impregnant loading. The lines are a guide for the eye. The data in panel (a) has been corrected for sample absorption.

Figure 6.8 shows that there is excellent agreement between the observed trends in the SAXS and XRD data regarding the formation of large CuO particles. The trend of increasing amounts of relatively large impregnant ($\geq$ 10 nm) with increased loading is illustrated in the data obtained from IACs prepared without any HNO_3 in panels (a) and (b). The average impregnant grain size calculated from the XRD data using Eq. 2.5 is displayed in Table 6.2. Figures 6.8(a) and (b) show that as the concentration of HNO_3 present in the impregnating solution is increased, the scattering intensity at q = 0.02 Å^{-1} and hence total volume of large size CuO impregnant particles decreased.

The XRD data provides useful information about the impregnant grain size and distribution when diffraction peaks are present, however it does not give information about relatively small impregnant particles (< 30 Å approximately). To learn how the HNO_3 co-impregnation is affecting relatively small impregnant particles, the SAXS data in the q $\geq$ 0.06 Å^{-1} range is useful. Figure 6.9 shows parameters extracted from the fits to the SAXS data using Eq. 2.14 and Eq. 6.2. Panel (a) shows the

Table 6.2: Average CuO impregnant grain size for IACs in loading study. Calculated for the 2 Bragg peaks at $2\theta = 35.5°$ and $38.8°$ using the Scherrer equation (Eq. 2.5).

% impregnant loading (wt.)	Impregnant loading (mmol Cu^{2+}/g GC)	[HNO_3] (M)	L_{hkl} (Å)
2	0.2	0	118 ± 10
6	0.6	0	113 ± 10
11	1.2	0	115 ± 10
16	1.8	0	107 ± 10
21	2.3	0	141 ± 10
4	0.2	0.5	n/a
7	0.6	0.5	93 ± 10
12	1.2	0.5	134 ± 10
16	1.8	0.5	127 ± 10
20	2.4	0.5	136 ± 10
4	0.2	2	n/a
7	0.6	2	59 ± 30
12	1.2	2	80 ± 40
16	1.8	2	129 ± 10
20	2.4	2	149 ± 10
5	0.2	4	n/a
8	0.6	4	n/a
12	1.2	4	n/a
16	1.9	4	40 ± 40
19	2.1	4	40 ± 40
5	0.2	8	n/a
7	0.6	8	n/a
12	1.2	8	n/a
13	1.5	6.6	n/a

term related to micropore (and small mesopore) surface area, B, and panel (b) shows $CR_{g2}{}^4$. Both parameters are plotted against impregnant loading.

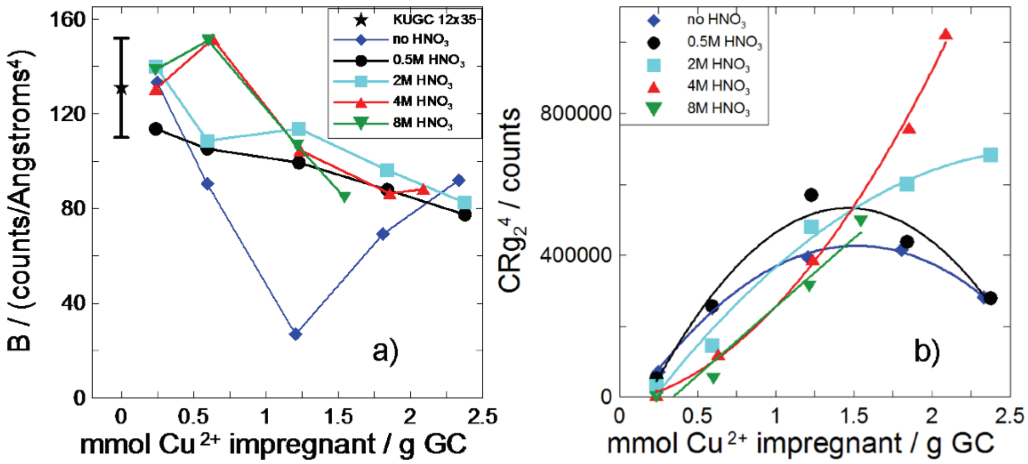

Figure 6.9: Extracted parameters from fits to the SAXS data using Eq. 2.14 and Eq. 6.2. Panel (a) shows the term related to micropore surface area (B term) and panel (b) shows $CR_{g2}{}^4$ both plotted against impregnant loading. The lines are a guide for the eye.

Figure 6.9(a) shows a general trend of decreasing B values with increasing impregnant loading for all of the IAC samples. This indicates that impregnant is being loaded into small pores for all of the aqueous solutions used in this study. Figure 6.9(b) shows that for loadings up to approximately 1.5 mmol Cu^{2+}/g GC the $CR_{g2}{}^4$ term, which represents the intensity of the scattering from small impregnant particles in mesopores, increases with increased impregnant loading. Above this loading samples prepared without HNO_3 or with 0.5 M HNO_3 have decreasing $CR_{g2}{}^4$ terms, the IAC with 2 M HNO_3 appears to begin to plateau and the sample with 4 M HNO_3 continues to increase in an approximately linear manner. We discuss the interesting behaviour observed in Figure 6.9(b) in further detail below.

Figure 6.10 shows a schematic depiction of pore filling as a function of increasing $Cu(NO_3)_2$ concentration. The schematic is based on the SAXS and XRD results shown in Figures 6.6 and 6.7 and the analysis of Figures 6.8 and 6.9. The left side of the Figure describes the case for IACs prepared from aqueous $Cu(NO_3)_2$ with no HNO_3 and the right side of the Figure describes the case for IACs prepared from aqueous $Cu(NO_3)_2$ co-impregnated with 4 M HNO_3.

Figures 6.10(a) and 6.10(b) show the un-impregnated GC. The largest openings (and surface) represent large mesopores (100 Å and larger) and macropores, the medium size passages are meant to depict smaller mesopores ($\approx$ 20 - 100 Å) and the smallest passages are the micropores ($\leq$ 20 Å). Panels (c) and (d) show schematics prepared from 0.31 M $Cu(NO_3)_2$ and $Cu(NO_3)_2$/4 M HNO_3 respectively. Pore filling in the micropores and small mesopores for these samples is similar, however the IAC co-impregnated with 4 M HNO_3 has smaller, more dispersed impregnant in the larger pores and on the carbon surface. Panels (e), (f), (g) and (h) show a similar trend. The small mesopores continue to fill with increasing $Cu(NO_3)_2$ concentration, in a similar manner for both types of IACs. The amount of large impregnant populating the macropores and large mesopores increases with increasing Cu^{2+} impregnant loading for the sample prepared without HNO_3, while the IACs co-impregnated with 4 M HNO_3 have a much smaller increase.

The greatest difference in the pore filling model is shown by comparison of Figures 6.10(i) and 6.10(j) (IACs impregnated with 2.4 M $Cu(NO_3)_2$ and 2.4 M $Cu(NO_3)_2$/4 M HNO_3 respectively). Figure 6.10(i) shows that the impregnant in the small mesopores is starting to agglomerate and "ball up", which results in larger particles presenting less surface area. The increasing size and amount of large ($>$ 100 Å) impregnant in the large pores and on the carbon surface may be causing pore blockage. Figure 6.10(j) shows that impregnant in the mesopores is probably increasing in size, but it is also spreading on the carbon surface, covering more surface area. The amount and size of impregnant in the larger pores is increasing at a much lower rate (relative to the IAC depicted in panel (i)). Figure 6.10(k) shows that impregnant in the small mesopores is agglomerating and continuing to ball up, resulting in larger impregnant occupying less surface area. The impregnant in the large pores and on the carbon surface is also increasing in size and amount. Figure 6.10(l) shows that impregnant size and surface coverage of the small mesopores is increasing, however the distribution of the impregnant, relative to that depicted in panel (k), is good. The amount of impregnant on the carbon surface and occupying larger pores is increasing, but is still relatively small in size and well dispersed.

In order to further investigate why co-impregnation with HNO_3 results in smaller,

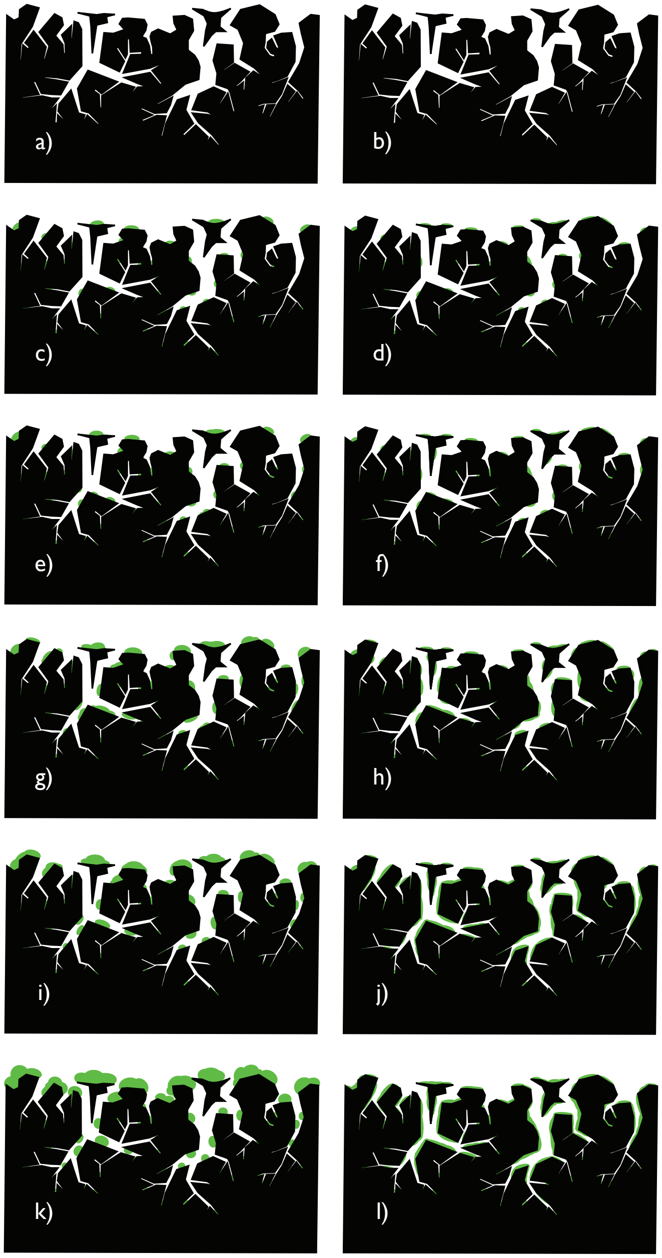

Figure 6.10: Schematic of pore filling as a function of increasing $Cu(NO_3)_2$ concentration. The left side of the Figure (panels (a), (c), (e), (g), (i) and (k)) describes IACs prepared without co-impregnating HNO_3. The right side (panels (b), (d), (f), (g), (h), (j) and (l)) describes samples co-impregnated with 4 M HNO_3. The green objects represent Cu^{2+} impregnant (present as CuO). The impregnant loading increases moving down the Figure and is the same for panels at the same horizontal level.

better dispersed impregnant, contact angle studies were performed on an HOPG substrate. Figure 6.11 shows contact angle data plotted against $Cu(NO_3)_2$ concentration in the impregnating solution for aqueous $Cu(NO_3)_2$ solutions and $Cu(NO_3)_2/HNO_3$ solutions. The concentration of HNO_3 is indicated in the legend. For reference, the measured contact angle for deionized water has been included. Each data point in Figure 6.11 is an average of 6-12 measurements.

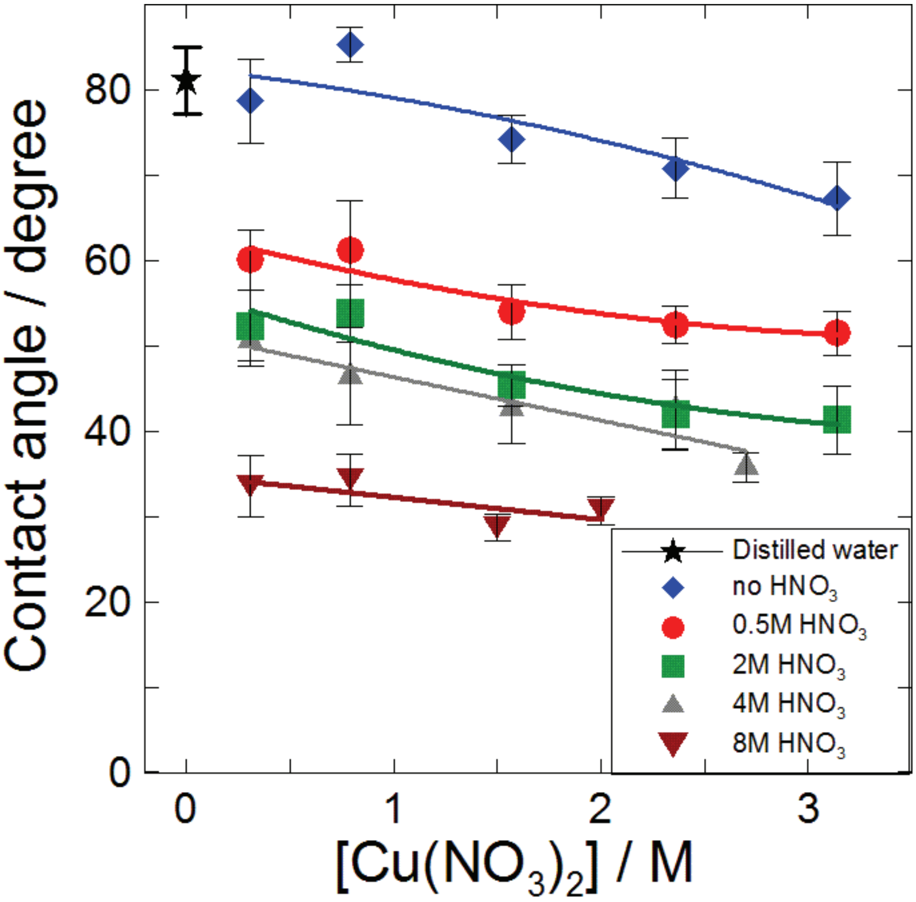

Figure 6.11: Contact angle measurements plotted against $Cu(NO_3)_3$ concentration for $Cu(NO_3)_2$ and $Cu(NO_3)_2/HNO_3$ solutions. The concentration of HNO_3 is indicated in the legend. For reference the measured contact angle for deionized water has been included. The lines are guides for the eye.

Figure 6.11 shows that the contact angle for deionized water is 81 ± 4°, in reasonable agreement with the literature [33] and previous measurements by our group [41]. The data from the $Cu(NO_3)_2$ solution (with no HNO_3) shows a slightly decreasing contact angle with increasing concentration. The $Cu(NO_3)_2$/4 M HNO_3 solutions follow a similar trend; however the contact angle for these solutions is approximately 30° lower than those measured for the $Cu(NO_3)_2$ (with no HNO_3) solutions. The data in Figure 6.11 shows that increasing HNO_3 concentration in the impregnating solution decreases contact angle. This implies that solutions with higher HNO_3 concentration wet the carbon surface better, giving better impregnant distribution and smaller particle size.

6.2.4 Effect of Heating Temperature on Impregnant Distribution

Several IAC samples were prepared from either aqueous 2.4 M $Cu(NO_3)_2$/4 M HNO_3 or 2.4 M $Zn(NO_3)_2$/4 M HNO_3 impregnating solutions to allow a comparative heating study using SAXS and XRD analysis. The samples were heated under flowing argon at T_f = 120, 140, 160, 180, 200, 250 and 300°C. The impregnant loadings after heating are shown in Figure 6.2. Figure 6.12 shows SAXS and XRD data collected from all of the IACs in the heating study as detailed in the caption.

Figure 6.12(c) shows that Cu-based IACs heated at $T_f \leq 200$°C have either no obvious or low intensity, broad impregnant related diffraction peaks. This implies the Cu-based impregnant has relatively small impregnant grain size according to Eq. 2.5. Data from IACs heated at $T_f \geq 250$°C that are shown in Figure 6.12(c) display Cu_2O diffraction peaks that increase in sharpness and intensity with increasing T_f, implying relatively large grain size Cu_2O. This is consistent with the SAXS data (at q ≈ 0.02 - 0.03 $Å^{-1}$) in Figure 6.12(a) and with the data shown in Figure 5.2. Figure 6.12(d) shows that IACs heated at $T_f \leq 300$°C display either no obvious, or broad, low intensity ZnO diffraction peaks, implying relatively small grain size impregnant. These results are consistent with the SAXS data (at q ≈ 0.02 - 0.03 $Å^{-1}$) in Figure 6.12(b).

The good agreement between SAXS results at low q values (q ≈ 0.02 - 0.03 $Å^{-1}$) and the XRD data supports our interpretation of how the impregnant is being distributed on the GC substrate during heating. The XRD data does not give useful information about small sized impregnant ($\leq$ 30 Å). Figure 6.12(a) shows interesting features in the intermediate q regime (q = 0.06 $Å^{-1}$ to 0.2 $Å^{-1}$) for the Cu-based IACs. Samples heated at T_f = 120, 140 and 160°C had similar SAXS curves. The

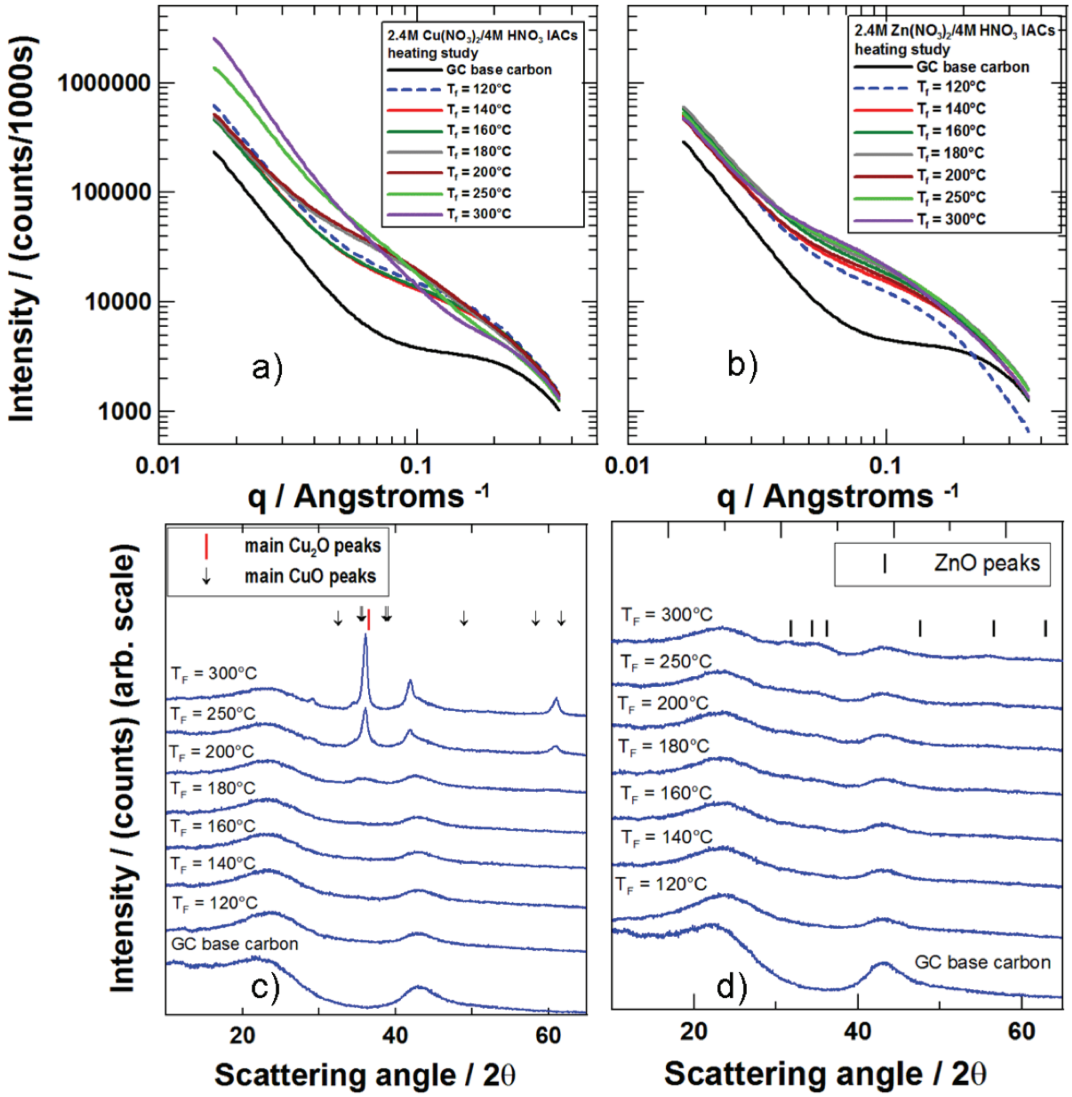

Figure 6.12: SAXS and XRD data from IACs prepared for the heating study. Panels (a) and (c) show SAXS and XRD data collected from the 2.4 M Cu(NO$_3$)$_2$/4 M HNO$_3$ IACs and panels (b) and (d) show SAXS and XRD data collected from the 2.4 M Zn(NO$_3$)$_2$/4 M HNO$_3$ IACs. The values for T$_f$ are indicated in all of the panels. For reference, the Bragg peak positions for CuO, Cu$_2$O and ZnO have been indicated in panels (c) and (d) respectively. The SAXS data has been corrected for absorption.

data from Cu-based IACs heated at 180°C and 200°C had higher intensity in the q = 0.06 Å^{-1} to 0.2 Å^{-1} range, but the SAXS signals from these two samples were also similar with each other. The data from the IACs heated at T$_f$ = 250°C and 300° intersected the other SAXS curves in the intermediate q range. In Figure 5.2 it was shown that IACs impregnated with Cu(NO$_3$)$_2$ or Cu(NO$_3$)$_2$/HNO$_3$ had the following thermal decomposition: at $T_f < 180°C$ the dominant impregnant phase was $Cu_2(OH)_3NO_3$, at $T_f = 180 - 200°C$ it was CuO and heating at $T_f \geq 250°C$ resulted in Cu_2O or Cu. The SAXS data from Cu-based IACs (Figure 6.12(a)) shows that the impregnant particle size and distribution in the small mesopores is changing with increasing heating temperature in a manner consistent with these impregnant phase changes. When the phase present does not change, the SAXS pattern does not change. At $T_f \geq 250°C$ the SAXS data indicates that impregnant is clustering, possibly due to the loss of oxygen, allowing for agglomeration of nearby impregnant particles.

Figure 6.12(b) shows SAXS data collected from the Zn-based IACs. The intensity of the data in the intermediate q range ($q = 0.06 - 0.2$ Å^{-1}) increased with increasing T_f and shifted to lower values of q. This implies that impregnant populating the mesopores is increasing in size with increasing T_f. Comparison of the data in this q range, between Figures 6.12(a) and 6.12(b) shows that the intensity changes of the Zn-based samples are more gradual relative to the Cu-based IACs. This is because the ZnO impregnant does not undergo a decomposition to a new phase during thermal treatment which, apparently, leads to significant particle aggregation in the Cu-based samples during transitions from $Cu_2(OH)_3NO_3$ to CuO to Cu_2O.

Figures 6.12(a) and 6.12(b) show interesting features in the $q = 0.2 - 0.4$ Å^{-1} range. The data in panel (a) shows the intensity of the Cu-based IACs is close to that of GC. Any difference in intensity (at these impregnant loadings) can be interpreted as a loss in electron density contrast, implying that the micropores are filling with Cu-based impregnant. The difference in intensity between the Zn-based IAC heated at 120°C and the base carbon (panel (b)) is more pronounced. This indicates that the Zn-based impregnant populates micropores at lower heating temperatures, but does not as heating temperatures are increased. The % impregnant loading shown in Figure 6.2 indicates that the dominant impregnant phase of the Zn-based IAC heated at 120°C was $Zn(NO_3)_2$.

6.3 Nitrogen Adsorption Porosimetry

Nitrogen adsorption isotherms were collected on certain Cu-based IACs to allow comparison with the SAXS and XRD data. Samples were examined to comparatively study the effects of Cu-impregnant loading and the effect of HNO_3 concentration at constant Cu-impregnant loading. Figure 6.13 shows nitrogen adsorption isotherms collected from the Cu-based IACs detailed in Figure 6.6(a). The impregnant loading is detailed in the legend.

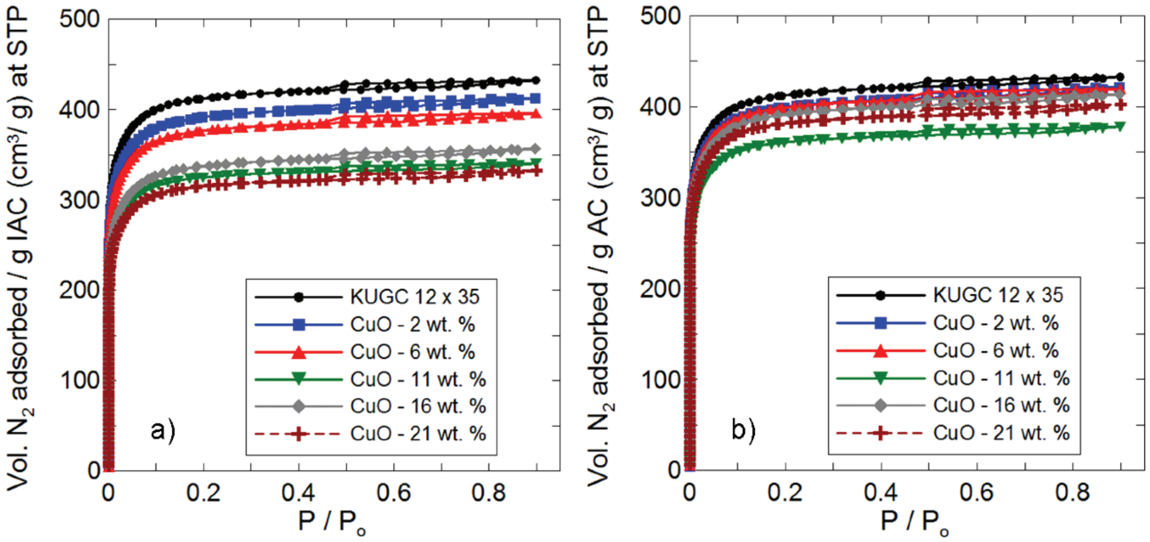

Figure 6.13: Nitrogen adsorption isotherms collected from the Cu-based IACs detailed in Figure 6.6(a). The impregnant loading is given in the legend. The volume of N_2 adsorbed per gram of IAC and per gram of un-impregnated AC is shown in panels (a) and (b), respectively. Data obtained from un-impregnated GC has been included for reference.

Figure 6.13(a) shows that the volume of N_2 adsorbed per gram of IAC decreases with increasing impregnant loading. The one exception to this trend is the Cu-based IAC with 11 % (wt.) loading which had lower N_2 adsorption than the sample with 16 % loading. Figure 6.13(b) shows that the volume of N_2 adsorbed per gram of AC for the impregnated samples was lower, but relatively close to the volume adsorbed by the un-impregnated GC sample.

Figure 6.14 shows the differential pore volume plotted against pore width for the IACs displayed in Figure 6.13. Values for pore widths up to 30 Å are shown. The pore size distribution calculations were based on a slit shaped pore model [53] and calculated using software provided by the manufacturer of the porosimeter. The impregnant loading of each sample is indicated in each panel.

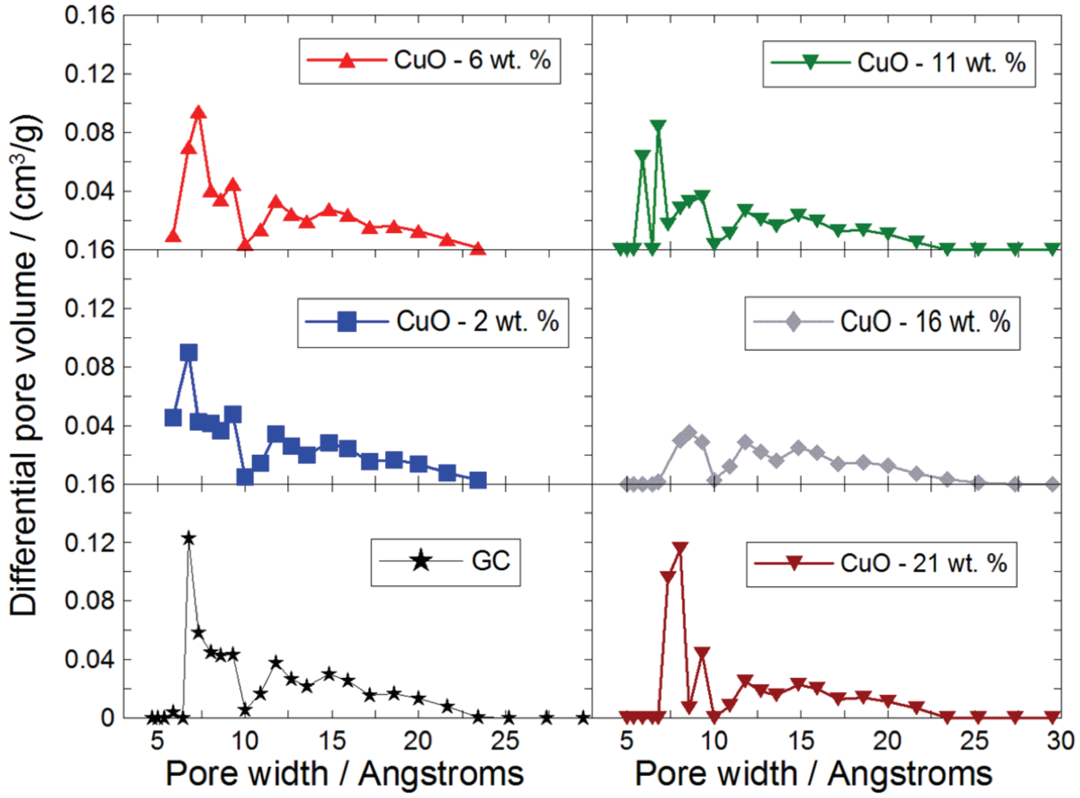

Figure 6.14: Differential pore volume plotted against pore width for the IACs displayed in Figure 6.13. Values for pore widths up to 30 Å are shown. The impregnant loading is indicated in each panel.

Figure 6.14 shows that all of the Cu-based IACs shown here have reasonably similar pore size distributions and appear to retain a relatively high degree of microporosity when compared to the un-impregnated GC sample, even at the highest impregnant loading. This indicates that there was not a significant amount of micropore filling and or pore blockage. Table 6.3 lists the micropore and mesopore volumes for the samples shown in Figure 6.14.

The values listed in Table 6.3 column 2 (micropore volume (cm^3 / g IAC)) show that even at the highest impregnant loading there is less than a 25 % reduction in the micropore volume of the IAC samples relative to the un-impregnated GC. This

Table 6.3: Volume of micropores and mesopores for the IACs shown in Figure 6.14. The pore volumes are given with respect to the mass of IAC and AC.

Impregnant loading (mmol Cu^{2+}/g GC)	micropore volume (cm^3/g IAC)	mesopore volume (cm^3/g IAC)	micropore volume (cm^3/g AC)	mesopore volume (cm^3/g AC)
0 (GC)	n/a	n/a	0.529	0.016
0.2	0.501	0.021	0.511	0.021
0.6	0.484	0.018	0.513	0.019
1.2	0.417	0.010	0.463	0.011
1.8	0.434	0.022	0.503	0.026
2.3	0.412	0.016	0.499	0.020

shows that the majority of micropores are still accessible for gas adsorption. This data also supports the earlier assumption (see number 4 on page 98) that for the IACs in this study there is less than 40% impregnant occupying the micropores. Table 6.3 column 4 (micropore volume (cm^3 / g AC)) shows there is less than a 12 % reduction in micropore volume when the IAC with the highest impregnant loading (2.3 mmol Cu^{2+} / g GC) is compared to the un-impregnated GC sample.

Figure 6.15 shows nitrogen adsorption isotherms collected from Cu-based IACs with approximately constant Cu^{2+} impregnant loading and varying HNO_3 concentration. The impregnant loading was 1.8 ± 0.1 mmol Cu^{2+}/g GC for all the samples except for the IAC co-impregnated with 8 M HNO_3 which had 1.5 ± 0.1 mmol Cu^{2+}/g GC. The concentration of co-impregnated HNO_3 is indicated in the legend for each sample.

Figure 6.15 shows that the volume of N_2 adsorbed decreases slightly with increasing HNO_3 concentration. The IAC with 1.5 mmol Cu^{2+}/g GC and 8 M HNO_3 had slightly higher N_2 adsorption compared to the sample with 1.9 mmol Cu^{2+}/g GC and 4 M HNO_3. This was likely due to the differences in Cu^{2+} impregnant loading between the two samples. Figure 6.15(b) shows that the volume of N_2 adsorbed per gram of AC for the impregnated samples were all within 20 % (or less) of the volume adsobed by the un-impregnated GC sample.

Figure 6.16 shows the differential pore volume plotted against pore width for the IACs displayed in Figure 6.15 as detailed in the figure caption.

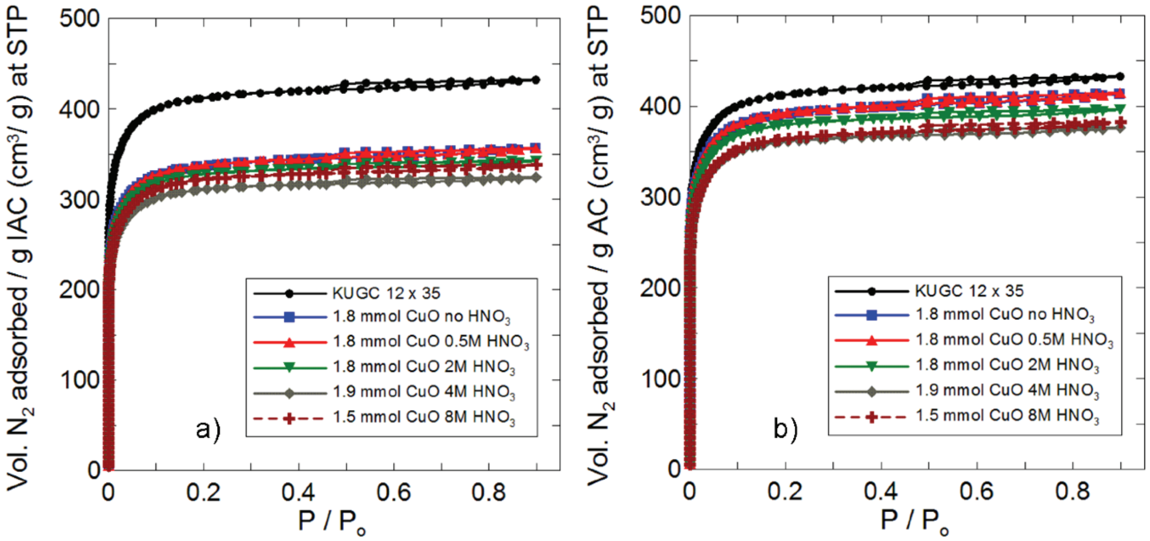

Figure 6.15: Nitrogen adsorption isotherms collected from the Cu-based IACs with approximately constant Cu^{2+} impregnant loading and varying HNO_3 concentration. The Cu^{2+} impregnant loading and concentration of co-impregnated HNO_3 are indicated in the legend. The volume of N_2 adsorbed per gram of IAC and per gram of un-impregnated AC is shown in panels (a) and (b), respectively. Data obtained from the un-impregnated GC has been included for reference.

Figure 6.16 shows that the Cu-based IACs with approximately constant impregnant loading and varying HNO_3 concentration have similar pore size distributions. This implies that the HNO_3 treatment does not dramatically change the micropores. Table 6.4 lists the micropore and mesopore volumes for the IACs shown in Figure 6.16. The data in Figure 6.16 and Table 6.4 shows that the reduction in micropore volume for the IAC samples, relative to un-impregnated GC, is 20 - 25%. When the micropore volume per gram of AC is considered for these samples the reduction in micropore volume, relative to the un-impregnated GC sample, is less than 15 %. This shows that the majority of micropores are still available for gas adsorption.

6.4 Comparison of X-ray Data and N_2 Gas Adsorption Data

6.4.1 Impregnant Loading Study

When fitting the SAXS data it was assumed that the average micropore width of the activated carbon remained constant. Values listed in Table 3.3 show that for GC

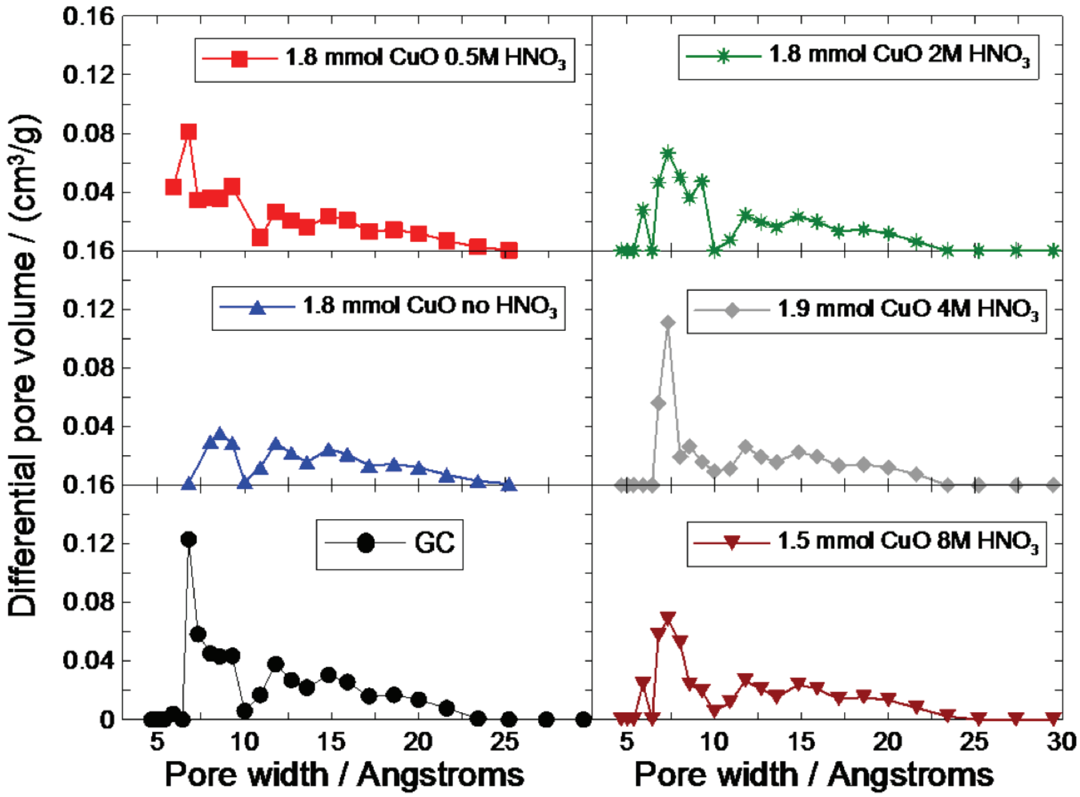

Figure 6.16: Differential pore volume plotted against pore width for the IACs displayed in Figure 6.15. Values for pore widths up to 30 Å are shown. The impregnant loading and concentration of co-impregnated HNO_3 is indicated in the appropriate panel.

the average micropore diameter (d_{SAXS}), determined from SAXS, and the average volume weighted pore width (W_{Vol}) were in good agreement. Using Eq. 3.1 and Eq. 3.2 the average pore widths from the data shown in Figures 6.13 and 6.14 were calculated. Table 6.5 lists the average volume and area weighted pore widths for the Cu-based IACs analyzed in the impregnant loading study. The samples listed were not co-impregnated with HNO_3.

Table 6.5 shows that the IACs have the same average pore width (within error) as the un-impregnated GC sample. This data further demonstrates that micropore filling and or micropore blockage was not significant even at the highest impregnant loadings listed in Table 6.5.

Figure 6.17 shows SAXS and N_2 adsorption data collected from the samples listed in Table 6.5. The data in panel (a) shows the B term from Eq. 6.2 (related to surface

Table 6.4: Micropore and mesopore volumes for the IACs shown in Figure 6.16. The pore volumes are given with respect to the mass of IAC and AC.

Impregnant loading (mmol Cu^{2+}/g GC)	$[HNO_3]$ (M)	micropore volume (cm^3/g IAC)	mesopore volume (cm^3/g IAC)	micropore volume (cm^3/g AC)	mesopore volume (cm^3/g AC)
0 (GC)	0 (GC)	n/a	n/a	0.529	0.016
1.8	0	0.434	0.022	0.503	0.026
1.8	0.5	0.431	0.020	0.500	0.023
1.8	2	0.424	0.011	0.490	0.012
1.9	4	0.391	0.011	0.454	0.013
1.5	8	0.413	0.018	0.466	0.020

Table 6.5: Average pore widths for the Cu-based IACs in the impregnant loading study. The samples listed were not co-impregnated with HNO_3. The volume and area weighted pore widths were calculated using Eq. 3.1 and Eq. 3.2 respectively.

% impregnant loading (wt.)	Impregnant loading (mmol Cu^{2+}/g GC)	W_{Vol} (Å)	W_{Area} (Å)
0 (GC)	0 (GC)	12 ± 1	9.4 ± 0.1
2	0.2	12 ± 1	9.3 ± 0.1
6	0.6	12 ± 1	9.3 ± 0.1
11	1.2	11 ± 1	8.9 ± 0.1
16	1.8	13 ± 2	9.7 ± 0.1
21	2.3	13 ± 2	9.7 ± 0.1

area of micropores and small mesopores) plotted versus impregnant loading. Note that the reported B values were obtained while holding the 'a' term (Debye length for micropores) constant in Eq. 6.2. Panel (b) shows the specific surface areas for the samples listed in Table 6.5. Values calculated using Eq. 2.4 and the differential surface area data are denoted S_{BET} and SSA respectively. The data is plotted against impregnant loading.

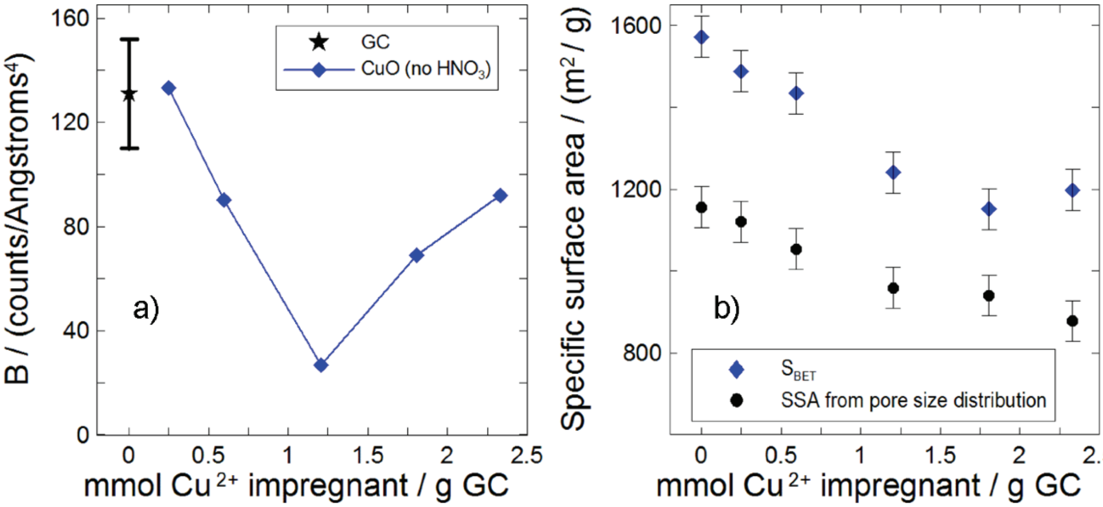

Figure 6.17: SAXS and N_2 gas adsorption data collected from the samples listed in Table 6.5. Panel (a) shows the B term from Eq. 6.2 (which is related to micropore surface area) plotted versus impregnant loading. Panel (b) shows specific surface area values calculated using Eq. 2.4 and the differential surface area data, denoted as S_{BET} and SSA respectively. The data is plotted versus impregnant loading.

Figures 6.17(a) and 6.17(b) show that B, S_{BET} and SSA decrease with increasing impregnant loading up to 1.2 mmol Cu^{2+}/g GC. Above this loading the B term (panel (a)) increases with increasing impregnant loading, the S_{BET} and SSA values plateau or show a minor increase with increasing impregnant loading. Panel (b) shows that the values of S_{BET} are approximately 25 % higher than those calculated for SSA. The reason for this is not known. A possible explanation for the discrepancy may be that S_{BET} is calculated from N_2 adsorption data collected over a restricted range of partial pressures ($P/P_o \leq 0.1$), but SSA is calculated using data from the entire N_2 adsorption isotherm.

Figure 6.18 shows SAXS and N_2 adsorption isotherm data collected from the Cu-based samples (with no co-impregnated HNO_3) in the impregnant loading study as detailed in the figure caption.

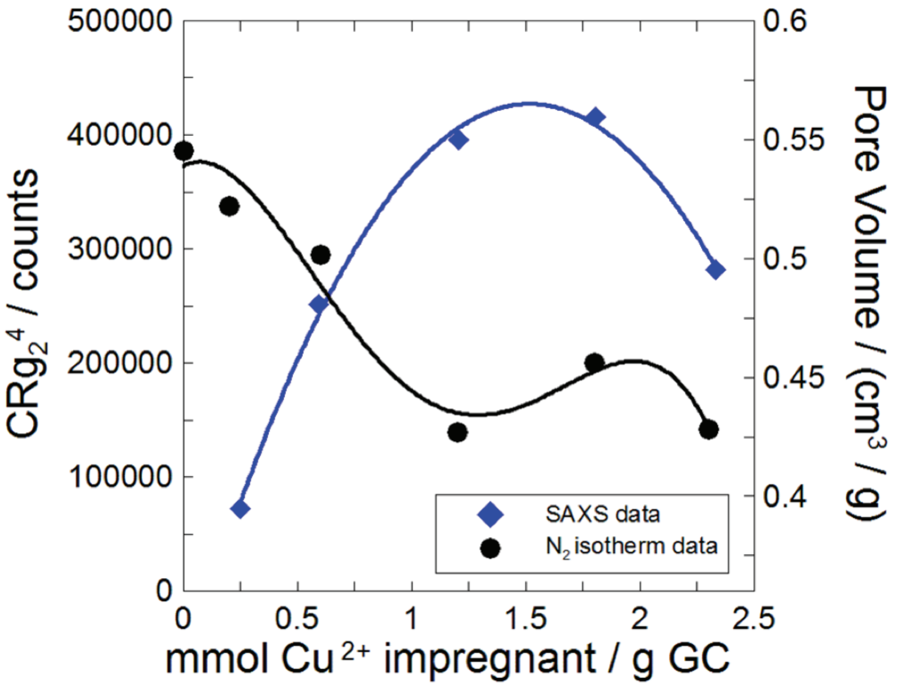

Figure 6.18: SAXS and N_2 adsorption isotherm data collected from the Cu-based samples (with no co-impregnated HNO_3) in the impregnant loading study. The $CR_{g2}{}^4$ term (SAXS data, blue diamonds) is related to the volume of small particle size impregnant occupying small pores in the carbon. The pore volume (N_2 isotherm data, black circles) corresponds to the sum of the differential pore volume data for pore widths up to 16 nm. Both $CR_{g2}{}^4$ and pore volume are plotted versus impregnant loading.

Figure 6.18 shows that $CR_{g2}{}^4$ increases and pore volume decreases with increasing impregnant loading for values up to 1.2 mmol Cu^{2+}/g GC. Above this loading the $CR_{g2}{}^4$ data continues to slowly increase up to an impregnant loading of 1.9 mmol Cu^{2+}/g GC. The SAXS data shows a sharp decrease between samples with impregnant loading of 1.9 and 2.3 mmol Cu^{2+}/g GC. The pore volume data increases between samples with 1.2 and 1.9 mmol Cu^{2+}/g GC and decreases between 1.9 and 2.3 mmol Cu^{2+}/g GC. It is expected that the $CR_{g2}{}^4$ and pore volume terms should be inversely related. For example if $CR_{g2}{}^4$ increases, the pore volume should decrease. The physical meaning of this inverse relation is that if impregnant is occupying a pore, the volume of pore available for gas adsorption would decrease accordingly. There is reasonable agreement in in the trends of the $CR_{g2}{}^4$ and pore volume data with increasing loading for values up to 1.9 mmol Cu^{2+}/g GC.

6.4.2 Effect of Varying HNO_3 Concentration for Samples with Constant Cu^{2+} Impregnant Loading

In this section XRD, SAXS and N_2 adsorption isotherm data will be compared for IACs with approximately constant Cu^{2+} impregnant loading and varying HNO_3 concentration. The impregnant loading was 1.8 ± 0.1 mmol Cu^{2+}/g GC for all of the IACs except the sample co-impregnated with 8 M HNO_3 which had 1.5 ± 0.1 mmol Cu^{2+}/g GC loading. Samples co-impregnated with 0 M, 0.5 M, 2 M, 4 M and 8 M HNO_3 are discussed in this section.

Figure 6.19 shows SAXS and XRD data plotted versus HNO_3 concentration for Cu-based IACs with approximately 1.8 mmol Cu^{2+}/g GC loading as detailed in the figure caption. Figure 6.19 shows there is excellent agreement between the SAXS and XRD data that describes scattering from relatively large particle size impregnant. The data shows that as the concentration of HNO_3 in the impregnating solution increases, the scattering intensity from large size Cu^{2+} impregnant decreases. This is indicative of the HNO_3 treatment reducing Cu^{2+} impregnant particle size and improving impregnant dispersion.

Figure 6.20 shows SAXS and specific surface area data collected from the Cu-based IACs with approximately constant Cu^{2+} impregnant loading and varying HNO_3 concentration. The data in panel (a) shows the B term from Eq. 6.2 (related to surface area of micropores and small mesopores) plotted versus HNO_3 concentration. Note that the reported B values were obtained while holding the 'a' term (Debye length for micropores) constant in Eq. 6.2. Panel (b) shows the specific surface areas for the IACs in this study. Values calculated using Eq. 2.4 and the differential surface area data are denoted S_{BET} and SSA respectively. The data is plotted against HNO_3 concentration.

Figure 6.20 shows that there is good agreement in the trends of the B (panel (a)), S_{BET} and SSA (panel (b)) data with increasing HNO_3 concentration. A possible explanation for the discrepancy between the S_{BET} data and SSA data was given earlier. The data in Figure 6.20 shows that the surface area of the IAC samples

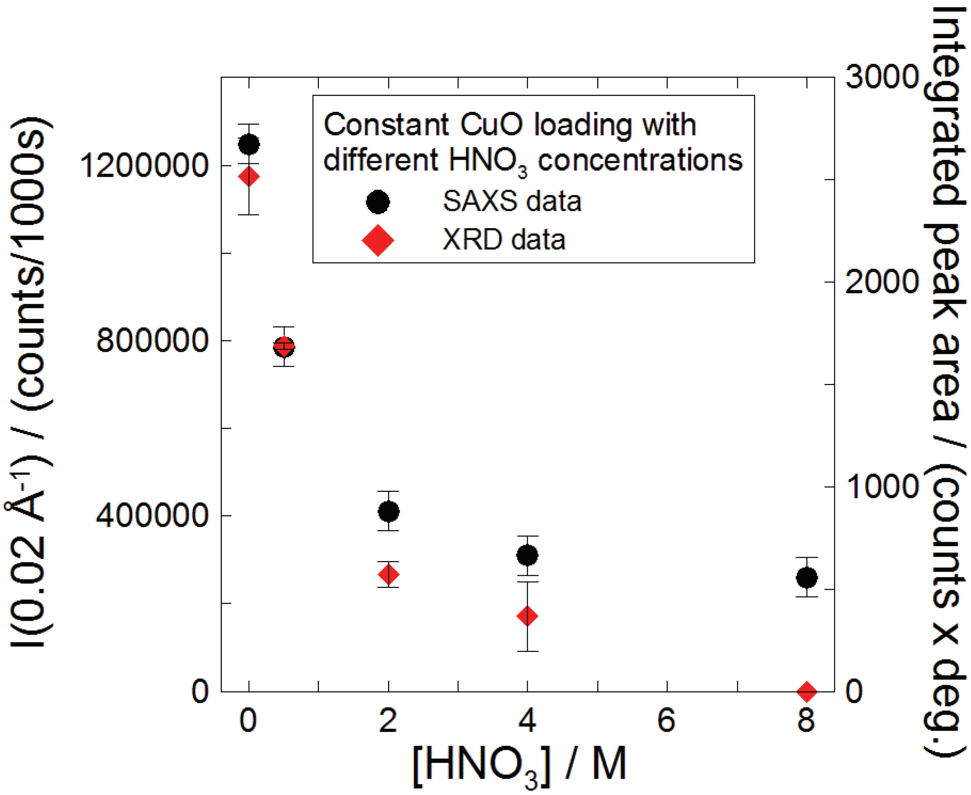

Figure 6.19: SAXS and XRD data plotted versus HNO_3 concentration for Cu-based IACs with approximately 1.8 mmol Cu^{2+}/g GC loading. The intensity at q = 0.02 $Å^{-1}$ (SAXS data, black circles) and integrated peak area (XRD data, red diamonds) values were selected from the data shown in Figures 6.8(a) and 6.8(b) respectively.

decreases with respect to the un-impregnated GC sample due to the presence of the Cu^{2+} impregnant. The surface area of the IAC samples stays relatively constant with increasing HNO_3 concentration. This implies the HNO_3 treatment does not significantly change the surface area of the activated carbon substrate.

Figure 6.21 shows SAXS and N_2 adsorption isotherm data collected from the Cu-based samples with approximately 1.8 ± 0.1 mmol Cu^{2+}/g GC loading and varying HNO_3 concentration as detailed in the figure caption.

Figure 6.21 shows that there is good agreement between the trends in the $CR_{g2}{}^4$ and pore volume data with increasing HNO_3 concentration. As the HNO_3 concentration increases, the $CR_{g2}{}^4$ term increases and the pore volume term decreases. This indicates that as the HNO_3 concentration is increased, more small particle size impregnant is occupying the small pores ($\leq$ 16nm) in the activated carbon. This is

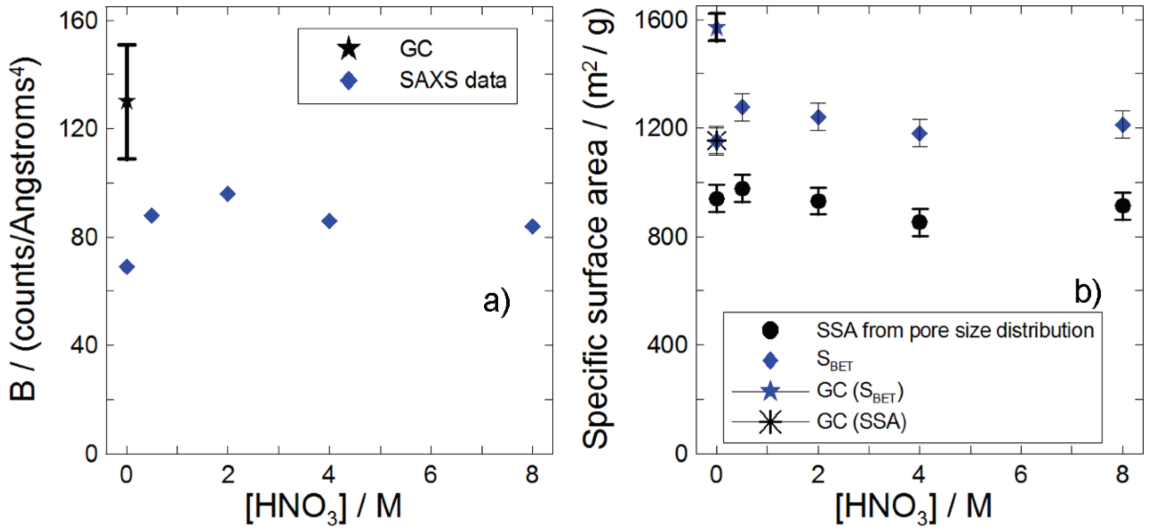

Figure 6.20: SAXS and N_2 gas adsorption data collected from the samples with approximately 1.8 mmol Cu^{2+}/g GC impregnant loading and varying HNO_3 concentration. Panel (a) shows the B term (from Eq. 6.2) and panel (b) shows S_{BET} and SSA specific surface area values. The data is plotted versus HNO_3 concentration in both panels.

indicative of improved impregnant dispersion with increasing HNO_3 concentration. The data points corresponding to the IAC prepared with 8 M HNO_3 do not agree with the trend of the other data. This is most likely due to the lower Cu^{2+} impregnant loading of this IAC relative to the other samples. It is worth recalling that the data in Table 6.4 shows that even at the highest impregnant loading there is only a $\approx 25\%$ decrease in pore volume relative to the un-impregnated GC sample. This implies that the majority of pores are still accessible for gas adsorption. The importance of good impregnant distribution and co-impregnation with HNO_3 will be discussed in terms of multi-gas adsorption capacity below.

6.5 Flow Test Results

6.5.1 Impregnant Loading Study Results

Figure 6.22 shows dry SO_2 and NH_3 breakthrough times obtained from flow testing IACs prepared from aqueous $Cu(NO_3)_2$ and $Cu(NO_3)_2$/4 M HNO_3 solutions.

Figure 6.22(a) shows that the Cu-based samples that were co-impregnated with

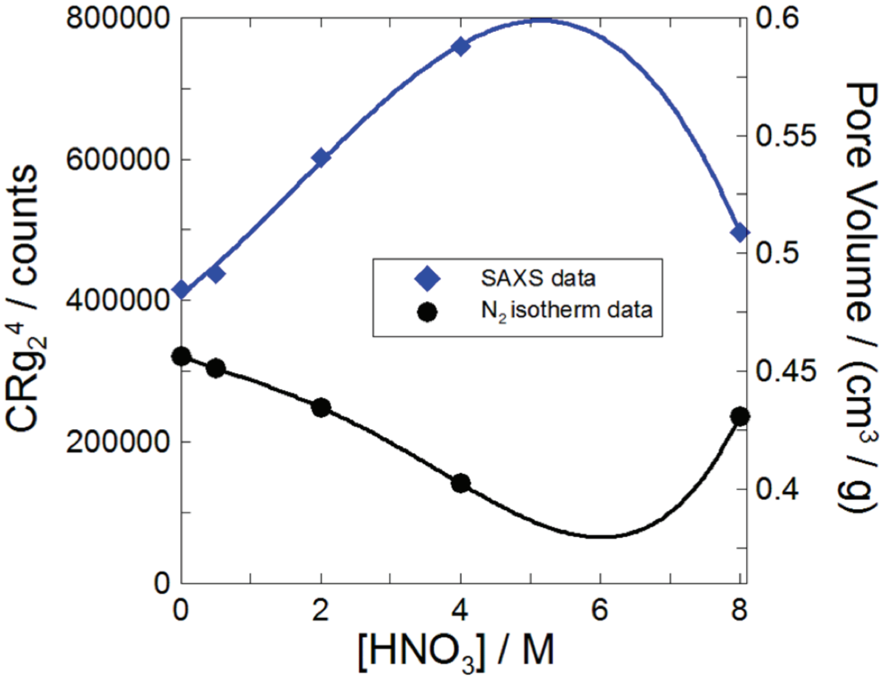

Figure 6.21: SAXS and N_2 adsorption isotherm data data collected from the Cu-based samples with approximately 1.8 ± 0.1 mmol Cu^{2+}/g GC loading and varying HNO_3 concentration. The $CR_{g2}{}^4$ term (SAXS data, blue diamonds) is related to the volume of small particle size impregnant occupying small pores in the carbon. The pore volume (N_2 isotherm data, black circles) corresponds to the sum of the differential pore volume data for pore widths up to 16 nm. Both $CR_{g2}{}^4$ and pore volume are plotted versus HNO_3 concentration.

4 M HNO_3 had longer dry SO_2 breakthrough times, relative to samples prepared with no co-impregnated HNO_3, for all impregnant loadings. Figures 6.6 and 6.7 show that co-impregnation with HNO_3 reduces the impregnant particle size and improves impregnant dispersion and this apparently results in improved dry SO_2 adsorption capacity. Figure 6.22 shows that all of the Cu-based IACs had longer dry SO_2 breakthrough times than the GC sample and IACs with $\geq$ 1.2 mmol Cu^{2+}/g GC had longer breakthrough times than the URC sample.

Figure 6.22(b) shows that Cu-based IACs co-impregnated with 4 M HNO_3 had much longer dry NH_3 breakthrough times compared to samples prepared with no HNO_3. Comparing the trend of the data obtained from IACs co-impregnated with 4 M HNO_3 to those prepared without HNO_3 shows there may be different reaction mechanisms responsible for the removal of the NH_3 gas. The Cu-based samples

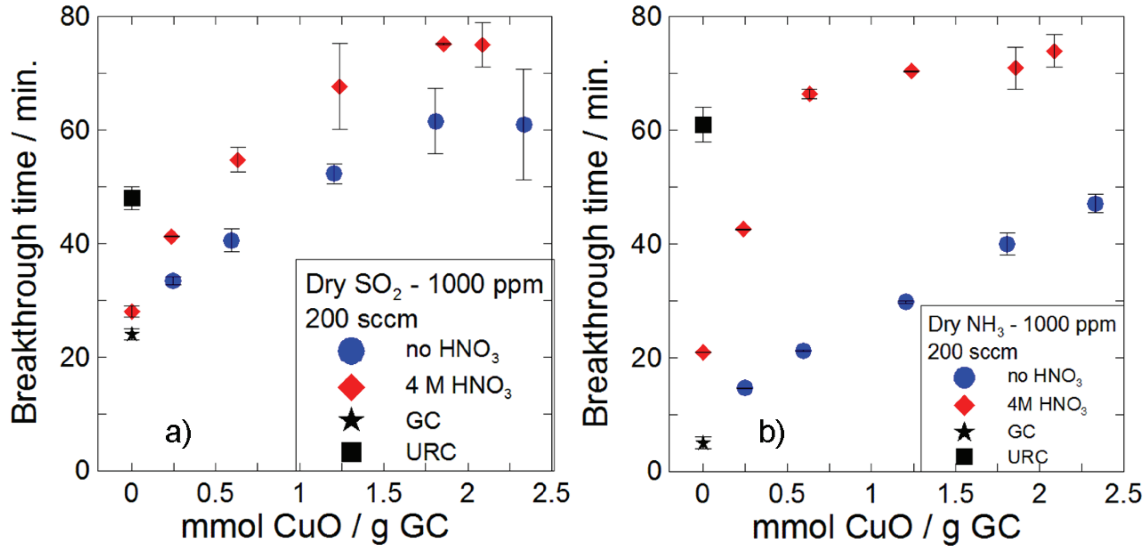

Figure 6.22: Breakthrough times for IACs prepared from $Cu(NO_3)_2$ and $Cu(NO_3)_2$/4 M HNO_3. The samples were heated at $T_f = 180°C$ prior to flow testing. Dry SO_2 data and dry NH_3 data are shown in panels (a) and (b) respectively. The breakthrough times are plotted versus impregnant loading. Results obtained from GC and URC samples are indicated for reference.

prepared without HNO_3 show linearly increasing NH_3 breakthrough times with increasing impregnant loading. This is indicative of chemisorption being responsible for NH_3 removal. The data obtained from the Cu-based IACs co-impregnated with 4 M HNO_3 shows a sharp increase in NH_3 breakthrough times for loadings up to 0.6 mmol Cu^{2+}/g GC followed by a more gradual increase in NH_3 capacity with increasing impregnant loading. The data in Figure 6.1 shows that Cu-based samples with ≤ 0.6 mmol Cu^{2+}/g GC that were co-impregnated with 4 M HNO_3 had higher impregnant loadings than samples prepared with less concentrated HNO_3, possibly due to the introduction of more oxygen rich surface groups. The presence of additional acidic surface groups could help explain the dramatic increase in dry NH_3 breakthrough times at low impregnant loadings. Figure 6.22(b) shows that all of the Cu-based IACs have longer NH_3 breakthrough times than the GC sample. Panel (b) also shows that Cu-based IACs co-impregnated with 4 M HNO_3 with impregnant loading $\geq$ 0.6 mmol Cu^{2+}/g GC had longer NH_3 breakthrough times than the commercially available URC sample.

Figure 6.23 shows dry HCN breakthrough times and SAXS data ($CR_{g2}{}^4$ term) versus Cu^{2+} impregnant loading in panels (a) and (b) respectively as detailed in the figure caption.

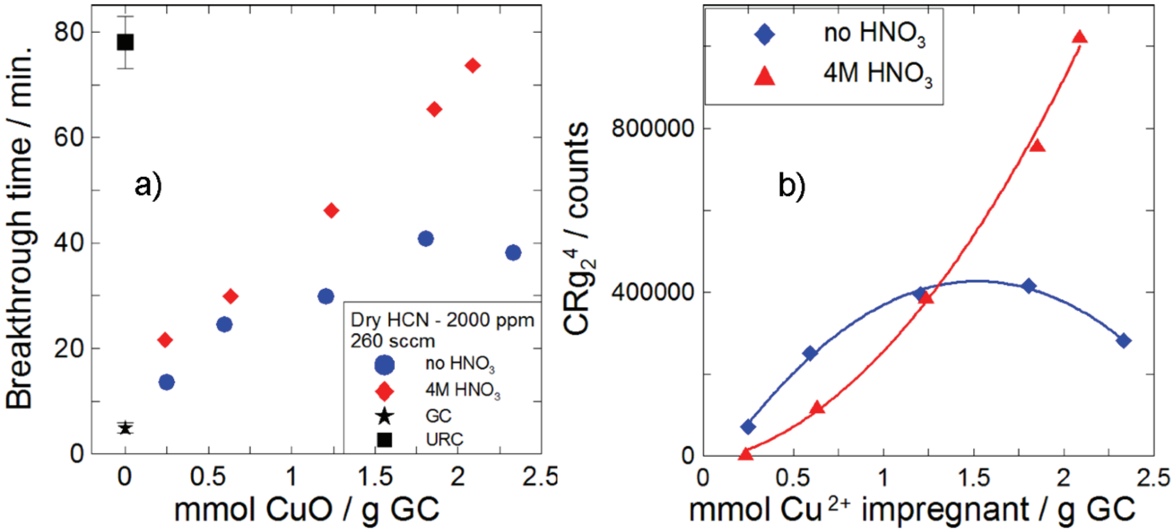

Figure 6.23: Dry HCN breakthrough times and SAXS data ($CR_{g2}{}^4$ term) are shown in panels (a) and (b) respectively. Data obtained from Cu-based samples with no HNO_3 and 4 M co-impregnated HNO_3 is shown. The data is plotted against Cu^{2+} impregnant loading. Flow test results obtained from GC and URC are shown in panel (a) for reference.

Figure 6.23(a) shows that Cu-based IACs have longer dry HCN breakthrough times than samples with no co-impregnated HNO_3 at all impregnant loadings shown. The IACs that were co-impregnated with 4 M HNO_3 have breakthrough times that increase linearly with increasing Cu^{2+} impregnant loading. Cu-based samples prepared with no HNO_3 have a relatively large increase in dry HCN breakthrough times with increased impregnant loading for values up to 0.6 mmol Cu^{2+}/g GC. Above this loading the dry HCN capacity shows a more gradual increase with increasing impregnant loading that plateaus for IACs with 1.8 and 2.3 mmol Cu^{2+}/g GC. Figure 6.23(b) shows that the volume of small particle size impregnant ($CR_{g2}{}^4$ term) increases with increasing impregnant loading for IACs co-impregnated with 4 M HNO_3. The trend of the $CR_{g2}{}^4$ term with increasing impregnant loading, for Cu-based samples prepared with no co-impregnated HNO_3, is similar in shape to an inverted parabola. The trend of the data in panel (b) indicates that IACs co-impregnated with 4 M HNO_3 have a higher volume of small particle size impregnant compared to IACs with no co-impregnated HNO_3. The data in panels (a) and (b) have similar trends with increasing impregnant loading. The SAXS data in panel (b) shows co-impregnating the Cu-based IACs with 4 M HNO_3 improves impregnant dispersion and this results in better HCN adsorption. The data in panel (a) shows that the IAC with 2.1 ± 0.1 mmol Cu^{2+}/g GC impregnant loading that was co-impregnated with 4 M HNO_3 has dry HCN capacity that is equivalent to URC. Based on earlier studies [23] and the preferred patent recipe [13] the impregnant loading for URC is approximately 2.3 mmol Cu^{2+}/g AC.

Figure 6.24 shows C_6H_{12} breakthrough times obtained from Cu-based IACs with no HNO_3 and 4 M co-impregnated HNO_3 as detailed in the figure caption.

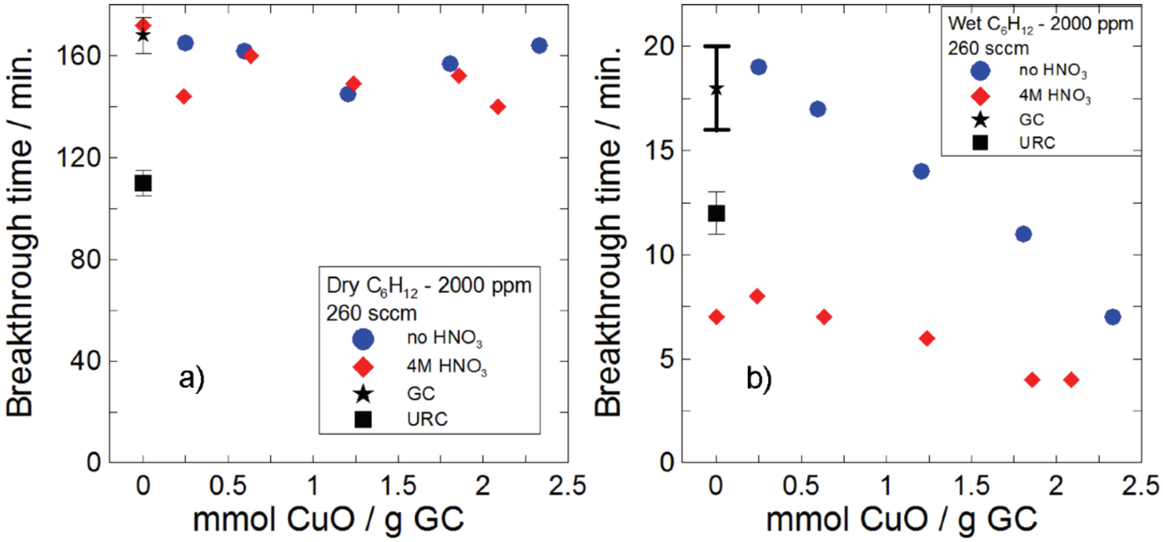

Figure 6.24: C_6H_{12} breakthrough times versus impregnant loading for Cu-based IACs with no HNO_3 and 4 M co-impregnated HNO_3 under dry and humid conditions are shown in panels (a) and (b) respectively. Flow test results obtained from GC and URC are included for reference.

Figure 6.24(a) shows that the Cu-based IACs have similar dry C_6H_{12} breakthrough times compared to un-impregnated GC. The dry C_6H_{12} capacity stays reasonably constant with increasing impregnant loading. The samples co-impregnated with 4 M HNO_3 have slightly lower C_6H_{12} capacity compared to IACs with no HNO_3. This shows that co-impregnation with 4 M HNO_3 does not significantly reduce dry C_6H_{12} capacity. The SAXS and N_2 adsorption data, shown in Figure 6.6 and Table 6.3 respectively, shows that even at the highest impregnant loadings used in this work the majority of micropores were not filled with impregnant and were available for physical gas adsorption. All of the Cu-based IACs had longer dry C_6H_{12} breakthrough times than the URC sample.

Figure 6.24(b) shows that all samples in this study have much shorter C_6H_{12} breakthrough times under humid conditions compared to dry conditions. This was discussed in Chapter 5. The Cu-based IACs show decreasing humid C_6H_{12} breakthrough times with increasing impregnant loading. The IACs that were co-impregnated with 4 M HNO_3 have much lower humid C_6H_{12} capacity compared to samples with no HNO_3 at all impregnant loadings. All of the Cu-based IACs with ≥ 0.6 mmol Cu^{2+} had shorter humid C_6H_{12} breakthrough times than GC. Cu-based IACs with no co-impregnated HNO_3 had wet C_6H_{12} breakthrough times equal to or greater than URC for samples with ≤ 1.8 mmol Cu^{2+}/g GC impregnant loading. The data in panel (b) shows that for IACs co-impregnated with 4 M HNO_3, decreasing the impregnant loading will not result in significant improvements in humid C_6H_{12} capacity.

6.5.2 Effect of Varying HNO_3 Concentration for IACs with Constant Cu^{2+} Impregnant Loading

Figure 6.25 shows dry HCN breakthrough times versus HNO_3 concentration for IACs with 1.8 ± 0.1 mmol Cu^{2+}/g GC impregnant loading as detailed in the figure caption. Figure 6.25 shows that dry HCN breakthrough times increase with increasing HNO_3 concentration for IACs with 1.8 ± 0.1 mmol Cu^{2+}/g GC impregnant loading. The data in Figures 6.6 and 6.7 shows that increasing HNO_3 concentration improves impregnant distribution and this explains the increase in dry HCN breakthrough times with increasing HNO_3 concentration. The sample co-impregnated with 8 M HNO_3 had lower (1.5 mmol Cu^{2+}/g GC) impregnant loading and this may explain why it does not follow the trend of the data. All of the Cu-based IACs shown in Figure 6.25 have shorter dry HCN breakthrough times than URC and longer breakthrough times than GC.

Figure 6.26 shows C_6H_{12} breakthrough times obtained from IACs with 1.8 ± 0.1 mmol Cu^{2+}/g GC impregnant loading versus HNO_3 concentration as detailed in the figure caption. Figure 6.26(a) shows that the dry C_6H_{12} breakthrough times remain

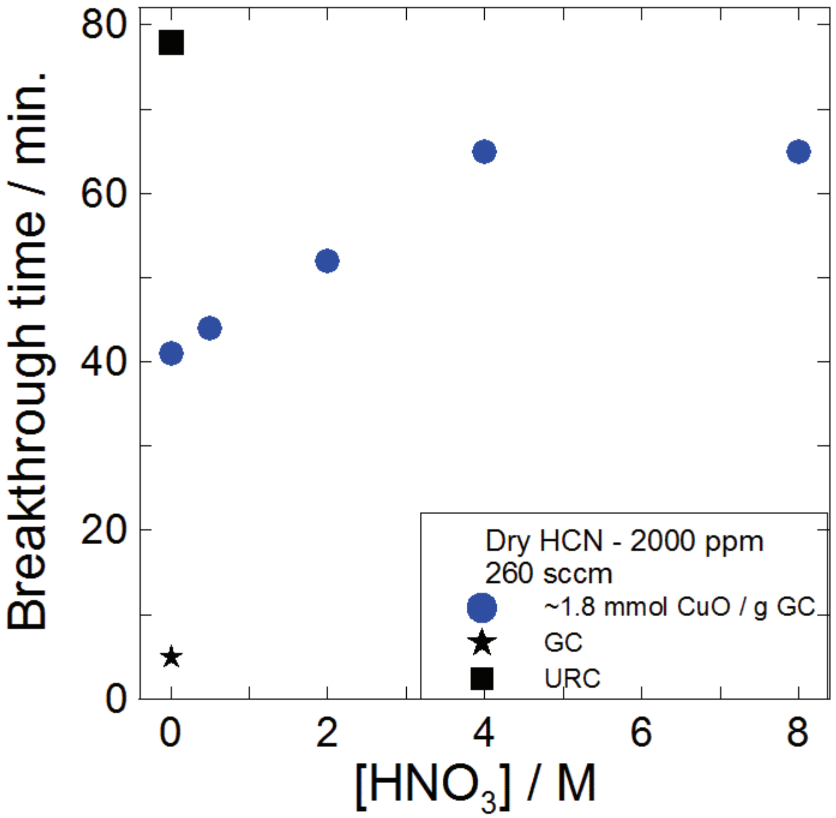

Figure 6.25: Dry HCN breakthrough times plotted against HNO_3 concentration for IACs with 1.8 ± 0.1 mmol Cu^{2+}/g GC impregnant loading. The sample co-impregnated with 8 $MHNO_3$ had 1.5 ± 0.1 mmol Cu^{2+}/g GC. For reference flow test results obtained from GC and URC have been included.

reasonably constant for the Cu-based IACs with increasing HNO_3 concentration. This shows that the HNO_3 treatment does not effect dry C_6H_{12} capacity. All of the Cu-based IACs in panel (a) had longer breakthrough times than URC and slightly shorter breakthrough times than GC. Figure 6.26(b) shows that humid C_6H_{12} breakthrough times decrease with increasing HNO_3 concentration for the Cu-based IACs in this study. Figure 5.7 shows that samples with more aggressive HNO_3 treatments require more thermal energy to desorb water. In order for C_6H_{12} to be physically adsorbed, under humid conditions, water must be desorbed. It appears more concentrated HNO_3 treatments result in stronger retention of water and therefore lower humid C_6H_{12} adsorption. All of the Cu-based IACs in panel (b) have shorter humid C_6H_{12} breakthrough times compared to URC and GC.

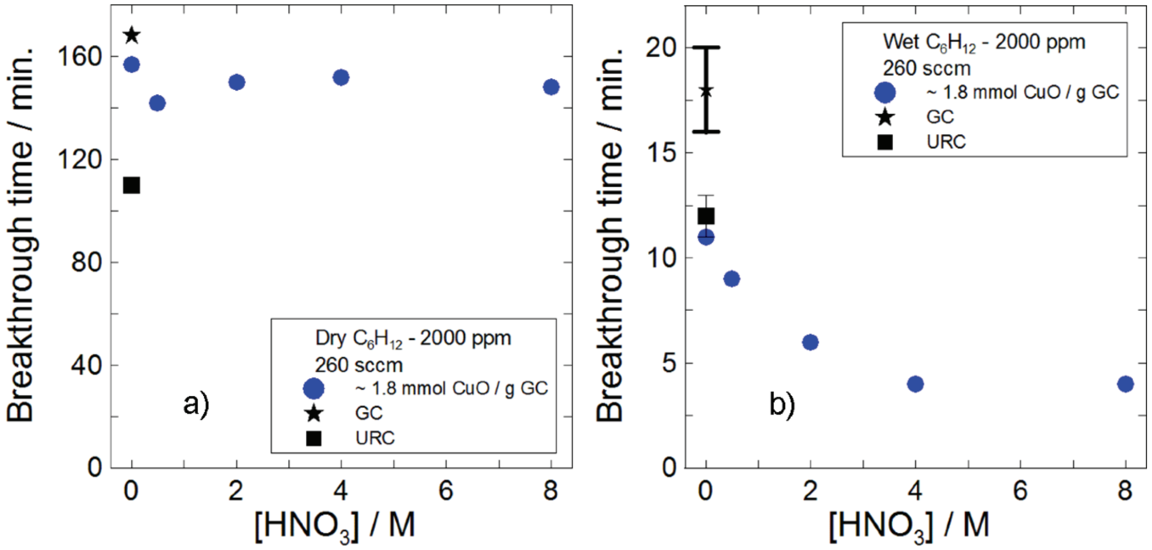

Figure 6.26: C_6H_{12} breakthrough times obtained from IACs with 1.8 ± 0.1 mmol Cu^{2+}/g GC impregnant loading and varying HNO_3 concentration. The sample co-impregnated with 8 M HNO_3 had 1.5 ± 0.1 mmol Cu^{2+}/g GC. The data is plotted against HNO_3 concentration. Dry and humid C_6H_{12} breakthrough times are shown in panels (a) and (b) respectively. For reference flow test results obtained from GC and URC have been indicated.

6.6 Conclusions

SAXS and XRD measurements were found to be useful tools for studying impregnant dispersion on AC. Good agreement between the SAXS and XRD methods was observed. It was found that the SAXS method provides useful information about the relatively small size impregnant ($\leq$ 30 Å) on the AC substrate. Good agreement between the SAXS data and data from N_2 gas adsorption isotherms was observed. The XRD method could not provide information on such small nanocrystallites.

Co-impregnating the AC substrate with $\geq$ 4 M HNO_3, followed by heating at T_f = 180°C resulted in relatively small, well dispersed CuO impregnant. At loadings $\geq$ 1.5 mmol CuO/g GC, the impregnant surface coverage in the small mesopores plateaued or decreased for IACs co-impregnated with $HNO_3 \leq 2$ M, but increased for samples co-impregnated with $HNO_3 \geq 4$ M. Contact angle measurements demonstrated that as HNO_3 concentration increased, the contact angle decreased, implying better surface coverage for $Cu(NO_3)_2$ co-impregnated with more concentrated HNO_3.

Results obtained from the heating temperature study showed that IACs prepared from 2.4 M $Zn(NO_3)_2$/4 M HNO_3 remained better dispersed than samples prepared from 2.4 M $Cu(NO_3)_2$/4 M HNO_3 at heating temperatures $\geq$ 250°C. The SAXS data obtained from the Cu-based IACs showed that heating temperature had an effect on the size of the impregnant in the meso and macro pores. SAXS and XRD data showed that heating the Cu-based samples $\geq$ 250°C resulted in large size, predominantly Cu_2O impregnant.

Good agreement between SAXS and N_2 adsorption isotherm data was observed in Cu^{2+} impregnant loading studies and in studies with constant Cu^{2+} impregnant loading with varying HNO_3 concentration. The SAXS and N_2 adsorption data showed that even at high impregnant loading and high HNO_3 concentration, the majority of the small mesopores and micropores were not filled with impregnant and were available for gas adsorption. The SAXS, XRD and N_2 adsorption data showed that increasing HNO_3 concentration resulted in well dispersed CuO impregnant and this resulted in improved dry SO_2, NH_3 and HCN adsorption capacity. Increased Cu^{2+} impregnant loading and increased HNO_3 concentration resulted in lower humid C_6H_{12} adsorption capacity but did not significantly effect dry C_6H_{12} adsorption.

Chapter 7

The Effect of Co-impregnation with Mixed Metal Nitrate Precursors and Phosphomolybdic Acid on Broad Spectrum Respirator Carbons

In this chapter a comparative study of IACs prepared from aqueous solutions containing $Cu(NO_3)_2$ and different metal nitrate precursors is presented. Some of the samples were also co-impregnated with HNO_3 and $H_3PO_4\bullet 12MoO_3$. In the first section the effect of co-impregnating IACs prepared from aqueous $Cu(NO_3)_2$ and other metal nitrate precursors is discussed. The motivation for this study was to see if overall multi-gas adsorption could be maintained or improved by substituting $Cu(NO_3)_2$ for different (in most cases less expensive) metal nitrate precursors.

In the second section a comparative study of IACs prepared from aqueous $Cu(NO_3)_2$ and $Mn(NO_3)_2$ or $Zn(NO_3)_2$ and $Mn(NO_3)_2$ solutions of varying concentration is presented. The IACs in this study were heated at $T_f = 200°C$. The motivation for this study was to better understand if, or how, the impregnants interacted during heating. HNO_3 was not used as a co-impregnant to allow better observation of the impregnant species present after heating using XRD analysis.

In the final section a comparative study of IACs prepared from aqueous solutions containing $Cu(NO_3)_2$, $Zn(NO_3)_2$, HNO_3 and $H_3PO_4\bullet 12MoO_3$ is presented. As the concentration of $Cu(NO_3)_2$ and $H_3PO_4\bullet 12MoO_3$ in the impregnating solution was decreased, the concentration of $Zn(NO_3)_2$ was increased. All samples prepared in this study had 1.7 ± 0.1 mmol of Cu^{2+} and Zn^{2+} (present as CuO and ZnO after heating) impregnant per gram of GC carbon. The motivation for this study was to see if the amount of relatively expensive Mo^{6+} impregnant could be reduced, without losing overall multi-gas adsorption capacity.

7.1 Chemicals Used

The chemicals used to prepare the impregnating solutions were copper nitrate hemipentahydrate ($Cu(NO_3)_2 \bullet 2.5H_2O$) and 12-Molybdophosphoric acid hydrate ($H_3PO_4 \bullet 12MoO_3 \bullet xH_2O$) (both obtained from Alfa Aesar, reagent grade), zinc nitrate hexahydrate ($Zn(NO_3)_2 \bullet 6H_2O$), manganese nitrate hydrate ($Mn(NO_3)_2 \bullet xH_2O$), aluminium nitrate nonahydrate ($Al(NO_3)_3 \bullet 9H_2O$) (all obtained from Sigma-Aldrich reagent grade), iron (III) nitrate nonahydrate ($Fe(NO_3)_3 \bullet 9H_2O$, Anachemia, A.C.S. grade) and 70% concentrated nitric acid (HNO_3). The solutions were prepared by dissolving the selected compounds in deionized water. Solutions prepared with $Mn(NO_3)_2 \bullet xH_2O$ used deaerated, deionized water. Values of $x = 4$ for $Mn(NO_3)_2 \bullet xH_2O$ and $x = 27$ $H_3PO_4 \bullet 12MoO_3 \bullet xH_2O$ were determined from TGA experiments.

7.2 The Effect of Co-impregnating Cu-based IACs with Different Metal Nitrate Precursors and $H_3PO_4 \bullet 12MoO_3$

7.2.1 Sample Preparation

IAC samples were prepared by impregnating GC activated carbon. GC was previously described in section 3.1. The GC substrate was impregnated using the imbibing method. The IAC samples were prepared in either one or two heating and imbibing steps, depending on the solubility of the mixture. Table 7.1 lists the sample names and the contents of each imbibing solution used to prepare IACs in this work.

All of the IACs prepared in this study were heated under argon flowing at approximately 60 mL/min. Prior to heating the furnace was purged for at least $\frac{1}{2}$ hour. The samples were heated to $T_f = 200°C$. Typically the IACs were held at T_f for approximately 0.2 hours per gram of sample (e.g. a 15 g sample would be held at T_f for approximately 3 hours). The samples that required 2 imbibing steps also required 2 heating steps. After the first imbibe the samples were heated (under argon) at 115°C for approximately 2 hours, then allowed to cool to room temperature prior to the second imbibe.

The overall weight percent impregnant loading was determined by gravimetric analysis according to Eq. 2.1. Commercially available URC samples were used for

Table 7.1: Contents of each imbibing solution used to prepare IACs in this work.

Sample name	Imbibe 1	Imbibe 2
Cu/HNO_3	11.3 mL of 2.4 M $Cu(NO_3)_2$ / 4 M HNO_3 per 15 g GC	
Cu/HNO_3/PMA	8 mL of 2.4 M $Cu(NO_3)_3$ / 4 M HNO_3 / 0.035 M $H_3PO_4\bullet 12MoO_3$ per 10 g GC	
Zn/HNO_3	11.3 mL of 2.4 M $Zn(NO_3)_2$ / 4 M HNO_3 / per 15 g GC	
Zn/HNO_3/PMA	7.5 mL of 1.2 M $Zn(NO_3)_2$ / 2 M HNO_3 / 0.018 M $H_3PO_4\bullet 12MoO_3$ per 10 g GC	7.0 mL of 1.2 M $Zn(NO_3)_2$ / 2 M HNO_3 / 0.018 M $H_3PO_4\bullet 12MoO_3$ per 10 g GC
Zn/Cu/HNO_3/PMA	7.5 mL of 0.6 M $Zn(NO_3)_2$ / 0.6 M $Cu(NO_3)_2$ / 2 M HNO_3 / 0.018 M $H_3PO_4\bullet 12MoO_3$ per 10 g GC	7.0 mL of 0.6 M $Zn(NO_3)_2$ / 0.6 M $Cu(NO_3)_2$ / 2 M HNO_3 / 0.018 M $H_3PO_4\bullet 12MoO_3$ per 10 g GC
Fe/HNO_3	7.0 mL of 1.3 M $Fe(NO_3)_3$ / 2 M HNO_3 per 10 g GC	7.0 mL of 1.3 M $Fe(NO_3)_3$ / 2 M HNO_3 per 10 g GC
Fe/HNO_3/PMA	7.5 mL of 1.3 M $Fe(NO_3)_3$ / 2 M HNO_3 / 0.018 M $H_3PO_4\bullet 12MoO_3$ per 10 g GC	7.0 mL of 1.3 M $Fe(NO_3)_3$ / 2 M HNO_3 / 0.018 M $H_3PO_4\bullet 12MoO_3$ per 10 g GC
Fe/Cu/HNO_3/PMA	7.5 mL of 0.6 M $Fe(NO_3)_3$ / 0.6 M $Cu(NO_3)_2$ / 2 M HNO_3 / 0.018 M $H_3PO_4\bullet 12MoO_3$ per 10 g GC	7.0 mL of 0.6 M $Fe(NO_3)_3$ / 0.6 M $Cu(NO_3)_2$ / 2 M HNO_3 / 0.018 M $H_3PO_4\bullet 12MoO_3$ per 10 g GC
Mn/Cu	12 mL of 1.2 M $Cu(NO_3)_2$ / 1.2 M $Mn(NO_3)_2$ per 15 g GC	
Mn/Cu/PMA	11.3 mL of 0.6 M $Cu(NO_3)_2$ / 0.6 M $Mn(NO_3)_2$ / 0.018 M $H_3PO_4\bullet 12MoO_3$ per 15 g GC	11.3 mL of 0.6 M $Cu(NO_3)_2$ / 0.6 M $Mn(NO_3)_2$ / 0.018 M $H_3PO_4\bullet 12MoO_3$ per 15 g GC
Mn/Cu/HNO_3/PMA	11.3 mL of 0.6 M $Cu(NO_3)_2$ / 0.6 M $Mn(NO_3)_2$ / 4 M HNO_3 / 0.018 M $H_3PO_4\bullet 12MoO_3$ per 15 g GC	11.3 mL of 0.6 M $Cu(NO_3)_2$ / 0.6 M $Mn(NO_3)_2$ / 4 M HNO_3 / 0.018 M $H_3PO_4\bullet 12MoO_3$ per 15 g GC
Al/HNO_3	11 mL 0f 1.3 M $Al(NO_3)_3$ / 2 M HNO_3 per 15 g GC	10 mL 0f 1.3 M $Al(NO_3)_3$ / 2 M HNO_3 per 15 g GC
Al/HNO_3/PMA	11 mL 0f 1.3 M $Al(NO_3)_3$ / 2 M HNO_3 / 0.018 M $H_3PO_4\bullet 12MoO_3$ per 15 g GC	10 mL 0f 1.3 M $Al(NO_3)_3$ / 2 M HNO_3 / 0.018 M $H_3PO_4\bullet 12MoO_3$ per 15 g GC
Al/Cu/HNO_3/PMA	11 mL 0f 0.6 M $Al(NO_3)_3$ / 0.6 M $Cu(NO_3)_2$ / 2 M HNO_3 / 0.018 M $H_3PO_4\bullet 12MoO_3$ per 15 g GC	11 mL 0f 0.6 M $Al(NO_3)_3$ / 0.6 M $Cu(NO_3)_2$ / 2 M HNO_3 / 0.018 M $H_3PO_4\bullet 12MoO_3$ per 15 g GC

comparative purposes. Flow test results obtained from the URC samples will be denoted 'URC'. Prior to flow testing the GC and URC samples were pre-dried at 120°C in air to lower their moisture content to $< 5\%$ (wt.).

7.2.2 Impregnant Loading

Figure 7.1 shows the observed and predicted % impregnant loading for the IACs prepared from the impregnating solutions detailed in Table 7.1. The predicted % loading was calculated using the following assumptions:

1. The heating temperature was sufficient to promote full conversion of the precursor to the metal oxide phase.
2. The different components in the impregnating solution do not interact during heating.
3. The $H_3PO_4 \bullet 12MoO_3$ impregnant does not thermally decompose.
4. Mass gain to due the introduction of oxygen rich surface groups by the HNO_3 treatment is not accounted for.
5. Mass loss due to the evolution of CO or CO_2 gas is not accounted for.

Figure 7.1 shows that there is good agreement between the observed and predicted % impregnant loading for the IACs in this study. In most cases there is $\leq 3\%$ difference between the observed and predicted values. The Zn/HNO_3/PMA, Fe/HNO_3/PMA and Fe/Cu/HNO_3/PMA IACs had 5-6 % difference. The reasons for this larger discrepency have not been determined. The gravimetric data in Figure 7.1 indicates that the metal nitrate precursors converted primarally to metal oxide impregnants.

7.2.3 XRD Characterization

Figure 7.2 shows XRD data obtained from the Zn/HNO_3, Zn/HNO_3/PMA, Zn/Cu/HNO_3/PMA, Al/HNO_3 and Al/Cu/HNO_3/PMA samples. XRD data from

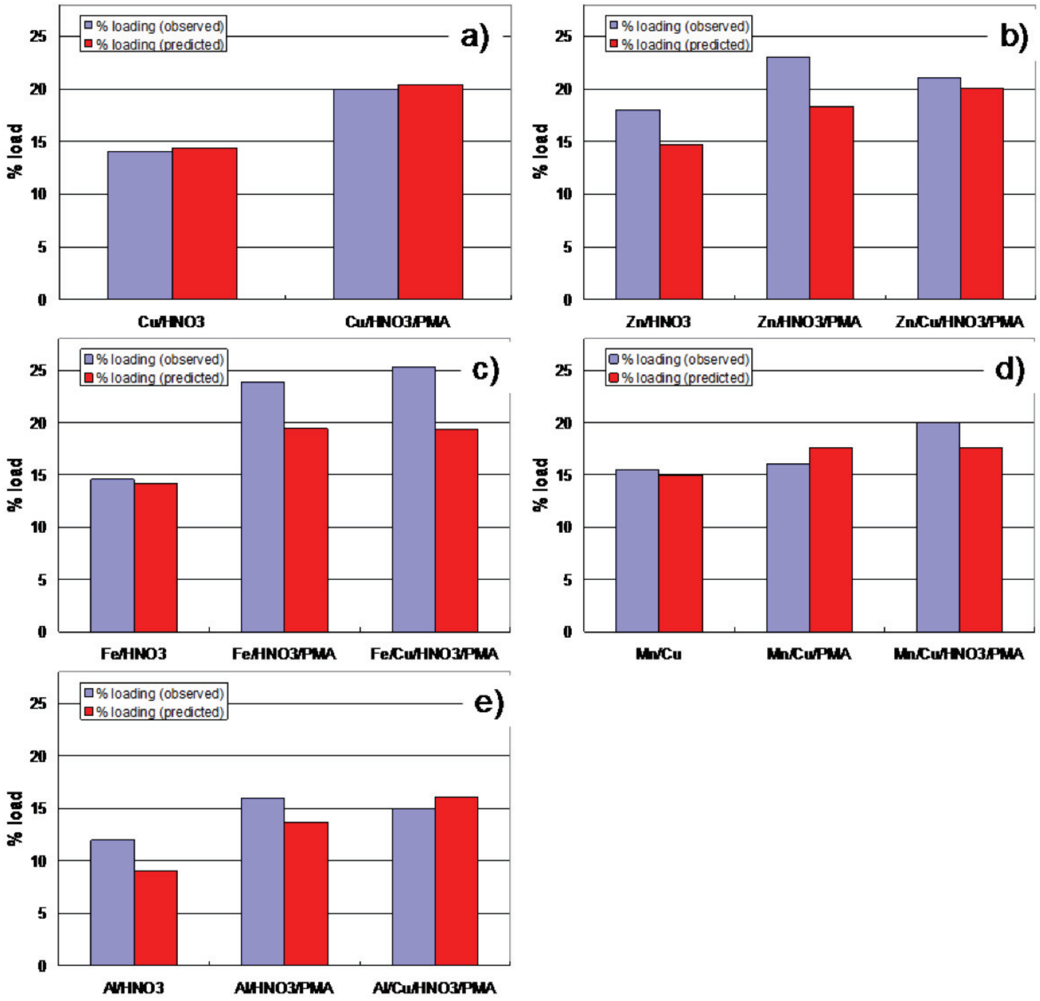

Figure 7.1: Observed and predicted % impregnant loading for the IACs prepared from the impregnating solutions detailed in Table 7.1.

Cu/HNO_3/PMA has been reported extensively in earlier work [39,78]. XRD data obtained from samples co-impregnated with $Cu(NO_3)_2$ and $Mn(NO_3)_3$ will be presented in the next section.

Figure 7.2 shows that none of the XRD patterns collected from these IACs display impregnant-related diffraction peaks. This is indicative of small grain size impregnant as can be inferred from Eq. 2.5. The Al^{3+} impregnant species is likely amorphous as was discussed in section 4.2.1. The differences in the baselines of the XRD data is due to the measurments being performed on different x-ray machines. The Al-containing samples and the Zn/HNO_3 sample were measured using the Inel.

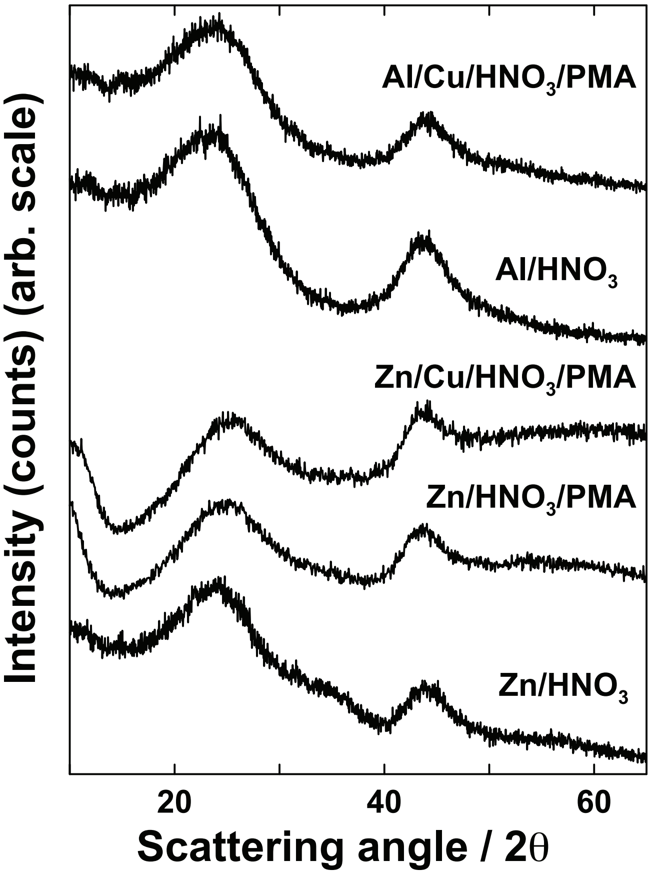

Figure 7.2: XRD data obtained from the Zn/HNO$_3$, Zn/HNO$_3$/PMA, Zn/Cu/HNO$_3$/PMA, Al/HNO$_3$ and Al/Cu/HNO$_3$/PMA samples.

The Zn/HNO$_3$/PMA and Zn/Cu/HNO$_3$/PMA IACs were measured using the Rigaku diffractometer.

7.2.4 Flow Test Results

Figure 7.3 shows dry breakthrough times obtained from the IACs in this study. Sample preparation information was detailed in Table 7.1. SO_2, NH_3, HCN and C_6H_{12} challenge gases were used. Results obtained from GC and URC are included for reference.

Figure 7.3 shows that co-impregnation with $H_3PO_4 \bullet 12MoO_3$ does not improve dry SO_2 breakthrough times. In most cases, preparing IACs using $Cu(NO_3)_2$ and a second

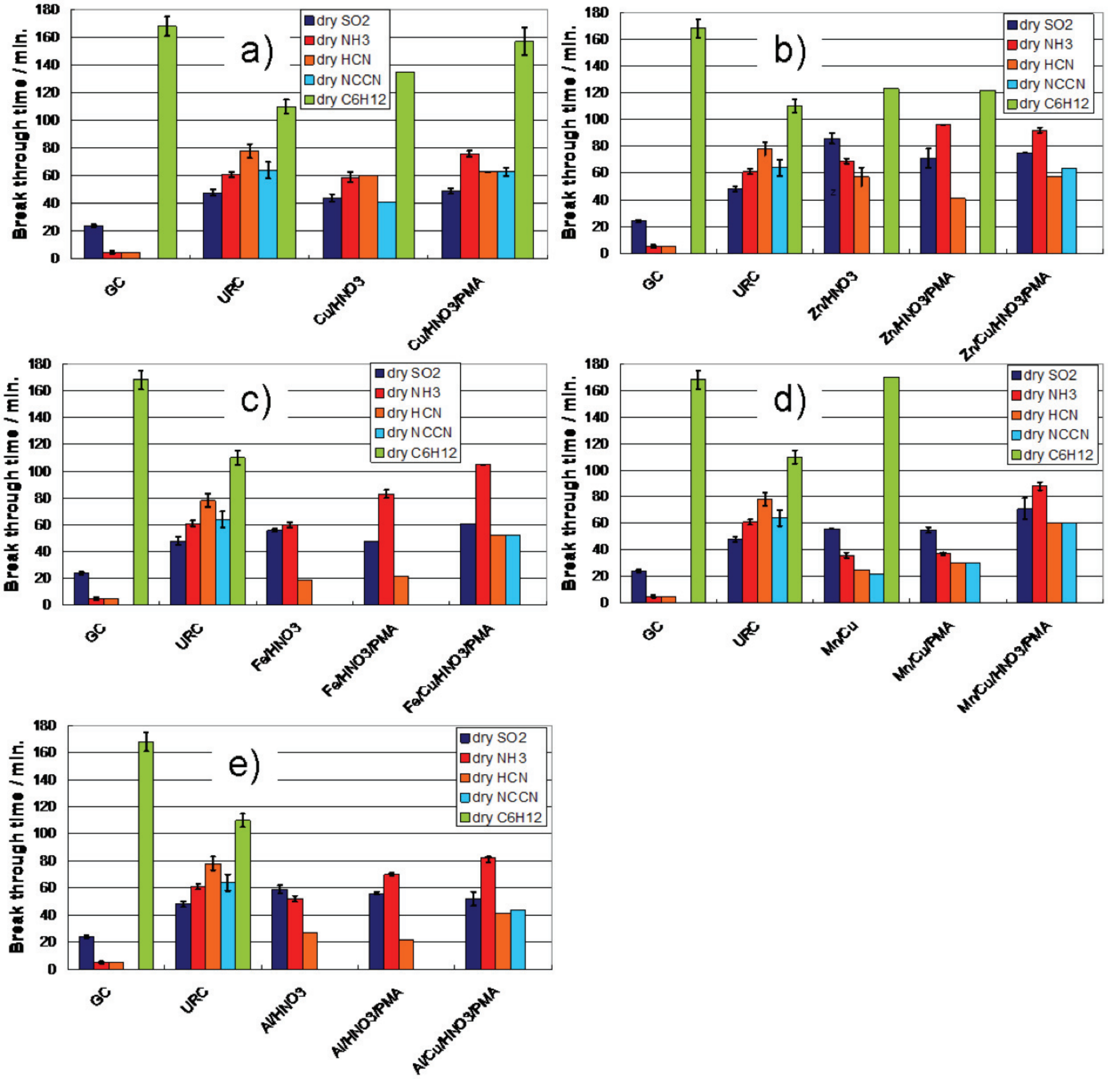

Figure 7.3: Dry breakthrough times obtained from the IACs in this study. SO_2, NH_3, HCN and C_6H_{12} challenge gases were used. Results obtained from GC and URC are included for reference.

metal nitrate precursor did not improve SO_2 adsorption capacity relative to IACs prepared from a single metal nitrate precursor. Panel (d) shows the Mn/Cu/HNO_3/PMA sample had a longer dry SO_2 breakthrough time than the Mn/Cu/PMA and Mn/Cu IACS. Improvments in gas adsorption capacity due to co-impregnation with HNO_3 were discussed in chapters 5 and 6. The overall dry SO_2 capacity ranking of IACs prepared from $Cu(NO_3)_2$, a second metal nitrate precursor, HNO_3 and $H_3PO_4{\bullet}12MoO_3$

(heated at $T_f = 200°C$) was: Zn/Cu-based > Mn/Cu-based ≈ Fe/Cu-based > Al/Cu-based. All of the IACs had dry SO_2 breakthrough times equal to or greater than URC and greater than GC.

Figure 7.3 shows that all of the IACs that were co-impregnated with $H_3PO_4 \bullet 12MoO_3$ had longer dry NH_3 breaktrhough times compared to samples with no $H_3PO_4 \bullet 12MoO_3$ present. Increased NH_3 adsorption in IACs with a Mo-containing compound present has been reported in earlier work [21, 23, 39] and has been reported in the literature [104]. The Fe/Cu-based and Al/Cu-based IACs had longer dry NH_3 breakthrough times than the Fe-based and Al-based samples respectively. The Zn/Cu-based and Zn-based IACs had approximately the same dry NH_3 capacity. The overall dry NH_3 capacity ranking of IACs prepared from $Cu(NO_3)_2$, a second metal nitrate precursor, HNO_3 and $H_3PO_4 \bullet 12MoO_3$ (heated at $T_f = 200°C$) was: Fe/Cu-based > Zn/Cu-based > Mn/Cu-based > Al/Cu-based All of the IACs shown in Figure 7.3, with the exception of the Mn/Cu and Mn/Cu/PMA samples, had dry NH_3 breakthrough times equal to or greater than URC. All of the IACs had longer dry NH_3 breakthrough times than GC.

Figure 7.3(a) shows that the Cu/HNO_3 IAC had an equal HCN breakthrough time and shorter NCCN breakthrough time than the Cu/HNO_3/PMA sample. Equation 1.1 explains that when Cu^{2+} impregnant reacts with HCN gas, NCCN gas is generated. The pressence of the $H_3PO_4 \bullet 12MoO_3$ impregnant gives Cu-based IACs better NCCN retention when challenged with HCN gas. The use of Mo^{6+}, W^{6+} or Cr^{6+} impregnants to control NCCN generation has been reported in the litterature [9, 13, 14]. Figure 7.3 shows that all of the IACs with Cu^{2+} impregnant and $H_3PO_4 \bullet 12MoO_3$ present have NCCN breakthrough times greater than or equal to their respective dry HCN breakthrough times. For respirator carbons it is important that the IAC have long, well balanced HCN and NCCN breakthrough times. The overall dry HCN/NCCN capacity ranking of IACs prepared from $Cu(NO_3)_2$, a second metal nitrate precursor, HNO_3 and $H_3PO_4 \bullet 12MoO_3$ (heated at $T_f = 200°C$) was: Mn/Cu/HNO_3/PMA ≈ Zn/Cu/HNO_3/PMA > Fe/Cu/HNO_3/PMA > Al/Cu/HNO_3/PMA. The Mn/Cu/HNO_3/PMA, Fe/Cu/HNO_3/PMA and Zn/Cu/HNO_3/PMA samples had HCN/NCCN breakthrough times approximately equal to the URC sample. Figure 7.3 shows that 50% of the Cu-based impregnant in a multi-gas IAC can be replaced with either Mn-based, Zn-based or Fe-based impregnant without decreasing the dry HCN/NCCN adsorption capacity. The pressence of Cu^{2+} dramatically increased dry HCN breakthrough times for the Fe-based, Mn-based and Al-based IACs when compared to samples prepared with no Cu^{2+} impregnat present. The Zn/HNO_3 IAC and the Zn/Cu/HNO_3/PMA IAC had equivalent dry HCN breakthrough times. The Zn/HNO_3/PMA sample had a shorter dry HCN breakthrough time than the other Zn-based IACs in this study.

Figure 7.3 shows that the Cu/HNO_3, Cu/HNO_3/PMA, Zn/HNO_3, Zn/HNO_3/PMA and Mn/Cu samples had longer dry C_6H_{12} breakthough times than URC and shorter breakthrough times than GC. Dry C_6H_{12} flow tests were not performed on IACs that do not have a result indicated. The shortest dry C_6H_{12} breakthrough times observed for the samples in this study were obtained from the Zn/HNO_3 and Zn/HNO_3/PMA IACs. These samples had approximately 75% of the dry C_6H_{12} capacity of the unimpregnated GC samples. The dry C_6H_{12} breakthrough times reported here indicate that pore filling or pore blockage due to impregnation was not a major issue for the IACs in this work.

Figure 7.4 shows humid flow test results obtained from selected IACs in this study. Panels (a) and (b) show results obtained from humid HCN and humid C_6H_{12} flow tests respectively. Due to limited sample size and testing availability not all of the IACs prepared from the solutions listed in Table 7.1 could be tested. Flow test results obtained from URC and GC samples have been included for reference.

Figure 7.4(a) shows that the Mn/Cu/HNO_3/PMA IAC had a longer humid HCN breakthrough time and a shorter humid NCCN breakthrough time than the URC sample. The Mn/Cu-containg IACs do not have well balanced humid HCN/NCCN breakthrough times. Comparison of the Mn/Cu/PMA and Mn/Cu/HNO_3/PMA IAC results shows that the sample co-impregnated with HNO_3 had significantly longer, better balanced, HCN/NCCN breakthrough times. Comparison of the Cu/HNO_3 and Cu/HNO_3/PMA samples illustrates the critical importance of the co-impregnated $H_3PO_4{\bullet}12MoO_3$ species. The Cu/HNO_3 IAC had a relatively long humid HCN breakthrough time, but little NCCN retention. The Cu/HNO_3/PMA IAC had relatively

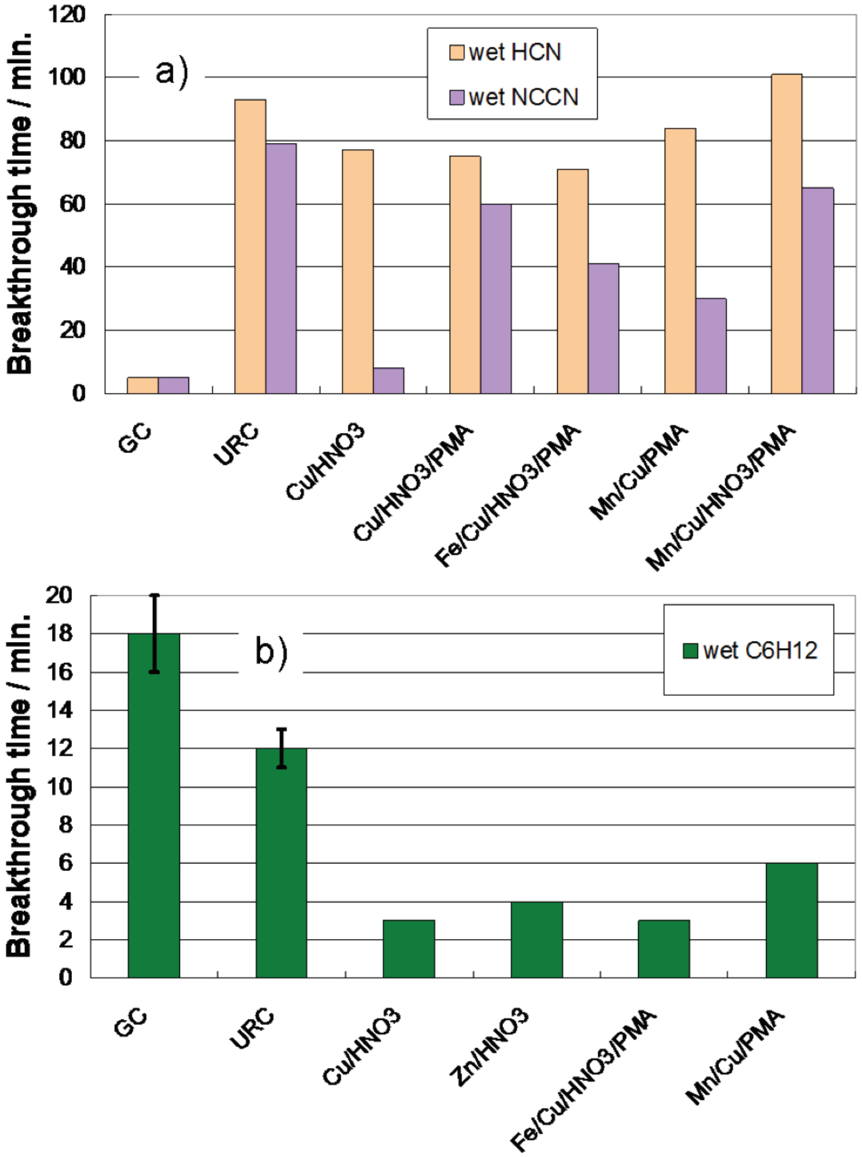

Figure 7.4: Humid breakthrough times obtained from the IACs in this study. Panels (a) and (b) show results obtained from humid HCN and humid C_6H_{12} flow tests respectively. The IACs tested are clearly indicated in each respective figure. Flow test results obtained from URC and GC samples have been included for reference.

long, well balanced humid HCN/NCCN breakthrough times. The Cu/HNO_3/PMA IAC has approximately 75% the humid HCN/NCCN capacity of the URC sample. The Cu/HNO_3/PMA IAC had approximately 80% of the Cu^{2+} impregnant loading of the URC sample based on values from the "prefered recipe" in Ref. [13]. The

Fe/Cu/HNO_3/PMA IAC had a similar humid HCN breakthrough time compared to the Cu/HNO_3/PMA sample, but had a shorter NCCN breakthrough time. A loading study to determine the optimal $H_3PO_4 \bullet 12MoO_3$ loading in co-impregnated, Cu-based IACs is reported below.

Figure 7.4(b) shows that all of the IACs reported here have shorter humid C_6H_{12} breakthrough times than the URC and GC samples. Data explaining why IACs treated with HNO_3 have lower humid C_6H_{12} capacity relative to un-treated samples was presented in Figure 5.7. The Mn/Cu IAC had the longest wet C_6H_{12} breakthrough time of the samples tested in this study. This IAC was not co-impregnated with HNO_3.

7.3 Comparative Study of IACs Prepared from $Cu(NO_3)_2$ and $Mn(NO_3)_2$ or $Zn(NO_3)_2$ and $Mn(NO_3)_2$

7.3.1 Sample Preparation

IAC samples were prepared by impregnating GC activated carbon. GC was previously described in section 3.1. The GC substrate was impregnated using the imbibing method. All of the IACs reported in this work were prepared in a single imbibing and heating step. Approximately 12 mL of impregnating solution was added to 15 g of GC. All of the IACs in this work were heated at T_f = 200°C for approximately 3 hours. Details of the heating conditions used and determination of the % impregnant loading have been discussed in earlier sections (see section 2.1 or section 7.2.1 for example).

7.3.2 Impregnant Loading

Figure 7.1 shows the observed and predicted % impregnant loading, after heating, for the IACs prepared from $Cu(NO_3)_2$ and $Mn(NO_3)_2$ (panel (a)) or $Zn(NO_3)_2$ and $Mn(NO_3)_2$ (panel (b)) solutions. The ratio of Mn^{2+} to Cu^{2+} ions in the impregnating solution (or ratio of Mn^{2+} to Zn^{2+}) is denoted by Mn:Cu (or Mn:Zn) and is clearly indicated in the appropriate panel. All of the IACs have 1.9 ± 0.1 mmol impregnant/g GC. The predicted % loading was calculated based on the assumptions in section 7.2.2.

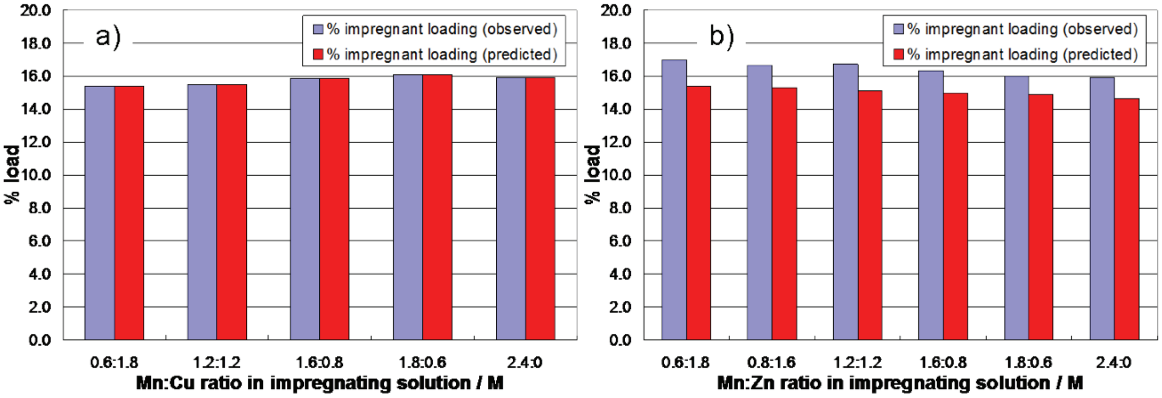

Figure 7.5: Observed and predicted % impregnant loading for the IACs prepared from $Cu(NO_3)_2$ and $Mn(NO_3)_2$ or $Zn(NO_3)_2$ and $Mn(NO_3)_2$ solutions. The ratio of Mn^{2+} to Cu^{2+} ions in the impregnating solution (or ratio of Mn^{2+} to Zn^{2+}) is indicated.

Figure 7.5(a) shows that there is excellent agreement between the observed and predicted % impregnant loading for the Mn/Cu-based samples. This is indicative of full conversion of the impregnant to its respective metal oxide phase. Figure 7.5(b) shows there is reasonable agreement between the observed and predicted % impregnant loading for the Mn/Zn-based IACs; however in all cases the observed loading was greater than predicted. Possible explanations for the observed discrepency will be discussed in terms of XRD results below.

7.3.3 XRD Characterization

Figure 7.6 shows XRD patterns obtained from selected Mn/Cu-based and Mn/Zn-based IACs in panels (a) and (b) respectively. For reference the main Bragg peaks from CuO, Mn_3O_4, ZnO and $ZnMn_2O_4$ ([00-089-2529], [00-089-4837], [00-089-1397] and [00-071-2499] in [56] respectively) have been indicated. The XRD pattern from un-impregnated GC has been included for reference.

Figure 7.6(a) shows that the XRD data obtained from the Mn/Cu IACs only display CuO diffraction peaks. Analysis of the 2 main CuO peaks (located at $2\theta \approx 35.5°$ and $38.7°$ respectively) of the 0.6 M Mn^{2+}:1.8 M Cu^{2+} sample using Eq. 2.5 yields an average CuO grain size of 18 ± 2 nm. No XRD peaks corresponding to a Mn- or Mn/Cu-impregnant phase were observed in these samples. The XRD pattern obtained from the Mn-based IAC (with no Cu-impregnant present) was well

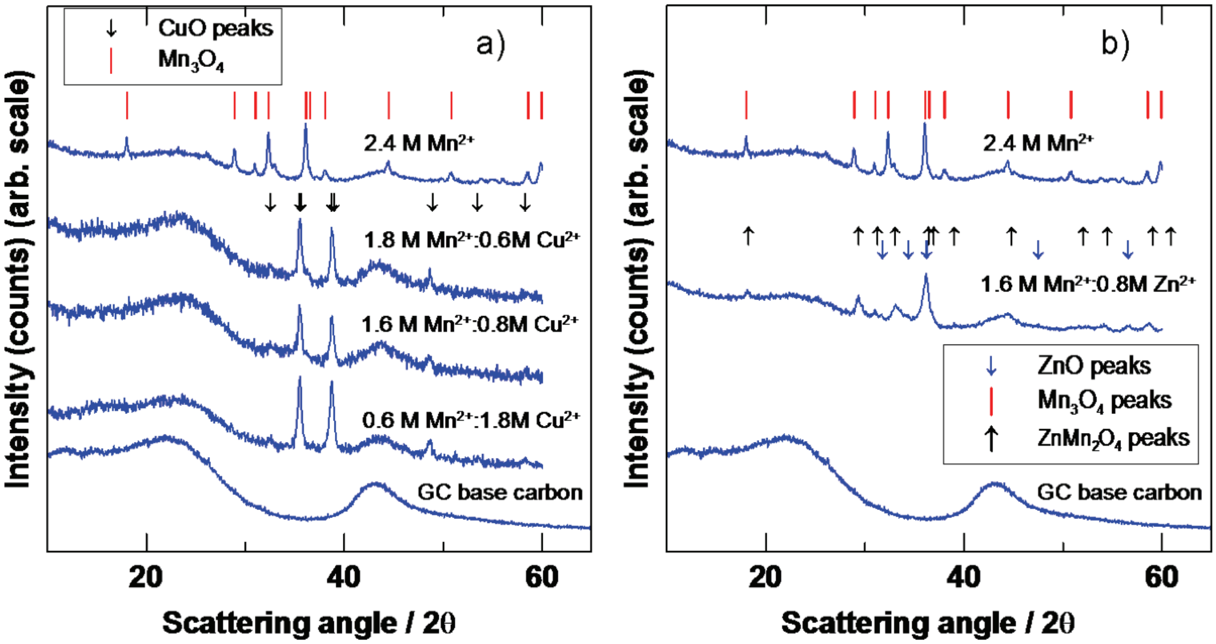

Figure 7.6: XRD patterns obtained from selected Mn/Cu-based and Mn/Zn-based IACs in panels (a) and (b) respectively. For reference the main Bragg peaks from CuO, Mn_3O_4, ZnO and $ZnMn_2O_4$ have been indicated. The XRD pattern from GC has been included for reference.

matched by the Mn_3O_4 pattern. Panel (a) shows that all of the Mn- and Mn/Cu-based IACs had relatively narrow, intense impregnant-related diffraction peaks. This indicates relatively large grain size CuO or Mn_3O_4 impregnant that is not well dispersed for the Mn/Cu- and Mn-based IACs respectively. Figure 7.6(a) shows that co-impregnating $Mn(NO_3)_2$ with $Cu(NO_3)_2$ affects the way the Mn-based impregnant crystallizes during heating. The dispersion of the impregnant probably could be improved by co-impregnation with HNO_3.

Figure 7.6(b) shows that the XRD pattern obtained from the 1.6 M Mn^{2+}:0.8 M Zn^{2+} IAC is well matched by the $ZnMn_2O_4$ impregnant phase. It was not determined why co-impregnating GC with a 1.6 M Mn^{2+}:0.8 M Zn^{2+} solution resulted in the formation of a spinel structure after heating, but co-impregnating GC with a 1.6 M Mn^{2+}:0.8 M Cu^{2+} solution did not. The predicted % impregnant loading for the IAC with 1.6 M Mn^{2+}:0.8 M Zn^{2+} is 15 % assuming decomposition to the $ZnMn_2O_4$ phase. The predicted % impregnant loading for the non-interacting case was also 15%. These values are both close to the observed % impregnant loading which was ≈ 16%. The interaction between the Mn^{2+} and Zn^{2+} impregnants during heating does not explain the relatively small discrepency between the observed and predicted % impregnant loadings shown in Figure 7.5(b).

7.3.4 Flow Test Results

Figure 7.7 shows dry flow test results obtained from the IACs prepared from $Cu(NO_3)_2$ and $Mn(NO_3)_2$ (panel (a)) or $Zn(NO_3)_2$ and $Mn(NO_3)_2$ (panel (b)) solutions, after heating, as described by the figure caption. Figure 7.7(a) shows the dry SO_2 breaktrhough times obtained from the Mn/Cu-based IACs are constant and do not change by changing Mn:Cu impregnant ratio. These IACs have longer dry SO_2 breakthrough times than the URC and GC samples. Figure 7.7(b) shows the IAC with the most Zn^{2+} impregnant present has the longest dry SO_2 time. The IACs prepared from solutions with ≤ 1.6 M Zn^{2+} had constant dry SO_2 breakthrough times, that were shorter than those obtained from the Mn/Cu-based samples.

Figure 7.7 shows that dry NH_3 breakthrough times decrease with increasing Mn-based impregnant. Figure 4.4 showed that Mn-based IACs had poor NH_3 capacity. These results show that Mn-based, Mn/Cu-based or Mn/Zn-based impregnants do not have good dry NH_3 capacity. Figure 7.7 shows that all of the IACs tested here had shorter dry NH_3 breakthrough times than URC and longer times than GC.

Figure 7.7 shows that dry HCN breakthrough times decrease with increasing Mn-impregnant loading. Comparison of Figures 7.7 and 7.3(d) indicates that co-impregnation with HNO_3 might improve the HCN capacity of the Mn/Cu- and Mn/Zn-based IACs. All of the IACs tested here had shorter dry HCN breakthrough times than URC and longer times than GC. IACs prepared without Cu^{2+} impregnant present did not generate any NCCN during the HCN flow tests. Figure 7.7 shows that all of the IACs tested here had longer dry C_6H_{12} breakthrough times than URC. Comparing the dry C_6H_{12} breakthrough times obtained from the Mn/Cu-based or Mn/Zn-based IACs to those obtained from un-impregnated GC inicates that micropore blockage or micropore filling due to impregnation was not a major issue for the IACs in this study.

Figure 7.8 shows wet C_6H_{12} flow test results obtained from the IACs prepared

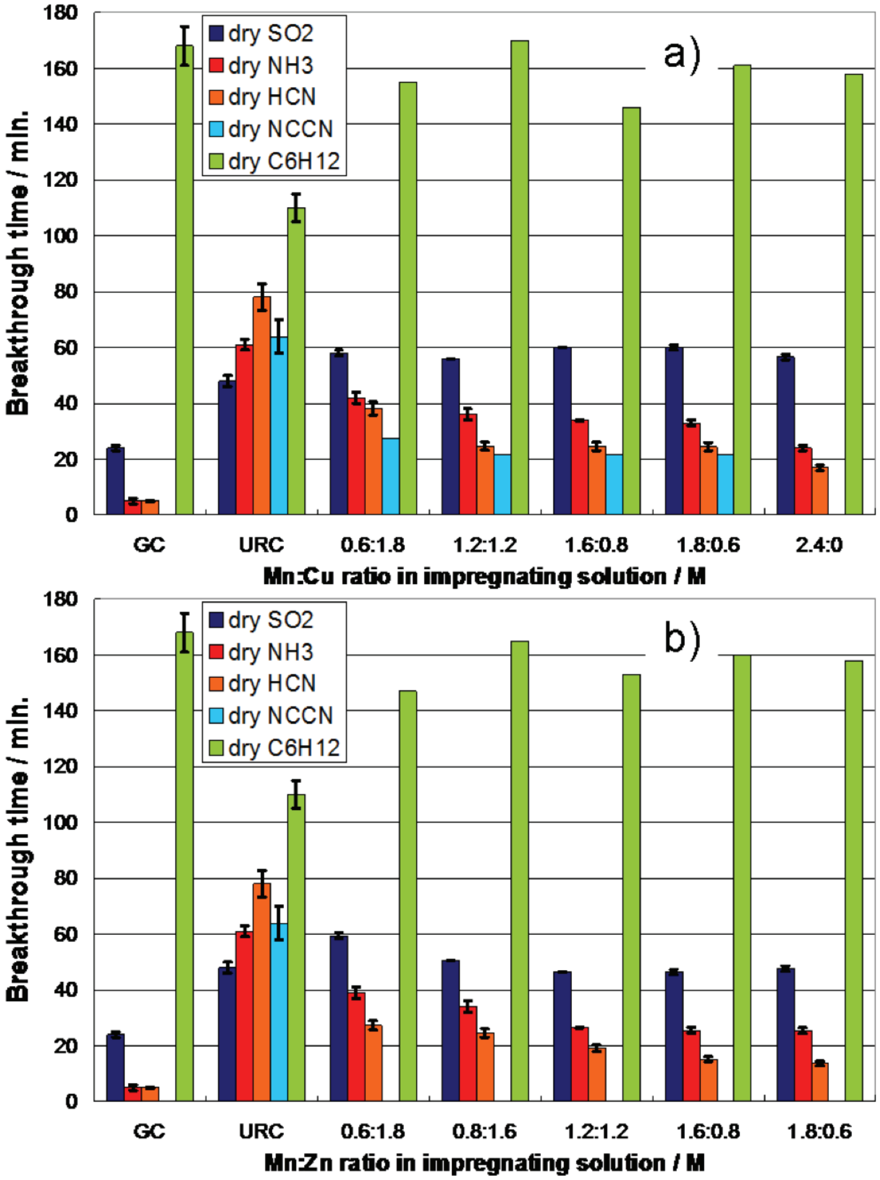

Figure 7.7: Dry flow test results obtained from the IACs prepared from $Cu(NO_3)_2$ and $Mn(NO_3)_2$ (panel (a)) or $Zn(NO_3)_2$ and $Mn(NO_3)_2$ (panel (b)) solutions, after heating. SO_2, NH_3, HCN and C_6H_{12} challenge gases were used. The ratio of Mn^{2+} to Cu^{2+} ions in the impregnating solution (or ratio of Mn^{2+} to Zn^{2+}) is denoted by Mn:Cu (or Mn:Zn) and is clearly indicated in the appropriate panel. All of the IACs have 1.9 ± 0.1 mmol impregnant/g GC. Flow test results obtained from URC and GC are indicated for reference.

from $Cu(NO_3)_2$ and $Mn(NO_3)_2$ (panel (a)) or $Zn(NO_3)_2$ and $Mn(NO_3)_2$ (panel (b)) solutions, after heating, as described by the figure caption.

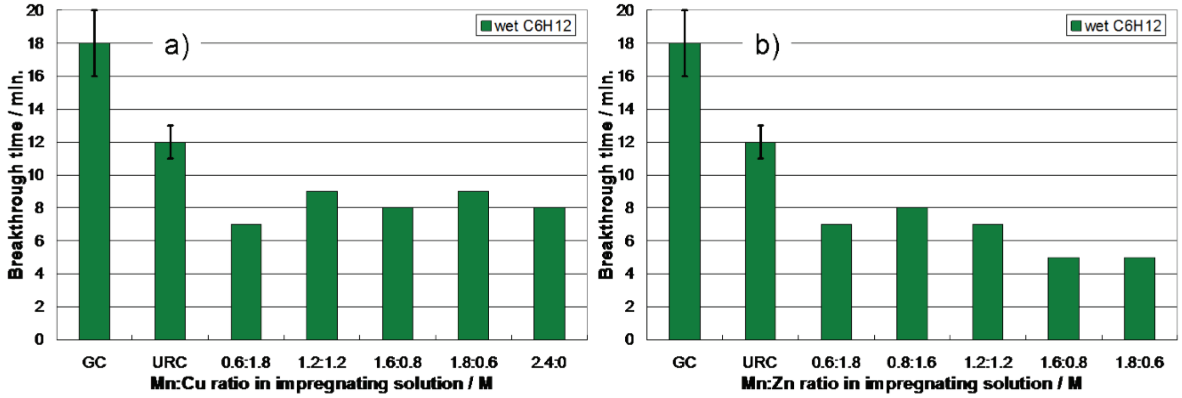

Figure 7.8: Wet C_6H_{12} flow test results obtained from the IACs prepared from $Cu(NO_3)_2$ and $Mn(NO_3)_2$ (panel (a)) or $Zn(NO_3)_2$ and $Mn(NO_3)_2$ (panel (b)) solutions, after heating. The ratio of Mn^{2+} to Cu^{2+} ions in the impregnating solution (or ratio of Mn^{2+} to Zn^{2+}) is denoted by Mn:Cu (or Mn:Zn) and is clearly indicated in the appropriate panel. All of the IACs have 1.9 ± 0.1 mmol impregnant/g GC. Flow test results obtained from URC and GC are indicated for reference.

Figure 7.8 shows that all of the IACs prepared and tested in this study have shorter C_6H_{12} breakthrough times than URC or GC. The data does not indicate that there is an optimal Mn:Cu- or Mn:Zn-impregnant ratio. The Mn/Cu-based IACs had slightly longer wet C_6H_{12} breakthrough times than the Mn/Zn-based samples. The data shown in Figure 6.24(b) indicates that decreasing the impregnant loading would improve wet C_6H_{12} adsorption, however this would also decrease the multi-gas capacity of the IACs.

7.4 The Effect of CuO, H_3PO_4•$12MoO_3$ and ZnO Loading on Multi-gas IACs

7.4.1 Sample Preparation

IAC samples were prepared by impregnating GC activated carbon using the imbibing method. GC was previously described in section 3.1. All of the IACs reported in this work were prepared in a single imbibing and heating step. Approximately 11.3 mL of impregnating solution was added to 15 g of GC. Details of the impregnating solutions used to prepare samples in this work are listed in Table 7.2. The IACs that were prepared according to Table 7.2 had a total of 1.7 ± 0.1 mmol Cu^{2+} and

Zn^{2+} impregnant/g GC. Table 7.2 shows that the concentration of $Cu(NO_3)_2$ and $H_3PO_4 \bullet 12MoO_3$ decreases and the concentration of $Zn(NO_3)_2$ increases from sample A → E.

All of the IACs in this work were heated under flowing argon at $T_f = 180°C$. Details of the heating conditions and determination of the % impregnant loading have been discussed earlier (See section 2.1 or section 7.2.1).

Table 7.2: Contents of the impregnating solutions used to prepare IACs for the $Cu(NO_3)_2$ / $H_3PO_4 \bullet 12MoO_3$ / HNO_3 / $Zn(NO_3)_2$ loading study.

Sample name	Imbibing solution contents
A	11.3 mL of 2.20 M $Cu(NO_3)_2$ / 0.12 M $Zn(NO_3)_2$ / 3.80 M HNO_3 / 0.031 M $H_3PO_4 \bullet 12MoO_3$ per 15 g GC
B	11.3 mL of 1.70 M $Cu(NO_3)_2$ / 0.61 M $Zn(NO_3)_2$ / 3.80 M HNO_3 / 0.024 M $H_3PO_4 \bullet 12MoO_3$ per 15 g GC
C	11.3 mL of 1.20 M $Cu(NO_3)_2$ / 1.20 M $Zn(NO_3)_2$ / 3.90 M HNO_3 / 0.017 M $H_3PO_4 \bullet 12MoO_3$ per 15 g GC
D	11.3 mL of 0.65 M $Cu(NO_3)_2$ / 1.70 M $Zn(NO_3)_2$ / 3.90 M HNO_3 / 0.00.009 M $H_3PO_4 \bullet 12MoO_3$ per 15 g GC
E	11.3 mL of 0.12 M $Cu(NO_3)_2$ / 2.30 M $Zn(NO_3)_2$ / 4.00 M HNO_3 / 0.002 M $H_3PO_4 \bullet 12MoO_3$ per 15 g GC

7.4.2 Impregnant Loading

Figure 7.9 shows the observed and predicted % impregnant loading, after heating, for the IACs prepared from the solutions listed in Table 7.2. Figure 7.9 shows that there is reasonable agreement between the observed and predicted % impregnant loading. The amount of Cu^{2+} impregnant (present as CuO presumably) and $H_3PO_4 \bullet 12MoO_3$ impregnant decreases and the amount of Zn^{2+} impregnant (presumably ZnO) increases from sample A → E. The agreement between observed and predicted % impregnant loading is better for samples with more Cu^{2+} impregnant present. The largest observed discrepency in the loading was for sample E, which had the highest Zn^{2+} impregnant loading. The observed loading for this sample was $\approx$ 3% higher than predicted.

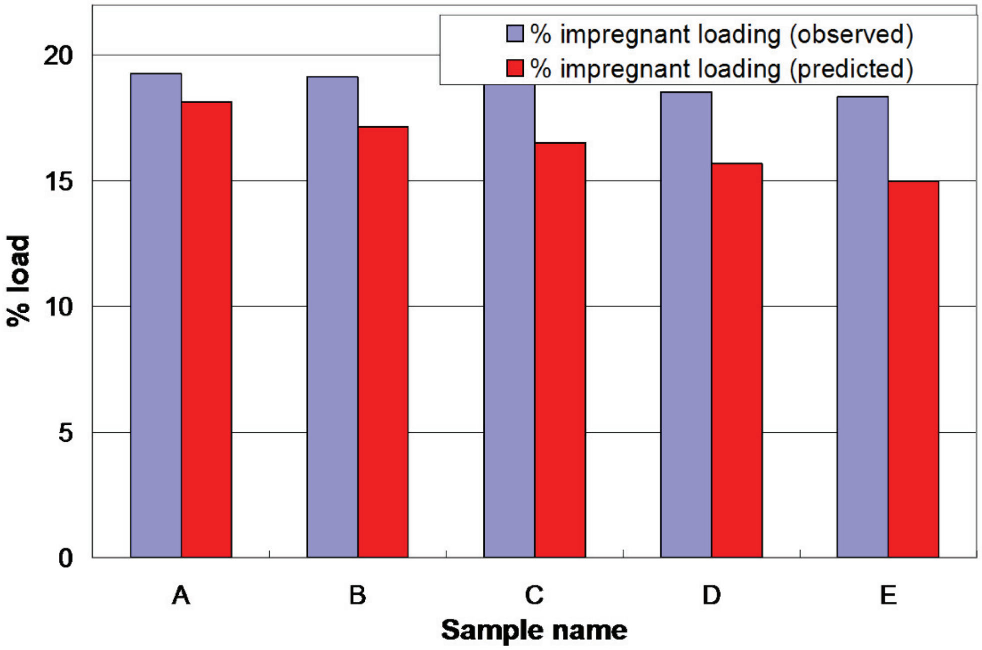

Figure 7.9: Observed and predicted % impregnant loading, after heating, for the IACs prepared from the solutions listed in Table 7.2.

7.4.3 X-ray Characterizations

Figure 7.10 shows SAXS and XRD data collected from samples A, B, C, D and E in panels (a) and (b) respectively. For reference, data collected from GC has been included. Fits to the SAXS data in panel (a) are not shown. Parameters extracted from fitting the data in panel (a) with Eq. 6.2 are listed in Table 7.3.

Table 7.3: Parameters extracted from fits to the SAXS data shown in Figure 7.10(a) using Eq. 6.2. The values given for GC are the average values shown in Table 3.2. The values given for A are in units of counts/Å^n and the values for B and C are given in units of counts/Å^4.

Sample name	A	n	B	R_{g1}(Å)	C	R_{g2} (Å)	χ^2
GC	0.18	3.54	130	6.2	0	0	1.9
A	0.42	3.5	77	6.2	15	16	0.8
B	0.40	3.5	59	6.2	18	14	0.8
C	0.42	3.5	39	6.2	32	12	0.8
D	0.31	3.5	23	6.2	34	12	0.5
E	0.33	3.5	11	6.2	39	12	0.5

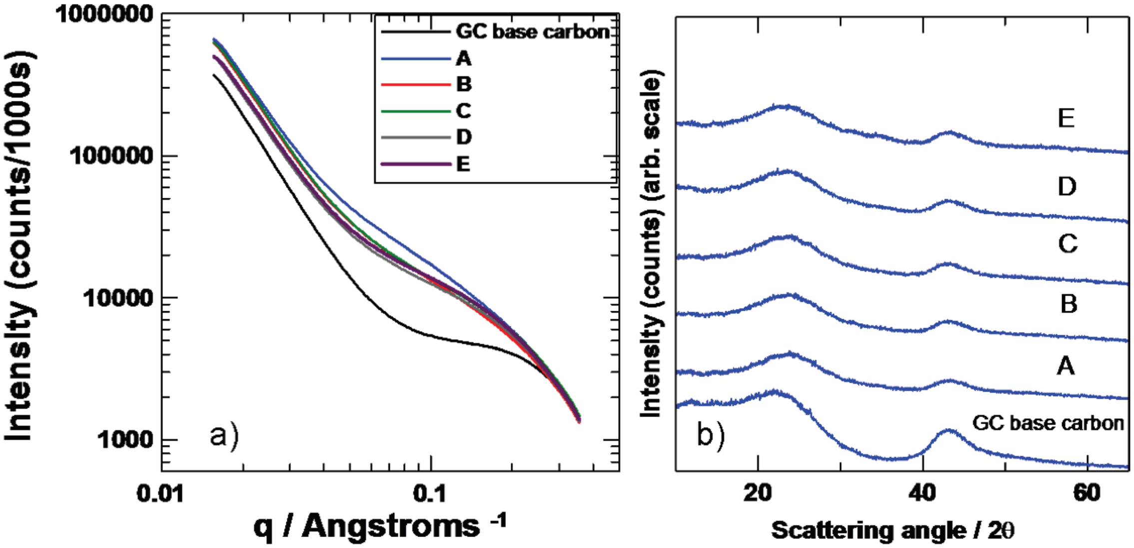

Figure 7.10: SAXS and XRD data collected from samples A, B, C, D and E in panels (a) and (b) respectively. For reference data collected from GC has been included.

Figure 7.10(a) shows the intensities of the SAXS data collected from samples A, B and C are higher than those collected from samples D and E in the range of q $\approx$ 0.015 - 0.03 Å^{-1}. This implies that samples A, B and C have more large particle size impregnant occupying the macropores and large mesopores. Comparing the intensity of the SAXS data collected from samples A - E with data collected from GC over this scattering range shows that all of the IACs in this study have reasonably small, well dispersed impregnant. Comparing the data in the 0.03 Å^{-1} $\leq$ q $\leq$ 0.15 Å^{-1} range shows that samples B, C, D and E had similar curves. The SAXS data from sample A had higher intensity in this range. The data in Table 7.3 shows sample A has the largest R_{g2} value of the IACs in this study. Sample A has the highest overall impregnant loading of the samples in this study when the total contributions from the Cu^{2+}, Zn^{2+} and $H_3PO_4\bullet12MoO_3$ impregnants are considered. The intensity of the SAXS data obtained from samples A - E in the q > 0.2 Å^{-1} range is similar to the data obtained from the GC sample. This suggests that little impregnant enters the micropores.

Figure 7.10(b) shows that the XRD data obtained from samples A, B, C, D and E do not exhibit impregnant-related diffraction peaks. This implies relatively small, well dispersed impregnant is present on the GC substrate for these IACs. Figure 7.10

shows that all of the IACs in the CuO/H_3PO_4•$12MoO_3$/HNO_3/ZnO loading study had well dispersed, small particle size impregnant. These results will be discussed in terms of flow test results below.

7.4.4 Flow Test Results

Figure 7.11 shows dry breakthrough times obtained from flow testing the samples in this study. Details of the sample preparation are listed in Table 7.2. The samples were challenged with SO_2, NH_3 and C_6H_{12} challenge gases. Results obtained from URC and GC are included for reference.

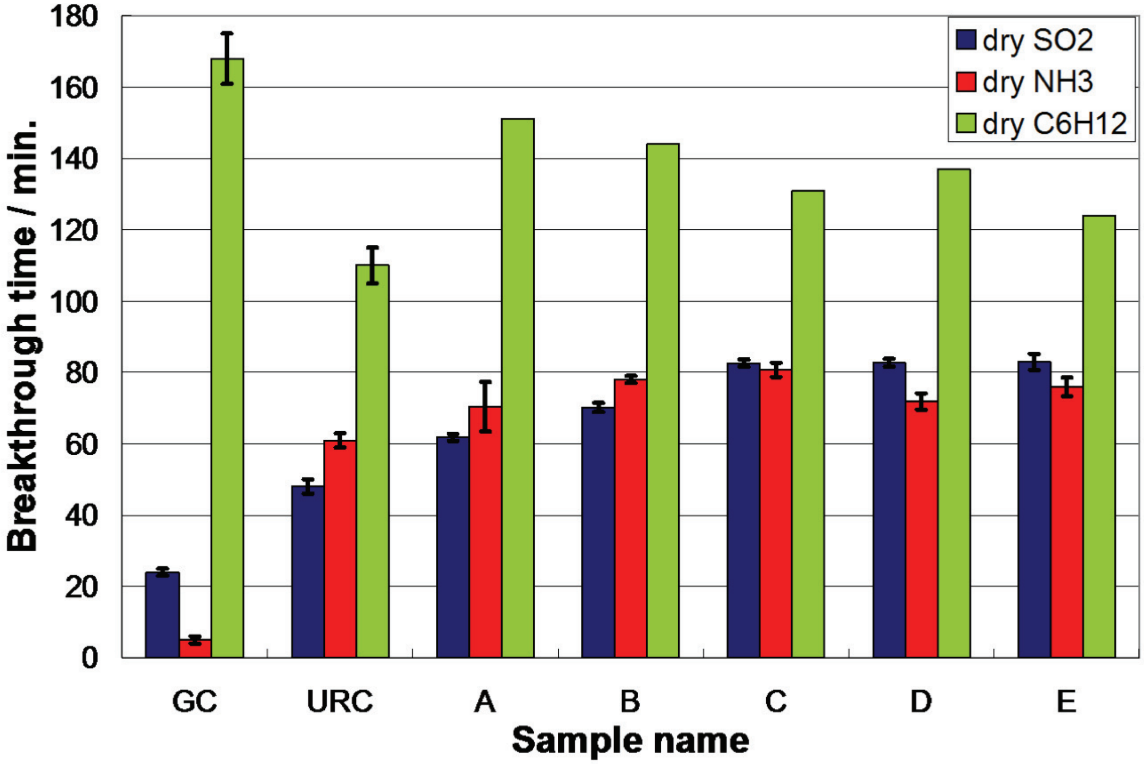

Figure 7.11: Dry breakthrough times obtained from flow testing samples A, B, C, D and E. The samples were challenged with SO_2, NH_3 and C_6H_{12} challenge gases. Results obtained from URC and GC are included for reference.

Figure 7.11 shows that the dry SO_2 breakthrough times increase for samples A through C, then remain constant for samples C through E. The CuO loading is decreasing and ZnO loading is increasing (total CuO + ZnO = 1.7 ± 0.1 mmol/g

GC) for samples A through E. The longer dry SO_2 breakthrough times are due to the higher amounts of well dispersed ZnO impregnant. This is consistent with the results in Figure 5.16 which show that for IACs with similar loading, thermal treatment and HNO_3 co-impregnation, the Zn-based IACs had longer dry SO_2 breakthrough times compared to Cu-based samples. Figure 7.11 shows that all of the IACs prepared and tested in this study had longer dry SO_2 breakthrough times than URC or GC.

Figure 7.11 shows that samples A, B, C, D and E all had similar dry NH_3 breakthrough times that were longer than those obtained from URC or GC. Sample C had the longest dry NH_3 breakthrough time of the IACs tested here. Figure 7.11 shows that all of the IACs prepared and tested in this study had longer dry C_6H_{12} breakthrough times than URC and shorter breakthrough times than GC. The samples with the highest Cu^{2+} impregnant loading (samples A and B) had the longest dry C_6H_{12} breakthrough times. Sample E had the shortest dry C_6H_{12} breakthrough time of the IACs prepared and tested in this study. This sample had a breakthrough time that was approximately 75% as long as un-impregnated GC. This indicates that the majority of micropores are available for physical gas adsorption.

Figure 7.12 shows humid C_6H_{12} breakthrough times obtained from flow testing samples A, B, C, D and E. Results obtained from URC and GC have been included for reference. Figure 7.12 shows that all of the IACs prepared and tested in this work had shorter humid C_6H_{12} breakthrough times than the GC or URC samples. The poor C_6H_{12} adsorption under humid conditions is mainly due to co-impregnation with 4 M HNO_3. The data shows that the ratio of Cu^{2+}:Zn^{2+} impregnant does not effect the humid C_6H_{12} adsorption capacity.

7.5 Summary of the Most Effective Multi-gas IACs

Figure 7.13 shows a radar plot summarizing the most effective multi-gas IACs discussed in chapter 7. Flow test results obtained from the Cu/HNO_3/PMA, Zn/Cu/HNO_3/PMA, Fe/Cu/HNO_3/PMA and Mn/Cu/HNO_3/PMA samples are shown. Due to limited sample size and gas testing availibility wet SO_2 and NH_3 tests were not performed. There are no humid results for the Zn/Cu/HNO_3/PMA IAC. There are no humid C_6H_{12} results for the Cu/HNO_3/PMA and Mn/Cu/HNO_3/PMA samples

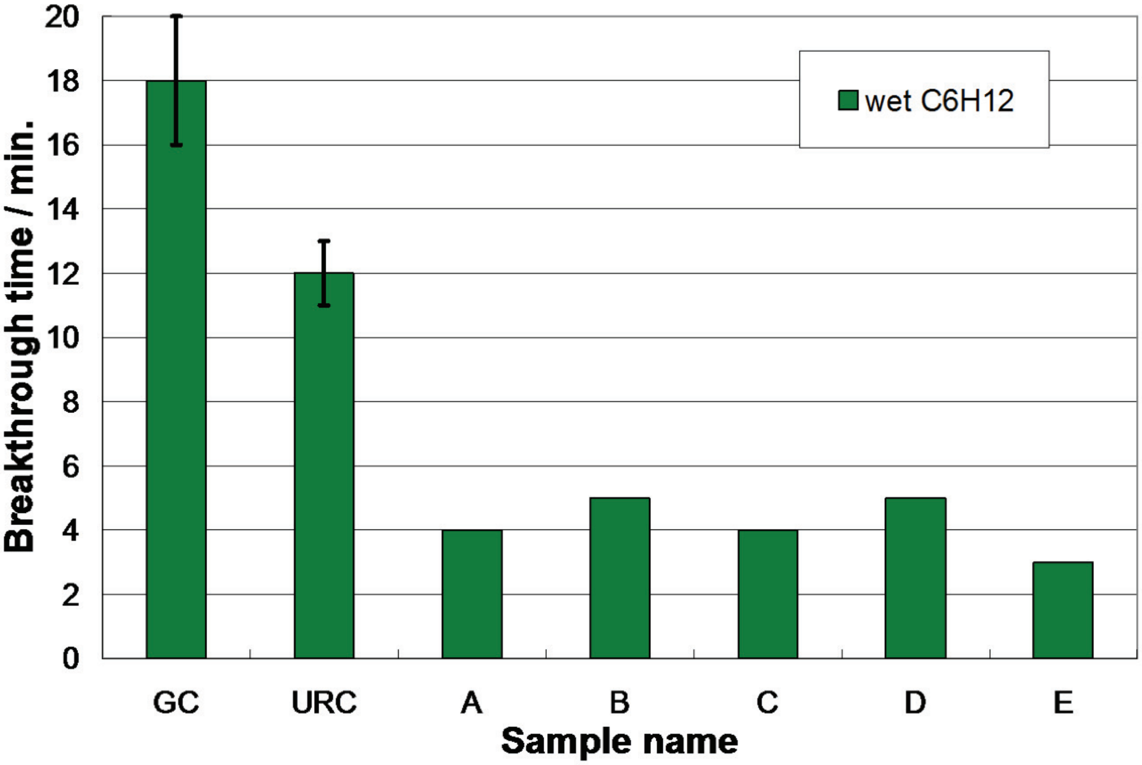

Figure 7.12: Humid C_6H_{12} breakthrough times obtained from flow testing samples A, B, C, D and E. Results obtained from URC and GC have been included for reference.

and no dry C_6H_{12} results for samples Zn/Cu/HNO_3/PMA, Fe/Cu/HNO_3/PMA and Mn/Cu/HNO_3/PMA samples.

Figure 7.13 shows that the IACs prepared from mixed metal nitrates had longer dry SO_2 and NH_3 breakthrough times than the GC, Cu/HNO_3/PMA and URC samples. Samples Zn/Cu/HNO_3/PMA and Mn/Cu/HNO_3/PMA had equivalent dry HCN/NCCN adsorption capacity compared to the Cu/HNO_3/PMA and URC samples. The Fe/Cu/HNO_3/PMA IAC had slightly lower dry HCN/NCCN capacity compared to the other samples. All the IACs prepared from mixed metal nitrates had longer dry HCN breakthrough times than GC.

Dry C_6H_{12} testing was not performed on the IACs prepared from mixed metal nitrates. The Cu/HNO_3/PMA sample had a longer dry C_6H_{12} breakthrough time than URC and a shorter time than GC. The Mn/Cu/HNO_3/PMA sample had the longest humid HCN breakthrough time of the samples tested here. When humid

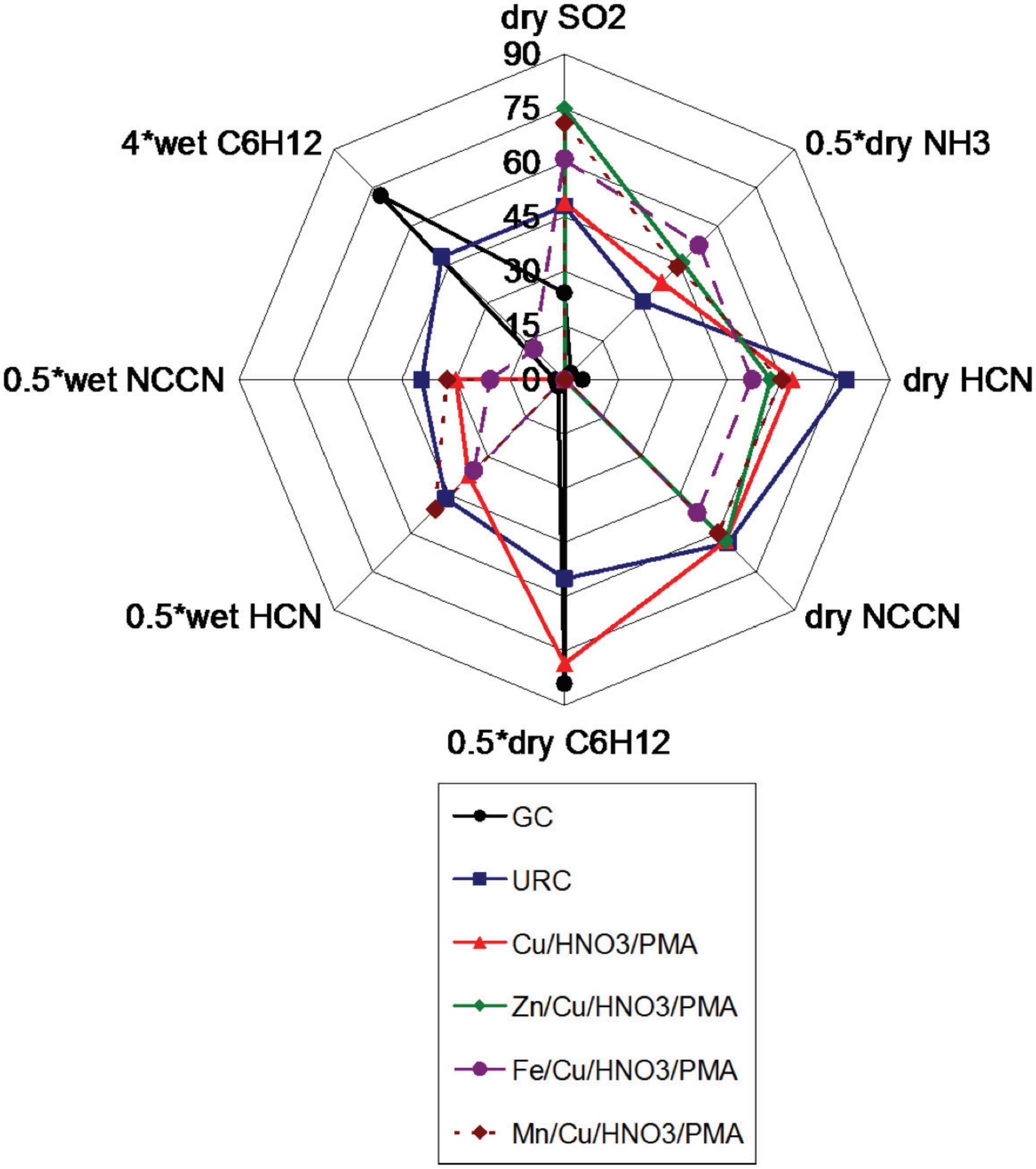

Figure 7.13: Radar plot summarizing flow test results obtained from the most effective multi-gas IACs discussed in chapter 7. The breakthrough times are reported in minutes. Gas test results obtained from the different challenge gases are presented on individual axes. Dry NH_3 and C_6H_{12} breakthrough times and wet HCN, NCCN and C_6H_{12} breakthrough times have been scaled, by the amount indicated on their respective axis, to allow for better presentation of the data. Results obtained from GC and URC are included for reference.

HCN/NCCN capacity is considered the Mn/Cu/HNO_3/PMA sample and URC sample were equivalent. The Fe/Cu/HNO_3/PMA and the Cu/HNO_3/PMA samples had reasonably good humid HCN/NCCN adsorption capacity. All of the IAC samples had longer wet HCN breakthrough times than GC. The Fe/Cu/HNO_3/PMA sample had poor humid C_6H_{12} capacity compared to the URC and GC samples.

7.6 Conclusions

IACs prepared from $Cu(NO_3)_2$, a second metal nitrate precursor, HNO_3 and $H_3PO_4\bullet 12MoO_3$, that were heated at $T_f = 200°C$, were observed to have good overall multi-gas adsorption capacity. The $H_3PO_4\bullet 12MoO_3$ impregnant improved NCCN retention in Cu^{2+} containing IACs that had been exposed to HCN. $H_3PO_4\bullet 12MoO_3$ impregnant also improved dry NH_3 adsorption capacity. When co-impregnated with HNO_3 and $H_3PO_4\bullet 12MoO_3$, the Zn/Cu-, Mn/Cu- and Fe/Cu-based IACs had overall multi-gas capacity that was as good as or better than the Cu-based IACs and the URC sample. Being able to reduce the amount of $Cu(NO_3)_2$ by substituting $Zn(NO_3)_2$, $Mn(NO_3)_2$ or $Fe(NO_3)_3$ may provide cost savings, without loss in performance, to producers of multi-gas respirator carbons.

XRD data was used to show IACs produced from 1.8 M $Mn(NO_3)_2$ and 0.8 M $Zn(NO_3)_2$, that were heated at $T_f = 200°C$, formed $ZnMn_2O_4$ as their dominant impregnant phase. IACs prepared from $Cu(NO_3)_2$ and $Mn(NO_3)_2$ solutions, heated at $T_f = 200°C$, formed primarily CuO impregnant. Co-impregnating $Mn(NO_3)_2$ with $Cu(NO_3)_2$ appears to effect the way the Mn-based impregnant crystallizes during heating. None of the Mn/Cu- or Mn/Zn-based IACs had full multi-gas capacity.

IACs prepared from aqueous $Cu(NO_3)_2$, $Zn(NO_3)_2$, HNO_3 and $H_3PO_4\bullet 12MoO_3$ solutions, that were heated at $T_f = 180°C$, were found to be useful multi-gas IACs under dry conditions. XRD and SAXS data showed that relatively small particle size, well dispersed impregnant was formed after heating on IACs prepared from these impregnants. These samples were found to have poor humid C_6H_{12} capacity due to co-impregnation with HNO_3. No other humid flow tests were performed on these IACs. The best overall multi-gas IAC (sample C) had approximately (0.9 mmol CuO, 0.9 mmol ZnO, 0.2 mmol Mo^{6+}) impregnant/g GC.

The work presented up to this point has shown that preparing IACs with co-impregnated HNO_3 gives good impregnant dispersion. This results in good SO_2,

NH_3, HCN and dry C_6H_{12} adsorption capacity. IACs prepared with co-impregnated HNO_3 have poor humid C_6H_{12} adsorption. Work presented in the following chapters was aimed at improving humid C_6H_{12} adsorption, without losing overall multi-gas adsorption capacity.

Chapter 8

The Effect of Co-impregnated Acids on the Performance of Zn-based Broad Spectrum Respirator Carbons

Sections of this chapter, including figures and tables, have been submitted for publication in the Journal of Hazardous Materials. The manuscript title is "The Effect of Co-impregnated Acids on the performance of Zn-based Broad Spectrum Respirator Carbons". The authors are Jock Smith, Jennifer Romero, Tara Dahn, Kevin Dunphy, Lisa Croll and Jeff Dahn. The contribution of Jock Smith to the manuscript consists of organization of sample preparation and experiments, assistance with sample preparation and characterization, all of the data analysis and figure and manuscript preparation. The figures have been reproduced by permission of the Journal in accordance with the terms of the publishing company (Elsevier) copyright release (see Appendix A). Some of the text, figure numbers and references have been modified for inclusion in this thesis.

8.1 Introduction

In this work a comparative study of some common acids co-impregnated with a $Zn(NO_3)_2$ precursor on an AC substrate was performed. The samples were heated at temperatures sufficient to promote conversion of the $Zn(NO_3)_2$ impregnant to ZnO. For comparative purposes, AC samples impregnated with different types of acids, and no metallic impregnant were also studied. The acids studied in this work were phosphoric acid (H_3PO_4), tartaric acid ($C_4H_6O_6$), sulphuric acid (H_2SO_4), hydrochloric acid (HCl) and acetic acid ($C_2H_4O_2$). For comparative purposes IACs were prepared using HNO_3. The goal of this work was to determine if multi-gas IACs, with improved humid C_6H_{12} capacity, could be prepared by co-impregnating $Zn(NO_3)_2$ with acids other than HNO_3.

8.2 Experimental Details

8.2.1 Chemicals Used

The chemicals used to prepare the impregnating solutions (and the supplier they were obtained from) were $Zn(NO_3)_2 \bullet 6H_2O$ and HNO_3 (Sigma-Aldrich), $C_4H_6O_6$ (Aldrich), HCl (AMD), H_3PO_4, H_2SO_4 and $C_2H_4O_2$ (Fisher Scientific). All chemicals were reagent grade.

8.2.2 Sample Preparation

All of the IACs described in this chapter were prepared using GC activated carbon which was previously described in section 3.1. IACs containing $Zn(NO_3)_2$ precursors were prepared by impregnating GC with 2.4 M $Zn(NO_3)_2$ and 4 M acidic solutions. The samples prepared from solutions containing tartaric acid were impregnated with 1.2 M $Zn(NO_3)_2$/2 M $C_4H_6O_6$ due to solubility issues. IAC samples prepared without $Zn(NO_3)_2$ in the impregnating solution were prepared from 0.5 M and 4 M acidic solutions. The GC substrate was impregnated using the imbibing method. Typically 10 - 12 mL of solution was applied to 15 g of GC.

The IACs reported in this work were heated under flowing argon in a tube furnace. Typically, a 15 g sample would be heated at 115°C and held for 1 hour, then ramped to 200°C and held at this temperature for $2\frac{1}{2}$ - 3 hours. Details of the heating conditions and determination of the % impregnant loading have been discussed earlier (see section 2.1 or section 7.2.1 for example).

8.3 Results and Discussion

8.3.1 Impregnant Loading

Samples with no metallic impregnant were prepared by impregnating GC with 0.5 M and 4 M acidic solutions. Figure 8.1 shows the observed % impregnant loading of the IACs impregnated with acidic solutions as determined by gravimetric analysis. Figure 8.1 shows that IACs prepared from HNO_3, $C_2H_4O_2$ and HCl had relatively low impregnant loading after heating but samples prepared from H_3PO_4, H_2SO_4 and

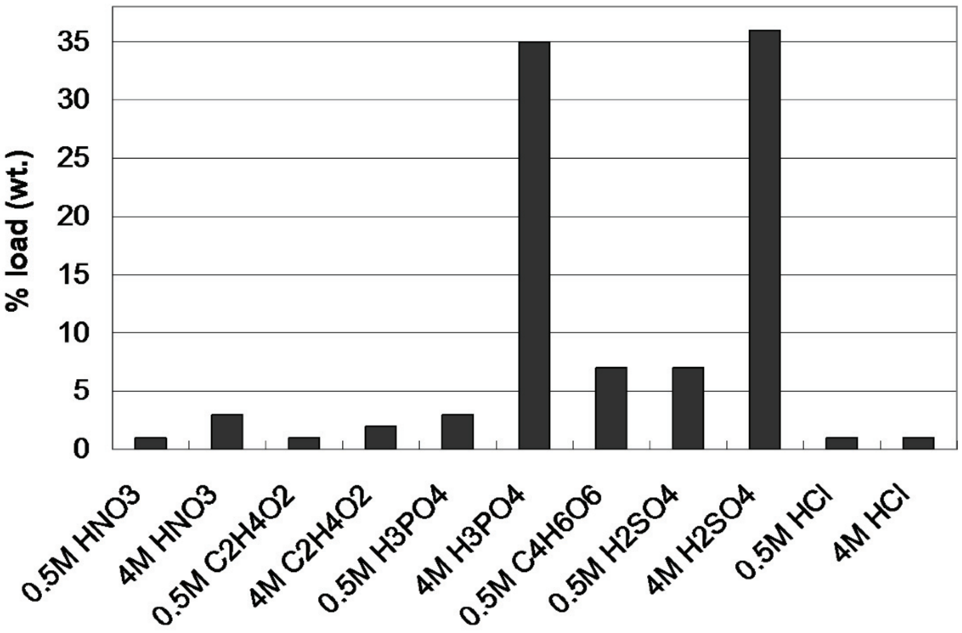

Figure 8.1: Observed % impregnant loading of the IACs impregnated with acidic solutions as determined by gravimetric analysis.

$C_4H_6O_6$ had impregnant loadings consistent with all of the impregnating material being present after heating. These findings are reasonable when the boiling points of these materials are considered [93]. There was no IAC prepared from 4 M $C_4H_6O_6$ due to solubility issues. The samples shown in Figure 8.1 were prepared for comparative purposes and will be discussed further below.

IACs were also prepared by co-impregnating GC with 2.4-2.5 M $Zn(NO_3)_2$ and 4 M acidic solutions. These samples were heated at T_f = 200°C under argon and their impregnant loading was determined after cooling to room temperature. Figure 8.2 shows the observed % impregnant loading of the co-impregnated IACs as determined by gravimetric analysis. For reference the predicted loading for GC impregnated with ZnO is indicated.

Figure 8.2 shows that the IAC prepared from $Zn(NO_3)_2$ and HNO_3 had slightly higher than predicted impregnant loading. The additional mass can be explained by the introduction of surface oxygen groups from the HNO_3 treatment. A comparison of the Zn/HNO_3 data to the 4 M HNO_3 data in Figure 8.1 shows that the gravimetric

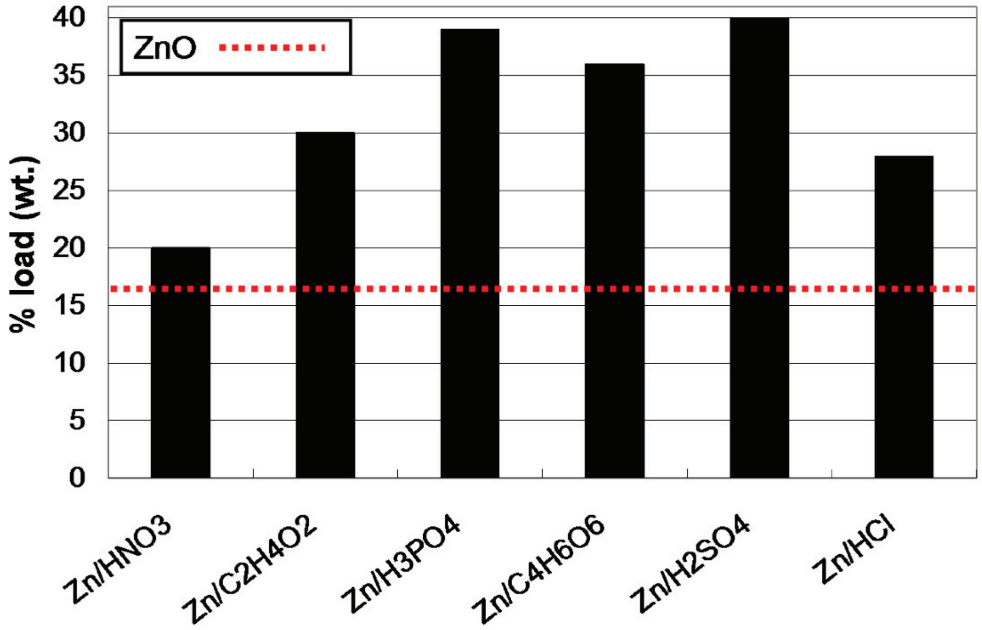

Figure 8.2: Observed % impregnant loading of the co-impregnated IACs as determined by gravimetric analysis. For reference the predicted loading for GC impregnated with ZnO is indicated.

data are consistent with ZnO being the dominant impregnant phase. The IACs co-impregnated with $Zn(NO_3)_2$ and $C_2H_4O_2$, or $Zn(NO_3)_2$ and HCl, show higher than expected impregnant loading. The % impregnant loading shown in Figure 8.2 for these two cases is greater than the sum of the loading due to the heated $C_2H_4O_2$, or HCl, alone (as shown in Figure 8.1) and the loading of ZnO alone (as indicated in Figure 8.2) on the IAC. Similarly, if the co-impregnated chemicals $Zn(NO_3)_2$ and H_3PO_4, or $Zn(NO_3)_2$ and H_2SO_4 are assumed not to interact during thermal decomposition, the observed impregnant loading (in Figure 8.2) does not make sense. Calculations based on the co-impregnated chemicals interacting, or not interacting, during thermal decomposition are shown in Table 8.1. The non-interacting calculations are the sum of the data shown in Figure 8.1 (for IACs prepared from 4 M solutions) and the loading of ZnO impregnant (indicated in Figure 8.2). The interacting calculations are based on the volume and concentration of the impregnating solution added to the GC. The predicted decomposition products (for the interacting case) are indicated in Table 8.1.

Table 8.1: Observed and predicted % impregnant loadings for the IACs prepared in this study. The asterisk denotes that only mass due to the ZnO impregnant was used in the predicted % load calculation.

Sample	Observed % load (wt.)	Predicted % load (non-interacting)	Predicted % load (interacting)	Predicted decomposition product
Zn/HNO_3	20	19	16*	ZnO
$Zn/C_2H_4O_2$	30	18	30	ZnC_2O_4
Zn/H_3PO_4	39	51	35	$Zn_3(PO_4)_2 + H_3PO_4$
$Zn/C_4H_6O_6$	36	n/a	35	$ZnC_4H_4O_6$
Zn/H_2SO_4	40	52	42	$ZnSO_4 + H_2SO_4$
Zn/HCl	28	17	29	$ZnCl_2 \bullet H_2O$

Table 8.1 shows that all of the co-impregnated acids, except for HNO_3, are interacting with the $Zn(NO_3)_2$ precursor during heating. The interacting % impregnant loading calculations indicate that samples impregnated with $Zn(NO_3)_2$ and $C_2H_4O_2$, $Zn(NO_3)_2$ and HCl, or $Zn(NO_3)_2$ and $C_4H_6O_6$ form ZnC_2O_4 (zinc oxalate), $ZnCl_2 \bullet H_2O$ (zinc chloride hydrate) and $ZnC_4H_4O_6$ (zinc tartrate) respectively. Samples prepared from $Zn(NO_3)_2$ and H_3PO_4 or $Zn(NO_3)_2$ and H_2SO_4 appear to have formed $Zn_3(PO_4)_2$ (zinc phosphate) and $ZnSO_4$ (zinc sulphate) respectively as the dominant impregnant phases after heating. In both latter cases the excess acid appears to have remained on the IAC sample after heating, this is expected based on the results shown in Figure 8.1.

8.3.2 XRD Characterization

To study the phase of the impregnant present after heating, powder XRD experiments were performed. Figure 8.3 shows XRD patterns obtained from the samples listed in Table 8.1. An IAC sample prepared from 2.4 M $Zn(NO_3)_2$ with no co-impregnant, that recieved the same thermal treatment as the other IAC samples in this study, has been included for comparative purposes. For reference the main Bragg peak positions for the expected decomposition products have been indicated [56]. The Bragg peak positions for $ZnC_4H_4O_6$ were obtained by digitizing data from Figure 1 of Ref. [106].

Figure 8.3(a) shows that the heating conditions used in this study were sufficient to thermally decompose $Zn(NO_3)_2$ to ZnO. Comparing Figures 8.3(a) and 8.3(c) shows

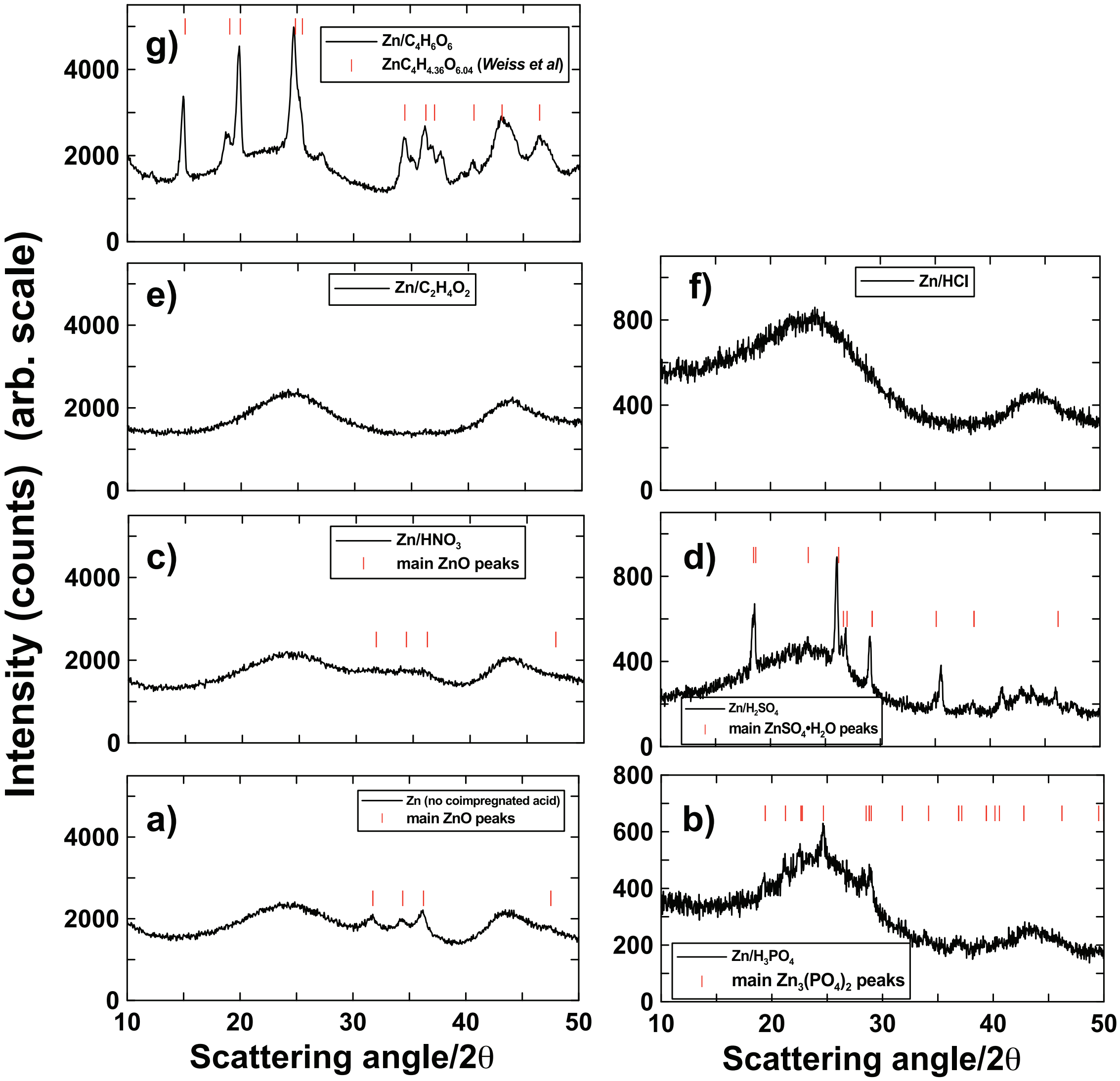

Figure 8.3: XRD patterns obtained from the samples listed in Table 8.1. For reference the main Bragg peak positions for the expected decomposition products have been indicated.

that co-impregnating $Zn(NO_3)_2$ and HNO_3 results in a dramatic reduction (or elimination) of the ZnO diffraction peaks. This is indicative of small grain size ZnO as can be inferred from the Scherrer equation (Eq. 2.5). Work presented in chapters 5, 6 and 7 shows co-impregnation with HNO_3 improves dispersion of the impregnant on the AC substrate. This is consistent with results reported in the literature [24,41,91]. Work presented in chapters 5, 6 and 7 shows that well distributed, small particle size impregnant has optimal gas adsorption capacity for SO_2, NH_3 and HCN gases. Figures 8.3(e) and 8.3(f) show diffraction patterns obtained from the $Zn/C_2H_4O_2$ and Zn/HCl samples respectively. These diffraction patterns do not display impregnant related diffraction peaks. The broad humps centered at $2\theta \approx 22^\circ$ and 44° are consistent with scattering from disordered carbon [2].

Figure 8.3(b) shows the diffraction pattern obtained from the Zn/H_3PO_4 sample. Relatively weak impregnant related diffraction peaks, that match $Zn_3(PO_4)_2$, are observed. The diffraction data shown in 8.3(d) and 8.3(g) have intense, narrow peaks, implying relatively large impregnant grain size. The pattern obtained from Zn/H_2SO_4 is well charecterized by the reference pattern for $ZnSO_4 \bullet H_2O$. The IAC prepared from $Zn/C_4H_6O_6$ is matched by $ZnC_4H_4O_6$. The results shown in Figures 8.3(a), 8.3(b), 8.3(c), 8.3(d) and 8.3(g) support the proposed impregnant phases in Table 8.1. The effect of impregnant phase and distribution will be discussed in terms of gas adsorption capacity below.

8.3.3 Flow Test Results

Figure 8.4 shows flow test results obtained from the samples prepared in this study. Panels (a) and (b) show results obtained from samples impregnated with 0.5 M and 4 M acidic solutions respectively. The IACs prepared from 0.5 M and 4 M acidic solutions in this study were not tested for HCN adsorption capacity due to limited sample size and testing availability. Un-impregnated AC and AC samples treated with oxidizing agents were shown to react weakly with HCN gas in Figures 3.4, 3.10 and 5.10. This is consistent with results reported in the literature [18]. These samples were observed to have short HCN breakthrough times relative to IACs impregnated with metallic oxides. Figure 8.4(c) shows flow test results obtained from IACs co-impregnated with $Zn(NO_3)_2$ and 4 M acidic solutions. The flow test results for IACs containing Zn^{2+} impregnant are reported in terms of breakthrough time of the challenge gas. All the metal containing samples had approximately the same loading of Zn^{2+} impregnant so the breakthrough time is proportional to the relative stoichiometric ratio of reaction [22,25]. Due to limited sample size and testing availibility no dry C_6H_{12} flow tests were performed.

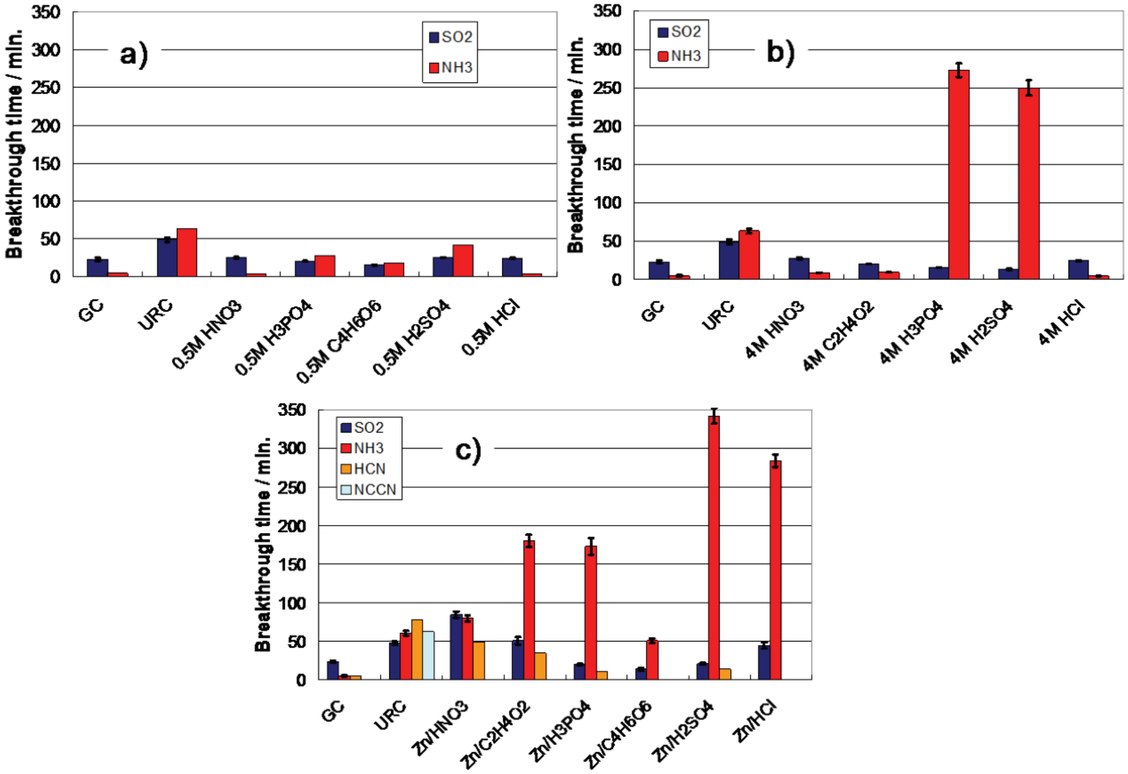

Figure 8.4: Flow test results obtained from the samples prepared in this study. Panels (a) and (b) show results obtained from samples impregnated with 0.5 M and 4 M acidic solutions respectively. Panel (c) shows results obtained from IACs co-impregnated with $Zn(NO_3)_2$ and 4 M acidic solution. Results obtained from GC and URC are indicated for reference.

Figure 8.4(a) shows that samples prepared from 0.5 M acidic solutions had relatively low dry SO_2 and NH_3 capacity. All of the samples had dry SO_2 breakthrough times approximately equal to GC and shorter than URC. The 0.5 M $C_4H_6O_6$ sample had the lowest SO_2 capacity of the samples and it was also lower than GC. The 0.5 M H_3PO_4, 0.5 M $C_4H_6O_6$ and 0.5 M H_2SO_4 samples all displayed some dry NH_3 adsorption capacity. These samples had impregnant loadings (see Figure 8.1) that were consistent with all of the impregnated acid being present after heating so some adsorption of the basic NH_3 gas was expected. The 0.5 M HNO_3 and 0.5 M HCl samples had almost no NH_3 capacity. These samples displayed little impregnant loading after heating, as was shown in Figure 8.1. The data in Figure 8.4(b) shows a similar trend for the samples impregnated with 4 M acidic solutions. IACs that displayed relatively high impregnant loading in Figure 8.1 show high NH_3 capacity in Figure 8.4(b). The 4 M H_3PO_4 and 4 M H_2SO_4 samples have NH_3 breakthrough times $\geq$ 250 minutes. High NH_3 capacity for AC activated with H_2SO_4 has been reported in the literature [107]. The 4 M HNO_3, 4 M $C_2H_4O_2$ and 4 M HCl samples all displayed low impregnant loadings (Figure 8.1) and have poor NH_3 capacity (Figure 8.4). The 4 M H_3PO_4 and 4 M H_2SO_4 IACs have lower SO_2 capacity than GC. It is likely that the pressence of impregnated acid in these samples is responsible for their reduced ability to adsorb the acidic SO_2 gas. The 4 M HNO_3, 4 M $C_2H_4O_2$ and 4 M HCl samples all had SO_2 capacity approximately equal to GC and less than URC.

Figure 8.4(c) shows that the Zn/HNO_3 sample had the best SO_2 capacity of all the samples tested in this study, including the URC sample. The Zn/$C_2H_4O_2$ and Zn/HCl samples had dry SO_2 breakthrough times that were similar to those observed for the URC sample. The SO_2 capacities of the samples in this study rank as: Zn/HNO_3 > Zn/$C_2H_4O_2$ > Zn/HCl > Zn/H_2SO_4 $\approx$ Zn/H_3PO_4 > Zn/$C_4H_6O_6$. Comparison of the SO_2 breakthrough times to the XRD patterns in Figure 8.3 shows that IACs with less intense impregnant diffraction peaks had longer dry SO_2 breakthrough times. $ZnCl_2$ is not known to be a good impregnant for the adsorption of SO_2. The longer than expected breakthrough time reported for the Zn/HCl sample in Figure 8.4(c) may be due to a combination of good impregnant distribution and the presence of a small amount of water on the impregnant (as indicated in Table 8.1). The pressence of water was shown to improve IACs and ACs ability to adsorb SO_2 in Figures 3.14 and 3.4 and has been reported in the literature [13, 42].

Comparing Figures 8.4(b)and 8.4(c) shows that NH_3 capacity is much higher when the Zn^{2+} impregnant was present. The NH_3 capacity of the IACs shown in Figure 8.4(c) ranks as: Zn/H_2SO_4 > Zn/HCl > Zn/H_3PO_4 $\approx$ Zn/$C_2H_4O_2$ > Zn/HNO_3 > Zn/$C_4H_6O_6$. All of the samples except for the Zn/$C_4H_6O_6$ IAC had better NH_3 adsorption capacity than the URC sample. The Zn/H_2SO_4 sample has the longest dry NH_3 breakthrough time. The dominant impregnant phase in this sample was $ZnSO_4 \bullet H_2O$ as was indicated in Table 8.1 and Figure 8.3(d). The pressence of the $SO_4{}^{2-}$ anion has been corelated with NH_3 adsorption in the literature [13, 23]. The

XRD data imply that this sample had relatively large grain size $ZnSO_4{\bullet}H_2O$ impregnant, however the NH_3 adsorption was good. The Zn/HCl IAC had long NH_3 breakthrough times. In comparison samples impregnated with the same concentration of HCl, with no Zn^{2+} impregnant present had almost no NH_3 capacity. The results presented in Table 8.1 indicated that $ZnCl_2{\bullet}H_2O$ was the dominant impregnant phase in this sample and the flow test results shown in Figure 8.4(c) support this. $ZnCl_2$ IACs have been reported to be effective for removing NH_3 from gas streams and reaction mechanisims have been presented in the literature [22, 108]. Comparison of the $Zn/C_2H_4O_2$, and 4 M $C_2H_4O_2$ IACs shows that the pressence of the Zn^{2+} impregnant results in an approximately 20 fold increase in the NH_3 breakthrough time. The dominant impregnant phase for the $Zn/C_2H_4O_2$ IAC was ZnC_2O_4. By contrast, the Zn/H_3PO_4 IAC displayed a reduction in NH_3 capacity compared to the 4 M H_3PO_4 sample. This sample had $Zn_3(PO_4)_2$ as the dominant impregnant phase after heating. The $Zn/C_4H_6O_6$ IAC had $ZnC_4H_4O_6$ as its dominant impregnant phase. This sample had the lowest NH_3 (and SO_2) capacity of the IACs in this study.

Due to sample size and testing limitations the Zn/HCl and $Zn/C_4H_6O_6$ IACs were not tested for HCN capacity. Figure 8.4(c) shows that the HCN capacity of the IACs ranks as: $Zn/HNO_3 > Zn/C_2H_4O_2 > Zn/H_2SO_4 > Zn/H_3PO_4$. None of the Zn^{2+} impregnated samples had HCN capacity that was as good as URC. Optimal impregnation recipes for URC are predominately based on Cu^{2+} impregnant [13] and it has been reported that Cu^{2+} impregnants (typically present as CuO) typically have better HCN capacity than Zn^{2+} impregnants (refer to Figures 5.10 and 4.5). The advantage of Zn-based samples is that unlike Cu^{2+} impregnants they do not usually generate toxic NCCN as a reaction by-product (see Equations 1.1 and 5.4). Reaction mechanisims are discussed in the litterature [4, 9, 17]. None of the Zn-based IACs in this work generated NCCN during their HCN flow tests. Comparing the NCCN breakthrough time from the URC sample to the HCN breakthrough time for the Zn/HNO_3 sample shows that their overall HCN/NCCN capacity is similar. The $Zn/C_2H_4O_2$ IAC displayed reasonably good HCN capacity indicating that the ZnC_2O_4 impregnant phase may be useful for broad spectrum respirator carbon applications. The Zn/H_2SO_4 and Zn/H_3PO_4 IACs displayed relatively poor HCN capacity that was only slightly better than un-impregnated GC.

Figure 8.5 shows humid C_6H_{12} flow test results obtained from the Zn-based IACs in this study as detailed in the figure caption. The Zn/HNO_3 sample was not tested. ZnO based samples prepared with HNO_3 co-impregnation were shown to have poor humid C_6H_{12} capacity in Figure 5.15(a). For reference flow test results obtained from GC and URC are included.

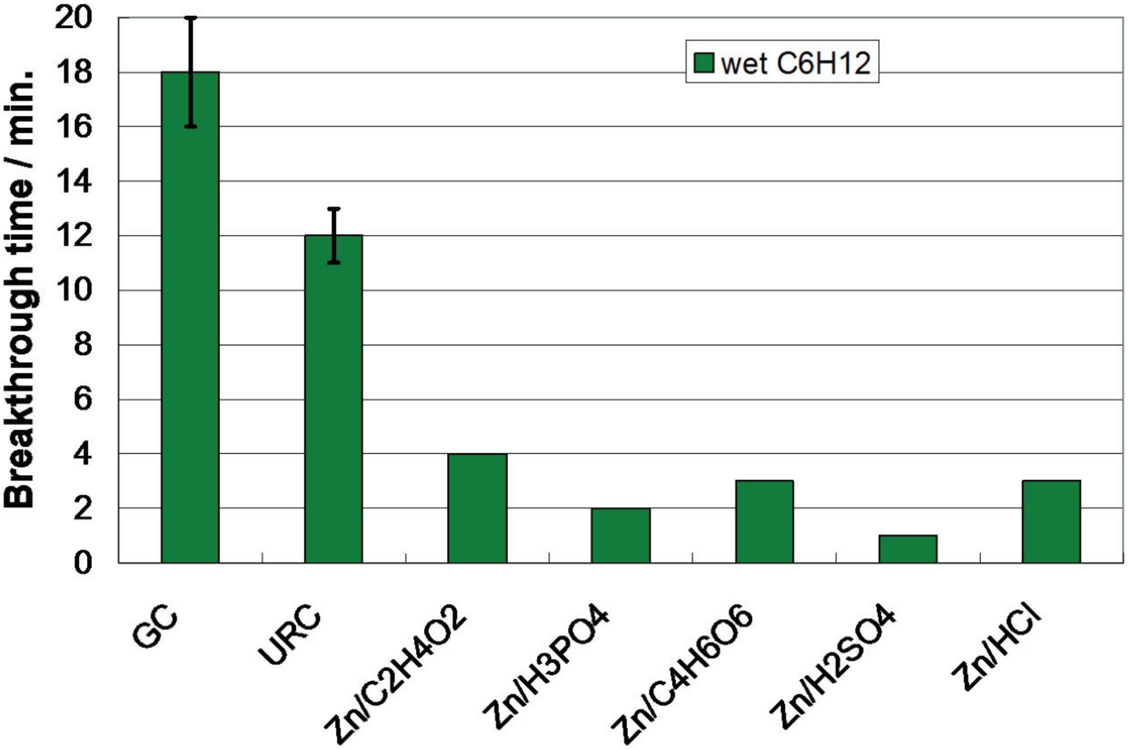

Figure 8.5: Humid C_6H_{12} flow test results obtained from the samples prepared in this study. The Zn/$C_2H_4O_2$, Zn/H_3PO_4, Zn/$C_4H_6O_6$, Zn/H_2SO_4 and Zn/HCl IACs were tested. Results obtained from GC and URC are indicated for reference.

Figure 8.5 shows that all of the Zn-based IACs prepared and tested in this work had shorter humid C_6H_{12} breaktrhough times than GC or URC. These results indicate that none of the co-impregnated acids chosen here can be used to replace HNO_3 in the preparation of multi-gas IACs with improved humid C_6H_{12} adsorption.

8.4 Summary of the Most Effective Samples

Figure 8.6 shows a radar plot summarizing the flow test results obtained from the most effective multi-gas IACs discussed in chapter 8 as detailed in the figure caption. Figure 8.6 shows that the Zn/HNO_3, Zn/$C_2H_4O_2$ and Zn/HCl samples all had longer dry SO_2 breakthrough times than GC and had breakthrough times that were longer than or equal to URC. The Zn/HNO_3 sample had the longest dry SO_2 breakthrough time of the samples in this study and had the same SO_2 capacity as the Zn-4M A-180 sample.

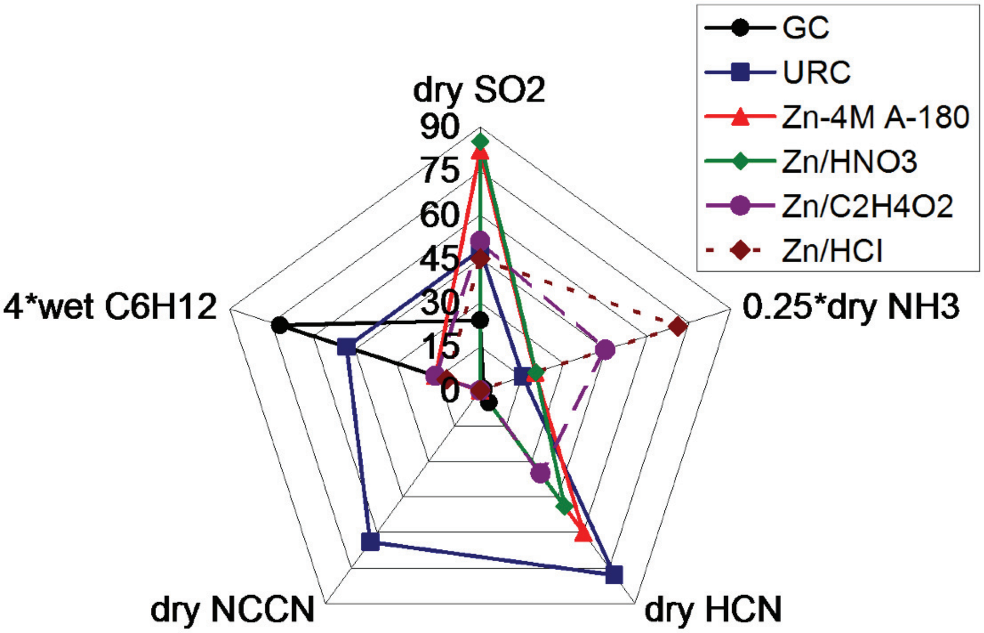

Figure 8.6: Radar plot summarizing flow test results obtained from the Zn/HNO_3, Zn/$C_2H_4O_2$ and Zn/HCl samples. Results obtained from dry SO_2, NH_3, HCN, NCCN and humid C_6H_{12} tests are reported on individual axes. Results obtained from the dry NH_3 and humid C_6H_{12} flow tests have been scaled, by the amount indicated on their respective axis, to allow for improved data presentation. Results obtained from GC, URC and the Zn-4M A-180 sample (discussed in chapter 5) have been included for reference.

Figure 8.6 shows that the Zn/HNO_3, Zn/$C_2H_4O_2$ and Zn/HCl samples all had longer dry NH_3 breakthrough times than GC and breakthrough times equal to or greater than the URC and Zn-4M A-180 samples. Sample Zn/HCl had a dry NH_3

breakthrough time that was 3 - 4 times longer than the URC, Zn/HNO_3 and Zn-4M A-180 samples. The Zn/$C_2H_4O_2$ sample had over 2 times the NH_3 capacity of the URC, Zn/HNO_3 and Zn-4M A-180 samples.

Figure 8.6 shows that the Zn/HNO_3 and Zn/$C_2H_4O_2$ samples had longer dry HCN breakthrough times than GC, but shorter times than URC or the Zn-4M A-180 sample. No HCN test was performed on the Zn/HCl sample. None of the Zn-based IACs evolved NCCN during HCN exposure. When the HCN/NCCN breakthrough times are considered together, the Zn/HNO_3 has close to the same capacity as the Zn-4M A-180 and URC samples. All of the Zn-based IACs co-impregnated with 4 M acidic solutions had poor humid C_6H_{12} capacity relative to the URC and un-impregnated GC samples.

8.5 Conclusions

Using gravimetric analysis, XRD and dynamic flow testing, IAC samples prepared from acidic solutions and $Zn(NO_3)_2$/acidic solutions were characterized. It was observed that samples prepared from HNO_3, $C_2H_4O_2$ or HCl had low impregnant loading after heating. These samples had poor gas adsorption capacity. Co-impregnating these acids with $Zn(NO_3)_2$, followed by heating at T_f = 200°C under argon produced IACs with ZnO, ZnC_2O_4 and $ZnCl_2 \bullet H_2O$ as their respective dominant impregnant phases. XRD data obtained from these samples were consistent with small impregnant grain size. These samples had relatively good SO_2, NH_3 and HCN gas adsorption capacity.

Samples prepared from H_2SO_4, H_3PO_4 and $C_4H_6O_6$ had relatively high impregnant loading after heating. These IACs had good NH_3 capacity but poor SO_2 capacity. This was attributed to the pressence of residual acid after heating. IACs co-impregnated with $Zn(NO_3)_2$ and H_2SO_4 had $ZnSO_4 \bullet H_2O$ as the dominant impregnant phase after heating. These samples had the best overall NH_3 capacity, but displayed relatively poor SO_2 and HCN capacities. Co-impregnating $Zn(NO_3)_2$ and H_3PO_4 produced IACs with lower NH_3 capacity than samples prepared from H_3PO_4 alone. These samples did not have good SO_2 or HCN capacity. IACs prepared using $C_4H_6O_6$ and $Zn(NO_3)_2$/$C_4H_6O_6$ were found to have the lowest overall gas adsorption capacity of the samples studied in this work.

The overall gas adsorption capacity of the IACs co-impregnated with $Zn(NO_3)_2$ and 4 M acid ranks as: $HNO_3 > C_2H_4O_2 > HCl > H_2SO_4 > H_3PO_4 > C_4H_6O_6$. None of the IACs reported in this work have humid C_6H_{12} capacity that is as good as the comercially available URC sample. These results indicate that in addition to HNO_3, $C_2H_4O_2$ and HCl may be useful co-impregnants when preparing broad spectrum respirator carbons if humid C_6H_{12} adsorption is not required. The samples prepared from $Zn(NO_3)_2$ and H_2SO_4 had the highest NH_3 capacity. $Zn(NO_3)_2$ is much more soluble in water than $ZnSO_4$, so co-impregnating ACs with $Zn(NO_3)_2$ and H_2SO_4 may be a useful way to produce $ZnSO_4$-based IACs when high impregnant loading is required. Co-impregnating with H_3PO_4 or $C_4H_6O_6$ was not found to be benificial in this work.

Chapter 9

The Effect of Co-impregnation with Sugars on Broad Spectrum Respirator Carbons

Work presented in the preceding chapters has shown that multi-gas IACs can be prepared by co-impregnating AC with a metal nitrate precursor(s) and properly selected acid (e.g. HNO_3, HCl or $C_2H_4O_2$). Samples that were heated at 180 - 200°C, were effective for adsorption of SO_2, NH_3, HCN and dry C_6H_{12} gases, but had poor wet C_6H_{12} adsorption. In this chapter a comparative study of multi-gas IACs prepared by co-impregnation with sugars is presented. The motivation for this study was to improve humid C_6H_{12} capacity without losing adsorption capacity for the other challenge gases. It was postulated that co-impregnation with sugar might allow a "sacrificial burn-off" of carbon from the sugar, to prevent the oxidation of the AC substrate (see Eq. 5.1 for example). Care must be taken when preparing samples with a strong oxidizing agent (e.g $Cu(NO_3)_2$) and a reducing agent (e.g. sucrose) due to the possibility of thermal runaway. In this work the temperature of the sample was monitored using a thermocouple to ensure the IACs did not go into thermal runaway.

9.1 Chemicals Used

The chemicals used to prepare the impregnating solutions were copper nitrate hemipentahydrate ($Cu(NO_3)_2 \bullet 2.5H_2O$) and 12- Molybdophosphoric acid hydrate ($H_3PO_4 \bullet 12MoO_3 \bullet xH_2O$) (obtained from Alfa Aesar, reagent grade), zinc nitrate hexahydrate ($Zn(NO_3)_2 \bullet 6H_2O$) (Sigma-Aldrich reagent grade), copper sulfate pentahydrate ($CuSO_4 \bullet 5H_2O$) (Anachemia, reagent grade), zinc sulfate heptahydrate ($Zn(SO_4 \bullet 7H_2O)$), sucrose ($C_{12}H_{22}O_{11}$), glucose ($C_6H_{12}O_6$) and copper D-gluconate ($C_{12}H_{22}CuO_{14}$) (obtained from Aldrich, reagent grade) and D-gluconic acid solution ($C_6H_{12}O_7$) (obtained from Sigma-Aldrich, 49 - 53% in H_2O).

9.2 Co-impregnation with Copper D-gluconate

9.2.1 Sample Preparation

Prior to sample preparation a TGA experiment was performed to determine the optimal heating temperature to use in the $C_{12}H_{22}CuO_{14}$ IAC study. Figure 9.1 shows TGA data obtained from a sample that was impregnated with 0.6 M $C_{12}H_{22}CuO_{14}$. Prior to the TGA experiment the sample was heated, in air, at 90°C. The TGA experiment was performed under 50 mL/min argon flow at a heating rate of 5°C/min. Figure 9.1 shows a peak in the derivative TGA data that is centered at $\approx$ 200°C. It

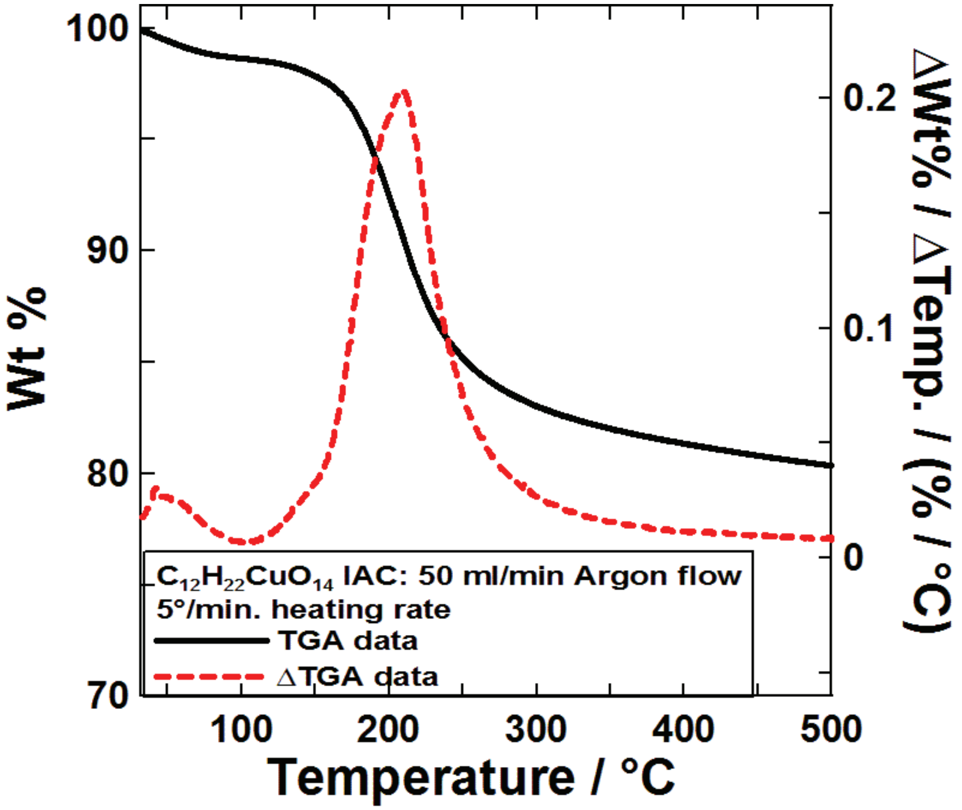

Figure 9.1: TGA data obtained from a GC sample impregnated with 0.6 M $C_{12}H_{22}CuO_{14}$. The experimental conditions are indicated in the legend. The TGA data (solid black line) is displayed with respect to the Wt% axis, the derivative TGA data (ΔTGA, red dashed line) is associated with the ΔWt%/Δ Temp. axis.

was decided that IAC samples impregnated or co-impregnated with $C_{12}H_{22}CuO_{14}$

should be heated at $T_f = 180°C$ and 250°C. These heating temperatures correspond to points before and after the peak on the derivative TGA curve shown in Figure 9.1.

IAC samples were prepared by impregnating GC activated carbon. GC was previously described in section 3.1. The GC substrate was impregnated using the imbibing method. The IAC samples were prepared in one imbibing and heating step. Details of the heating conditions and determination of the % impregnant loading have been discussed in earlier sections (see section 2.1 or section 7.2.1). Table 9.1 lists the sample names, imbibing solution contents and heating temperatures used to prepare IACs in this work.

Table 9.1: Sample preparation details of IACs impregnated or co-impregnated with $C_{12}H_{22}CuO_{14}$.

Sample	Imbibing solution contents	T_f (°C)
A	11 mL of 0.3 M $C_{12}H_{22}CuO_{14}$ per 15 g GC	180
B	11 mL of 0.6 M $C_{12}H_{22}CuO_{14}$ per 15 g GC	180
C	11.5 mL of 2.3 M $Zn(NO_3)_2$ / 0.1 M $C_{12}H_{22}CuO_{14}$ per 15 g GC	180
D	11.5 mL of 2.1 M $Zn(NO_3)_2$ / 0.3 M $C_{12}H_{22}CuO_{14}$ per 15 g GC	180
E	11.5 mL of 1.8 M $Zn(NO_3)_2$ / 0.6 M $C_{12}H_{22}CuO_{14}$ per 15 g GC	180
F	11.5 mL of 2.3 M $Zn(NO_3)_2$ / 0.1 M $C_{12}H_{22}CuO_{14}$ per 15 g GC	250
G	11.5 mL of 2.1 M $Zn(NO_3)_2$ / 0.3 M $C_{12}H_{22}CuO_{14}$ per 15 g GC	250
H	11.5 mL of 1.1 M $Zn(NO_3)_2$ / 1.0 M $ZnCl_2$ / 0.3 M $C_{12}H_{22}CuO_{14}$ per 15 g GC	250
I	11.5 mL of 1.4 M $Zn(NO_3)_2$ / 0.7 M $ZnCl_2$ / 0.3 M $C_{12}H_{22}CuO_{14}$ per 15 g GC	250
J	11.5 mL of 1.2 M $Zn(NO_3)_2$ / 1.1 M $ZnCl_2$ / 0.1 M $C_{12}H_{22}CuO_{14}$ per 15 g GC	250
K	11.5 mL of 1.6 M $Zn(NO_3)_2$ / 0.7 M $ZnCl_2$ / 0.1 M $C_{12}H_{22}CuO_{14}$ per 15 g GC	250

Table 9.1 shows that for samples C → K the overall concentration of the impregnating solution was 2.4 M. Samples A and B were impregnated with $C_{12}H_{22}CuO_{14}$ only. For samples C → E the concentration of $Zn(NO_3)_2$ in the impregnating solution decreased and the concentration of $C_{12}H_{22}CuO_{14}$ increased. Samples F and G were

impregnated with the same solutions as samples C and D respectively. These pairs of IACs were heated at different temperatures. Samples H → K were prepared from solutions containing combinations of $Zn(NO_3)_2$, $ZnCl_2$ and $C_{12}H_{22}CuO_{14}$.

9.2.2 Impregnant Loading

Table 9.2 shows the observed and predicted % impregnant loading for the IACs prepared from the impregnating solutions detailed in Table 9.1. The predicted % loading was calculated using the following assumptions:

1. The heating temperature was sufficient to promote full conversion of the $Zn(NO_3)_2$ precursor to ZnO.

2. The first predicted % impregnant loading (Predicted % load (1)) assumes 50% mass loss of the $C_{12}H_{22}CuO_{14}$ impregnant after heating. This assumption was based on TGA data of the thermal decomposition of $C_{12}H_{22}CuO_{14}$ (not shown) in the heating temperature range used during sample preparation.

3. The second predicted % impregnant loading (Predicted % load (2)) assumes ZnO, Cu and zinc gluconate ($C_{12}H_{22}ZnO_{14}$) are the only impregnants present on the GC substrate after heating.

Table 9.2: Observed and predicted % impregnant loadings for the IACs detailed in Table 9.1.

Sample	Observed % load (wt.)	Predicted % load (1)	Predicted % load (2)
A	5	5	n/a
B	11	10	n/a
C	18	16	18
D	22	18	23
E	25	22	31
F	20	16	18
G	16	18	23
H	22	23	20
I	24	21	26
J	19	21	22
K	18	19	28

Table 9.2 shows that there is reasonable agreement between the observed and predicted % impregnant loading. The predicted % load (2) values tend to be higher than the observed % load values when 0.3 M or 0.6 M $C_{12}H_{22}CuO_{14}$ was used. To try to better identify the impregnant phase present after heating powder XRD experiments were performed.

9.2.3 XRD Characterization

Figure 9.2 shows XRD data collected from samples A, B, C, D and E in panel (a) and samples F, G, H, I, J and K in panel (b). For reference the diffraction pattern obtained from GC has been included. The main Bragg peak positions for Cu_2O, Cu and ZnO ([00-078-2076], [00-004-0836] and [00-089-1397] in [56]) have been indicated.

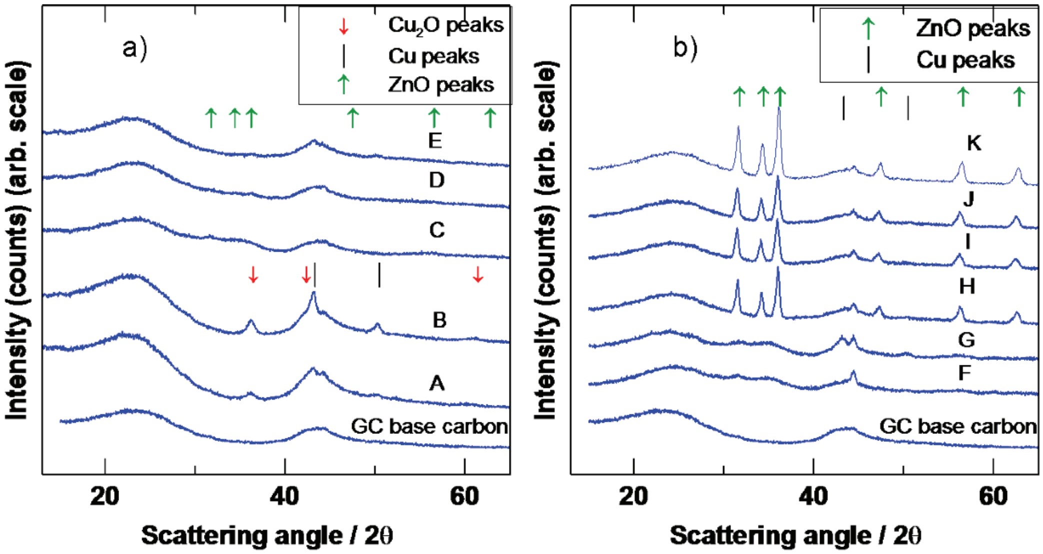

Figure 9.2: XRD data obtained from the samples described in Table 9.1. Samples A → E are shown in panel (a) and samples F → K are shown in panel (b). For reference XRD data from GC is included in both panels. The main Bragg peak positions for Cu_2O, Cu and ZnO are indicated.

Figure 9.2 shows that Cu_2O and Cu impregnant are present after heating samples A and B. The intensity of the impregnant related peaks increases from sample A to sample B. Sample B had more impregnated $C_{12}H_{22}CuO_{14}$ than sample A. There are no obvious impregnant related diffraction peaks present in the data obtained from samples C, D and E. Comparison of the data obtained from the sample C and the GC sample in the scattering angle range $30° \leq 2\theta \leq 40°$ shows that there is a broad hump present in the data from sample C, but no hump is present in the data from the GC sample. The broad hump in the data from sample C may indicate that small grain size ZnO impregnant is present.

Figure 9.2(b) shows that the data obtained from samples F and G has broad humps present in the scattering angle range $30° \leq 2\theta \leq 40°$. This may indicate the presence of small grain size ZnO impregnant. These samples had relatively weak impregnant related diffraction peaks at $\approx 44°$ which may be related to the presence of Cu_2O or Cu. Comparing the data obtained from samples F and G to the data from samples C, D and E shows that the increased heating temperature did not result in a significant increase in impregnant grain size.

Figure 9.2 shows that the data obtained from samples H, I, J and K have relatively intense ZnO diffraction peaks present. This indicates the pressence of relatively large grain size ZnO impregnant as can be inferred from the Scherrer equation (Eq. 2.5). No diffraction peaks corresponding to the $ZnCl_2$ impregnant phase were observed in samples H → K. Comparing the XRD data obtained from samples H and G shows that sample H has larger grain size ZnO present. Table 9.1 shows that sample G had almost two times the concentration of $Zn(NO_3)_2$ present in it's impregnating solution compared to sample H. Sample H had $ZnCl_2$ present, but sample G did not. It appears that the pressence of co-impregnated $ZnCl_2$ results in the formation of large grain size ZnO impregnant during heating.

9.2.4 Flow Test Results

Figure 9.3 shows the dry breakthrough times obtained from flow testing the samples described in Tables 9.1 and 9.2 with SO_2, NH_3, HCN and C_6H_{12} gases as detailed in the figure caption. Figure 9.3(a) shows that samples C, D and E have much longer dry SO_2, NH_3 and HCN breakthrough times than samples A and B. This is due to the pressence of the Zn^{2+} impregnant (presumably present as ZnO). For samples C → E the dry SO_2, HCN and C_6H_{12} breakthrough times decrease and the dry NH_3 breakthrough times increase. Table 9.1 shows that for samples C → E the amount

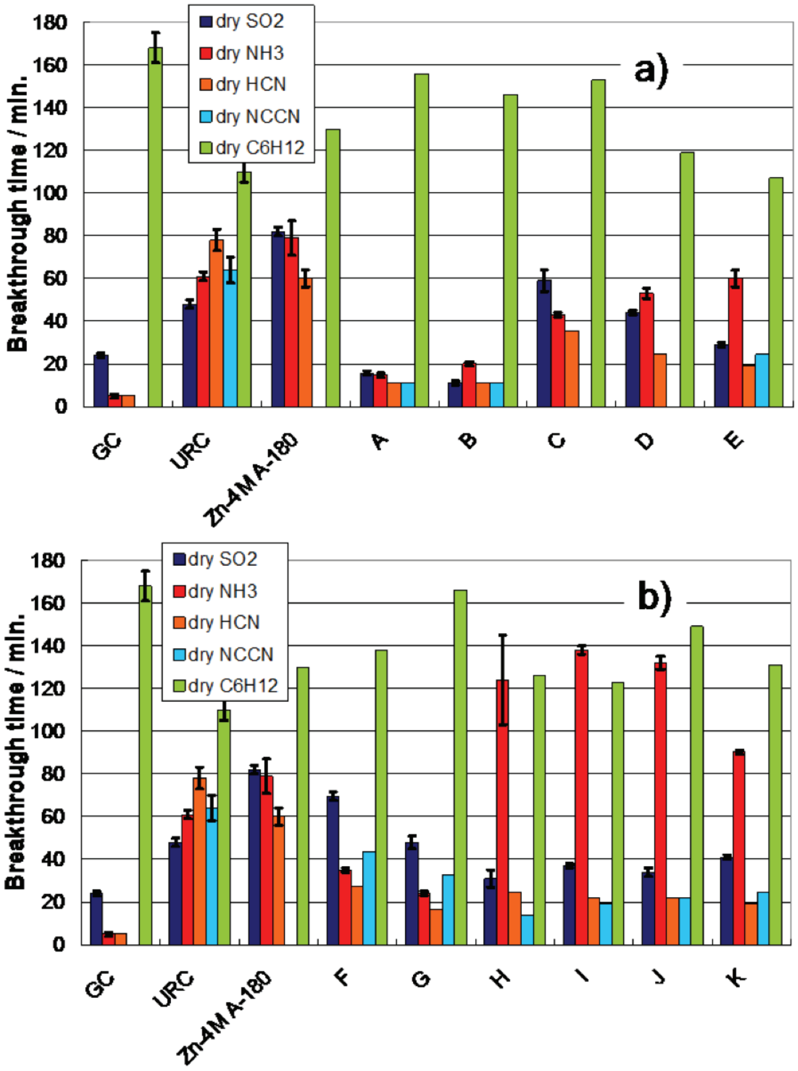

Figure 9.3: Dry breakthrough times obtained from testing the samples, detailed in Tables 9.1 and 9.2, with SO_2, NH_3, HCN and C_6H_{12} gases. Samples A, B, C, D and E are shown in panel (a) and samples F, G, H, I, J and K are shown in panel (b). Flow test results obtained from GC, URC and Zn-4M A-180 (described in chapter 5) samples have been included for reference. .

of Zn^{2+} impregnant decreased and the amount of co-impregnated $C_{12}H_{22}CuO_{14}$ increased. This implies that the Zn^{2+} impregnant (presumably present as ZnO) is responsible for the higher SO_2 and HCN capacity observed in sample C relative to sample E. Sample E shows that NCCN was evolved during its exposure to HCN. NCCN was not detected in the HCN flow test results obtained from samples C and

D. The evolution of NCCN during an HCN flow test may indicate some CuO impregnant is present [9]. The decrease in dry C_6H_{12} breakthrough times with increasing amounts of $C_{12}H_{22}CuO_{14}$ may indicate that residual sugar is blocking micropores, making them unavailable for physical adsorption. The increase in dry NH_3 adsorption with increasing amounts of co-impregnated $C_{12}H_{22}CuO_{14}$ may be due to the pressence of residual sugar. Reactions between sugar and ammonia, in solution, have been reported to form pyrazine ($C_4H_4N_2$) [109]. To the authors knowledge reaction mechanisims for the adsorption of gaseous NH_3 by sugar impregnated AC have not been reported. The formation of $C_4H_4N_2$ was not verified in this work.

Figure 9.3 shows that samples C and F had the longest dry SO_2 and HCN breakthrough times of any of the $C_{12}H_{22}CuO_{14}$ impregnated or co-impregnated samples. Table 9.1 shows that samples C and F had the highest concentration of $Zn(NO_3)_2$ in their impregnating solutions. The longer SO_2 and HCN breakthrouh times are presumably due to the higher ZnO impregnant loading in these samples. The data in Figure 9.2 indicates that these IACs had well dispersed, small grain size impregnant. Figure 9.3 shows that samples H → K had much longer dry NH_3 breakthrough times than samples A → G. Table 9.1 shows that samples H → K all had $ZnCl_2$ present. $ZnCl_2$ had been shown to be an effective impregnant for NH_3 removal in Figure 8.4(c) and in the literature [22, 108]. Samples F → K all had reasonably good dry C_6H_{12} adsorption, with breakthrough times all > 120 minutes.

Figure 9.3 shows that none of the $C_{12}H_{22}CuO_{14}$ impregnated or co-impregnated IACs had overall multi-gas adsorption capacity that was as good as the Zn-4M A-180 or URC samples. Samples C, D, F and G had dry SO_2 breakthrough times that were greater than GC, greater than or equal to URC and less than Zn-4M A-180. The samples that were co-impregnated with $ZnCl_2$ (samples H → K) had longer NH_3 breakthrough times than GC, URC or the Zn-4M A-180 samples. All of the $C_{12}H_{22}Cu_{14}$ impregnated samples had longer dry HCN breakthrough times than GC, but they were much shorter than the breakthrough times obtained from the Zn-4M A-180 or URC samples. All of the $C_{12}H_{22}CuO_{14}$ impregnated samples had dry C_6H_{12} breakthrough times that were greater than or equal to URC, but shorter than GC.

Figure 9.4 shows breakthrough times obtained from testing the samples in this study with humid HCN and humid C_6H_{12} gases as detailed in the figure caption. Figure 9.4(a) shows that samples A, B, C, D and E have longer humid HCN breakthrough times than GC, but shorter breakthrough times than URC. Samples C, D and E have humid HCN capacity that is greater than or equal to the Zn-4M A-180

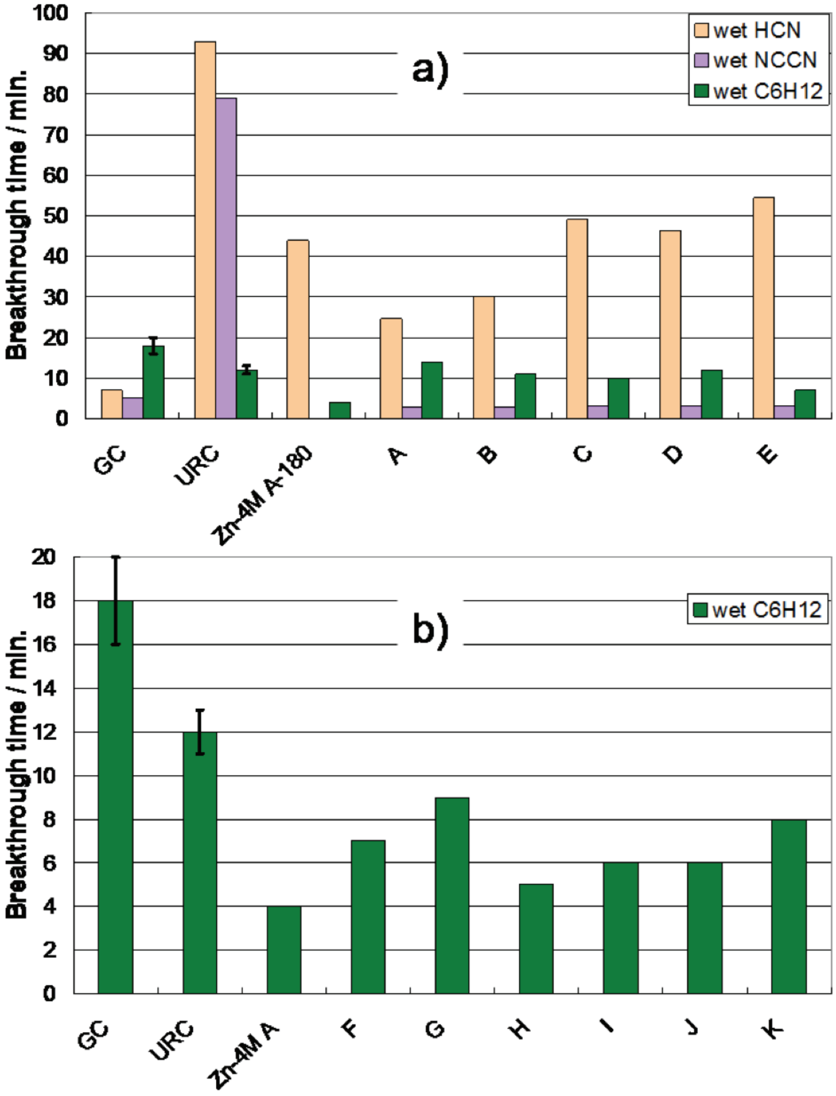

Figure 9.4: Wet breakthrough times obtained from testing the samples in this study with humid HCN and humid C_6H_{12} gases. Results from samples A, B, C, D and E are shown in panel (a) and samples F, G, H, I, J and K are shown in panel (b). Samples F → K were not tested for humid HCN capacity. Details of the sample preparation are given in Tables 9.1 and 9.2. Flow test results obtained from GC, URC and Zn-4M A-180 (described in chapter 5) samples have been included for reference.

IAC. Samples A → E all display relatively short NCCN breakthrough times when challenged with HCN gas. The concentration of NCCN detected in the gas stream after HCN breakthrough for samples A → E was approximately 60 - 200 ppm. The concentraion of NCCN detected after HCN breakthrough in the GC sample was approximately 10 ppm. Equation 1.1 indicates that when CuO impregnant is exposed to HCN, NCCN gas is evolved as a by-product. The higher concentrations of NCCN detected in the gas stream of samples A → E compared to GC may indicate that small amounts of CuO impregnant are present. This was not confirmed experimentally.

Figure 9.4 shows that the GC sample had the longest humid C_6H_{12} breakthrough time of the samples tested here. Samples A, B, C and D had humid C_6H_{12} breakthrough times greater than or equal to URC. Samples A → K all have wet C_6H_{12} breakthrough times that are greater than or equal to the Zn-4M A-180 IAC. These results indicate that co-impregnating multi-gas IACs with $C_{12}H_{22}CuO_{14}$ instead of HNO_3 results in samples with better humid C_6H_{12} adsorption capacity.

9.3 Comparative Study of IACs Co-impregnated with Sucrose, Glucose or Gluconic Acid

9.3.1 Sample Preparation

IAC samples were prepared on GC activated carbon which has been previously described in section 3.1. All of the IACs described in this section were prepared in one imbibing and one heating step.

IACs prepared from sugar-containing solutions were co-impregnated with either 2.4 M $Cu(NO_3)_2$ or 2.4 M $Zn(NO_3)_2$. Solutions containing sucrose had 0.10 M $C_{12}H_{22}O_{11}$ concentration and the solutions containing glucose had 0.20 M $C_6H_{12}O_6$ concentration. IACs co-impregnated with $C_{12}H_{22}O_{11}$ or $C_6H_{12}O_6$ had 4 mL of solution added to 5 g of GC. Solutions containing gluconic acid had either 0.05, 0.20, 0.25, 0.50, 0.75 or 1.0 M $C_6H_{12}O_7$ concentration. IACs prepared from $C_6H_{12}O_6$ had 4 mL solution added to 5 g GC for small sample sets and 12 mL solution added to 15 g GC for large sample sets.

All of the samples were heated, under flowing argon, at T_f = 180°C. Details of the heating conditions and determination of the % impregnant loading after heating have been previously discussed (see section 2.1 or section 7.2.1 for example).

9.3.2 Impregnant Loading

A comparative study of IACs co-impregnated with 2.4 M $Cu(NO_3)_2$ (or 2.4 M $Zn(NO_3)_2$) and $C_{12}H_{22}O_{11}$, $C_6H_{12}O_6$ or $C_6H_{12}O_7$ was performed to determine which co-impregnated sugar gave the best impregnant distribution. Table 9.3 lists the impregnating solution contents and the observed and predicted % impregnant loading for the samples prepared in this study. The predicted % impregnant loading assumes full conversion of the metal nitrate precursor to a metal oxide and assumes that all of the co-impregnated sugar is present after heating. It is unlikely that all of the co-impregnated sugar will remain after heating however experiments to determine the extent of burn-off for these sugars were not performed.

Table 9.3: Details of IACs prepared from aqueous solutions containing a metal nitrate precursor and sugar.

Imbibing solution contents	Observed % load (wt.)	Predicted % load
4 mL of 2.4 M $Zn(NO_3)_2$ / 0.10 M $C_{12}H_{22}O_{11}$ per 5 g GC	21	18
4 mL of 2.4 M $Zn(NO_3)_2$ / 0.20 M $C_6H_{12}O_6$ per 5 g GC	19	19
4 mL of 2.4 M $Zn(NO_3)_2$ / 0.20 M $C_6H_{12}O_7$ per 5 g GC	22	19
4 mL of 2.4 M $Cu(NO_3)_2$ / 0.10 M $C_{12}H_{22}O_{11}$ per 5 g GC	15	18
4 mL of 2.4 M $Cu(NO_3)_2$ / 0.20 M $C_6H_{12}O_6$ per 5 g GC	18	18
4 mL of 2.4 M $Cu(NO_3)_2$ / 0.20 M $C_6H_{12}O_7$ per 5 g GC	16	18

Table 9.3 shows that the IACs prepared with $Zn(NO_3)_2$ present all had observed % impregnant loading that was greater than or equal to the predicted % impregnant loading. This indicates that the Zn-based IACs are not burning off co-impregnated sugar during heating. The data from the Cu-based IACs shows that the observed % impregnant loading is less than or equal to the predicted % impregnant loading. This

indicated that some burn-off of the co-impregnated sugar might be occuring during heating in the Cu-based samples.

Samples were prepared to determine the optimal concentration of $C_6H_{12}O_7$ to co-impregnate with. Figure 9.5 shows the observed % impregnant loading plotted against the concentration of $C_6H_{12}O_7$ present in the imbibing solution for the samples prepared in this study as detailed in the figure caption.

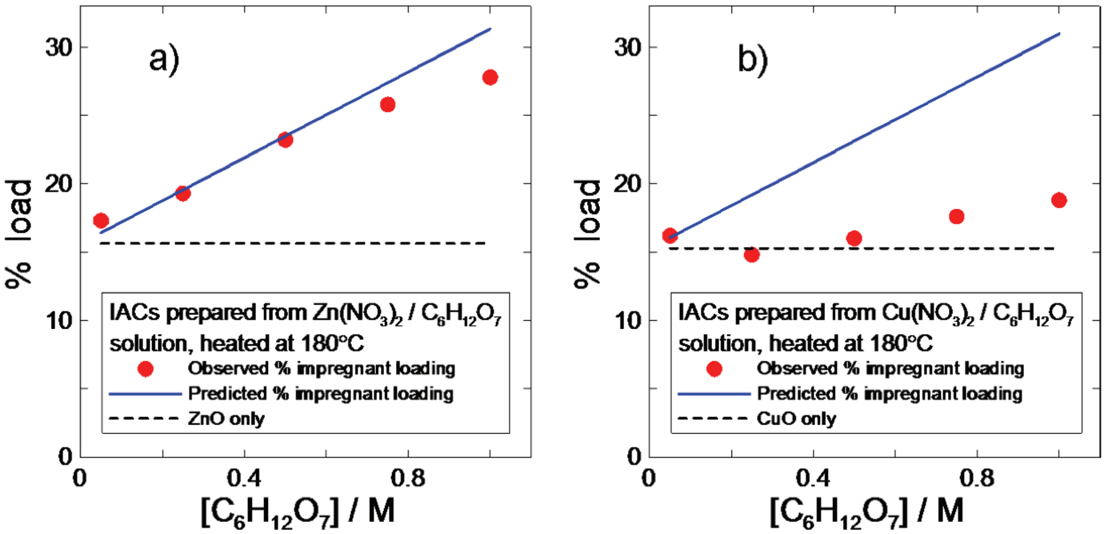

Figure 9.5: Observed impregnant loading (% load) versus concentration of $C_6H_{12}O_7$ data for the IACs in this study. Panel (a) shows data from IACs co-impregnated with 2.4 M $Zn(NO_3)_2$ and $C_6H_{12}O_7$ and panel (b) shows data from IACs co-impregnated with 2.4 M $Cu(NO_3)_2$ and $C_6H_{12}O_7$. The predicted loading for ZnO and CuO are indicated in panels (a) and (b) respectively.

Figure 9.5(a) shows that the observed and predicted % impregnant loading for the Zn-based samples are in reasonable agreement. At $C_6H_{12}O_7$ concentrations $\geq$ 0.75 M the observed loading is less than predicted. This may indicate some degree of burn-off is occuring at higher $C_6H_{12}O_7$ concentrations. Figure 9.5(b) shows that the observed impregnant loading is less that predicted for all of the Cu-based IACs. This indicates a high degree of $C_6H_{12}O_7$ burn-off is occuring in the Cu-based samples compared to the Zn-based samples. It is also possible that the Cu^{2+} impregnant may be getting reduced by the $C_6H_{12}O_7$ during heating. To determine if this is occuring XRD experiments were performed. The results are discussed below.

9.3.3 XRD Characterization

Figure 9.6 shows XRD data obtained from the IACs described in Table 9.3 (after heating) as detailed in the figure caption.

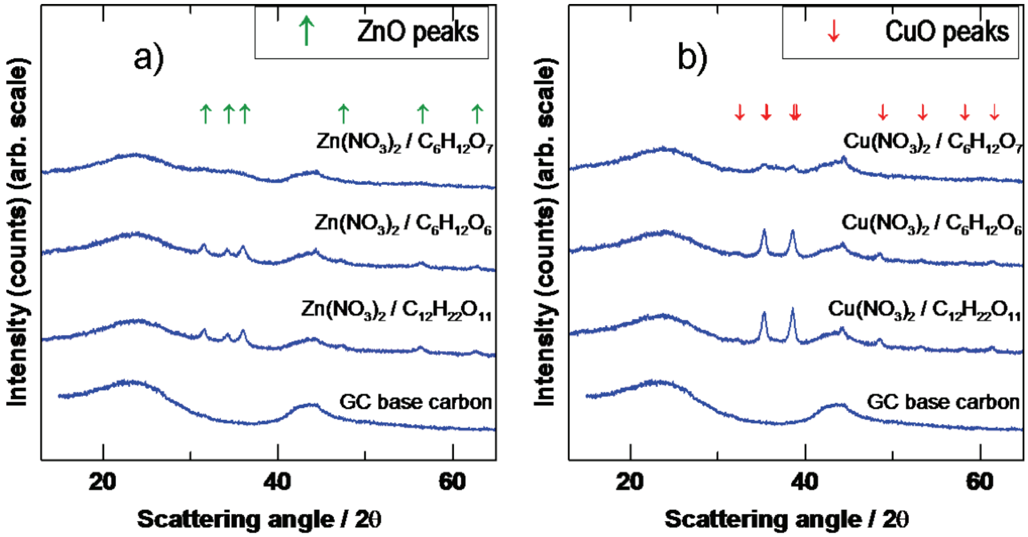

Figure 9.6: XRD data obtained from the IAC samples described in Table 9.3. Data from IACs co-impregnated with $Zn(NO_3)_2$ and $C_{12}H_{22}O_7$, $C_6H_{12}O_6$ or $C_6H_{12}O_7$ is shown in panel (a). Panel (b) shows data from IACs co-impregnated with $Cu(NO_3)_2$ and $C_{12}H_{22}O_7$, $C_6H_{12}O_6$ or $C_6H_{12}O_7$. For reference XRD data from GC carbon is included. The main Bragg peak positions for ZnO and CuO are indicated in panels (a) and (b) respectively.

Figure 9.6(a) shows that the XRD data obtained from the Zn-based IACs co-impregnated with sugar (after heating) had ZnO as the dominant impregnant phase. The $Zn(NO_3)_2$ / $C_6H_{12}O_7$ impregnated sample had broad, low intensity impregnant related diffraction peaks in the scattering angle range between $30° \leq 2\theta \leq 40°$. This indicates the formation of small grain size ZnO impregnant. Comparing the data obtained from the Zn-based IACs that were co-impregnated with either $C_{12}H_{22}O_{11}$, $C_6H_{12}O_6$ or $C_6H_{12}O_7$ shows that the sample co-impregnated with $C_6H_{12}O_7$ produced IACs with the smallest grain size ZnO after heating. A similar observation was made for the Cu-based IACs. Figure 9.6(b) shows that CuO was the dominant impregnant phase after heating the Cu-based IACs co-impregnated with sugar. Comparing the data obtained from the Cu-based IACs that were co-impregnated with either $C_{12}H_{22}O_{11}$, $C_6H_{12}O_6$ or $C_6H_{12}O_7$ shows that the sample co-impregnated with

$C_6H_{12}O_7$ produced IACs with the smallest grain size CuO after heating. Based on these results it was decided to use $C_6H_{12}O_7$ as the co-impregnant for the rest of the multi-gas IACs prepared in this study.

XRD experiments were conducted on the IACs prepared in the $C_6H_{12}O_7$ loading study. Figure 9.7 shows XRD data obtained from the samples presented in Figure 9.5 as detailed in the figure caption. Figure 9.7(a) shows that there are no obvious impregnant related diffraction peaks present in the Zn-based samples. Broad humps can be observed in the scattering angle range between 30° $\leq 2\theta \leq$ 40°. This may indicate the presence of small grain size ZnO impregnant.

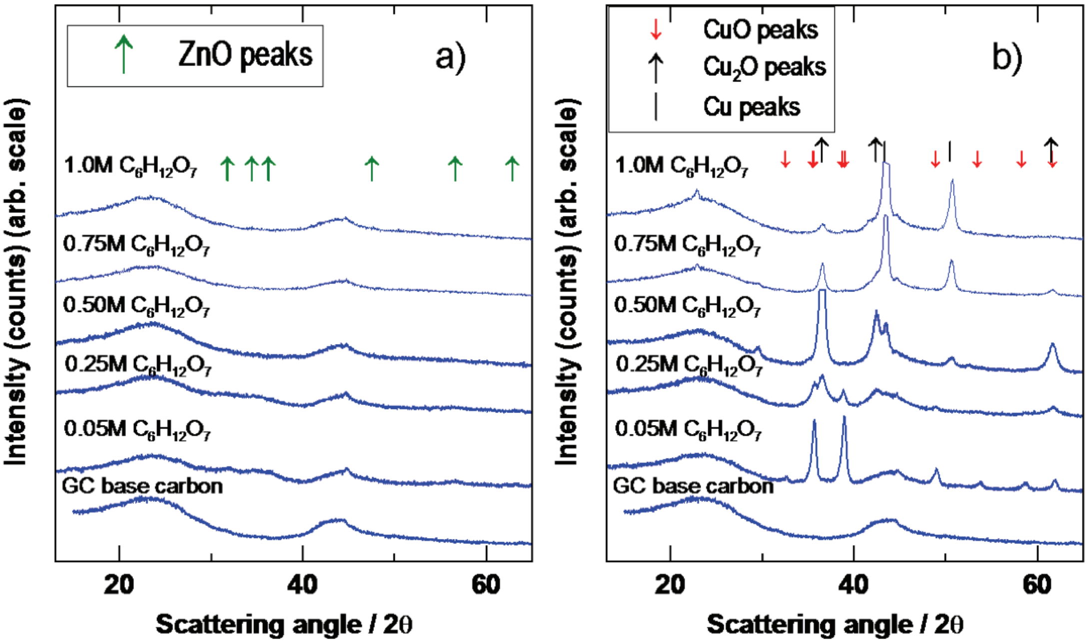

Figure 9.7: XRD data obtained from the IAC samples presented in Figure 9.5. Data from IACs co-impregnated with $Zn(NO_3)_2$ and $C_6H_{12}O_7$ or $Cu(NO_3)_2$ and $C_6H_{12}O_7$ are shown in panels (a) and (b) respectively. The data obtained from IACs co-impregnated with 0.50, 0.75 and 1.0 M $C_6H_{12}O_7$ in panel (b) has been clipped to allow it to be presented on the same scale as the other samples. The concentration of $C_6H_{12}O_7$ present in the imbibing solution is indicated in each panel. For reference XRD data from GC carbon has been included. The main Bragg peak positions for ZnO, CuO, Cu_2O and Cu are indicated.

Figure 9.7(b) shows that the XRD data obtained from the Cu-based IAC that was co-impregnated with 0.05 M $C_6H_{12}O_7$ had relatively intense CuO diffraction peaks after heating. This indicates that large grain size CuO impregnant is forming as can be inferred from the Scherrer equation (Eq. 2.5). The data obtained from the sample co-impregnated with 0.25 M $C_6H_{12}O_7$ displays CuO impregnant peaks with much lower intensity than the sample prepared with 0.05 M $C_6H_{12}O_7$. This implies the 0.25 M $C_6H_{12}O_7$ sample has smaller grain size CuO that is better dispersed on the AC substrate. The XRD data also indicates that Cu_2O impregnant is forming during the heating of this sample. As the concentration of co-impregnated $C_6H_{12}O_7$ was increased from 0.25 M to 1.0 M the dominant impregnant phase present on the IACs changed from CuO to Cu_2O to Cu. The samples co-impregnated with ≥ 0.50 M $C_6H_{12}O_7$ had intense impregnant related diffraction peaks indicative of large grain size impregnant. Cu-based samples with Cu_2O or Cu impregnant were shown to have reduced gas adsorption capacity in chapter 5. Flow test results obtained from the samples studied in this section will be discussed below.

9.3.4 Flow Test Results

Figure 9.8 shows the dry flow test results obtained from the $Zn(NO_3)_2$ / $C_6H_{12}O_7$- and $Cu(NO_3)_2$ / $C_6H_{12}O_7$-impregnated samples, after heating, as detailed in the figure caption. Dry NCCN flow test results are not shown. The Cu-based IACs did evolve NCCN when challenged with HCN. Cu-based IACs with a co-impregnated Mo^{6+} impregnant species for NCCN retention will be discussed in the next section. Figure 9.8(a) shows that the dry SO_2 breakthrough times decrease with increasing $C_6H_{12}O_7$ loading for the Zn-based and Cu-based IACs in this study. The Zn-based IACs had longer breakthrough times than the Cu-based samples at each $C_6H_{12}O_7$ concentration. The decrease in dry SO_2 breakthrough times observed for the Cu-based IACs is due to the CuO impregnant being reduced to less reactive Cu_2O or Cu as higher concentrations of $C_6H_{12}O_7$ were used (see Figure 9.7). The observed decrease in dry SO_2 times for the Zn-based IACs may be due to the presence of residual $C_6H_{12}O_7$ impregnant. The data in Figure 9.5(a) indicates that most of the co-impregnated $C_6H_{12}O_7$ is still present after heating the Zn-based IACs. Cu- and Zn-based IACs with ≤ 0.25 M $C_6H_{12}O_7$ co-impregnant had dry SO_2 breakthrough times greater than or equal to URC. All of the Cu- and Zn-based IACs in this study had longer SO_2 breakthrough times than GC and shorter breakthrough times than

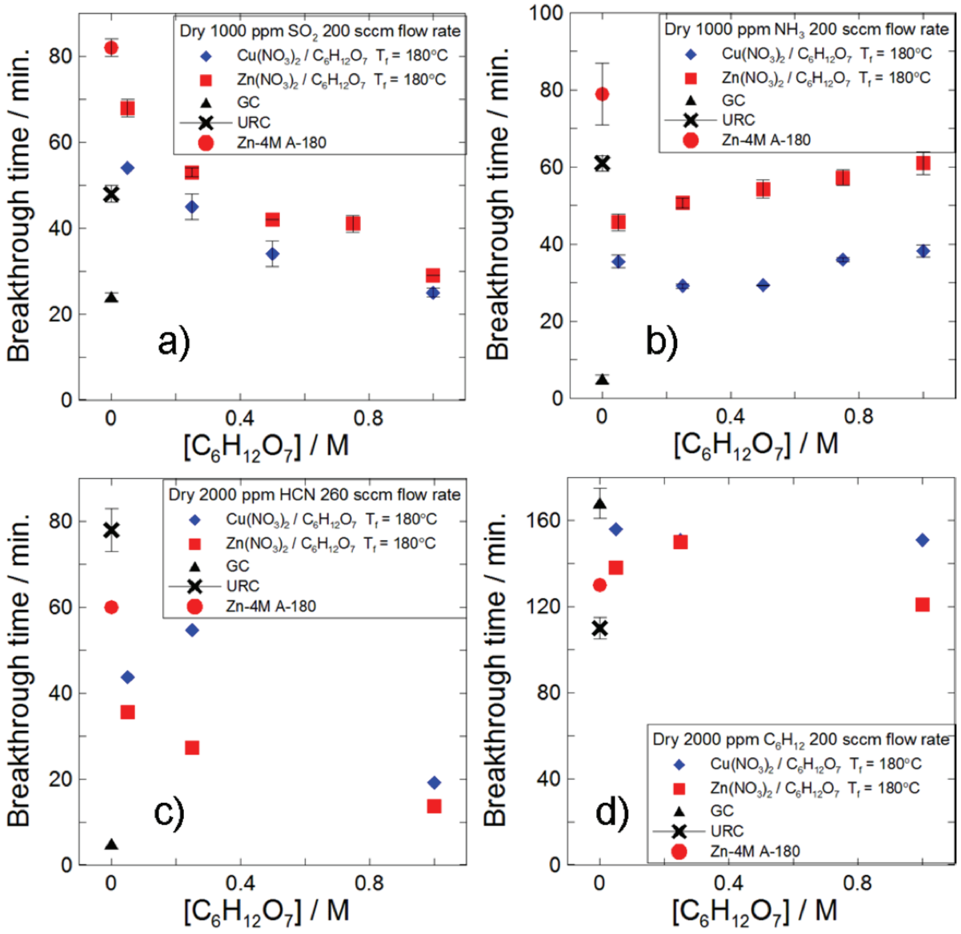

Figure 9.8: Dry flow test results obtained from the $Zn(NO_3)_2$ / $C_6H_{12}O_7$- and $Cu(NO_3)_2$ / $C_6H_{12}O_7$-impregnated samples after heating. Results obtained from dry SO_2, NH_3, HCN and C_6H_{12} flow tests are shown in panels (a), (b), (c) and (d) respectively. Flow test results obtained from GC, URC and the Zn-4M A-180 sample (described in chapter 5) have been included in each panel for reference.

the Zn-4M A-180 sample.

Figure 9.8(b) shows dry NH_3 breakthrough times increase moderately with increasing $C_6H_{12}O_7$ concentration. The Zn-based samples have longer dry NH_3 breakthrough times than the Cu-based IACs at each concentration of $C_6H_{12}O_7$. All of the Zn- and Cu-based IACs in this study had longer dry NH_3 breakthrough times than GC and shorter breakthrough times than the Zn-4M A-180 sample. The Zn-based IAC co-impregnated with 1.0 M $C_6H_{12}O_7$ had a dry NH_3 breakthrough time that was equivalent to URC, all of the other samples had shorter breakthrough times than

URC.

Figure 9.8(c) shows that the Zn-based IACs dry HCN breakthrough times decrease with increasing $C_6H_{12}O_7$ concentration, likely due to residual sugar impregnant. The Cu-based IACs have increasing dry HCN times between 0.05 M and 0.25 M $C_6H_{12}O_7$, then have a significant decrease when 1.0 M co-impregnated $C_6H_{12}O_7$ was used. The increase in dry HCN breakthrough time might be due to the improved impregnant dispersion that was observed in the Cu-based IAC co-impregnated with 0.25 M $C_6H_{12}O_7$ (see Figure 9.6(b)). The decrease in HCN capacity for the Cu-based IAC co-impregnated with 1.0 M $C_6H_{12}O_7$ is due to the reduction of the CuO impregnant to Cu_2O and primarily Cu. The Zn-based and Cu-based IACs co-impregnated with 0.50 and 0.75 M $C_6H_{12}O_7$ were not tested. All of the Cu-based IACs in this study had shorter dry HCN breakthrough times than URC and the Zn-4M A-180 sample.

Figure 9.8(d) shows that co-impregnation with $C_6H_{12}O_7$ does not improve dry C_6H_{12} breakthrough times for the Zn- and Cu-based IACs tested in this study. The Zn-based and Cu-based IACs co-impregnated with 0.50 and 0.75 M $C_6H_{12}O_7$ were not tested. All of the Zn- and Cu-based IACs tested in this study had dry $C_6H_{12}O_7$ breakthrough times that were longer than URC, greater than or equal to the Zn-4M A-180 sample and shorter than the GC sample.

Figure 9.9 shows humid C_6H_{12} breakthrough time obtained from the samples in this study as detailed in the figure caption. Figure 9.9 shows that humid C_6H_{12} breakthrough times do not increase with increasing $C_6H_{12}O_7$ concentration. All of the Zn- and Cu-based IACs tested in this work had shorter humid C_6H_{12} breakthrough times than GC or URC. Most of the Zn- and Cu-based samples had longer humid C_6H_{12} breakthrough times than the Zn-4M A-180 sample.

9.4 IACs Prepared with Metal Nitrate, Metal Sulfate, $H_3PO_4 \bullet 12MoO_3$ and $C_6H_{12}O_7$ Impregnants

Results shown in section 9.3 shows that when co-impregnating Cu-based IACs with $C_6H_{12}O_7$ the concentration must be < 0.25 M to prevent reduction of the Cu^{2+} impregnant. Flow test results in section 9.3.4 show that additional impregnants

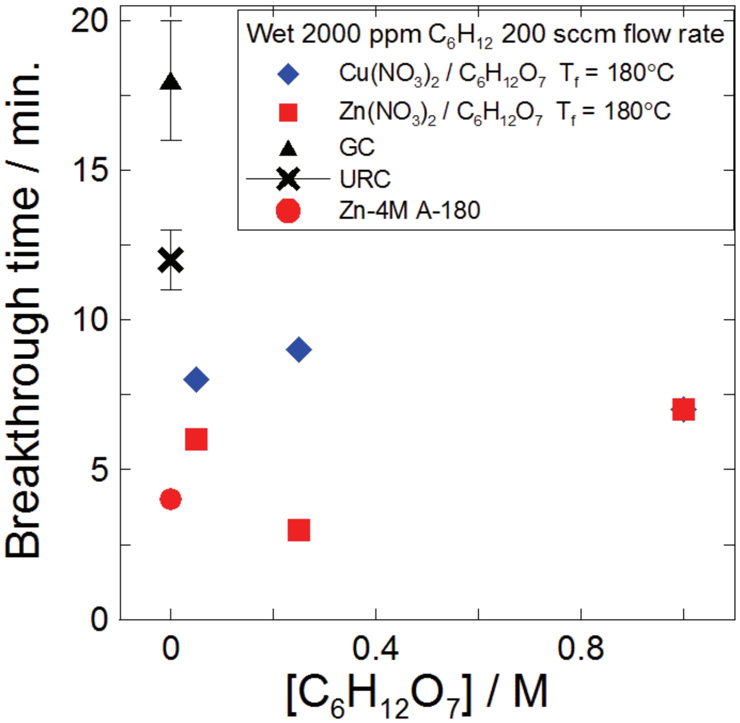

Figure 9.9: Wet $C_6H_{12}O_7$ flow test results obtained from the $Zn(NO_3)_2$ / $C_6H_{12}O_7$- and $Cu(NO_3)_2$ / $C_6H_{12}O_7$-impregnated samples after heating. Data obtained from samples co-impregnated with 0.05, 0.25 and 1.0 M $C_6H_{12}O_7$ are shown. Flow test results obtained from GC, URC and the Zn-4M A-180 sample (described in chapter 5) have been included for reference.

are required to improve the multi-gas adsorption capacity of Zn- or Cu-based IACs co-impregnated with $C_6H_{12}O_7$. In this section attempts to improve gas adsorption capacity with a variety of different co-impregnants is reported.

9.4.1 Sample Preparation

IAC samples were prepared on GC activated carbon which has been previously described in section 3.1. Most of the IACs described in this section required two imbibing and heating steps due to solubility issue with the components of the impregnating solutions. The sample names and imbibing solution contents for the IACs prepared in this study are listed in Table 9.4. In a typical imbibing step 10 - 12 mL of impregnating solution was added to 15 g of GC carbon.

All of the samples were heated, under flowing argon, at T_f = 180°C. Details of

Table 9.4: Details of impregnating solutions used to prepare IACs in this study.

Sample name	Imbibe 1	Imbibe 2
Zn-A	2.4 M $Zn(NO_3)_2$ / 0.2 M $C_6H_{12}O_7$	
Zn-B	1.2 M $Zn(NO_3)_2$ / 0.25 M $CuSO_4$ / 0.05 M $C_6H_{12}O_7$	1.2 M $Zn(NO_3)_2$ / 0.25 M $CuSO_4$ / 0.05 M $C_6H_{12}O_7$
Zn-C	1.2 M $Zn(NO_3)_2$ / 0.25 M $ZnSO_4$ / 0.05 M $C_6H_{12}O_7$	1.2 M $Zn(NO_3)_2$ / 0.25 M $ZnSO_4$ / 0.05 M $C_6H_{12}O_7$
Cu-A	2.4 M $Cu(NO_3)_2$ / 0.2 M $C_6H_{12}O_7$	
Cu-B	1.2 M $Cu(NO_3)_2$ / 0.25 M $CuSO_4$ / 0.05 M $C_6H_{12}O_7$	1.2 M $Cu(NO_3)_2$ / 0.25 M $CuSO_4$ / 0.05 M $C_6H_{12}O_7$
Cu-C	1.2 M $Cu(NO_3)_2$ / 0.25 M $ZnSO_4$ / 0.05 M $C_6H_{12}O_7$	1.2 M $Cu(NO_3)_2$ / 0.25 M $ZnSO_4$ / 0.05 M $C_6H_{12}O_7$
Cu-D	1.2 M $Cu(NO_3)_2$ / 0.25 M $CuSO_4$ / 0.05 M $C_6H_{12}O_7$ / 0.02 M $H_3PO_4 \bullet 12MoO_3$	1.2 M $Cu(NO_3)_2$ / 0.25 M $CuSO_4$ / 0.05 M $C_6H_{12}O_7$ / 0.02 M $H_3PO_4 \bullet 12MoO_3$
Cu-E	1.2 M $Cu(NO_3)_2$ / 0.25 M $ZnSO_4$ / 0.05 M $C_6H_{12}O_7$ / 0.02 M $H_3PO_4 \bullet 12MoO_3$	1.2 M $Cu(NO_3)_2$ / 0.25 M $ZnSO_4$ / 0.05 M $C_6H_{12}O_7$ / 0.02 M $H_3PO_4 \bullet 12MoO_3$

the heating conditions and determination of the % impregnant loading after heating have been previously discussed (see section 2.1 or section 7.2.1 for example).

9.4.2 Impregnant Loading

Figure 9.10 shows the observed and predicted % impregnant loading after heating for the IACs prepared from the impregnating solutions listed in Table 9.4. The predicted % impregnant loading assumes full conversion of the metal nitrate precursor to a metal oxide and assumes that all of the co-impregnated sugar is present after heating. The predicted % impregnant loading assumes that, when present, the metal sulfate impregnants dehydrate, but do not decompose (i.e. are present as $CuSO_4$ or $ZnSO_4$ after heating) and that after heating the Mo^{6+} compound is present as $H_3PO_4 \bullet 12MoO_3$. Interactions between the impregnated species during heating were not accounted for.

Figure 9.10 shows there is reasonable agreement between the observed and predicted % impregnant loading values for the samples in this study. Sample Cu-A had lower than predicted loading, possibly due to $C_6H_{12}O_7$ burnoff. Samples Cu-B, Cu-C

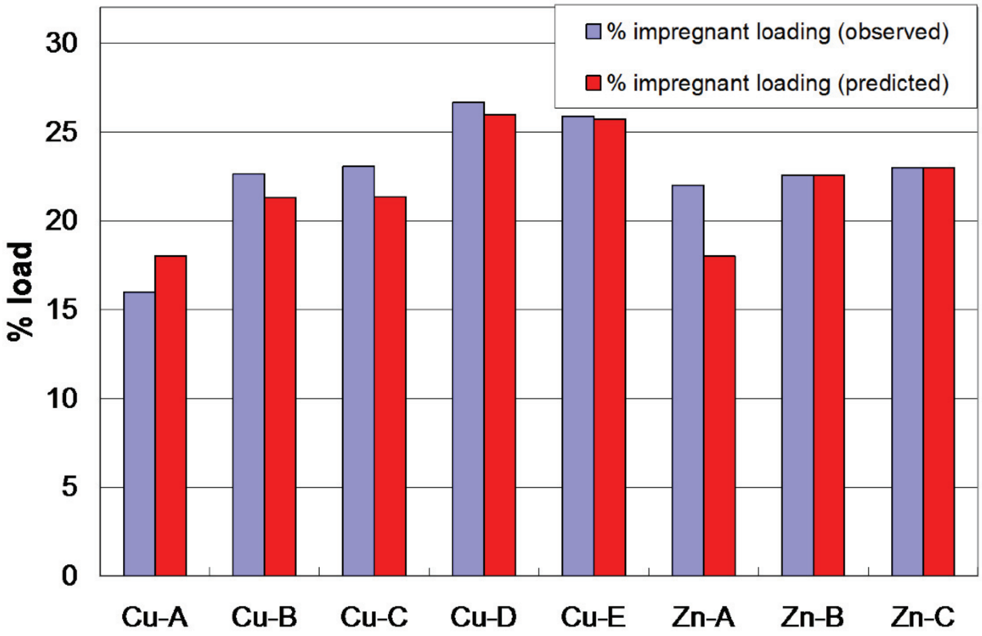

Figure 9.10: Observed and predicted % impregnant loading values for the Zn- and Cu-based samples in this study. All of the IACs were heated at T_f = 180°C prior to weighing. The imbibing solutions used to prepare these IACs are listed in Table 9.4.

and Cu-D all had higher than predicted impregnant loading, but the discrepency was within the estimated error (2 - 3 %). Sample Zn-A had approximately 4% higher than predicted impregnant loading. Samples Zn-B and Zn-C had excellent agreement between the observed and predicted values. The discrepencies between observed and predicted % impregnant loading will be discussed further when the XRD results are presented.

9.4.3 XRD Characterization

Figure 9.11 shows XRD data obtained from the IACs described in Table 9.4 and Figure 9.10 as detailed in the figure caption. Figure 9.11(a) shows that none of the data obtained from IACs prepared using the $Zn(NO_3)_2$ precursor have obvious impregnant related diffraction peaks. Figure 9.11(b) shows that the dominant impregnant phase observed in the data from the Cu-A sample is CuO. There is some evidence of the formation of Cu_2O in this sample as well. XRD data from samples Cu-B and

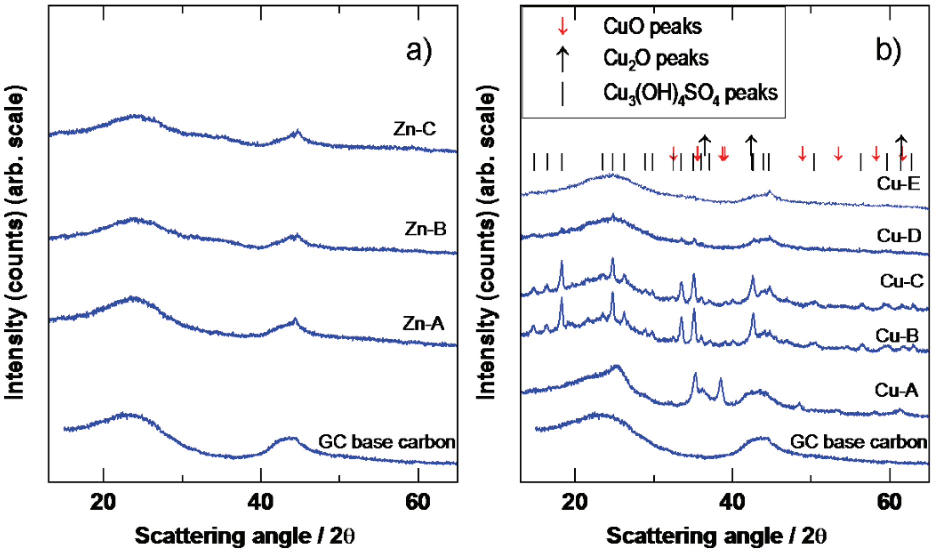

Figure 9.11: XRD data obtained from the IACs in this study. Information about the IACs is presented in Table 9.4 and Figure 9.10. IACs prepared with $Zn(NO_3)_2$ and $Cu(NO_3)_2$ precursors are shown in panels (a) and (b) respectively. All the samples were heated at $T_f = 180°C$ prior to analysis. For reference the diffraction pattern from GC has been included. The main Bragg peaks for CuO, Cu_2O and antlerite ($Cu_3(OH)_4SO_4$) are indicated.

Cu-C shows that $Cu_3(OH)_4SO_4$ is the dominant impregnant phase present after heating. Comparing the data from samples Zn-B to samples Cu-B and Cu-C shows that $Cu_3(OH)_4SO_4$ did not form in IACs impregnated with $Zn(NO_3)_2$ / $CuSO_4$, but it did form (after heating) in samples prepared from $Cu(NO_3)_2$ / $CuSO_4$ and $Cu(NO_3)_2$ / $ZnSO_4$. Weak diffraction peaks associated with the $Cu_3(OH)_4SO_4$ impregnant phase are observed in the data obtained from sample Cu-D. No impregnant related diffraction peaks are observed in the data from sample Cu-E. Samples Cu-D and Cu-E were co-impregnated with $H_3PO_4•12MoO_3$, but samples Cu-B and Cu-C were not. The presence of the Mo^{6+} compound appears to effect the crystallization of the other impregnants.

9.4.4 Flow Test Results

Figure 9.12 shows dry flow test data obtained from the IACs in this study as detailed in the figure caption.

Figure 9.12 shows that none of the IACs prepared and tested in this study had

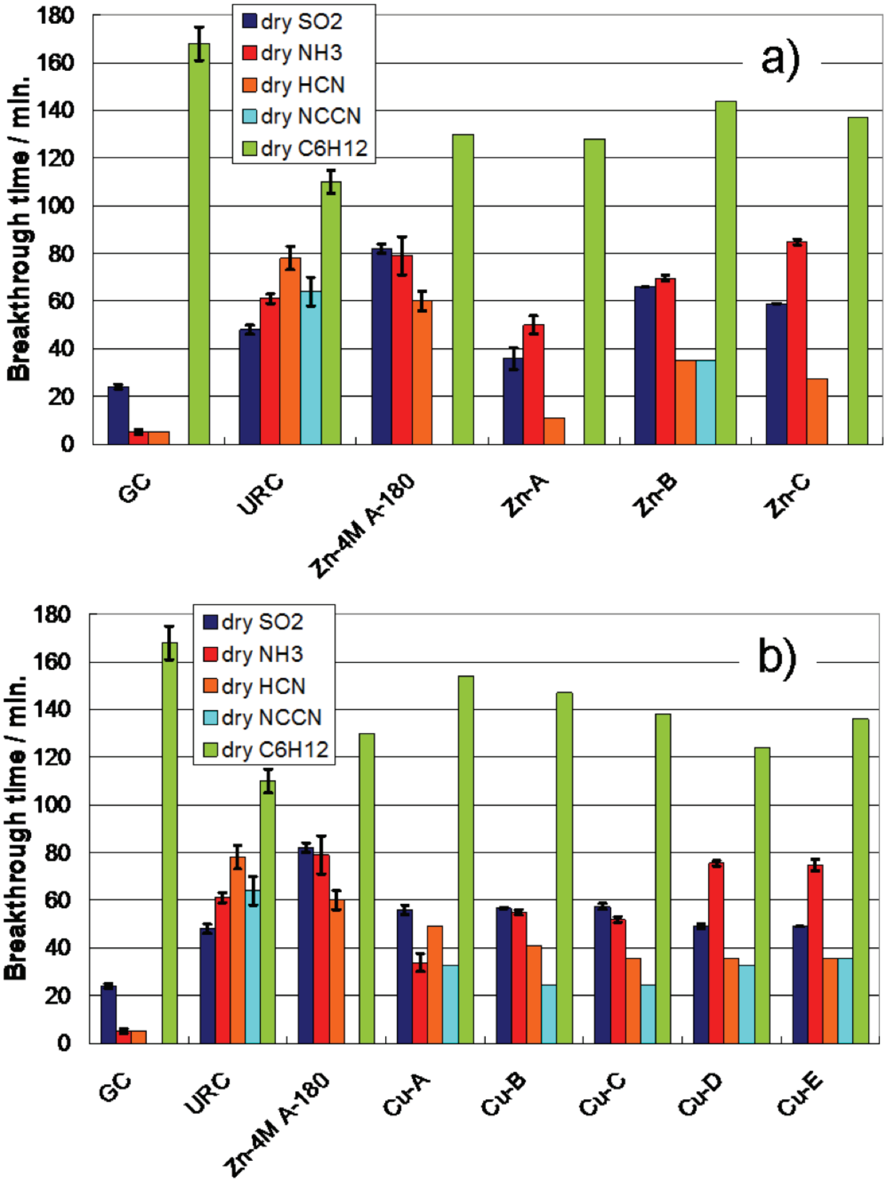

Figure 9.12: Dry flow test results obtained from the IACs in this study. Details of the sample preparation are presented in Table 9.4. Data from IACs prepared with a $Zn(NO_3)_2$ precursor and a $Cu(NO_3)_2$ precursor are shown in panels (a) and (b) respectively. Results from testing the samples versus dry SO_2, NH_3, HCN and C_6H_{12} gases are shown. For reference flow test results obtained from GC, URC and the Zn-4M A-180 sample (discussed in chapter 5) have been included.

dry SO_2 breakthrough times that were as long as those observed for the Zn-4M A-180 sample. All of the samples had longer dry SO_2 breakthrough times than GC, and

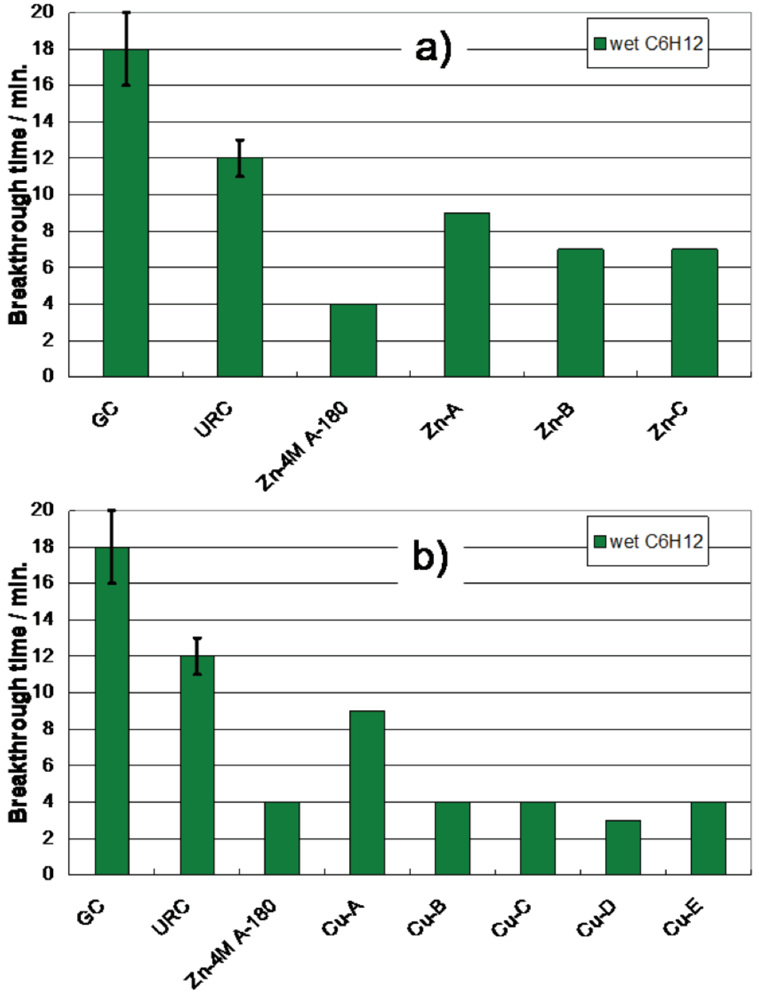

Figure 9.13: Humid C_6H_{12} flow test results obtained from the IACs in this study. Details of the sample preparation are presented in Table 9.4. Data from IACs prepared with a $Zn(NO_3)_2$ precursor and a $Cu(NO_3)_2$ precursor are shown in panels (a) and (b) respectively. For reference flow test results obtained from GC, URC and the Zn-4M A-180 sample (discussed in chapter 5) have been included.

with the exception of the Zn-A sample, all the IACs had longer SO_2 times than URC. Sample Zn-B had the longest dry SO_2 breakthrough time of the IACs studied in this section.

Figure 9.12 shows that IACs co-impregnated with either $CuSO_4$ (samples Zn-B, Cu-B and Cu-D) or $ZnSO_4$ (samples Zn-C, Cu-C and Cu-E) had longer dry NH_3 breakthrough times than the samples without a co-impregnated $SO_4{}^{2-}$ species. IACs with a $SO_4{}^{2-}$ species present were shown to have good NH_3 adsorption in Figure 8.4

and have been reported in the literature [13, 23]. Samples Cu-D and Cu-E had co-impregnated $H_3PO_4 \bullet 12MoO_3$, samples Cu-B and Cu-C did not. Samples Cu-D and Cu-E had longer dry NH_3 breakthrough times than samples Cu-B and Cu-C, possibly due to the $H_3PO_4 \bullet 12MoO_3$ impregnant, This is consistent with results presented in Figure 7.3. All of the IACs prepared and tested in this work had longer dry NH_3 breakthrough times than GC. Samples Zn-B, Zn-C, Cu-D and Cu-E had longer NH_3 times than URC and samples Zn-C, Cu-D and Cu-E had breakthrough times greater than or equal to the Zn-4M A-180 sample.

Figure 9.12 shows that all of the IACs prepared and tested in this study had longer dry C_6H_{12} breakthrough times than the URC or Zn-4M A-180 samples, but had shorter breakthrough times than the GC sample. The relatively good dry C_6H_{12} adsorption indicates that micropore blockage or filling due to impregnant was not a major issue for the samples in this study.

Figure 9.13 shows humid C_6H_{12} breakthrough times obtained from the samples in this study as detailed in the figure caption. Figure 9.13 shows that all of the IACs prepared and tested in this study have shorter wet C_6H_{12} breakthrough times than GC and URC. The Zn-A and Cu-A samples have the longest wet C_6H_{12} breakthrough times of the samples prepared in this study. Samples Cu-B → Cu-E had equivalent breakthrough times to the Zn-4M A-180 sample.

9.5 Summary of the Most Effective Samples

Figure 9.14 shows a radar plot summarizing flow test results obtained from the most effective multi-gas IACs discussed in chapter 9.

Figure 9.14 shows that the URC sample has the most balanced, best overall multi-gas adsorption capacity of the samples reported here. Sample C (co-impregnated $Zn(NO_3)_2$ and $C_{12}H_{22}CuO_{14}$, heated at 180°C) had longer dry SO_2 and C_6H_{12} times and similar wet C_6H_{12} breakthrough times compared to URC. This sample had reasonable dry and wet HCN capacity, but relatively low NH_3 adsorption and poor NCCN retention. Sample J (co-impregnated $Zn(NO_3)_2$, $ZnCl_2$ and $C_{12}H_{22}CuO_{14}$, heated at 250°C) had the longest dry NH_3 breakthrough time of all the samples reported here

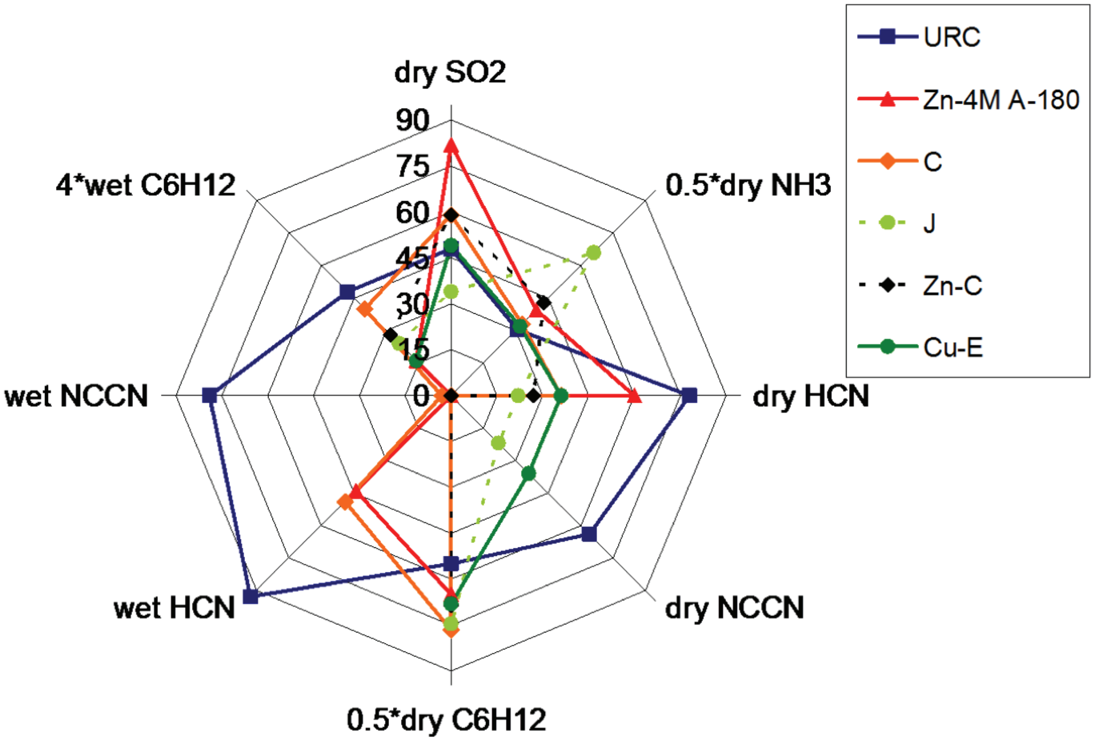

Figure 9.14: Radar plot summarizing flow test breakthrough times obtained from the most effective multi-gas IACs discussed in chapter 9. The breakthrough times are reported in minutes. Results obtained from tests using the different challenge gases are displayed on individual axes. Results obtained from dry NH_3, dry C_6H_{12} and wet C_6H_{12} flow tests have been scaled, by the amount indicated on their respective axis, to allow for improved data presentation. Results from URC and the Zn-4M A-180 sample (discussed in chapter 5) have been included for reference.

(including URC and the Zn-4M A-180 sample). Sample J had good dry C_6H_{12} adsorption, but relatively short dry SO_2, dry HCN and wet C_6H_{12} breakthrough times and poor NCCN retention. The Zn-C sample (co-impregnated $Zn(NO_3)_2$, $ZnSO_4$ and $C_6H_{12}O_7$, heated at 180°C) had relatively good dry SO_2, NH_3 and C_6H_{12} breakthrough times. This sample had relatively poor dry HCN capacity, but did not generate NCCN. It was not tested for humid HCN capacity and had a relatively short wet C_6H_{12} breakthrough time. The Cu-E sample (co-impregnated $Cu(NO_3)_2$, $ZnSO_4$, $C_6H_{12}O_7$ and $H_3PO_4\bullet 12MoO_3$, heated at 180°C) had dry SO_2 and NH_3 breakthrough times that were equivalent to URC and longer dry C_6H_{12} breakthrough times than

URC. Sample Cu-E had moderate HCN capacity and well balanced HCN:NCCN breakthrough times. This sample was not tested for humid HCN capacity and had relatively poor humid C_6H_{12} adsorption.

All of the IACs prepared in this study had shorter dry SO_2 and dry HCN breakthrough times than the Zn-4M A-180 sample. All of the samples in this study had humid C_6H_{12} breakthrough times that were longer than or equal to the Zn-4M A-180 sample.

9.6 Conclusions

IACs impregnated or co-impregnated with $C_{12}H_{22}CuO_{14}$ had longer humid C_6H_{12} breakthrough times than the Zn-4M A-180 sample. This result shows it is possible to improve wet C_6H_{12} adsorption by co-impregnating with $C_{12}H_{22}CuO_{14}$ instead of HNO_3. IACs impregnated with 0.3 M or 0.6 M $C_{12}H_{22}CuO_{14}$ had longer humid C_6H_{12} breakthrough times than URC, but had little ability to adsorb SO_2, NH_3 or HCN gases. IACs prepared from 2.3 M $Zn(NO_3)_2$ / 0.1 M $C_{12}H_{22}CuO_{14}$ and 2.1 M $Zn(NO_3)_2$ / 0.3 M $C_{12}H_{22}CuO_{14}$ had wet and dry C_6H_{12}, and dry SO_2 breakthrough times that were greater than or equal to URC. These samples had moderate dry NH_3, dry HCN and wet HCN capacity and had poor humid NCCN retention. Samples prepared from $Zn(NO_3)_2$, $C_{12}H_{22}CuO_{14}$ and $ZnCl_2$ that were heated at 250°C had improved NH_3 capacity, but reduced dry SO_2 and HCN breakthrough times. XRD data obtained from these samples showed relatively large ZnO impregnant formed during heating.

A comparative study of XRD data obtained from IACs impregnated with either 2.4 M $Cu(NO_3)_2$ or 2.4 M $Zn(NO_3)_2$ and 0.1 M $C_{12}H_{22}O_{11}$, or 0.2 M $C_6H_{12}O_6$, or 0.2 M $C_6H_{12}O_7$, that were heated at 180°C found that the IACs co-impregnated with $C_6H_{12}O_7$ had the smallest grain size impregnant and best impregnant distribution after heating. XRD data obtained from IACs co-impregnated with $Cu(NO_3)_2$ and $C_6H_{12}O_7$ showed that using gluconic acid concentrations ≥ 0.25 M resulted in the the Cu^{2+} impregnant being reduced to Cu^+ or Cu^0 during heating. Cu-based IACs with Cu_2O or Cu present as the dominant impregnant phase had lower SO_2, NH_3 and HCN adsorption capacity relative to IACs with CuO present. Decreased dry SO_2

and HCN breakthrough times with increased $C_6H_{12}O_7$ loading was observed in the Zn-based samples. The loss of performance in these samples may be due to residual $C_6H_{12}O_7$ impregnant.

IACs prepared from solutions containing 3 - 4 different compounds ($Cu(NO_3)_2$, $CuSO_4$, $C_6H_{12}O_7$ and $H_3PO_4 \bullet 12MoO_3$ for example) were found to have moderate overall multi-gas adsorption capacity and relatively low humid C_6H_{12} adsorption when compared to the commercially available URC sample. IACs prepared from $Cu(NO_3)_2$ and $CuSO_4$ (or $ZnSO_4$) containing solutions were found to have $Cu_3(OH)_4SO_4$ as their dominant impregnant phase after heating. IACs with $Cu_3(OH)_4SO_4$ present were found to have limited potential for use in multi-gas respirator carbons in earlier work [39].

The potential for replacing HNO_3 with sugar containing solutions in the preparation of multi-gas IACs has been demonstrated. IACs were prepared, using sugar co-impregnation, with humid C_6H_{12} breakthrough times that were longer than those obtained from URC or HNO_3 co-impregnated samples (sample Zn-4M A-180 for example). When the overall multi-gas adsorption capacities were compared, IACs with co-impregnated sugar did not perform as well as URC or HNO_3 co-impregnated samples. Improving NH_3 adsorption and NCCN retention without decreasing humid C_6H_{12} capacity was the un-realized goal of this work; however promising results have been shown.

Chapter 10

Impregnants Aimed at Improving Humid C_6H_{12} Adsorption

Work presented in the preceding chapters has focused on impregnation schemes aimed at SO_2, NH_3 and HCN adsorption. Steps were taken to try to minimize the negative effects that impregnation had on the AC's ability to physically adsorb humid C_6H_{12}. In this chapter impregnants were chosen to try to improve humid C_6H_{12} adsorption. The most promising impregnants were then used in the preparation of IACs for multi-gas adsorption applications.

Boehm titrations presented in Table 3.1 show that GC has a reasonably small amount of oxygen containing surface groups present. The presence of oxygen rich surface functional groups is believed to be responsible for poor humid organic vapour (e.g. C_6H_{12}) adsorption. The oxygen scavenging impregnants carbohydrazide (CH_6N_4O) and sodium sulfite (Na_2SO_3) were chosen to impregnate the GC substrate. Ascorbic acid ($C_6H_8O_6$) was chosen as an impregnant due to its ability to act as a mild reducing agent. The sulfur containing impregnants sodium thiosulfate ($Na_2S_2O_3$), benzene sulfonic acid ($C_6H_6O_3S$) and ammonium sulfate ($(NH_4)_2SO_4$) were chosen for comparative purposes and because they had been studied as components of multi-gas respirator carbons in other work [9, 13].

10.1 Chemicals Used

The chemicals used to prepare the impregnating solutions were copper nitrate hemipentahydrate ($Cu(NO_3)_2 \bullet 2.5H_2O$), 12- Molybdophosphoric acid hydrate ($H_3PO_4 \bullet 12MoO_3 \bullet xH_2O$) and copper sulfate pentahydrate ($CuSO_4 \bullet 5H_2O$) (all obtained from Alfa Aesar, reagent grade), zinc nitrate hexahydrate ($Zn(NO_3)_2 \bullet 6H_2O$), sodium sulfite (Na_2SO_3), and carbohydrazide (CH_6N_4O) (all from Sigma-Aldrich, reagent grade), D-gluconic acid solution ($C_6H_{12}O_7$, 49 - 53% in H_2O), copper D-gluconate ($C_{12}H_{22}CuO_{14}$), glucose ($C_6H_{12}O_6$), sucrose ($C_{12}H_{22}O_{11}$) and zinc sulfate heptahydrate ($ZnSO_4 \bullet 7H_2O$) (all obtained from Aldrich, reagent grade), L- ascorbic acid ($C_6H_8O_6$) and ammonium sulfate ($(NH_4)_2SO_4$) (Sigma, reagent grade), Benzene sulfonic acid ($C_6H_6O_3S$) (Eastman, reagent grade), sodium thiosulfate ($Na_2S_2O_3$) (BDH, reagent grade).

10.2 Impregnants Aimed at Improving Humid C_6H_{12} Adsorption

10.2.1 Sample Preparation

IAC samples were prepared by impregnating GC activated carbon. GC was previously described in section 3.1. The GC substrate was impregnated using the imbibing method. The IAC samples reported in this section were prepared in one imbibing and heating step. The samples were heated at T_f = 200°C under flowing argon. Details of the heating conditions and determination of the % impregnant loading have been discussed in earlier sections (see section 2.1 or section 7.2.1).

10.2.2 Impregnant Loading

Figure 10.1 shows the observed and predicted % impregnant loading after heating for the IACs prepared in this study as detailed in the figure caption. The impregnant loading data is plotted against the concentration of the imbibing solution. Predicted % impregnant loading calculations assume that the impregnated species is intact after heating. Where indicated the % impregnant loading of proposed decomposition products has been included.

Figure 10.1(a) shows that the CH_6N_4O imbibed sample has low impregnant loading after heating. The gravimetric data does not indicate that CH_6N_4O or hydrazine (N_2H_4, a known decomposition product) are present after heating. Panel (b) shows that there is good agreement between the observed and predicted % impregnant loadings up to 0.75 M $C_6H_8O_6$. The gravimetric data indicates all of the impregnated $C_6H_8O_6$ was present after heating. This was expected based on the literature [93]. The gravimetric data in panel (c) shows that Na_2SO_3 is the impregnant phase after heating. The difference between the predicted % impregnant loading for Na_2SO_3 and Na_2SO_4 is less than 2%. The uncertainty on the observed % impregnant loading is

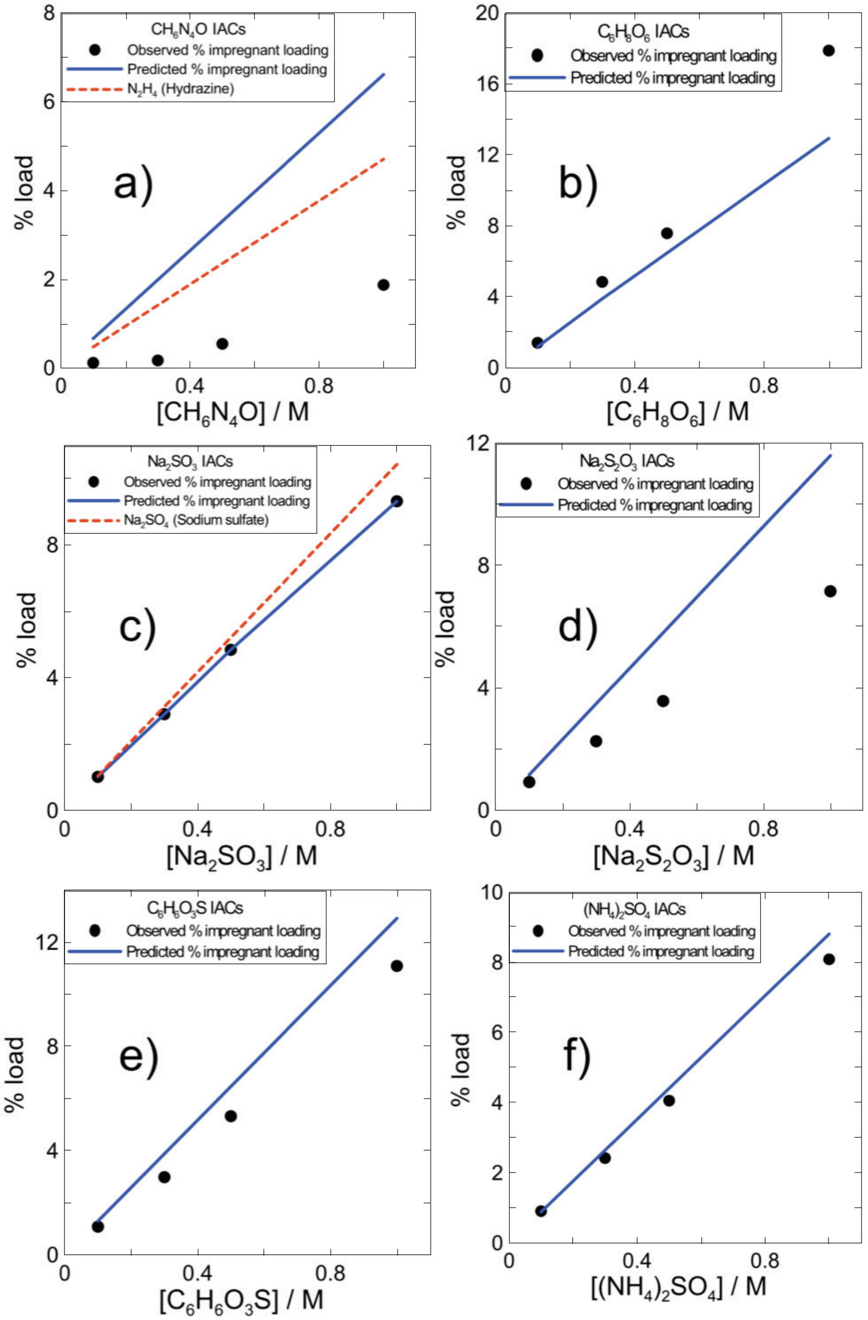

Figure 10.1: Observed and predicted % impregnant loading values for the IACs prepared in this study. Data obtained from samples imbibed with CH_6N_4O, $C_6H_8O_6$, Na_2SO_3, $Na_2S_2O_3$, $C_6H_6O_3$ and $(NH_4)_2SO_4$ containg solutions are shown in panels (a), (b), (c), (d), (e) and (f) respectively. The concentration of the imbibing solution is indicated on the lower axes. All of the IACs were heated at $T_f = 200°C$ prior to weighing.

2%. It may not be possible to identify the dominant impregnant phase after heating based on gravimetric data alone.

Figure 10.1(d) shows the observed impregnant loading for the $Na_2S_2O_3$-impregnated sample is lower than predicted after heating. A proposed decomposition product based on the gravimetric data was not identified. Panels (e) and (f) show there is good agreement between the observed and predicted % impregnant loadings obtained from the $C_6H_6O_3S$- and $(NH_4)_2SO_4$-impregnated samples respectively.

10.2.3 XRD Characterization

Figure 10.2 shows XRD data obtained from IACs prepared in this study as detailed in the figure caption. Figure 10.2 shows that the XRD data obtained from the CH_6N_4O-, $C_6H_8O_6$-, $Na_2S_2O_3$- and $(NH_4)_2SO_4$- impregnated samples, that were heated at T_f = 200°C, did not display any obvious impregnant related diffraction peaks when compared to data from the un-impregnated GC sample. The sharp peak located at $2\theta \approx 46°$ in the data obtained from the $(NH_4)_2SO_4$-impregnated sample is believed to be from the sample holder. The data obtained from the Na_2SO_3-impregnated sample displays weak diffraction peaks that suggest Na_2SO_4 impregnant may be present after heating.

10.2.4 Flow Test Results

Figure 10.3 shows dry and humid C_6H_{12} breakthrough times obtained from the samples in this study as detailed in the figure caption. Figure 10.3(a) shows that all of the IACs prepared and tested in this work have dry C_6H_{12} breakthrough times that are much longer than URC and less than or equal to GC. The dry C_6H_{12} capacity does not decrease significantly with higher impregnant loading (i.e. more concentrated impregnating solutions). This shows micropore blockage or pore filling due to impregnation is not an issue for this set of IACs.

10.3(b) shows that all of the IACs prepared and tested here, with the exception of the 1 M $C_6H_6O_3S$-impregnated sample, have longer wet C_6H_{12} breakthrough times than the URC sample. The CH_6N_4O-, $C_6H_8O_6$-, Na_2SO_3- and $Na_2S_2O_3$-impregnated samples that were prepared from imbibing solutions with ≤ 0.75 M concentration had

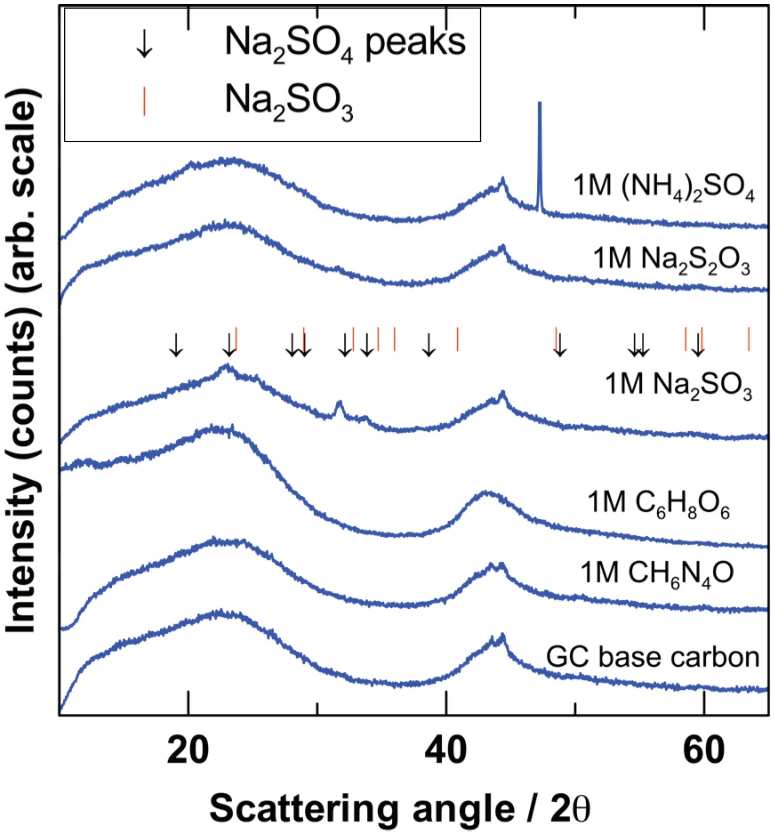

Figure 10.2: XRD data obtained from samples prepared in this study. Data obtained from IACs impregnated with aqueous 1 M CH_6N_4O, $C_6H_8O_6$, Na_2SO_3, $Na_2S_2O_3$ and $(NH_4)_2SO_4$ solutions are shown. The data was obtained from samples heated at $T_f = 200°C$ prior to XRD analysis. For reference data obtained from un-impregnated GC has been included. The main Bragg peak positions for Na_2SO_3 and Na_2SO_4 have been indicated.

humid C_6H_{12} breakthrough times that were greater than or equal to un-impregnated GC. The longest single humid C_6H_{12} breakthrough time was 28 minutes and was obtained from the 0.3 M Na_2SO_3 impregnated sample. Figure 10.3(b) shows that it is possible to prepare IACs with better C_6H_{12} adsorption than un-impregnated GC.

10.2.5 IACs Prepared for Multi-gas Applications

10.2.6 Sample Preparation

IAC samples were prepared by impregnating GC activated carbon. GC was previously described in section 3.1. The GC substrate was impregnated using the imbibing

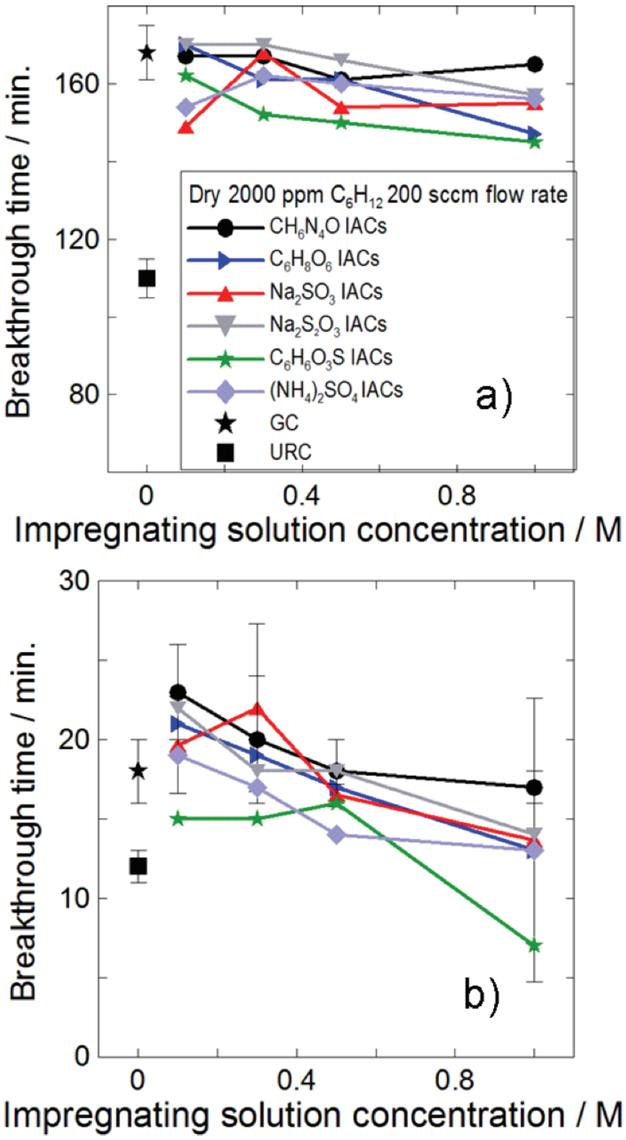

Figure 10.3: Dry and humid C_6H_{12} breakthrough times obtained from the samples in this study are shown in panels (a) and (b) respectively. Data was obtained by flow testing the samples described in Figure 10.1. The breakthrough times are plotted versus the concentration of impregnating solution used to prepare the samples. The type of impregnant used is detailed in the legend in panel (a). For reference flow test results obtained from GC and URC samples have been included. The lines have been included as a guide to the eye.

method. The IAC samples reported in this section were prepared by co-impregnation or post-treatment.

Co-impregnated samples were prepared in either one or two imbibing and heating steps. The sample names and imbibing solution contents of the co-impregnated IACs are listed in Table 10.1. A typical imbibing step for the co-impregnated IACs was to add 10 - 12 mL of impregnating solution to 15 g GC. These samples were heated, under flowing argon, at $T_f = 180°C$.

Post-treated samples were prepared in two imbibing and heating steps. The first step consisted of imbibing the impregnants used to target SO_2, NH_3 and HCN gases. The impregnant chosen to improve wet C_6H_{12} adsorption was added in the second imbibing step. The sample names and imbibing solution contents of the post-treated IACs are listed in Table 10.2. A typical imbibing step for the post-treated IACs was to add 10 - 12 mL of impregnating solution to 15 g GC. These samples were heated, under flowing argon, at $T_f = 200°C$. The sample post-treated with CH_6N_4O was heated at $T_f = 180°C$ for the first heating step and $T_f = 120°$ for the second heating step.

Details of the heating conditions and determination of the % impregnant loading have been discussed in earlier sections (see section 2.1 or section 7.2.1).

Table 10.1: Details of impregnating solutions used to prepare co-impregnated IACs in this study.

Sample name	Imbibe 1	Imbibe 2
A-10	2.4 M $Cu(NO_3)_2$ / 0.3 M $C_6H_8O_6$	
B-10	2.4 M $Zn(NO_3)_2$ / 0.3 M $C_6H_8O_6$	
C-10	1.2 M $Cu(NO_3)_2$ / 0.25 M Na_2SO_3 / 0.05 M $C_6H_{12}O_7$ / 0.02 M H_3PO_4•$12MoO_3$	1.2 M $Cu(NO_3)_2$ / 0.25 M Na_2SO_3 / 0.05 M $C_6H_{12}O_7$ / 0.02 M H_3PO_4•$12MoO_3$
D-10	1.2 M $Cu(NO_3)_2$ / 0.25 M $Na_2S_2O_3$ / 0.05 M $C_6H_{12}O_7$ / 0.02 M H_3PO_4•$12MoO_3$	1.2 M $Cu(NO_3)_2$ / 0.25 M $Na_2S_2O_3$ / 0.05 M $C_6H_{12}O_7$ / 0.02 M H_3PO_4•$12MoO_3$
E-10	1.2 M $Zn(NO_3)_2$ / 0.25 M $Na_2S_2O_3$	1.2 M $Zn(NO_3)_2$ / 0.25 M $Na_2S_2O_3$

10.2.7 X-ray Characterizations

Figure 10.4 shows XRD and SAXS data obtained from co-impregnated IACs prepared in this study. The XRD data is shown in panel (a) and the SAXS data is shown in panels (b) and (c). Figure 10.4(a) shows the XRD data obtained from

Table 10.2: Details of impregnating solutions used to prepare post-treated IACs in this study.

Sample name	Imbibe 1	Imbibe 2
F-10	2.4 M $Cu(NO_3)_2$ / 0.2 M $C_6H_{12}O_7$/ 0.035 M $H_3PO_4 \bullet 12MoO_3$	0.5 M $Na_2S_2O_3$
G-10	2.4 M $Cu(NO_3)_2$ / 0.2 M $C_6H_{12}O_7$/ 0.035 M $H_3PO_4 \bullet 12MoO_3$	0.5 M Na_2SO_3
H-10	2.4 M $Zn(NO_3)_2$	0.4 M CH_6N_4O

the co-impregnated IACs in this study have broad, low intensity impregnant-related diffraction peaks. This data indicates the presence of relatively small grain size impregnant and good impregnant distribution based on results shown in earlier chapters. The XRD data obtained from sample A-10 shows CuO is the dominant impregnant phase after heating. For samples B-10 and C-10 the weak diffraction peaks indicate the presence of ZnO and CuO or Cu_2O respectively. The data obtained from samples D-10 and E-10 does not identify the dominant impregnant phase after heating.

Figure 10.4(b) shows that the intensity of the data obtained from sample A-10 at low values of q (< 0.03 Å^{-1}) is similar to the data obtained from the IAC co-impregnated with 2.4 M $Cu(NO_3)_2$ and 4 M HNO_3 that was heated at $T_f = 180$°C. In chapter 6, Cu-based samples co-impregnated with 4 M HNO_3 were shown to have small, well dispersed CuO present after heating at $T_f = 180$ - 200°C. The data in Figure 10.4(b) implies that sample A-10 has relatively small particle size impregnant present after heating and is consistent with the XRD data obtained from this sample. The SAXS data obtained from the A-10 sample in the q = 0.06 - 0.2 Å^{-1} range is higher in intensity and shifted towards lower values of q compared to the data from the HNO_3 co-impregnated sample. This implies that the average small impregnant particle size (i.e. impregnant particle size < 3 nm) on the A-10 sample is larger than the impregnant on the HNO_3 co-impregnated sample. The same trends in the SAXS data described for the Cu-based samples were observed for the Zn-based samples shown in Figure 10.4(c).

Figure 10.5 shows XRD and SAXS data obtained from post-treated IACs prepared in this study. The XRD data is shown in panel (a) and the SAXS data is shown in

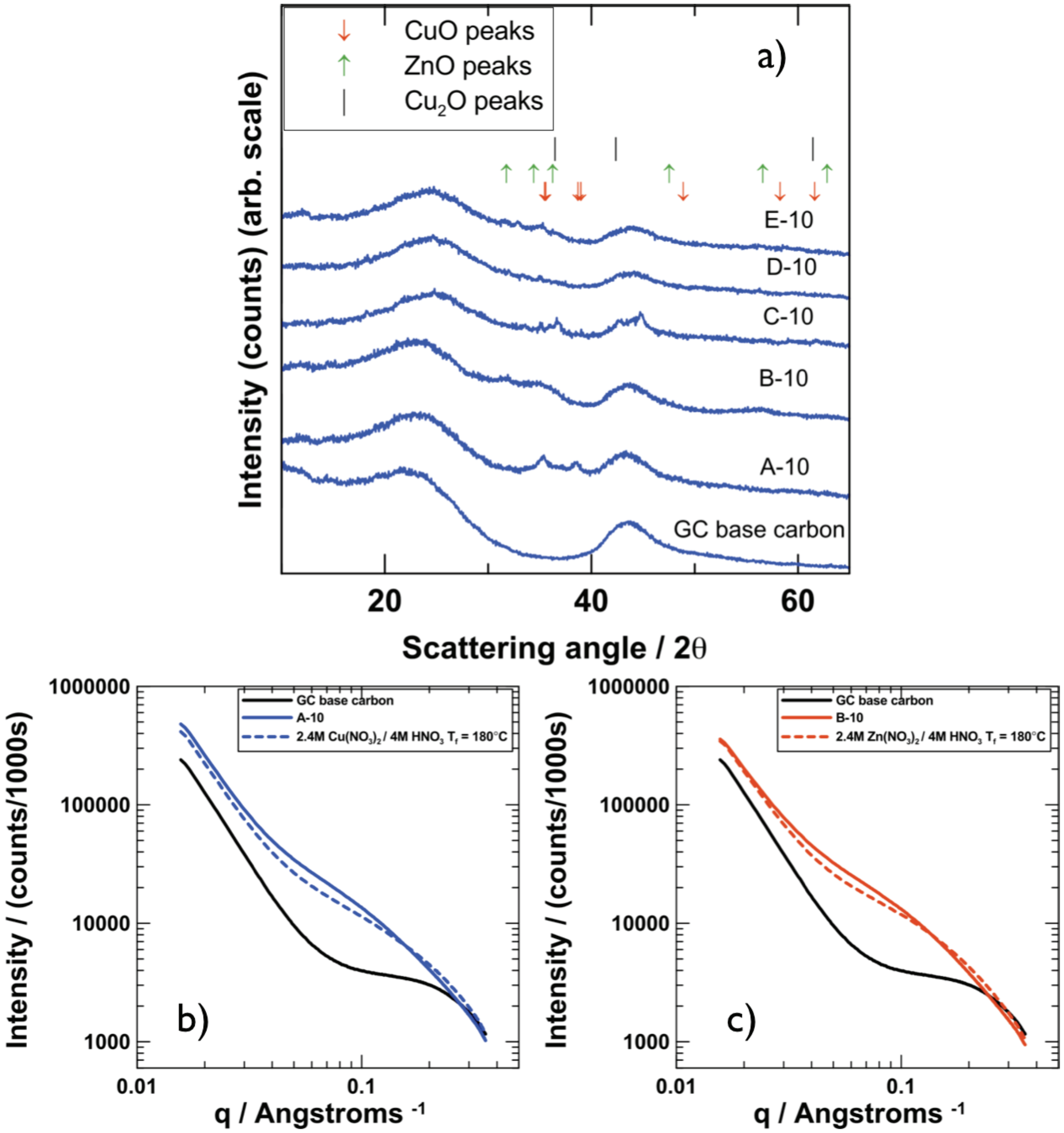

Figure 10.4: XRD and SAXS data obtained from co-impregnated IACs prepared in this study. The sample contents are described in Table 10.1. XRD data obtained from samples A-10, B-10, C-10, D-10 and E-10 are shown in panel (a). The main Bragg peak positions for CuO, Cu_2O and ZnO have been indicated. SAXS data obtained from samples A-10 and B-10 are shown in panels (b) and (c) respectively. XRD and SAXS data obtained from GC have been included. For reference SAXS patterns obtained from $Cu(NO_3)_2$ / HNO_3- and $Zn(NO_3)_2$ / HNO_3-impregnated samples are shown in panels (b) and (c), respectively.

panels (b) and (c). The XRD data obtained from samples G-10 (2^{nd} imbibe) and H-10 has been scaled to allow it to be displayed in the same panel as the data from the other samples.

Figure 10.5(a) shows that the dominant impregnant phase after heating for samples F-10 and G-10 is Cu_2O. Comparing the data obtained from sample G-10 shows that after the second imbibing step the intensity of the Cu_2O peaks increased dramatically and the width of the peaks decreased. This indicates increasing Cu_2O impregnant grain size after the second imbibing and heating step. Figure 10.5(a) shows that the intensity and width of the Cu_2O peak located at $2\theta \approx 36°$ in the sample F-10 (2^{nd} imbibe) data set decreased compared to data obtained from this sample after the first imbibe.

Figure 10.5(a) shows ZnO is the dominant impregnant phase present in the XRD data obtained from sample H-10 (2^{nd} imbibe). The high intensity, relatively narrow diffraction peaks indicate the presence of large grain size ($>$ 10 nm) ZnO impregnant as can be inferred from the Scherrer equation (Eq. 2.5). XRD data from sample H-10 (1^{st} imbibe) was not obtained. Figure 5.2(a) shows XRD data obtained from an IAC imbibed with 2.4 M $Zn(NO_3)_2$ that was heated at T_f = 180°C. The ZnO peaks observed in the data obtained from this sample have much lower intensity and are broader than the ZnO peaks in the data set obtained from sample H-10 (2^{nd} imbibe). This comparison indicates that post-treatment with CH_6N_4O causes increased ZnO impregnant grain size after heating. This may occur due to agglomeration of the ZnO impregnant as surface oxygen is removed (due to the CH_6N_4O treatment).

Figures 10.5(b) and 10.5(c) show that the SAXS data obtained from samples F-10 and G-10 are similar for the first and second imbibes respectively. The first imbibing and heating step (see Table 10.2) was the same, so the similarity of the SAXS curves obtained from samples F-10 and G-10 shows reproducibility in the sample preparation. Comparing the data obtained from samples after the first and second imbibing steps (for both samples due to the similarity of the data) shows that for q values $\leq$ 0.04 $Å^{-1}$, the intensity of the data from the second imbibe is higher than the intensity of the data from the first imbibe. For the data range q $\approx$0.05 - 0.2 $Å^{-1}$ the intensity of the data from the first imbibe is greater than the intensity of the data from the

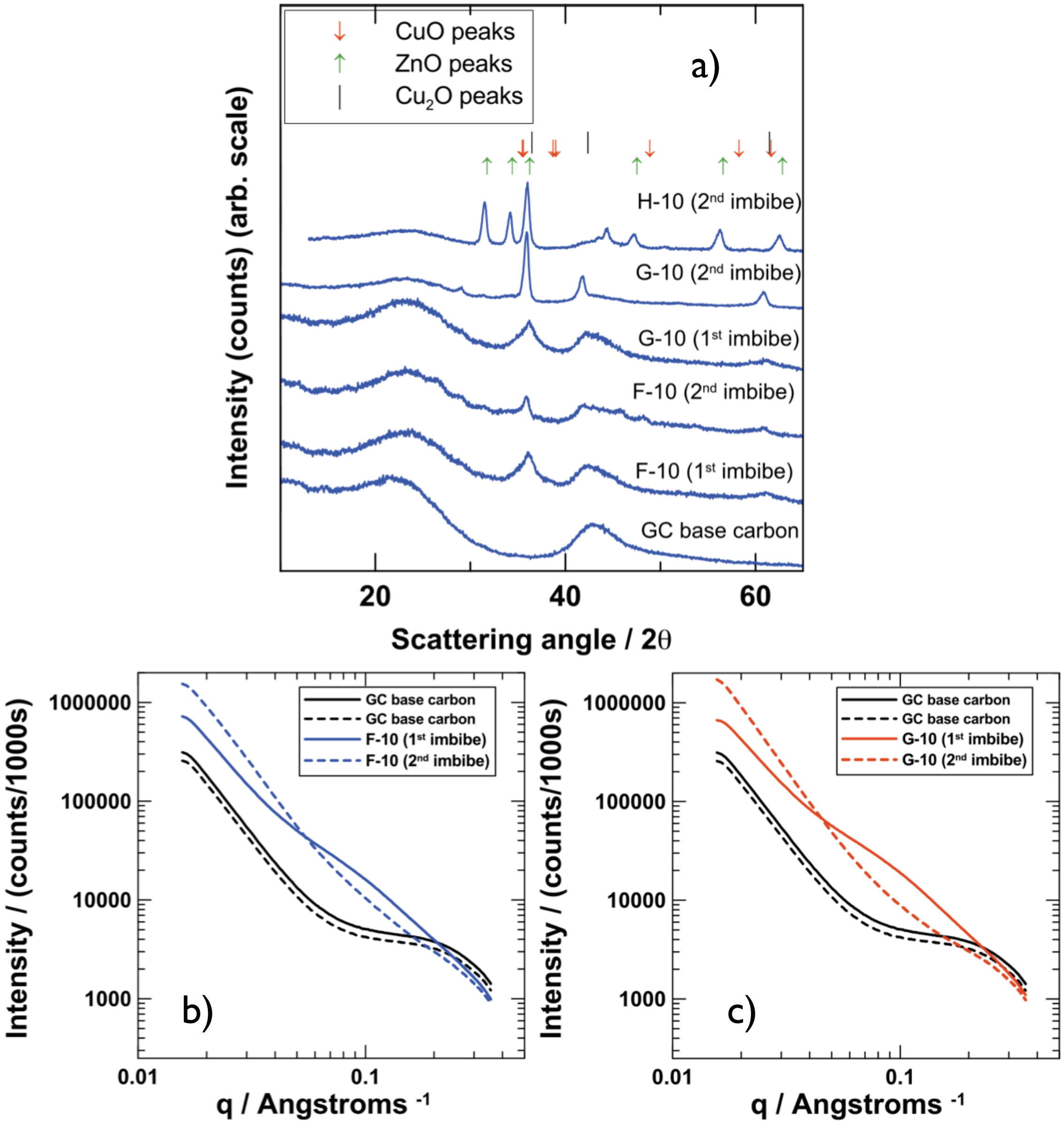

Figure 10.5: XRD and SAXS data obtained from post-treated IACs prepared in this study. The sample contents are described in Table 10.2. XRD data obtained from samples F-10, G-10 and H-10 are shown in panel (a). The data labelled 1st and 2nd imbibe was collected after the first and second imbibing and heating steps for samples F-10 and G-10. The main Bragg peak positions for CuO, Cu_2O and ZnO have been indicated. SAXS data obtained from samples F-10 and G-10 are shown in panels (b) and (c) respectively. For reference XRD and SAXS data obtained from GC has been included.

second imbibe. This implies that in the data sets obtained from samples F-10 and G-10, after the second imbibe the scattering intensity from relatively large particle size impregnant increases and the scattering intensity from relatively small particle size impregnant ($\leq$ 3 nm) decreases when compared to data obtained from samples after the first imbibe. There is good agreement between the SAXS and XRD data obtained from sample G-10.

10.2.8 Flow Test Results

Figure 10.6 shows dry flow test data obtained from the co-impregnated and post-treated samples in panels (a) and (b) respectively. Dry SO_2, NH_3, HCN and C_6H_{12} challenge gases were used. Figure 10.6 shows that all of the co-impregnated IACs (panel (a)) had longer dry SO_2 breakthrough times than the post-treated samples (panel (b)), the GC sample and the URC sample. Figures 10.4 and 10.5 show that the co-impregnated IACs have better impregnant dispersion compared to the post-treated IACs. In the case of Cu-based post-treated samples (samples F-10 and G-10) reduced SO_2 capacity may be due to the presence of Cu_2O impregnant. Sample B-10 had the longest dry SO_2 breakthrough time of the samples in this study.

Figure 10.6 shows that samples C-10, D-10 and E-10 had longer dry NH_3 breakthrough times than the other co-impregnated or post-treated samples in this study. Samples C-10, D-10 and E-10 all had dry NH_3 breakthrough times that were greater than or equal to URC and greater than GC. Samples C-10, D-10, E-10, F-10 and G-10 were all prepared with either Na_2SO_3 or $Na_2S_2O_3$ impregnants present. Comparing the data from these samples shows that the co-impregnated IACs had longer dry NH_3 breakthrough times than the post-treated IACs.

Figure 10.6 shows that sample D-10 had the longest dry HCN and NCCN breakthrough times of the co-impregnated or post-treated IACs tested in this study. Dry HCN test results were not available for the A-10 and B-10 samples. All of the co-impregnated or post-treated IACs tested here had longer dry HCN breakthrough times than URC and shorter HCN times than URC. Figure 10.6 shows that all of the co-impregnated and post-treated IACs tested in this work had longer dry C_6H_{12} breakthrough times than URC and shorter dry C_6H_{12} breakthrough times than GC.

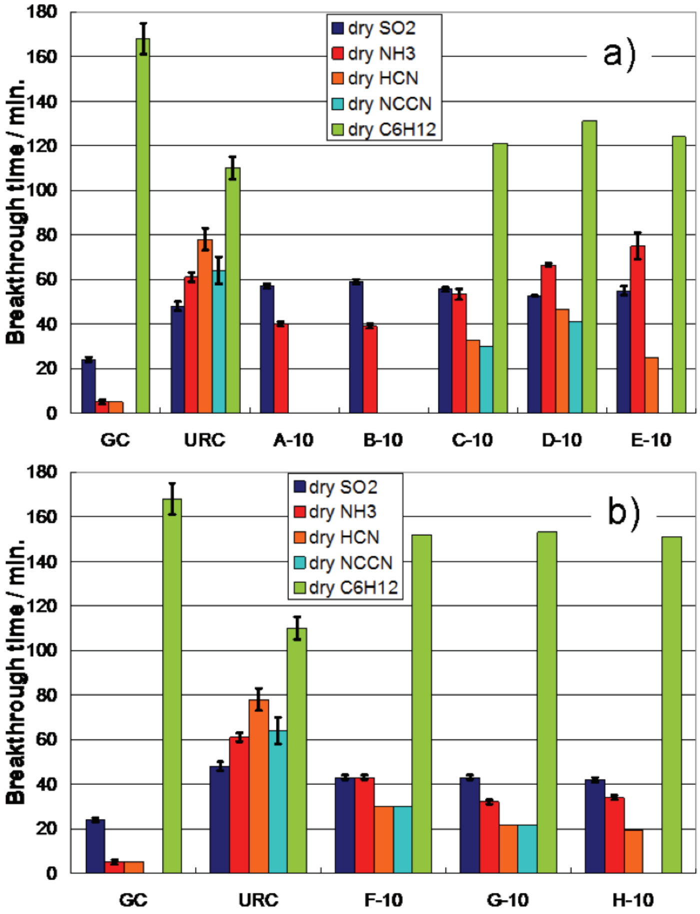

Figure 10.6: Dry flow test data obtained from the co-impregnated and post-treated samples in panels (a) and (b) respectively. The challenge gases used during the flow testing are indicated in the figure legend. Sample preparation details for the co-impregnated and post-treated IACs are listed in Tables 10.1 and 10.2 respectively. For reference data obtained from GC and URC samples has been included.

The relatively good dry C_6H_{12} adsorption indicates that pore blockage or micropore filling due to impregnation was not a major issue for the samples prepared in this study.

Figure 10.7 shows humid C_6H_{12} flow test data obtained from the co-impregnated and post-treated samples in panels (a) and (b) respectively. Figure 10.7 shows that all of the co-impregnated and post-treated IACs tested in this study had shorter humid C_6H_{12} breakthrough times than the URC and GC samples. Samples A-10 and B-10 had the longest wet C_6H_{12} breakthrough times of the co-impregnated or post-treated

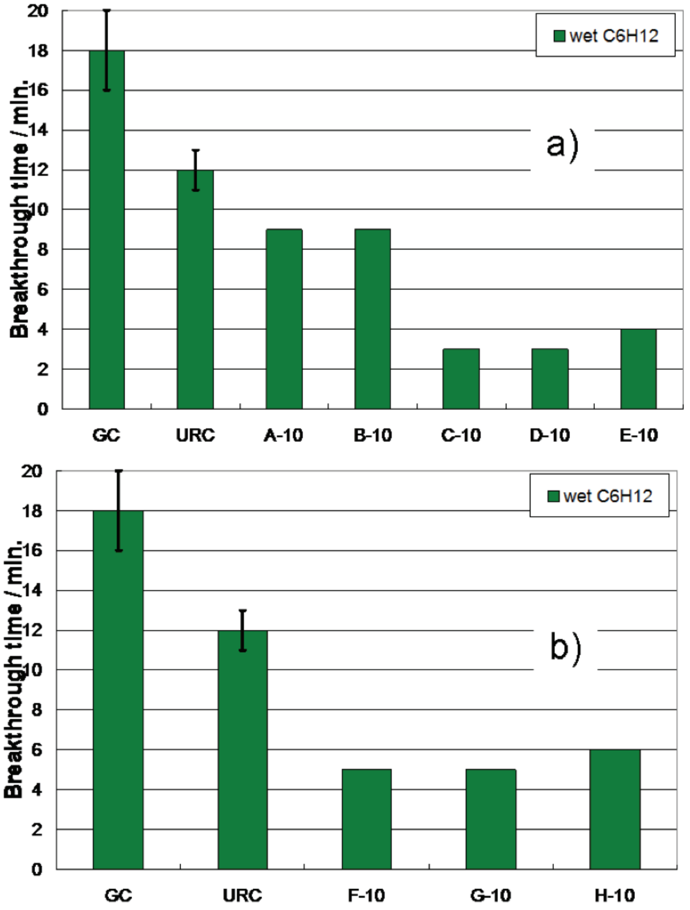

Figure 10.7: Humid C_6H_{12} flow test data obtained from the co-impregnated and post-treated samples in panels (a) and (b) respectively. Sample preparation details for the co-impregnated and post-treated IACs are listed in Tables 10.1 and 10.2 respectively. For reference data obtained from GC and URC samples has been included.

IACs in this study. Table 10.1 shows that samples A-10 and B-10 had relatively simple impregnating solutions and were prepared in one imbibing and heating step. These samples were also prepared with the lowest concentration imbibing solutions. The lower amount of impregnated species may explain why samples A-10 and B-10 had longer wet C_6H_{12} breakthrough times relative to the other co-impregnated and post-treated samples.

10.2.9 Summary of the Most Effective Co-impregnated and Post-treated IAC Samples

Figure 10.8 shows a radar plot summarizing the most effective co-impregnated and post-treated IACs from the samples discussed in chapter 10. Figure 10.8 shows that the URC sample had the most balanced, best overall multi-gas adsorption capacity of the samples studied here.

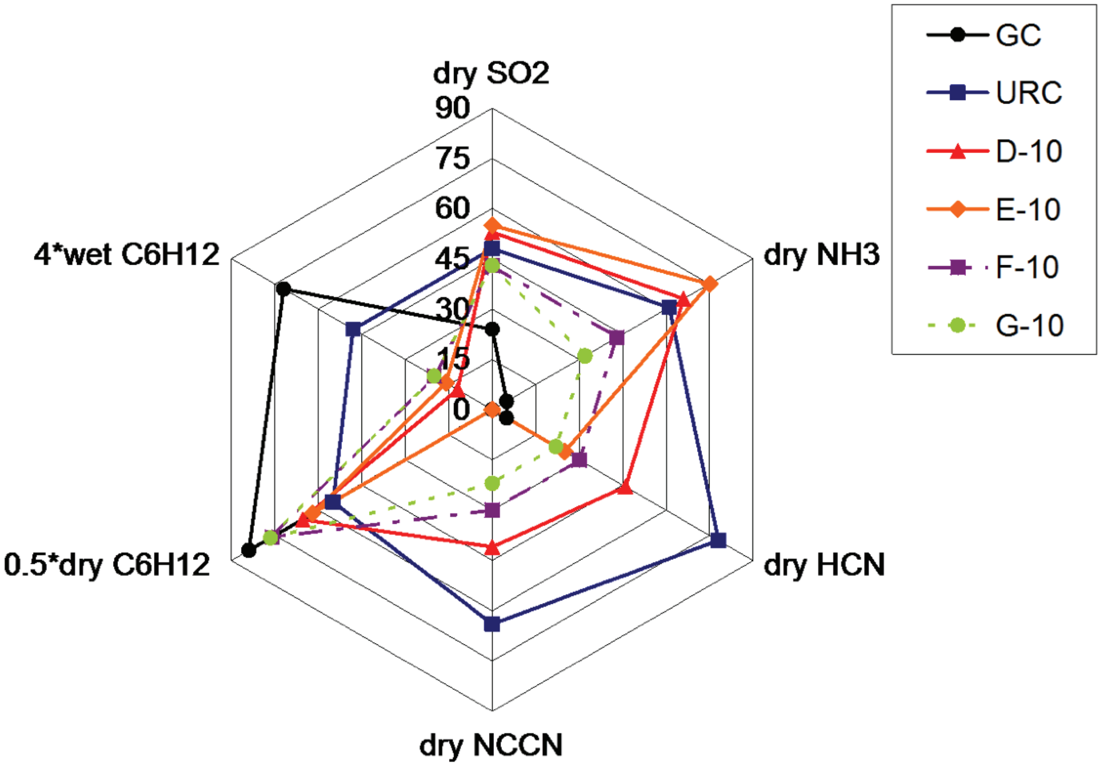

Figure 10.8: Radar plot summarizing the most effective co-impregnated and post-treated IACs discussed in chapter 10. The breakthrough times are reported in minutes. Results obtained from flow tests using different challenge gases are displayed on individual axes. Results obtained from dry and humid C_6H_{12} flow tests have been scaled by the amount indicated on their respective axis to allow for improved data presentation. Results obtained from GC and URC have been included for reference.

Figure 10.8 shows that the co-impregnated samples (samples D-10 and E-10) had better overall multi-gas performance than the post-treated IACs (samples F-10 and G-10). Samples D-10 and E-10 had dry SO_2, NH_3 and C_6H_{12} breakthrough times that were longer than times obtained from URC, but had shorter dry HCN, NCCN and humid C_6H_{12} breakthrough times. Sample D-10 (Cu(NO_30_2, Na_2S2O_3, $C_6H_{12}O_7$, H_3PO_4•$12MoO_3$, T_f = 180°C) had moderate, well balanced dry HCN and NCCN breakthrough times. Sample E-10 ($Zn(NO_3)_2$, $Na_2S_2O_3$, T_f = 200$^\bullet$C) had relatively low dry HCN capacity, and did not generate NCCN. Samples D-10, E-10, F-10 and G-10 all had longer dry C_6H_{12} breakthrough times than URC and shorter times than GC. Samples D-10, E-10, F-10 and G-10 all had relatively poor humid C_6H_{12} adsorption compared to the URC and GC samples.

10.3 Conclusions

IACs prepared from aqueous CH_6N_4O, $C_6H_8O_6$, Na_2SO_3 or $Na_2S_2O_3$ solutions with concentrations ≤ 0.75 M, that were heated at T_f = 200°C, had longer humid C_6H_{12} breakthrough times than URC and breakthrough times that were longer than or equal to those obtained from un-impregnated GC.

IAC samples prepared with Na_2SO_3 or $Na_2S_2O_3$ were found to have better overall multi-gas adsorption capacity when they were co-impregnated with other compounds in the same solution as opposed to being used as a post-treatment. XRD and SAXS data showed that the co-impregnated IACs had smaller, better dispersed impregnant present after heating compared to the post-treated samples.

The promising improvements in humid C_6H_{12} capacity that were obtained by impregnating GC with CH_6N_4O, $C_6H_8O_6$, Na_2SO_3 or $Na_2S_2O_3$ individually could not be retained when these impregnants were used with other compounds. Samples prepared in one imbibing and heating step from 2.4 M $Cu(NO_3)_2$ / 0.3 M $C_6H_8O_6$ or 2.4 M $Zn(NO_3)_2$ / 0.3 M $C_6H_8O_6$ had the longest humid C_6H_{12} breakthrough times of the co-impregnated or post-treated IACs prepared and tested in this study. These samples had shorter humid C_6H_{12} breakthrough times than URC or GC.

Chapter 11

Conclusions and Future Work

11.1 Conclusions

The goal of this research project was to discover, characterize and optimize an IAC capable of SO_2, NH_3, HCN and C_6H_{12} adsorption under dry and humid conditions. It was disappointing that this goal was not met. A variety of different IACs prepared in this study had good overall multi-gas adsorption capacity, but had poor humid C_6H_{12} adsorption.

A study of commercially available activated carbons has shown the wet and dry C_6H_{12} and wet SO_2 adsorption capacity of these materials can vary widely. ACs derived from coconut shells (GC and GG) were found to have the highest dry C_6H_{12} adsorption capacity of the ACs studied here. Data from SAXS and N_2 gas adsorption porosimetry experiments showed these materials were the most microporous and had the smallest average pore dimension of the ACs in this study. ACs derived from coal (NORIT and CDND) had the best humid C_6H_{12} adsorption of the ACs in this study. NORIT and CDND had the lowest equilibrium % mass gain on humidification of all the ACs in this study when exposed to 80% RH water vapour. SAXS experiments showed that C_6H_{12} and water vapour fill the micropores of the AC. The competition between C_6H_{12} gas and pre-adsorbed water for adsorption sites (micropores) resulted in dramatically lower organic vapour adsorption under humid conditions compared to dry conditions.

A comparative study of IACs prepared from metal nitrate precursors showed that samples prepared from $Zn(NO_3)_2$ or $Cu(NO_3)_2$ solutions were the most promising candidates for multi-gas applications. XRD studies showed the dominant impregnant phase after heating these samples was ZnO or CuO. Extensive studies of IACs prepared from aqueous $Zn(NO_3)_2$ or $Cu(NO_3)_2$ solutions were performed to determine the effect that co-impregnation with HNO_3 and heating temperature had on overall multi-gas adsorption capacity. A variety of experimental techniques such as XRD, SEM and TGA were used to study the IAC samples. It was observed that small, well distributed impregnant was key for optimal multi-gas adsorption to occur. The best overall samples were prepared from either 2.4 M $Zn(NO_3)_2$/4 M HNO_3 or $Cu(NO_3)_2$/ 4 M HNO_3 solutions, and were heated at $T_f = 180°C$. The Zn-based IAC had better dry SO_2 and NH_3 capacity; and dry C_6H_{12} and HCN/NCCN breakthrough times as good as or better than the Cu-based sample or the commercially available URC sample! The Zn-based IAC had reasonably good wet SO_2, NH_3 and HCN capacity, but had poor humid C_6H_{12} adsorption. The main advantage that the ZnO impregnated sample had over the CuO or URC samples was that it did not require an additional Mo^{6+} impregnant to be added. The simple, single step impregnation method and reasonable heating temperatures make IACs prepared from $Zn(NO_3)_2$/HNO_3 solutions of commercial interest. A patent based on this research was filed on November 8, 2010 [105].

IACs prepared from aqueous $Cu(NO_3)_2$ solutions were studied as a function of impregnant loading, co-impregnation with HNO_3 and heating temperature. IACs prepared from $Zn(NO_3)_2$ and HNO_3 were studied as a function of heating temperature. Good agreement was observed in the data obtained from XRD, SAXS and N_2 adsorption porosimetry experiments performed on these samples. For IACs prepared from $Cu(NO_3)_2$ that were heated at $T_f = 180°C$, it was shown that co-impregnation with more concentrated HNO_3 resulted in smaller, better distributed impregnant on the AC substrate after heating. Good impregnant distribution resulted in improved multi-gas adsorption capacity. A model describing pore filling in IACs prepared from $Cu(NO_3)_2$ or $Cu(NO_3)_2$/HNO_3 solutions was discussed. In the heating temperature study, changes in the SAXS data obtained from Cu-based IACs heated at different temperatures corresponded to impregnant phase changes. These observations agreed with XRD data. Changes in the intensity of the SAXS signal obtained from the Cu-based samples were observed during transitions from $Cu_2(OH)_3NO_3$ to CuO to Cu_2O as the heating temperatures were increased. The changes in the intensity of the SAXS data are due to impregnant agglomeration, which is apparently significant as the Cu-based impregnant is thermally decomposed. Much more gradual changes were observed in SAXS data from the Zn-based IACs. The dominant impregnant phase (ZnO) did not change over the heating range from T_f = 160 - 300°C. Increased intensity in the SAXS data may have been due to particle agglomeration due to the loss of surface oxygen during heating.

The comprehensive SAXS study of Cu- and Zn-based IACs (discussed in chapter 6) is thought to be the first of its kind. SAXS data in the $q \leq 0.06$ Å^{-1} range gave information about the relative amount of large particle size impregnant occupying meso- and macropores. The SAXS results obtained in this range were in excellent agreement with XRD data. SAXS data in the $q \approx 0.06$ - 0.2 Å^{-1} range gave information about relatively small ($\leq$ 3 nm) particle size impregnant. The XRD method does not provide information on such small impregnant nanocrystallites. SAXS data in the $q \approx 0.2$ - 0.4 Å^{-1} range gave information about how the impregnant was filling the micropores. Good agreement between parameters obtained from fitting the SAXS data and N_2 gas adsorption porosimetry experiments was observed. It takes approximately 4 - 5 hours to prepare and analyze 9 samples using SAXS. It takes 24 - 48 hours to prepare and analyze a single sample using N_2 gas adsorption porosimetry. The SAXS method was proven to be well-suited to rapid screening of IAC samples in this work.

IACs prepared from aqueous mixed metal nitrate, HNO_3 and H_3PO_4•$12MoO_3$ solutions that were heated at T_f = 200°C, had good overall multi-gas adsorption capacity but poor humid C_6H_{12} adsorption. The poor humid C_6H_{12} adsorption was caused by oxidation of the AC substrate from the HNO_3 treatment. When co-impregnated with HNO_3 and H_3PO_4•$12MoO_3$, the Zn/Cu-, Mn/Cu- and Fe/Cu-based IACs had overall dry multi-gas adsorption capacities that were better than Cu-based IACs or the commercially available URC sample. Reducing the amount of $Cu(NO_3)_2$ by substituting $Zn(NO_3)_2$, $Mn(NO_3)_2$ or $Fe(NO_3)_3$ may provide cost savings, without a loss in performance, to producers of multi-gas IACs. Substituting other impregnants for $Cu(NO_3)_2$ may also lower the amount of Mo^{6+} impregnant that is required, which would allow additional savings in raw materials cost.

IACs prepared from $Zn(NO_3)_2$ and different co-impregnated acids failed to identify a replacement for HNO_3 as an impregnant in multi-gas formulations. The overall gas adsorption capacity of the IACs co-impregnated with $Zn(NO_3)_2$ and 4 M acid that were heated at $T_f = 200°C$, ranked as: $HNO_3 > C_2H_4O_2 > HCl > H_2SO_4 > H_3PO_4 > C_4H_6O_6$. The humid C_6H_{12} adsorption of the samples in the co-impregnated acid study was poor.

A comparative study of IACs prepared with either $Zn(NO_3)_2$ or $Cu(NO_3)_2$ and $C_{12}H_{22}CuO_{14}$, $C_{12}H_{22}O_{11}$, $C_6H_{12}O_6$, or $C_6H_{12}O_7$ produced some promising results. IACs impregnated with $C_{12}H_{22}CuO_{14}$, or $Zn(NO_3)_2$ and $C_{12}H_{22}CuO_{14}$ that were heated at $T_f = 180°C$, had better dry and wet C_6H_{12} capacity than URC. The $Zn(NO_3)_2$ and $C_{12}H_{22}CuO_{14}$-impregnated sample had reasonably good dry SO_2, and wet and dry HCN breakthrough times, but had poor NH_3 adsorption. Adding $ZnCl_2$ to the impregnating formula resulted in increased NH_3 capacity but decreased SO_2 and HCN capacity (due to formation of large grain size ZnO). The humid C_6H_{12} capacity of this sample was poor. XRD data showed that 0.20 M $C_6H_{12}O_7$ could be co-impregnated with either $Zn(NO_3)_2$ or $Cu(NO_3)_2$ to produce IACs with relatively small, well distributed impregnant after heating. IACs prepared from solutions with these impregnants present did not show improvements in overall multi-gas adsorption capacity, but in some cases offered improved humid C_6H_{12} capacity.

A study of impregnants aimed at improving humid C_6H_{12} adsorption showed that IACs could be prepared with better humid C_6H_{12} capacity than URC or GC. IACs prepared from aqueous solutions with concentrations $\leq$ 0.75 M that were heated at $T_f = 200°C$, had longer humid C_6H_{12} breakthrough times than URC, and breakthrough times that were greater than or equal to those obtained from GC. It was found that when additional impregnants targeting SO_2, NH_3 and HCN were added, the humid C_6H_{12} adsorption decreased. Multi-gas IACs prepared by co-impregnation had better overall performance than post-treated samples.

11.2 Future Work

One of the most challenging aspects of this project is the large amount of gas testing required. For a single multi-gas IAC to be tested, under dry and humid conditions, for SO_2, NH_3, HCN and C_6H_{12} adsorption, requires approximately 7 - 12 hours. Results from approximately 261 different samples were presented in this thesis. This requires a lot of work and a coordinated effort between researchers at Dalhousie University and 3M Canada Company (Brockville, ON). In this project I have had the good fortune of being exposed to combinatorial screening methods for respirator carbons. This work has been led by Dr. Jennifer Romero in Dr. Dahn's lab [110]. This method allows for rapid screening of promising respirator carbon materials. More work is required to better correlate promising results from the combinatorial screening method to flow test results on larger samples. If promising materials discovered at Dalhousie University are to be fully realized, work involving scaling multi-gas IACs from laboratory sized samples ($\approx$ 15 grams of material) to production sized samples (tens to hundreds of kilograms of material) needs to be performed as well. It may be outside the scope off the current research project to perform this work.

It was shown that ACs derived from coal precursors (NORIT, CDND) had better humid C_6H_{12} adsorption and lower dry C_6H_{12} adsorption than ACs derived from coconut shells (GC and GG). Work involving the optimization of current multi-gas formulations and the discovery of new impregnants should be performed using coal based ACs (e.g. NORIT) as the base carbon. Although dry C_6H_{12} adsorption would decrease, in the author's opinion the higher humid C_6H_{12} adsorption afforded by the coal derived ACs is worthy of further investigation.

Studies involving layered beds would be interesting to perform. Choosing IACs with good overall multi-gas adsorption (the Zn-4M A-180 or Zn/Cu/HNO_3/PMA samples for example) and either mixing them with a good humid C_6H_{12} AC (NORIT for example) would be useful. Optimization of a mixed layer material may yield an IAC with good multi-gas capability and enhanced humid C_6H_{12} and SO_2 capacity. A configuration with a buffer layer of NORIT AC followed by a multi-gas IAC bed might be another useful way to improve humid organic vapour adsorption.

Transmission electron microscopy (TEM) studies of metal oxide IACs might be useful to better estimate the impregnant particle size and distribution. TEM experiments would be a nice compliment to the SAXS, XRD and SEM methods currently used in the respirator carbon project.

Theoretical studies may be useful to help identify impregnants (or alternative adsorbents) that have good humid organic vapour adsorption. Theory might be able to predict the optimal properties required for good humid organic vapour adsorption (e.g. a hydrophobic surface in a pore ?). Although it is outside the area of this author's expertise, a better theoretical understanding of the type of impregnant required to optimize humid organic vapour adsorption would be useful.

These suggestions barely scratch the surface of possible future research directions for multi-gas respirator carbons. Alternative adsorbents like zeolites or metal-organic frameworks [87] are promising, but can be expensive and technically challenging to prepare. The low cost and versatility of activated carbon ensures it will be used in respiratory protection devices for the foreseeable future. Work to improve existing multi-gas IACs or discover new ones must continue.

Appendix A

Copyright Releases

A.1 Journal of Colloid and Interface Science

A.2 Carbon

A.3 Journal of Hazardous Materials

The author retains the following rights*

The right to make copies (print or electronic) of the journal article for your own personal use, including for your own classroom teaching use;

The right to make copies and distribute copies of the journal article (including via e-mail) to research colleagues, for personal use by such colleagues for scholarly purposes*;

The right to post a pre-print version of the journal article on Internet websites including electronic pre-print servers, and to retain indefinitely such version on such servers or sites for scholarly purposes* (with some exceptions such as The Lancet and Cell Press. See also our information on External linkelectronic preprints for a more detailed discussion on these points)*;

The right to post a revised personal version of the text of the final journal article (to reflect changes made in the peer review process) on your personal or institutional website or server for scholarly purposes*, incorporating the complete citation and with a link to the Digital Object Identifier (DOI) of the article (but not in subject-oriented or centralized repositories or institutional repositories with mandates for systematic postings unless there is a specific agreement with the publisher. External linkClick here for further information);

The right to present the journal article at a meeting or conference and to distribute copies of such paper or article to the delegates attending the meeting;

For your employer, if the journal article is a work for hire, made within the scope of the authors employment, the right to use all or part of the information in (any version of) the journal article for other intra-company use (e.g. training);

Patent and trademark rights and rights to any process or procedure described in the journal article;

The right to include the journal article, in full or in part, in a thesis or dissertation;

The right to use the journal article or any part thereof in a printed compilation of your works, such as collected writings or lecture notes (subsequent to publication of the article in the journal); and

The right to prepare other derivative works, to extend the journal article into book-length form, or to otherwise re-use portions or excerpts in other works, with full acknowledgement of its original publication in the journal.

***Commercial purposes and systematic distribution**

Authors of Elsevier-published articles may use them only for scholarly purposes as set out above and may not use or post them for commercial purposes or under policies or other mechanisms designed to aggregate and openly disseminate manuscripts or articles or to substitute for journal-provided services. This includes the use or posting of articles for commercial gain or to substitute for the services provided directly by the journal including the posting by companies of their employee-authored works for use by customers of such companies (e.g. pharmaceutical companies and physician-prescribers); commercial exploitation such as directly associating advertising with such postings; the charging of fees for document delivery or access; the systematic distribution to others via e-mail lists or list servers (to parties other than known colleagues), whether for a fee or for free; the posting of links to sponsored articles by commercial third parties including pharmaceutical companies; institutional, funding body or government manuscript posting policies or mandates that aim to aggregate and openly distribute the accepted, peer reviewed manuscripts or published journal articles authored by its researchers or funded researchers; and subject repositories that aim to aggregate and openly distribute accepted peer reviewed manuscripts or published journal articles authored by researchers in specific subject areas.

As documented at http://www.elsevier.com/wps/find/authorsview.authors/rights.

Bibliography

[1] E. Frackowiak, "Carbon materials for supercapacitor application," *Physical Chemistry Chemical Physics*, vol. 9, pp. 1774–1785, 2007.

[2] J. R. Dahn, W. Xing, and Y. Gao, "The 'falling cards model' for the structure of microporous carbons," *Carbon*, vol. 35, pp. 825–830, 1997.

[3] B. E. Conway, *Electrochemical Supercapacitors: Scientific Fundamentals and Technological Applications*. Kluwer-Plenum Publishers Co., New York, 1999.

[4] T. J. Bandosz, ed., *Activated Carbon Surfaces in Enviromental Remediation*. Elsevier Ltd, 2006.

[5] P. J. Reucroft, W. H. Simpson, and L. A. Jonas, "Sorption properties of activated carbon," *The Journal of Physical Chemistry*, vol. 75, pp. 3526–3531, 1971.

[6] W. D. Miles, "The idea of chemical warfare in modern times," *Journal of the History of Ideas*, vol. 31, pp. 297–304, 1970.

[7] R. E. Wilson and J. C. Whetzel, "Impregnated Carbon and Process of Making Same," U.S. Patent No. 1519470, 1921.

[8] B. R. Alves and A. J. Clark, "An examination of the products formed on reaction of hydrogen cyanide and cyanogen with copper, chromium (6+) and copper-chromium (6+) impregnated activated carbons," *Carbon*, vol. 24, pp. 287–294, 1986.

[9] V. Bush, J. B. Conant, and W. A. Noyes, *Summary Technical Report of Division 10, Military Problems with Aerosols and Nonpersistent Gases*, vol. 1. NRDC Pentagon, Washington D.C., 1946.

[10] P. A. Barnes, M. J. Chinn, E. A. Dawson, and P. R. Norman, "Preparation, Characterisation and Application of Metal-doped Carbons for Hydrogen Cyanide Removal," *Adsorption Science and Technology*, vol. 20, pp. 817–833, 2002.

[11] J. P. Wise, Sr., S. S. Wise, and J. E. Little, "The cytotoxicity and genotoxicity of particulate and soluble hexavalent chromium in human lung cells," *Mutation Research/Genetic Toxicology and Environmental Mutagenesis*, vol. 517, pp. 221–229, 2002.

[12] http://www.osha.gov/OshDoc/data_General_Facts/hexavalent_chromium.pdf, "Health Effects of Hexavalent Chromium," July 2006.

[13] D. T. Doughty, W. J. Knebel, and J. W. Cobes III, “Chromium-free impregnated activated carbon for adsorption of toxic gases and/or vapours in industrial applications,” U.S. Patent No. 5492882, 1996.

[14] L. A. Brey, S. J. Smith, and G. E. Weagle., “Broad spectrum filter system including tungsten-based impregnant and being useful for filtering contaminants from air or other gases,” U.S. Patent No. 7309513, 2007.

[15] Enviroment Canada, “PRIORITY SUBSTANCES LIST ASSESSMENT REPORT: Ammonia in the Aquatic Environment,” 1999.

[16] A. Birenzvige, P. N. Krishnan, and G. K. Knoss, “Evolution of Ammonia from Type ASC Whetlerite,” Coppin State College Report for U.S. Army Armament Munitions Chemical Command, 1992.

[17] R. N. Nickolov and D. R. Mehandjiev, “Comparative study on removal efficiency of impregnated carbons for hydrogen cyanide vapors in air depending on their phase composition and porous textures,” *Journal of Colloid and Interface Science*, vol. 273, pp. 87–94, 2004.

[18] American Carbon Society, *The Reaction of Hydrogen Cyanide and Cyanogen with Unimpregnated Activated Carbons*, Presented at the 19th Biennial Conference on Carbon, Penn State University, American Carbon Society, 1989.

[19] R. H. Bradley, “Surface studies of Cu/Cr/Ag impregnated microporous carbons,” *Applied Surface Science*, vol. 90, pp. 271–276, 1995.

[20] J. A. Rossin and R. W. Morrison, “Spectroscopic analysis and performance of an experimental copper/zinc impregnated, activated carbon,” *Carbon*, vol. 29, pp. 887–892, 1991.

[21] L.M. Croll, J. R. Dahn, A. R. Siedle, J. W. H. Smith, P. Westreich, and T. E. Wood, “Ammonia-Free Gaseous Air Filter,” U.S. Patent Application No. 201000505832009, 2009.

[22] H. Fortier, P. Westreich, S. Selig, C. Zelenietz, and J. R. Dahn, “Ammonia, cyclohexane, nitrogen and water adsorption capacities of an activated carbon impregnated with increasing amounts of $ZnCl_2$, and designed to chemisorb gaseous NH_3 from an air stream,” *Journal of Colloid and Interface Science*, vol. 320, pp. 423–435, 2008.

[23] J. W. H. Smith, P. Westreich, L. M. Croll, J. H. Reynolds, and J. R. Dahn, “Understanding the role of each ingredient in a basic copper carbonate based impregnation recipe for respirator carbons,” *Journal of Colloid and Interface Science*, vol. 337, pp. 313–321, 2009.

[24] J. W. H. Smith, P. Westreich, H. Abdellatif, P. Filbee-Dexter, A. J. Smith, T. E. Wood, L. M. Croll, J. H. Reynolds, and J. R. Dahn, “The investigation of copper-based impregnated activated carbons prepared from water-soluble materials for broad spectrum respirator applications,” *Journal of Hazardous Materials*, vol. 180, pp. 419–428, 2010.

[25] J. W. H. Smith, P. Westreich, A. J. Smith, H. Fortier, L. M. Croll, J. H. Reynolds, and J. R. Dahn, “Investigation of copper oxide impregnants prepared from various precursors for respirator carbons,” *Journal of Colloid and Interface Science*, vol. 341, pp. 162–170, 2010.

[26] http://www.cdc.gov/niosh/npptl/respstds.html, “Respirator Standards,” November 2009.

[27] S.-T. Ding, H. Yao, and X.-B. Yang, “Respirator National Standard Development in China - A Perspective of Past Decade,” *Journal of the International Society for Respiratory Protection*, vol. 27, pp. 71–81, 2010.

[28] http://www.cbc.ca/thenational/indepthanalysis/story/2011/03/11/national-disasterinjapan.html, “Disaster in Japan,” June 2011.

[29] http://www.cbc.ca/news/politics/story/2011/12/01/pol-baird-committee.html, “Libya’s chemical weapons pose risk to Canada,” December 2011.

[30] M. Smisek and S. Cerny, *Active Carbon, Manufacture, Properties and Applications: Topics in Inorganic and General Chemistry.* Elsevier Publishing Company, 1970.

[31] J. W. Patrick, *Porosity in Carbons: Characterization and Applications.* John Wiley and Sons Inc., 1994.

[32] R. H. Dreyfus, J. L. Cornillot, and P. C. Fazio-Fluehr, *Annual Book of ASTM Standards: Section 15: General Products, Chemical Specialities and end Use Products, 15.01, Refactories, Activated Carbon; Advanced Ceramics.* ASTM, 2003.

[33] A. W. Adamson, *Physical Chemistry of Surfaces 5th Edition.* New York: John Wiley and Sons Inc., 1990.

[34] I. Langmuir, “The constitution and fundamental properties of solids and liquids. Part I. Solids,” *Journal of the American Chemical Society*, vol. 38, pp. 2221–2295, 1916.

[35] S. Brunauer, P. H. Emmett, and E. Teller, “Adsorption of Gases in Multimolecular Layers,” *Journal of the American Chemical Society*, vol. 60, pp. 309–319, 1938.

[36] T. Otowa, Y. Nojima, and T. Miyazaki, "Development of KOH activated high surface area carbon and its application to drinking water purification," *Carbon*, vol. 35, pp. 1315–1319, 1997.

[37] Z. Hu and M. P. Srinivasan, "Preparation of high-surface-area activated carbons from coconut shell," *Microporous and Mesoporous Materials*, vol. 27, pp. 11–18, 1999.

[38] G. O. Wood, "Activated carbon adsorption capacities for vapors," *Carbon*, vol. 30, pp. 593–599, 1992.

[39] J. W. H. Smith, "Investigation of Copper Based Impregnation Recipes for the Optimization of Respirator Carbons," Master's thesis, Department of Physics and Atmospheric Science, Dalhousie University, Nova Scotia, Canada, 2008.

[40] H. Fortier, *The Science of Impregnation and the Optimization of the Performance of Impregnated Activated Carbons for Gas Mask Applications.* PhD thesis, Department of Chemistry, Dalhousie University, Nova Scotia, Canada, 2007.

[41] P. Westreich, H. Fortier, S. Flynn, S. Foster, and J. R. Dahn, "Exclusion of Salt Solutions from Activated Carbon Pores and the Relationship to Contact Angle on Graphite," *Journal of Physical Chemistry C*, vol. 111, pp. 3680–3684, 2007.

[42] H. Fortier, C. Zelenietz, T. R. Dahn, P. Westreich, D. A. Stevens, and J. R. Dahn, "SO_2 adsorption capacity of K_2CO_3-impregnated activated carbon as a function of K_2CO_3 content loaded by soaking and incipient wetness," *Applied Surface Science*, vol. 253, pp. 3201–3207, 2007.

[43] R. C. Soares, J. M. Loureiro, C. Sereno, and A. E. Rodrigues, "Modeling and Simulation of Carbon Mask Adsorptive Reactors," *Industrial & Engineering Chemistry Research*, vol. 34, pp. 2762–2768, 1995.

[44] L. A. Jonas, "Reaction steps in gas sorption by impregnated carbon," *Carbon*, vol. 16, pp. 115–119, 1978.

[45] A. Wheeler and A. J. Robell, "Performance of fixed-bed catalytic reactors with poison in the feed," *Journal of Catalysis*, vol. 13, pp. 299–305, 1969.

[46] L. A. Jonas and J. A. Rehrmann, "Predictive equations in gas adsorption kinetics," *Carbon*, vol. 11, pp. 59–64, 1973.

[47] G. O. Wood and E. S. Moyer, "A review of the Wheeler equation and comparison of its applications to organic vapor cartridge breakthrough data," *American Industrial Hygiene Association Journal*, vol. 50, pp. 400–407, 1989.

[48] P. Lodewyckx, G. O. Wood, and S. K. Ryu, "The Wheeler−Jonas equation: a versatile tool for the prediction of carbon bed breakthrough times," *Carbon*, vol. 42, pp. 1351–1355, 2004.

[49] P. Lodewyckx and L. Verhoeven, “Using the modified Wheeler−Jonas equation to describe the adsorption of inorganic molecules: chlorine,” *Carbon*, vol. 41, pp. 1215–1219, 2003.

[50] L. Verhoeven and P. Lodewyckx, “Using the Wheeler−Jonas equation to describe adsorption of inorganic molecules: Ammonia,” in *Proceedings of the Second International Carbon Conference*, Carbon Conference, 2001.

[51] A. Dabrowski, “Adsorption - from theory to practice,” *Advances in Colloid and Interface Science*, vol. 93, pp. 135–224, 2001.

[52] D. A. Stevens, *Mechanisms for Sodium Insertion in Carbon Materials.* PhD thesis, Department of Chemistry, Dalhousie University, 2000.

[53] J. P. Olivier, “Modeling Physical Adsorption on Porous and Nonporous Solids Using Density Functional Theory,” *Journal of Porous Materials*, vol. 2, pp. 9–17, 1995.

[54] H. P. Klug and L. E. Alexander, *X-Ray Diffraction Procedures for Polycrystalline and Amorphous Materials.* London: John Wiley and Sons, 2nd ed., 1974.

[55] B. D. Cullity and S. R. Stock, *Elements of X-Ray Diffraction.* New Jersey: Prentice Hall, 3rd ed., 2001.

[56] International Center for Diffraction Data, *Joint Committee on Powder Diffraction Standards.* Powder Diffraction Files-2, Newton Square, 2002.

[57] M. Wojdyr, “*Fityk*: A general-purpose peak fitting program,” *Journal of Applied Crystallography*, vol. 43, pp. 1126–1128, 2010.

[58] B. B. He and U. Preckwinkel, “X-ray Optics for Two-Dimensional Diffraction,” *Advances in X-ray Analysis*, vol. 45, pp. 332–337, 2002.

[59] *Bruker Advanced X-Ray Solutions: NanoSTAR SAXS System User’s Manual Vol.2.* 2004.

[60] P. Debye, H. R. Anderson, and H. Brumberger, “Scattering by an Inhomogeneous solid. II. The Correlation Function and Its Application,” *Journal of Applied Physics*, vol. 28, pp. 679–683, 1957.

[61] A. Guinier and G. Fournet, *Small-Angle Scattering of X-Rays.* John Wiley and Sons, 1955.

[62] O. Glatter and O. Kratky, eds., *Small Angle X-ray Scattering.* London: Academic Press Inc., 1982.

[63] E. Buiel, *Lithium Insertion In Hard Carbon Anode Materials For Li-Ion Batteries*. Phd, Dalhousie University, 1998.

[64] M. Kalliat, C. Y. Kwak, and P. W. Schmidt, *Small-Angle X-Ray Investigation of the Porosity in Coals*. Washington, D.C.: American Chemical Society, 1981.

[65] G. Laudisio, R. K. Dash, J. P. Singer, G. Yushin, Y. Gogotsi, and J. E. Fischer, "Carbide−Derived Carbons: A Comparative Study of Porosity Based on Small-Angle Scattering and Adsorption Isotherms," *Langmuir*, vol. 22, pp. 8945–8950, 2006.

[66] L. He, S. M. Chathoth, Y. B. Melnichenko, V. Presser, J. McDonough, and Y. Gogotsi, "Small-angle neutron scattering characterization of the structure of nanoporous carbons for energy-related applications," *Microporous and Mesoporous Materials*, vol. 149, pp. 46–54, 2012.

[67] T. Zheng, W. Xing, and J. R. Dahn, "Carbons prepared from coals for anodes of lithium−ion cells," *Carbon*, vol. 34, pp. 1501–1507, 1996.

[68] R. Yang, T. R. Dahn, and J. R. Dahn, "Fe–N–C Oxygen-Reduction Catalysts Supported on "Burned-Off" Activated Carbon," *Journal of The Electrochemical Society*, vol. 156, pp. B493–B498, 2009.

[69] E. R. Buiel, A. E. George, and J. R. Dahn, "Model of micropore closure in hard carbon prepared from sucrose," *Carbon*, vol. 37, pp. 1399–1407, 1999.

[70] K. László, O. Czakkel, K. Josepovits, C. Rochas, and E. Geissler, "Influence of Surface Chemistry on the SAXS Response of Polymer-Based Activated Carbons," *Langmuir*, vol. 21, pp. 8443–8451, 2005.

[71] W. Weibull, "A Statistical Distribution Function of Wide Applicability," *Journal of Applied Mechanics*, pp. 293–297, 1951.

[72] M. Dubinin and V. Astakhov, "Development of the concepts of volume filling of micropores in the adsorption of gases and vapours by microporous adsorbents communication 1. Carbon adsorbents," *Izvestiya Akademii Nauk SSSR, Seriya Khimicheskaya*, pp. 5–11, 1971.

[73] S. G. Chen and R. T. Yang, "Theoretical Basis for the Potential Theory Adsorption Isotherms. The Dubinin-Radushkevich and Dubinin-Astakhov Equations," *Langmuir*, vol. 10, pp. 4244–4249, 1994.

[74] N. D. Hutson and R. T. Yang, "Theoretical basis for the Dubinin-Radushkevitch (D-R) adsorption isotherm equation," *Adsorption*, vol. 3, pp. 189–195, 1997.

[75] H. Fortier, S. Zhang, and J. Dahn, "Simulations of isothermal oven tests of impregnated activated carbons in cylindrical and cubic sample holders," *Carbon*, vol. 42, pp. 2385–2392, 2004.

[76] S. Zhang and J. R. Dahn, "Impact of moisture on the thermal behavior of K_2 CO_3 − impregnated respirator carbons," *Carbon*, vol. 41, pp. 1695–1705, 2003.

[77] S. Zhang, S. A. Stewart, T. D. Hatchard, and J. R. Dahn, "Thermal runaway prediction for impregnated activated carbons from isothermal DSC measurements," *Carbon*, vol. 41, pp. 903–913, 2003.

[78] J. W. H. Smith, J. V. Romero, T. R. Dahn, K. Dunphy, B. Sullivan, M. Mallay, L. M. Croll, J. H. Reynolds, C. Andress, and J. R. Dahn, "The effect of heating temperature and nitric acid treatments on the performance of Cu- and Zn-based broad spectrum respirator carbons," *Journal of colloid and interface science*, vol. 364, pp. 178–194, 2011.

[79] H. Boehm, "Some aspects of the surface chemistry of carbon blacks and other carbons," *Carbon*, vol. 32, pp. 759–769, 1994.

[80] D. Y. Kwok and A. W. Neumann, *Contact angle measurement and contact angle interpretation*, vol. 81. 1999.

[81] R. J. Dombrowski, D. R. Hyduke, and C. M. Lastoskie, "Pore Size Analysis of Activated Carbons from Argon and Nitrogen Porosimetry Using Density Functional Theory," *Langmuir*, vol. 16, pp. 5041–5050, 2000.

[82] C. Lastoskie, K. E. Gubbins, and N. Quirket, "Pore Size Hetrogeneity and the Carbon Slit Pore: A Density Functional Theory Model," *Langmuir*, vol. 9, pp. 2693–2702, 1999.

[83] A. A. Lizzio and A. Debarr, "Effect of surface area and chemisorbed oxygen on the SO_2 adsorption capacity of activated char," *Fuel*, vol. 75, pp. 1515–1522, 1996.

[84] S. Kisamori, K. Kuroda, S. Kawano, I. Mochida, Y. Matsumura, and M. Yoshikawat, "Oxidative Removal of SO_2 and Recovery of H_2SO_4 over Poly(acrylonitrile)-Based Active Carbon Fiber," *Energy & Fuels*, vol. 8, pp. 1337–1340, 1994.

[85] P. Davini, "The effect of certain metallic derivatives on the adsorption of sulphur dioxide on active carbon," *Carbon*, vol. 39, pp. 419–424, 2001.

[86] C. Moreno-Castilla, I. Fernandez-Morales, M. Domingo-Garcia, and F. J. Lopez-Garzon, "Carbon Molecular Sieves Produced by the Fixation of Sulphur Surface Complexes," *Chromatographia*, vol. 20, pp. 709–712, 1985.

[87] C. E. Wilmer, M. Leaf, C. Y. Lee, O. K. Farha, B. G. Hauser, J. T. Hupp, and R. Q. Snurr, "Large-scale screening of hypothetical metal-organic frameworks," *Nature Chemistry*, vol. 4, pp. 83–89, 2011.

[88] J. Chmiola, G. Yushin, Y. Gogotsi, C. Portet, P. Simon, and P. L. Taberna, "Anomalous Increase in Carbon Capacitance at Pore Sizes Less Than 1 Nanometer," *Science*, vol. 313, pp. 1760–1763, 2006.

[89] P. Lodewyckx and E. F. Vansant, "Influence of Humidity on Adsorption Capacity from the Wheeler−Jonas Model for Prediction of Breakthrough Times of Water Immiscible Organic Vapors on Activated Carbon Beds," *American Industrial Hygiene Association Journal*, vol. 60, pp. 612–617, 1999.

[90] K. László, O. Czakkel, G. Dobos, P. Lodewyckx, C. Rochas, and E. Geissler, "Water vapour adsorption in highly porous carbons as seen by small and wide angle X-ray scattering," *Carbon*, vol. 48, pp. 1038–1048, Apr. 2010.

[91] B. Xiao and K. M. Thomas, "Adsorption of Aqueous Metal Ions on Oxygen and Nitrogen Functionalized Nanoporous Activated Carbons," *Langmuir*, vol. 21, pp. 3892–3902, 2005.

[92] C.-C. Huang, H.-S. Li, and C.-H. Chen, "Effect of surface acidic oxides of activated carbon on adsorption of ammonia," *Journal of Hazardous Materials*, vol. 159, pp. 523–527, 2008.

[93] W. M. Haynes, ed., *CRC Handbook of Chemistry and Physics*. National Institute of Standards and Technology, Boulder, Colorado, USA: CRC Press, 91st ed., 2010.

[94] K. Wieczorek-Ciurowa and A. J. Kozak, "The Thermal Decomposition of $Fe(NO_3)_3 \cdot 9H_2O$," *Journal Of Thermal Analysis and Calorimetry*, vol. 58, pp. 647–651, 1999.

[95] B. Pacewska and M. Keshr, "Thermal transformations of aluminium nitrate hydrate," *Thermochimica Acta*, vol. 385, pp. 73–80, 2002.

[96] W. P. Griffith, "Cyanide Complexes of the Transition Metals," *Quarterly Reviews, Chemical Society*, vol. 16, pp. 188–207, 1962.

[97] C. Moreno-Castilla, M. A. Ferro-Garcia, J. P. Joly, I. Bautista-Toledo, F. Carrasco-Marin, and J. Rivera-Utrilla, "Activated Carbon Surface Modifications by Nitric Acid, Hydrogen Peroxide, and Ammonium Peroxydisulfate Treatments," *Langmuir*, pp. 4386–4392, 1995.

[98] Abdel-Nasser A. El-Hendawy, "Influence of HNO_3 oxidation on the structure and adsorptive properties of corncob-based activated carbon," *Carbon*, vol. 41, pp. 713–722, 2003.

[99] http://www.cdc.gov/niosh/npptl/standardsdev/cbrn/apr/standard/aprstd-a.html, "Respirator Testing," January 2004.

[100] H.-H. Tseng and M.-Y. Wey, “Study of SO_2 adsorption and thermal regeneration over activated carbon-supported copper oxide catalysts,” *Carbon*, vol. 42, pp. 2269–2278, 2004.

[101] F. Tomás-Alonso, “A New Perspective about Recovering SO_2 Offgas in Coal Power Plants: Energy Saving. Part II. Regenerable Dry Methods,” *Energy Sources*, vol. 27, pp. 1043–1049, 2005.

[102] A. Lisovskii, R. Semiat, and C. Aharoni, “Adsorption of sulfur dioxide by active carbon treated by nitric acid: I. Effect of the treatment on adsorption of SO_2 and extractability of the acid formed,” *Carbon*, vol. 35, pp. 1639–1643, 1997.

[103] A. A. Lizzio and J. A. DeBarr, “Mechanism of SO_2 Removal by Carbon,” *Energy & Fuels*, vol. 11, pp. 284–291, 1997.

[104] C. Petit and T. J. Bandosz, “Removal of Ammonia from Air on Molybdenum and Tungsten Oxide Modified Activated Carbons,” *Environmental Science & Technology*, vol. 42, pp. 3033–3039, 2008.

[105] L. M. Croll, J. R. Dahn, J. W. H. Smith, and J. V. Romero, “Zinc Oxide Containing Filter Media and Methods of Forming the Same,” U.S. Patent Application No. 20120111335, 2010.

[106] R. Weiss, S. Vukojević, C. Baltes, R. N. D’Alnoncourt, M. Muhler, and M. Epple, “Copper/Zinc L-Tartrates: Mixed Crystals and Thermolysis to a Mixture of Copper Oxide and Zinc Oxide That Is Catalytically Active in Methanol Synthesis,” *European Journal of Inorganic Chemistry*, vol. 2006, pp. 4782–4786, 2006.

[107] J. Guo, W. S. Xu, Y. L. Chen, and A. C. Lua, “Adsorption of NH_3 onto activated carbon prepared from palm shells impregnated with H_2SO_4,” *Journal of Colloid and Interface Science*, vol. 281, pp. 285–290, 2005.

[108] C. Petit, C. Karwacki, G. Peterson, and T. J. Bandosz, “Interactions of Ammonia with the Surface of Microporous Carbon Impregnated with Transition Metal Chlorides,” *The Journal of Physical Chemistry C*, vol. 111, pp. 12705–12714, 2007.

[109] T. Shibamoto and R. A. Bernhard, “Investigation of pyrazine formation pathways in sugar-ammonia model systems,” *Journal of Agricultural and Food Chemistry*, vol. 25, pp. 609–614, 1977.

[110] J. V. Romero, J. W. H. Smith, C. L. White, S. Trussler, L. M. Croll, and J. R. Dahn, “A combinatorial approach to screening carbon based materials for respiratory protection,” *Journal of Hazardous Materials*, vol. 183, pp. 677–687, 2010.